DESIGN OF GEROTOR GEAR GEOMETRY BY MULTI-OBJECTIVE OPTIMIZATION

by

Andrew Robison

A Dissertation

Submitted to the Faculty of Purdue University

In Partial Fulfillment of the Requirements for the degree of

Doctor of Philosophy

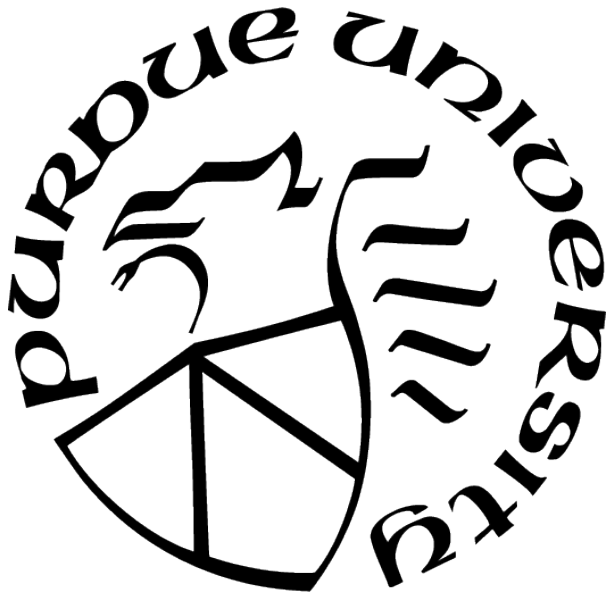

School of Mechanical Engineering

West Lafayette, Indiana

August 2021

THE PURDUE UNIVERSITY GRADUATE SCHOOL
STATEMENT OF COMMITTEE APPROVAL

Dr. Andrea Vacca, Chair

School of Mechanical Engineering

Dr. Farshid Sadeghi

School of Mechanical Engineering

Dr. Raymond J. Cipra

School of Mechanical Engineering

Dr. John Evans

School of Agricultural and Biological Engineering

Approved by:

Dr. Jay Gore

For Jesus Christ, my merciful and faithful savior.

TABLE OF CONTENTS

LIST OF TABLES

LIST OF FIGURES

"The geometry involved in gerotors is of absorbing interest. A whole field of geometry heretofore unexplored is opened up and destined to be studied by engineers and mathematicians."

Myron F. Hill – 1927

ABSTRACT

Gerotor pumps are positive displacement pumps that are frequently used in low-pressure applications such as lubrication and charge pumps. They are characterized by their unique gearset that is an internal gearset with one tooth difference that has continuous contact throughout the entire rotation. Recent trends especially in the automotive industry suggest an increased demand for greater performance from these pumps, e.g. operating with higher pressure, higher speed, lower viscosity fluid, less noise emission, and greater energy efficiency. The shape of the gears is one of the most important aspects of a gerotor pump, as it determines the pump's size and flow, affects its internal leakages, and influences its amount of wear. Although gerotors have been in operation for nearly 100 years, no design methodology has emerged in scientific literature that fully considers all the main performance aspects simultaneously and identifies the best designs. This problem is made more difficult, as gerotors can have an infinite number of different types of profiles. The main goals of this work are therefore to define a method to design gerotor gear geometry for several performance goals, identify the best designs for a given gear profile type, compare the best designs among the various profile types, and invent a new profile type that can offer improved performance over conventional designs.

Gerotor profile generation is described in the beginning, first for the conventional epitrochoidal, hypotrochoidal, and standard cycloidal profile types. Then a description of how to generate gerotors from an arbitrary curve is given and applied to elliptical, generalized cycloidal, cosine, and asymmetric elliptical gerotors. The generalized cycloidal profile type is new to this work.

Multi-objective optimization is used as the method to identify the best gear profiles for a given application considering seven performance metrics and ensuring a feasible gear profile. The seven performance goals to minimize are the radius of a pump for a given geometric displacement and face width, the kinematic flow ripple, the adhesive wear, the contact stress, the tooth tip leakage, the lateral gap leakage, and the mean displacement chamber inlet velocity. The conditions to generate feasible gerotor profiles without cusps or self-intersections are also given as constraints for the optimizations.

Seven gerotor profiles were then optimized using a genetic algorithm to consider all the performance aspects. The design space for each profile type was thoroughly explored, and clear Pareto fronts were identified. The Pareto fronts from each profile type were then combined, and a new Pareto front was identified from the best designs of each profile type. No single profile type proves to be objectively better than the others, but the epitrochoidal, hypotrochoidal, elliptical, and generalized cycloidal profile types tend to produce the best designs. Two methods to select a design from the Pareto front that consider the relative importance of each performance goal were presented.

The optimization strategy was then further validated by demonstrating significant possible performance improvement over state-of-the-art designs in industry and suggesting alternative designs to a specific gearset used in industry that were tested in simulation and experiment. Two generalized cycloidal profiles were selected as alternative designs: the first design matched the fluid dynamic performance of the reference design with significantly reduced contact stress, and the second is a profile that could reduce the outlet flow ripple while fitting within the same pump housing. The contact stress of the reference and alternative designs when including clearance between the gears was compared in finite element analysis. Prototypes of the alternative designs were then manufactured and tested in experiment. The experimental pressure ripples of the alternative designs were compared, and the second design showed a reduction in outlet pressure ripple that validates the proposed design methodology.

This work has thoroughly explored the performance possibilities of the gerotor mechanism and presented a method to select an optimal profile geometry depending on the desired performance characteristics. It has therefore accomplished its goals in making a contribution toward improving the performance gerotor gear geometry.

1. INTRODUCTION

Gerotor pumps are a type of positive displacement pump that are common in low pressure applications such as charge, lubrication, transmission, and fuel pumps. The geometry of their special gears is the topic of this thesis. Here an introduction to the operating principle of a gerotor is given followed by the motivation for seeking a better design methodology for the gear profiles. A brief overview of some of the most important academic work in the area is given, and this is followed by giving the research objectives of this present work.

1.1 Gerotor Operation

Gerotors pumps are an internal gearset with one tooth difference where all of the outer (internally-toothed) gear teeth remain in contact with the inner (externally-toothed) gear, and the centers of the two gears are separated by a center distance that is often called the eccentricity. Their name is the combination of the two words "generated" and "rotor" and was coined by their inventor Myron F. Hill [1]. The contact points between the gears created discrete control volumes that increase and decrease in size with rotation, which is used to generate a pumping action. Gerotor pumps are known for their simplicity, durability, manufacturability, low-noise operation, high-speed operation, and low cost. Their main downsides are difficulty to reach high pressure (over 75 bar) and that they are fixed displacement pumps.

An example gerotor gearset with its ports is shown in in fig. 1.1. As the gearset rotates counterclockwise, the volumes between the gear teeth (displacement chambers) will expand in the first half of their rotation. During this phase, the displacement chambers are connected to the suction port in blue to draw in fluid. In the second half of rotation, the displacement chambers will decrease in volume, so they are connected to the delivery port shown in red to discharge the fluid. An example 3D model of a gerotor pump is shown in fig. 1.2. A gerotor typically consists of only a few key parts: a gearset, a shaft, a case, and a cover. The inner gear usually drives the pump and is typically supported by a rolling element bearing, although it can be a journal bearing as well. The outer gear is typically supported by a journal bearing, although it can also be a rolling element bearing. The design of a gerotor pump has three key considerations: 1) the shape of the gear profiles that determine the

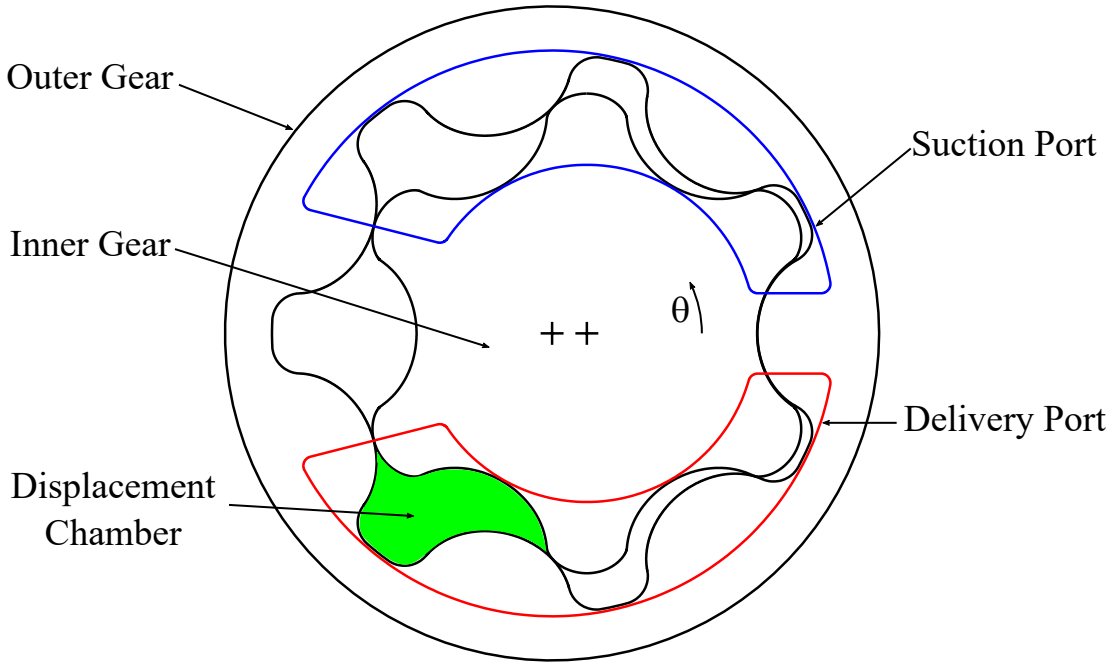

Figure 1.1. Example gerotor gearset with ports

pump's size, discharge flow, and flow rate variability; 2) the shape of the ports, which affects the internal pressurization in the pump and should account for compressibility and internal leakages; and 3) the lubricating interfaces, which are fluid films that separate the gears and the pump case but thereby create small leakage passages in the pump. Gerotors are typically used in open circuit applications, so the low-pressure port is usually at or below atmospheric pressure. The limiting factor on the maximum speed of the pump is then usually incomplete filling, which occurs when the displacement chambers are not able to draw in enough fluid to fill them completely. As the pump rotation speed increases, the volume derivative of the displacement chamber with respect to time also increases. The pressure drop from the suction port to the displacement chamber increases correspondingly, as increased flow must pass through the same restricted area, which leads to incomplete filling.

The three main lubricating interfaces are necessary to prevent excessive wear but also allow internal leakages in the pump are highlighted in figs. 1.3–1.5. The tooth tip gap exists because small clearances on the order of 25 microns are usually introduced to aid in the assembly of the pump, to reduce manufacturing costs, and to account for thermal

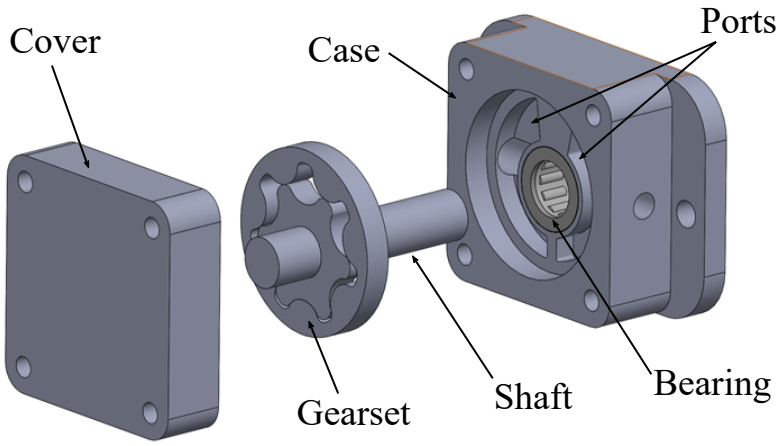

Figure 1.2. Example 3D model of a gerotor pump

expansion. When the displacement chamber transitions between low pressure (LP) and high pressure (HP), fluid can leak between the tips of the gearset as shown in fig. 1.3. The lateral gap exists between the faces of the gears and the pump case as shown in fig. 1.4. A thin film of fluid must separate the the gears from the case and cover, but this small gap creates a leakage path where fluid can move from the HP region to the LP region over the face of the gears. Lastly, if the outer gear is supported by a journal bearing, a thin film of fluid separates the outer gear from the pump case in the radial direction. This can be another source of internal leakage in the pump and is illustrated in fig. 1.5.

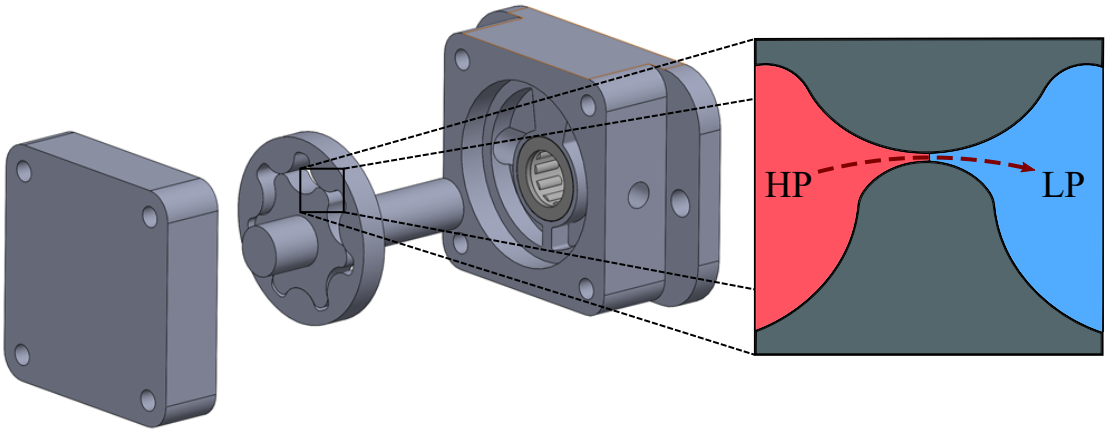

Figure 1.3. Tooth tip gap illustration

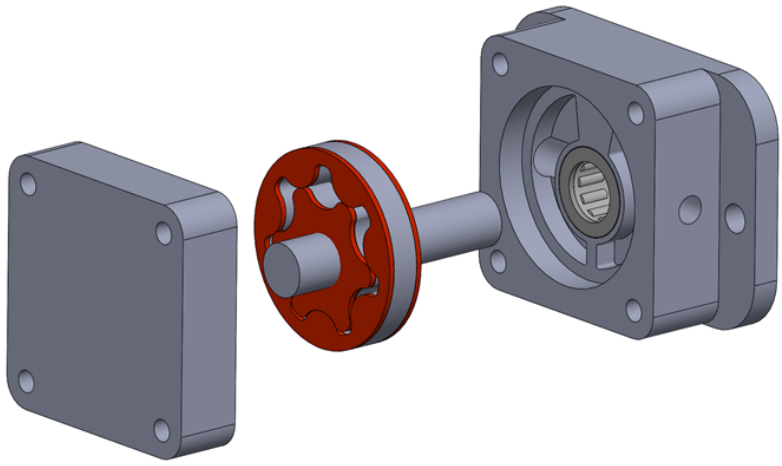

Figure 1.4. Lateral gap illustration

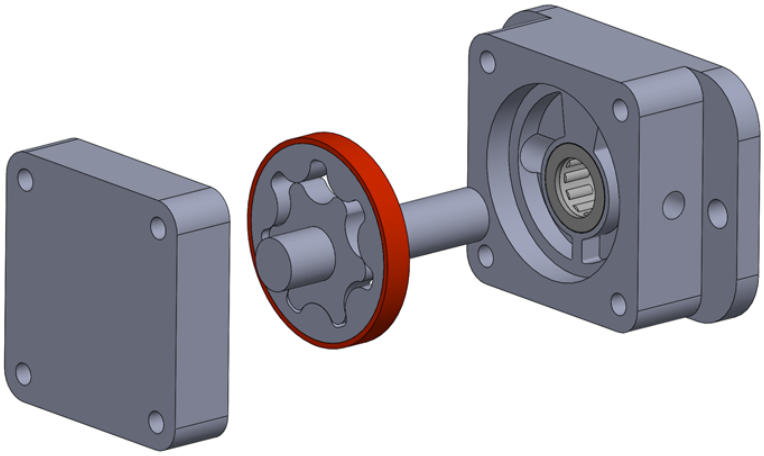

Figure 1.5. Journal bearing gap illustration

1.2 Motivation

Recent trends in the fluid power and automotive industries are demanding greater performance from gerotor pumps. Their low noise emissions, high speed operation, low outlet flow ripple, high durability, and low cost make them the best type of pump for many applications. The main drawbacks are low volumetric efficiency at higher pressures (above 25 bar) and being fixed displacement, although some of the best designs in industry have a maximum continuous operating pressure of 138 bar (2000 psi) [2]. Many applications could be improved with gerotors that are more compact, energy efficient, quiet, and perform in more extreme

operating conditions, i.e. higher speeds, higher pressures, and with lower viscosity fluids [3], [4].

Electrification is one of the greatest present trends in industry and is one of the main drivers for improved performance of gerotor pumps. As vehicles are increasingly becoming fully electric, the energy efficiency of the auxiliary components becomes more important to increase the range of the vehicle and/or decrease the required battery size. Gerotors can also be used in active suspension systems to increase fuel economy and improve user comfort, which is especially important in fully autonomous vehicles. Gerotors are frequently used in automatic transmissions and are one of the greatest sources energy losses, so they are a major focus in improving fuel economy [5]. Additionally, automatic transmissions for electric hybrid vehicles require a pump that can operate independently from the internal combustion engine. Gerotors driven by a variable-speed electric motor are well-suited for this application, and the variable-speed motor can compensate for a fixed-displacement pump to further reduce energy consumption. This type of electric motor and pump pair can also be used as an auxiliary pump to provide increased flow at low engine speeds, which can allow downsizing of main crankshaft-driven lubrication pump to save energy [6]. Both the overall and hydro-mechanical efficiency of these pumps are very important for electric motor downsizing and are therefore an important design consideration.

Another important factor for mobile applications is decreasing the weight of the components as much as possible. One obvious way to decrease the weight of a hydraulic pump is to operate a pump with a smaller volumetric displacement at higher speed and pressure. In the past, the speeds were limited by the internal combustion engine, but as hydraulic pumps are increasingly being driven by electric motors, the maximum speeds can be increased significantly. As the pressure and speeds are increased to improve the power density and the working fluid viscosity decreased to reduce energy loss due to viscous shear, the possibility of wear in gerotors increases significantly. Among charge pump failures in axial piston pumps for one large pump manufacturer, approximately 40% of the failures are due to failures of the gearset [7]. Although durability is one of gerotor pumps' advantages, wear and fatigue must be considered when increasing the power.

Several design challenges must be overcome in advancing the performance of gerotor pumps. Gerotors of the future must be increasingly compact with low outlet flow variability. The outlet flow variability is a major factor in determining the noise emissions from the pump and can have significant effects on the stability of the overall hydraulic system. As internal combustion engines are increasingly being replaced by quiet electric motors, the noise emitted from the pump becomes more noticeable and must therefore be reduced as much as possible. These pumps must also be more energy efficient regarding both their volumetric and hydro-mechanical efficiencies, and the maximum allowable speed must be increased. Gerotors must also become more durable as they work with lower viscosity fluids that do not lubricate as well as traditional fluids. As the power increases contact force and sliding speed between the gears which contributes to additional wear and contact stress between the profiles. To address all these challenges, modern design methodologies such as pump simulation tools and multi-objective optimization techniques must be developed.

One of the most important design considerations of a gerotor pump is the shape of its gears, as it determines the size, displacement, and outlet flow variability of the pump. The gear teeth also have a sealing function to restrict flow between the high- and low-pressure regions of the pump. The shape of the displacement chamber also affects the pump's tendency to experience incomplete filling. The gears also cannot be adjusted for wear, so the profiles should be designed as much as possible to reduce adhesive wear and contact stress. Most of these goals are in opposition to one another, which adds to the challenge of designing a good gerotor pump. The challenge of finding the best gerotor gearset design is further increased because, unlike spur gears, where the involute has proven to be the best tooth profile, an infinite number of possible gerotor profile types exist. Further, and an infinite number of profiles within each type also exist. Finding the best gerotor profile for a given application then is not at all straight-forward.

Many other factors are important beyond the shape of the gearset which include material selection, clearances, port geometry, journal bearing design, and face width, which affects the maximum speed before incomplete filling occurs. Each of these considerations are vitally important to the performance of a gerotor in real operation, but they should be determined after a good gearset has been selected. Most of the recent research in gerotors has been

concentrating in developing lumped parameter and/or CFD fluid dynamic and lubrication models that consider compressibility, internal leakages, micro-motions of the gears, and fluid structure interaction [8]–[10]. These models do a good job of predicting the performance of gerotor pumps in operation, but their long computation time makes them less than ideal for extensive optimization.

A design methodology should therefore be developed that is able to determine the best gerotor profile for a given application when considering the many possible profile types and all performance objectives for the pumps. Multi-objective optimization is a good method to use to answer this question, but because of the number of designs that must be evaluated to fully identify the optimal space, fast gear generation and evaluation algorithms must be developed first. The results from the optimizations can then be used to identify the best gerotor profile type and to identify the best design for new applications.

1.3 State of the Art

Many inventors and researchers have dedicated a significant portion of their careers to the development of gerotor gear geometry beginning in the early 20th century. Although the concept of a gerotor existed as early as 1787, the invention of gerotors is typically accredited to Myron. F. Hill, who published the book titled *Kinematics of Gerotors* in 1927 and was the first to manufacture a working gerotor pump [1]. Hill set out to invent "an efficient, durable and simple rotary engine movement for displacing the clumsy and troublesome piston and cylinder" [1, p. 5]. Eventually he discovered that trochoids have the correct geometric relationship to form a continuous contact internal gearset that can be used as a pump or compressor. He also determined that cycloids as well as other curves such as ellipses and even asymmetric curves can be used to form a gerotor.

The next most significant contributions to gerotor gear geometry in scientific literature were given by Earle Buckingham and Allen Hall. Buckingham gave a short description of gerotor profiles in his classic work *Analytical Mechanics of Gears* [11, p. 42-47]. There he describes secondary action in internal gearsets that is used to create continuous contact between the gears that is necessary to generate a pumping action. He also describes the

equations for the inner gear given a circular-toothed outer gear and states that the center of the outer gear tooth must lie outside its pitch circle for continuous secondary action to exist. Buckingham also showed that cycloids can be used to form a gerotor, and their path of contact is a circle. Hall then gave a the relation required to avoid undercutting in epitrochoidal gerotors [12], which can sometimes be called pin gears as the outer gear teeth are circular.

Perhaps the most influential work to date in the field of gerotor gear geometry was written by J. R. Colbourne titled "Gear Shape and Theoretical Flow Rate in Internal Gear Pumps" [13]. In this work, Colbourne gave a rigorous mathematical derivation of how to generate a gerotor gearset from any tooth profile. He also found the kinematic flow rate directly for circular-toothed gerotors, defined an alternative method to calculate the kinematic flow rate for gerotors generated from an arbitrary tooth profile, compared the flow ripple of circular, elliptical, and sinusoidal gerotors, and determined a method to reduce the curvature of the gear shapes to reduce wear. Colbourne followed this work with another paper titled "Reduction of the Contact Stress in Internal Gear Pumps" [14], where he gave a method to determine the contact force in a gerotor gearset with no tooth clearance by considering Hertzian contact at each of the tooth pairs. By adjusting the gerotor gear geometry, Colbourne demonstrated the possibility to reduce the contact stress in a pump primarily by reducing the curvature of the profiles.

Beard et al. studied the gerotor mechanism further with considerations of size, displacement, flow ripple, relative sliding speed, and compression ratio with special considerations for using the mechanism for rotary engines. A comparison between epitrochoidal and hypotrochoidal gerotors was made considering displacement, flow ripple, overall size, and compression ratio [15]. The main findings was that the epitrochoidal gerotors have a greater displacement when certain geometric ratios fixed and that epitrochoidal gerotors have greater compression ratios. This work was continued further to investigate how the size and position of the outer gear tooth for an epitrochoidal gerotor can be adjusted to affect the curvature of the profiles and how the curvature of a given profile could be reduced for a small increase in size [16]. This was some of the first work to analyze the performance trade-offs for different design goals for gerotors and to make a performance comparison between the profiles. Since wear,

contact stress, internal leakages, filling capacity, and drive relations were not considered and the optimal design space was not identified, further work is required. However, this work did give a very good direction of how further gear profile research should be approached.

Mimmi et al. then performed more design analysis of circular-toothed gerotors [17]. The authors found that when considering the size and flow ripple of the pumps, pumps with an even number of outer gear teeth have a decreasing flow ripple with increasing flow rate, while pumps with an odd number of displacement chambers have increasing flow ripple with increasing flow rate. The authors also considered the sliding speed and curvature of the profiles, but they did not perform a complete multi-objective optimization to investigate the relationship between flow rate, flow ripple, specific sliding, and profile curvature. Mimmi and Pennacchi then continued this research to compare circular, elliptical, sinusoidal, and polycircular profiles on the basis of flow rate, flow ripple, specific sliding, and curvature [18]. Their main findings were that for pumps with similar tooth dimensions pumps the flow rate and flow ripple is does not change very much between the profile types, but the specific sliding and curvature of the profile types can be significantly different. However, a full multi-objective optimization of the profiles was not performed to allow the full exploration between the trade-offs of the design goals.

Kwon et al. then described a wear metric that they named a wear rate proportional factor for gerotor gear design [19]. The wear rate proportional factor is the product of the peak contact pressure and the sliding speed that is normalized to the inner gear rotational speed. The authors determined the contact force at each contact point by assuming a zero clearance profile and using Hertzian contact mechanics to determine the deformation and force at each contact point to generate the required moment to rotate the pump. The downside to using this approach to quantify wear is that it assumes a zero clearance profile, requires solving a system of equations at each rotation angle to determine the contact force, and combines adhesive wear and pitting into one metric so that the individual contributions of adhesive wear and contact stress cannot be distinguished.

Hsieh and Yan then described a method to generate a hypotrochoidal gerotor profile and gave the conditions to ensure that neither gear contain cusps [20]. They also gave an expression to determine the curvature of both profiles. Bonandrini et al. then gave an

alternative set of equations to describe the hypotrochoidal profile with a clearer explanation of its concept [21]. They also gave a method to determine its flow rate as well as the angle between the contact force and the vector from the inner gear center to the contact point to determine if the profile can have a suitable driving relation without jamming.

At this point researchers began to apply optimization techniques to gerotor pumps. Kwon et al. used a genetic algorithm to minimize the wear rate proportional factor they developed for hypotrochoidal gerotors, and Yun et al. used the same approach circular-toothed (epitrochoidal) gerotors [22], [23]. The limitations of these works are that they only considered the wear rate proportional factor and no other important considerations such as size and flow ripple. Additionally, the wear rate proportional factor combines the contact pressure and sliding speed into one objective function, so the contribution of each effect relative to the other cannot be known. Karamooz Ravari extended this work to analyze elliptical profiles for both the wear rate proportional factor and the specific flow rate (flow rate to size ratio) [24]. A full optimization was not performed, but the number of gear teeth and the elliptical tooth aspect ratio were varied in a design study. The author found that the elliptical-toothed profile had the potential to reduce the wear rate proportional factor in comparison to the circular-toothed profile. Karamooz Ravari et al. then extended their approach to circular-toothed gerotors and optimized them for flow ripple and their wear rate proportional factor [25]. Their optimization approach combined the two objective functions into a single objective function for easier computation. They were able to identify an optimal design, but they did not identify the Pareto front and explore the trade-offs between the flow ripple and wear rate proportional factor. Jacazio and De Martin then performed a multi-objective optimization of circular, elliptical, and asymmetric gerotors for size, flow ripple, radial port spacing, and the wear rate proportional factor [26]. The input parameters were varied systematically to study their effect on each of the objective functions. They found that elliptical profiles could increase the flow through the radial port, and that asymmetric profiles could reduce the wear rate proportional factor while not affecting the displacement and flow ripple. This is likely the best work on gerotor profile optimization to date, but it is still limited by requiring the pump operating conditions to determine the contact forces at each of the contact points as well as the flow through the radial port. A Pareto front of the design space was

not produced to identify the best pumps. Further the radial port design objective is not a standard design, so the best designs for that application may not be the best designs for a standard gerotor that has only axial ports.

1.4 Research Objectives

The main goal of this present work is to present a design methodology for gerotor pumps that identifies the optimal designs when considering all of the main performance goals and seven different profile types. The optimal design space can then be used to quickly design a gerotor of any displacement. The design approach is then validated in a case study by both simulation and experiment. An additional consideration on a profile modification strategy to reduce micro-motion of the gears is also presented. The research objectives can be further split into the following:

- Implement a method to generate a gerotor gearset from any curve and identify the relationships required to form a feasible profile (e.g. without cusps)
- Formulate a methodology to evaluate a gerotor gear profile for all its main performance characteristics
- Explore the design space of conventional gerotor profiles and identify the optimal designs
- Invent a new gear profile that can improve the performance of gerotors compared to conventional profiles
- Define a methodology to compare the best designs among conventional profile types with the new profile types
- Validate the proposed performance metrics and optimization approach by simulation and experiment
- Determine a method to select the best gear design for a specific application

2. GEROTOR PROFILE GENERATION

The focus of this chapter is to give a description of how gerotor profiles can be generated. The three standard profile types are presented first: epitrochoidal, hypotrochoidal, and cycloidal. Another method to generate gerotor profiles from any smooth curve is also implemented to define elliptical, asymmetric, cosine, and generalized cycloidal profiles, the last of which was invented as a part of this work. Before showing how to generate the gerotor profiles, a brief consideration on the manufacturability of each profile type should be given. The majority of gerotor profiles used in industry are formed by powder metallurgy. The main cost in developing the tooling for the gearset then is assumed to be in developing the appropriate mold for the parts. For this reason each profile type is assumed to have similar manufacturing cost which allows for a study like this to be practical from a production standpoint.

2.1 Conventional Gerotor Profiles

Conventional gerotor profiles have been are formed using either trochoids or cycloids and were the first curves observed to have the properties necessary to form a gerotor. They include the epitrochoidal profile where the inner gear is a parallel curve to an epitrochoid, and the outer gear has circular teeth; the hypotrochoidal profile where the outer gear is a parallel curve to a hypotrochoid, and the inner gear is generated to be conjugate to it and has inner gear teeth with circular tooth tips; and the cycloidal profile where both gears are combinations of epicycloidal and hypocycloidal arcs formed about the pitch circles. Although these profiles have been well described in literature, they are included here for completeness. Additionally, some of the conceptual descriptions of these profiles in literature are unclear, so another attempt is made to describe how the profiles are generated. Further, the equations to describe the profiles are given in closed-form parametric equations that are simple to implement in a computer program.

2.1.1 Epitrochoidal Gerotors

The epitrochoidal profile is the most common gerotor profile type in practice, likely of its simplicity, and it is illustrated in fig. 2.1. For a gerotor gearset with m outer gear teeth and $m-1$ inner gear teeth and center distance e, if the tooth of an outer gear was a singular point located a distance ρ from its center C were used to generate an inner gear profile, the inner gear profile would be an epitrochoid (blue) generated from a base circle (green) with radius $\rho\frac{m-1}{m}$, a rolling disk radius $\frac{rho}{m}$, and the distance from the center of the rolling disk to the tracing point would be e. The epitrochoid inner gear can then be used to generate the outer gear roots shown in red. This curve resembles an epicycloid, but they are not equivalent. Because a gear profile that is driven by contact at sharp apexes would not be practical, the parallel curve offset by a distance d to both gear profiles can be used instead. Because the parallel curve to a point is a circle, the epitrochoidal profile can be thought to be a gerotor that uses circular outer gear teeth, and the inner gear is a parallel to an epitrochoid. The shape of the outer gear roots can be any shape provided it does not cause interference, so it is often an arc of a circle centered at point C. A property of parallel curves however is that a cusp will be present in the curve when the offset distance is equal to the radius of curvature of the parent curve. This gives a maximum allowable value for the tooth size for a given number of teeth and ratio of the pitch circle radius to tooth position $\frac{me}{\rho}$.

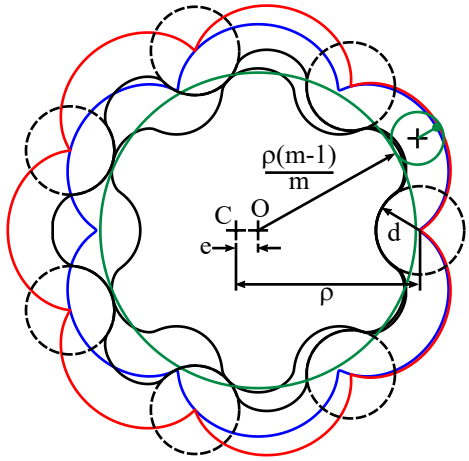

Figure 2.1. Epitrochoidal gerotor gearset [27]

2.1.2 Hypotrochoidal Gerotor Profiles

The hypotrochoidal profile has been known in literature since the first published work on gerotors [1] and has been the subject of other academic works as well [15], [20], [21], however it has not been used extensively in industry. An illustration of the hypotrochoidal profile type is shown in fig. 2.2. If instead of the outer gear teeth being reduced to points, the inner gear teeth are reduced instead to points a distance $\frac{\rho(m-1)}{m}$ from the inner gear center O for the same gerotor with m outer gear teeth, $m-1$ inner gear teeth, and a center distance e, the conjugate outer gear curve would this time be a hypotrochoid formed from a base circle with radius ρ with a rolling disk radius of $\frac{\rho}{m}$, and the distance between the center of the rolling disk and the trace point would again be e. The hypotrochoid can then be used to form the rest of the inner gear profile. To avoid sharp points in the gear profile the parallel curves are again used, but this time the outer parallel curves are used instead. In this way, a hypotrochoidal gerotor can be thought to be one where the tips of the inner gear teeth are circular, and the rest of the gearset is generated to match.

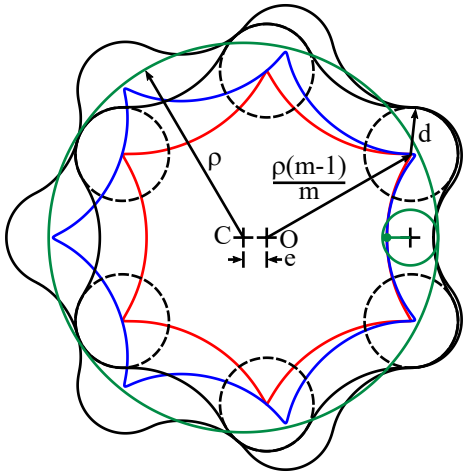

Figure 2.2. Hypotrochoidal gerotor gearset [27]

2.1.3 Cycloidal Gerotor Profiles

Cycloids have been known to be suitable curves to define spur gears as early as the 18th century [28]. Since then the cycloidal tooth form for spur gears has been almost entirely

replaced by the involute, as involutes have a much simpler basic rack, are still conjugate when the center distance changes, and are much more interchangeable. The exception is perhaps in watch making, where cycloidal gears can still be used because they can have greater gear ratios than involutes, and a portion of the tooth flank can be linear, which was traditionally much easier to manufacture [29, p.358]. Cycloids are still a convenient curve for gerotors because they can be used to generate a smooth, closed gear profile with a small number of teeth with simple parametric equations. They are known colloquially in industry to be more compact than epitrochoidal gerotors, however this statement has not been verified in scientific literature.

Cycloidal-toothed gerotors are the second most common profile type used in industry after the circular-toothed gerotor. Both the inner and outer gears are combinations of hypocycloidal and epicycloidal arcs that are formed about the pitch circles of the gears. Although the cycloidal profile type is common in industry, its presence is not well represented in literature. The profile type was first mentioned in literature in Buckingham's book *Analytical Mechanics of Gears* [11, p. 46], and he described that path of contact for this profile type is two circles tangent at the pitch point. The only other description of them is in a work by Choi et. al [30], where the authors describe circular-toothed gerotors as Type I gerotors and cycloidal gerotors as Type II gerotors in the introduction to a paper that described a non-standard profile type. Neither work presents the equations that describe the gear profiles nor explain why the cycloidal profile type is conjugate, so it is done presently.

The basic tooth form for a cycloidal gerotor outer gear tooth is shown in fig. 2.3. The addendum of the outer gear and the dedendum of the inner gear are formed by the locus of a point on the rim of a disk with radius d as it rolls around the inside of its respective pitch circle. This type of curve is known as a hypocycloid. Then the outer gear dedendum and the inner gear addendum are formed by the locus of a point on the rim of a disk with radius b as it rolls on the outside of its respective pitch circle. This type of curve is called an epicycloid, and the two curves connect where they touch the pitch circle. Three variables then fully define the standard cycloidal profile: the number of outer gear teeth m, the center distance e, and the hypocycloid disk radius d. The value of b is selected to close the gear profile with the correct number of teeth. The outer and inner pitch circle radii are given by

$r_{p,o}$ and $r_{p,i}$ respectively in eqs. (2.1) and (2.2), and the epicycloid rolling disk radius is given by eq. (2.3). The outer gear abscissa and ordinate are x and y and are defined in eqs. (2.4) and (2.5) respectively, while the inner gear abscissa and ordinate are ξ and η and are defined in eqs. (2.6) and (2.7) respectively. In eqs. (2.4) and (2.5), ϕ_o is the outer gear parameter and in eqs. (2.6) and (2.7) ϕ_i is the inner gear parameter. After the gear teeth are defined, they can be reflected and rotated to form a complete cycloidal gearset shown in fig. 2.4.

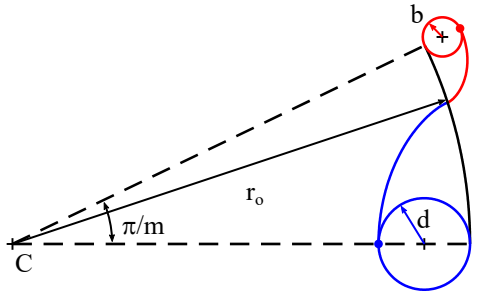

Figure 2.3. Basic tooth form for the standard cycloidal-toothed outer gear [31]

$$r_{p,o} = me \tag{2.1}$$

$$r_{p,i} = (m-1)e \tag{2.2}$$

$$b = e - d \tag{2.3}$$

$$x = \begin{cases} (me-d)\cos(\phi_o) - d\cos((\frac{me}{d}-1)\phi_o) & 0 \le \phi_o < \frac{\pi d}{me} \\ (me+b)\cos(\phi_o) - b\cos((\frac{me}{b}+1)\phi_o - \frac{\pi d}{b}) & \frac{\pi d}{me} \le \phi_o \le \frac{\pi}{m} \end{cases} \tag{2.4}$$

$$y = \begin{cases} (me-d)\sin(\phi_o) + d\sin((\frac{me}{d}-1)\phi_o) & 0 \le \phi_o < \frac{\pi d}{me} \\ (me+b)\sin(\phi_o) - b\sin((\frac{me}{b}+1)\phi_o - \frac{\pi d}{b}) & \frac{\pi d}{me} \le \phi_o \le \frac{\pi}{m} \end{cases} \tag{2.5}$$

$$\xi = \begin{cases} ((m-1)e - d)\cos(\phi_i) - d\cos\left(\left(\frac{(m-1)e}{d} - 1\right)\phi_i\right) & 0 \leq \phi_i < \frac{\pi d}{(m-1)e} \\ ((m-1)e + b)\cos(\phi_i) - b\cos\left(\left(\frac{(m-1)e}{b} + 1\right)\phi_i - \frac{\pi d}{b}\right) & \frac{\pi d}{(m-1)e} \leq \phi_i \leq \frac{\pi}{m-1} \end{cases} \tag{2.6}$$

$$\eta = \begin{cases} ((m-1)e - d)\sin(\phi_i) + d\sin((\frac{(m-1)e}{d} - 1)\phi_i) & 0 \leq \phi_i < \frac{\pi d}{(m-1)e} \\ ((m-1)e + b)\sin(\phi_i) - b\sin((\frac{(m-1)e}{b} + 1)\phi_i - \frac{\pi d}{b}) & \frac{\pi d}{(m-1)e} \leq \phi_i \leq \frac{\pi}{m-1} \end{cases} \tag{2.7}$$

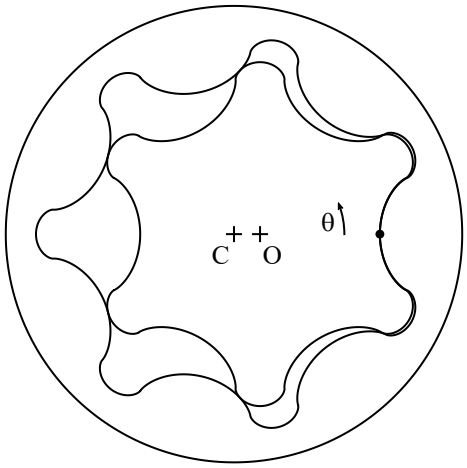

Figure 2.4. Cycloidal gearset with $m = 7$, $e = 3.57$, and $d = 2.5$ [31]

Cycloids satisfy the Law of Gearing by application Camus's principle, so they can be used as suitable gerotor profiles. Camus's principle states that the loci of a point that rolls about two pitch circles are conjugate [29, p.355]. For external gears the addendum of a tooth on one gear is formed by an epicycloid, and the matching dedendum on the opposite gear is formed by a hypocycloid using the same disk radius. In gerotors the epicycloidal portions as well as the hypocycloidal portions mesh in primary contact (positive pressure angle). However, in secondary contact (negative pressure angle), both the addenda of the teeth mesh even though the curves are generated with different rolling disks. The reason cycloids satisfy the Law of Gearing in secondary contact can be explained using fig. 2.5. Two pitch circles centered at points C and O can be drawn for an internal gearset shown in black

in fig. 2.5 that are tangent at the pitch point P. A path of contact for the gearset is assumed to be a circle and is shown in blue that is centered at point D and tangent to point P. For any contact point along the path of contact, the common normal to the two gear profiles must pass through the pitch point P to satisfy the Law of Gearing. Line segments AC and BO are then drawn to connect the centers of the pitch circles to where the common normal intersects the pitch circles. Because triangles BOP and ACP share angle α and are also isosceles, they must be similar. Another line segment can be drawn parallel to CO that passes through the contact point and intersects AC at F and the extension of BO at G. Triangle AEF is similar to triangle ACP, as angle AEF is equivalent to α and angle FAE is shared. If point D is offset from point C by a distance d, then line segments FE and AF must also have length d. Therefore, a circle with radius d can be drawn about point F that is tangent to the outer gear pitch circle at A and to the contact point E for any angle of α. Similarly, if point D is offset from point O by a distance b, a circle with radius b can be drawn about point G that is tangent to points E and B.

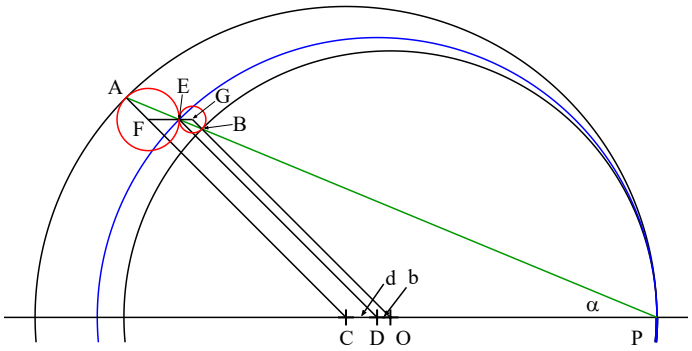

Figure 2.5. Contact diagram for cycloidal gerotor gearing

Cycloids have the interesting property that the normal to the curve at point B passes through the point A where the rolling disk contacts the plane as shown in fig. 2.6. This is true as the point of tangency at A is the instantaneous center as the disk rolls without slipping on the base curve regardless of whether it is a line or a curve. In fig. 2.5, because the common normal to the gear profiles passes through the points A, E, and B, and the circles centered at F and G have constant radii, the Law of Gearing is satisfied if the outer gear addendum is an hypocycloid formed by a rolling disk with radius d using the outer gear

pitch circle as a base circle and the inner gear addendum is an epicycloid formed by a rolling disk with radius b using the inner gear pitch circle as a base circle.

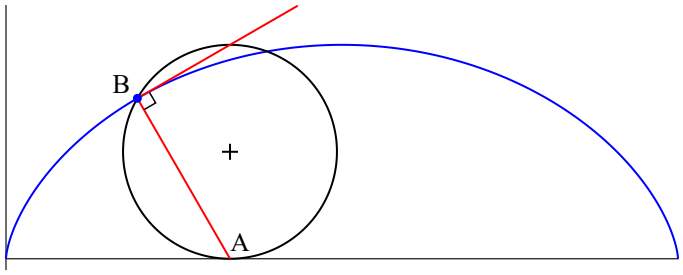

Figure 2.6. Cycloid with normal and tangent lines

The main problem with using cycloids to define gerotor profiles is that the radius of curvature of a cycloid is zero where the cycloid meets its base circle. The effect of this is that the contact stress is very high when the contact between the gears occurs at the pitch point, as the radius of curvature of both gears at that point is zero. Hertzian equations for contact stress would no longer apply in this region, as the curvature changes abruptly in that region, and the profiles would likely experience some degree of plastic deformation. Nevertheless, a good gear design should avoid contact in regions of high curvature when possible. The combined curvature of the gears at a contact point is the sum of the outer and inner gear curvatures, and it is used to determine the peak contact pressure in the standard Hertzian equations. The combined curvature for the cycloidal gerotor shown in fig. 2.4 as a function of outer gear rotation angle is plotted in fig. 2.7. When the contact is in the primary contact region with a positive pressure angle, the combined curvature is near zero, as the contact is or is nearly conformal. When the contact is at the pitch point, the inner gear curvature approaches negative infinity, while the outer gear curvature approaches positive infinity. Continuing to rotate slightly past the pitch point, both gear curvatures approach an infinite value, and this explains the asymptotic behavior seen in fig. 2.7.

2.2 Gerotor Profiles Generated from an Arbitrary Curve

The conventional gerotor profile types arise from identifying the correct curves to form a gerotor gearset if either the outer gear teeth, inner gear teeth, or path of contact is circular.

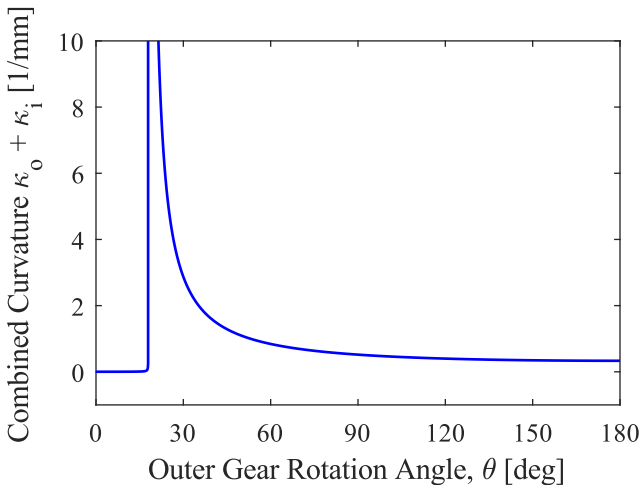

Figure 2.7. Plot of combined curvature for cycloidal gearset, $m = 7$ $r_{p,o} = 25$, $d = 2.5$ [31]

However, nearly any smooth curve can be used to generate a gerotor gear profile. The approach described by Colbourne [13] is straight-forward to implement and is the basis of the gerotor gear profiles used in the rest of the thesis. It is summarized here for continuity of nomenclature and completeness.

Either an inner gear tooth or an outer gear tooth can be used to define a gerotor. Typically starting with an outer gear tooth is easier, as then the inner gear can be generated in one step, and the roots of the outer gear can be arcs of a circle. In that configuration, only a portion of the outer gear tooth will contact the inner gear. However, if conjugate outer gear roots are desired, the inner gear should be generated from the outer gear tooth, and the inner gear tooth can be used to generate the outer gear root. Starting from the inner gear is more difficult, as the entire inner gear must contact the outer gear throughout the whole rotation to form a gerotor. The outer gear can be generated from the tip of the inner gear tooth, and then the generated outer gear tooth profile can be used to generate the dedendum of the inner gear.

Colbourne's approach [13] uses a gearset defined by parametric equations for x and y, which are the abscissa and ordinate of the outer gear tooth respectively, and the parameter is ϕ. Then the inner gear is determined by identifying the point the contact point on the outer gear tooth at every angle of rotation by applying the Law of Gearing, which states that the normal line to the contact point must pass through the pitch point for curves to be

conjugate, and then mapping that point on to the inner gear coordinate system. To do this a kinematic inversion is performed so that the outer gear is fixed, and the inner gear moves in an orbital fashion. This is illustrated in fig. 2.8 for an arbitrary tooth curve (x, y). The inner gear coordinates are (ξ, η) and will rotate clockwise by the angle ψ relative to the x-axis as the inner gear orbits. The line of centers will then rotate correspondingly by $(m-1)\psi$ counter-clockwise, and the outer gear rotation angle at which the point makes contact with the inner gear in the standard frame of reference where the line of centers is fixed is given by eq. (2.9). Two solutions for ψ exist for every point of the outer gear tooth that contacts the inner gear, and this is illustrated in fig. 2.8 by the blue and red inner gear curves shown in the two positions they contact the same point on the outer gear. The relative rotation angles can be found explicitly in eq. (2.8), and then a coordinate transformation can be performed in eqs. (2.10) and (2.11) to define the inner gear. The inner gear curve is generated in three sections shown in fig. 2.9 and can be rotated to form the complete inner gear. Primary contact refers to the portion of the curve that when in contact with the outer gear has a positive pressure angle, while secondary contact has a negative pressure angle. In this work, the pressure angle is defined as the angle that the normal to the contact point makes with the line tangent to the pitch point.

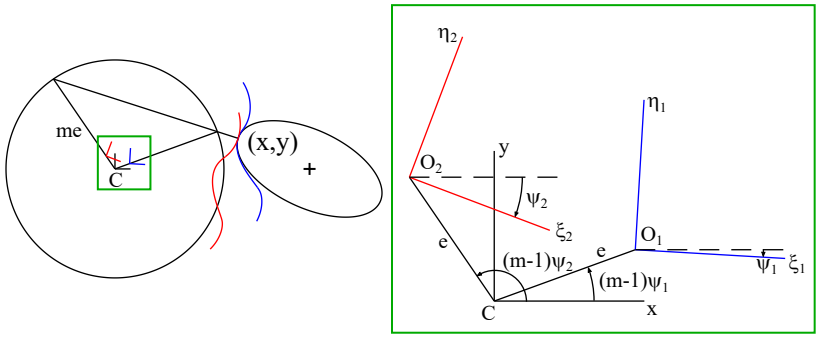

Figure 2.8. Illustration of kinematic inversion to apply the Law of Gearing [32]

$$\psi_{1,2} = \frac{1}{m-1} \arctan\left(\frac{y'(xx'+yy') \mp x'\sqrt{m^2e^2(x'^2+y'^2)-(xx'+yy')^2}}{x'(xx'+yy') \pm y'\sqrt{m^2e^2(x'^2+y'^2)-(xx'+yy')^2}}\right) \tag{2.8}$$

$$\theta_o = -(m-1)\psi \tag{2.9}$$

$$\xi_{1,2} = -e\cos(m\psi_{1,2}) + x\cos(\psi_{1,2}) - y\sin(\psi_{1,2}) \tag{2.10}$$

$$\eta_{1,2} = -e\sin(m\psi_{1,2}) + x\sin(\psi_{1,2}) + y\cos(\psi_{1,2}) \tag{2.11}$$

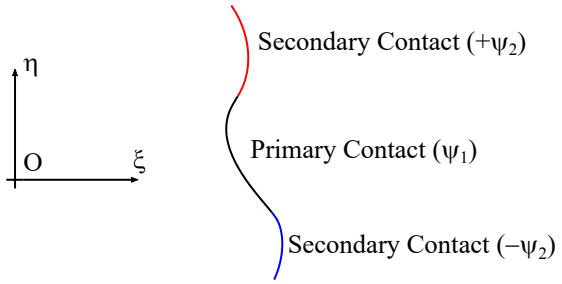

Figure 2.9. Illustration of inner gear tooth for an arbitrary curve [32]

Only points whose normal intersect the outer gear pitch circle can satisfy the Law of Gearing, so only a portion of an arbitrary outer gear tooth curve will contact the inner gear. The limit of contact is given by the two points on the outer gear tooth whose normal is tangent to the pitch circle shown in fig. 2.10, and the gear parameters corresponding to the limits of contact are $\phi_{m_{1,2}}$ given by the two solutions to eq. (2.12), which is the argument under the square root in eq. (2.8). The gear parameters corresponding to the limits of contact can be found analytically for the conventional profile types but must be found numerically in the general case. This relation also places a maximum value on the center distance for a given tooth configuration to ensure continuous contact. If the center distance is increased, the pitch circle radius also increases. Eventually no point on the outer gear tooth will have a normal line that is tangent to the pitch circle, so continuous contact cannot exist. However, cusps usually form in the inner gear profile before this limit is reached.

$$m^2e^2(x'^2 + y'^2) - (xx' + yy')^2 = 0 \tag{2.12}$$

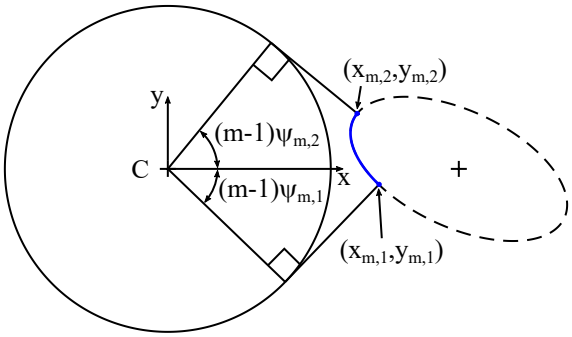

Figure 2.10. Illustration of the limits of the outer gear tooth that contact the inner gear [32]

2.3 Gerotor Profiles Investigated in this Work

The performance of seven different gerotor profiles are compared in this work and that are generated according to the procedure given in section 2.2. They are epitrochoidal, hypotrochoidal, standard cycloidal, elliptical, generalized cycloidal, cosine, and asymmetric elliptical. A brief description of each profile type is described here.

The epitrochoidal profile can be generated by using a circle for the outer gear tooth as shown in fig. 2.11, and the tooth curve is parameterized by eqs. (2.13) and (2.14). When the root radius is specified so that it would intersect the tooth curve past its center ($r_r > \sqrt{\rho^2 + d^2}$), horizontal, tangent extensions are used to connect the root to the tooth as shown in fig. 2.11. This is done to increase the feasible portion of the design space, reduce the bending stress in the outer gear, and to reduce leakage flow in the lateral gap. In application, fillets are often also used to reduce the stress concentration and to improve manufacturability. The limit of contact was solved and is given in eq. (2.15), and the minimum allowable outer gear root radius to avoid interference is given in eq. (2.16). The maximum allowable center distance for continuous contact is then given in eq. (2.17), which states that the center of the tooth must be located outside of the pitch circle.

$$x = \rho - d\cos(\phi) \tag{2.13}$$

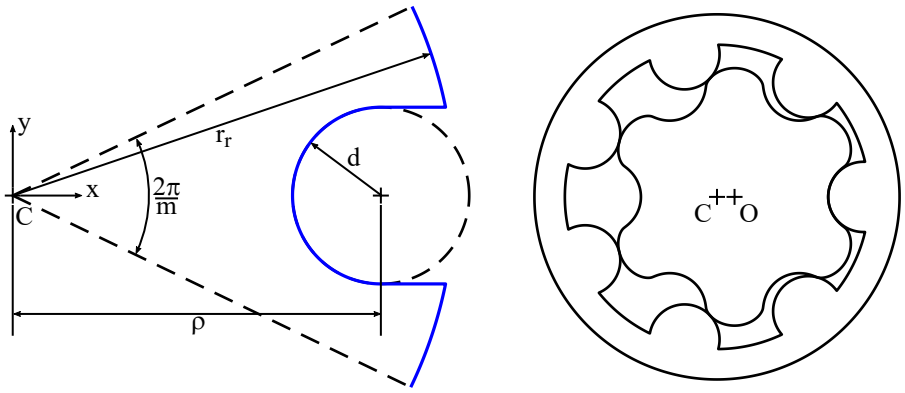

Figure 2.11. Epitrochoidal gerotor outer gear tooth form with $m = 7$, $\rho = 25$ mm, $d = 6mm$, and $r_r = 30$ mm (left) and corresponding complete outer gearset for $e = 3$ mm [27]

$$y = d\sin(\phi) \tag{2.14}$$

$$\phi_{m_{1,2}} = \mp\text{asin}\left(\frac{me}{\rho}\right) \tag{2.15}$$

$$r_{r,min} = \rho - d + 2e \tag{2.16}$$

$$e < \frac{\rho}{m} \tag{2.17}$$

The tooth form for the hypotrochoidal gerotors used in this work is shown in fig. 2.12. In fig. 2.12, the outer gear tooth is shown in blue, the parallel hypotrochoid is shown in dashed red, and the base circle and rolling disk used to generate the hypotrochoid are shown in dashed green. The abscissa and ordinate of the hypotrochoid are given as x_t and y_t in eqs. (2.18) and (2.19) respectively, and the standard parametric equations for a parallel curve are used to give define the outer gear tooth in eqs. (2.20) and (2.21). The gear parameters corresponding to the limit of contact were found and are given in eq. (2.22), and the minimum allowable outer gear root radius to prevent interference is given in eq. (2.23). Typically hypotrochoidal gerotor profiles have conjugate outer gear roots, but in this work

the outer gear roots are taken to be an arc of a circle, and tangent lines to the tooth profile at the limit of contact connect the tooth curve to the circular root. The shape of the outer gear root does not affect the overall size and flow variability of the pump, but it has a significant effect on the mean inlet velocity of the pump and also affects the leakage in the lateral gap and possibly the micro-motions of the gears in operation. For this reason, the outer gear roots are taken to be an arc of a circle for each case to give an fair comparison. The limit on the center distance to give continuous contact is the same as that for epitrochoidal gerotors and is given in eq. (2.24).

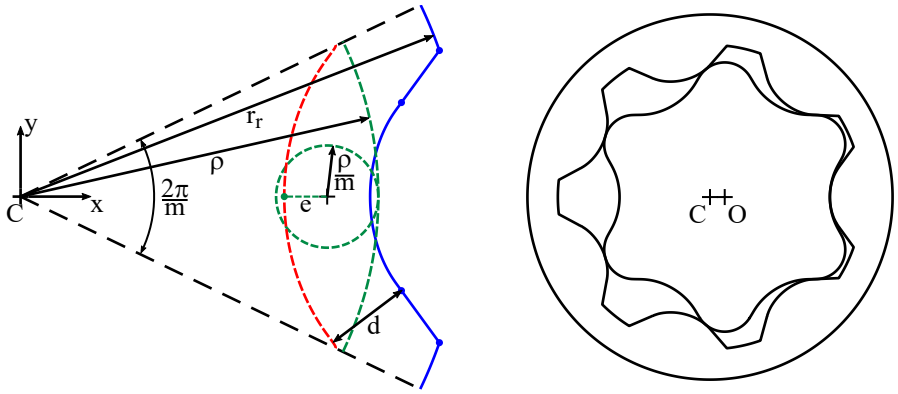

Figure 2.12. Hypotrochoidal gerotor outer gear tooth form with $m = 7$, $e = 3mm$, $\rho = 25$ mm, $d = 6$ mm, and $r_r = 31$ mm (left) with complete outer and matching inner gears (right) [27]

$$x_t = \frac{\rho(m-1)}{m}\cos(\phi) - e\cos((m-1)\phi) \tag{2.18}$$

$$y_t = \frac{\rho(m-1)}{m}\sin(\phi) + e\sin((m-1)\phi) \tag{2.19}$$

$$x = x_t + \frac{dy_t}{\sqrt{x_t^2 + y_t^2}} \tag{2.20}$$

$$y = y_t - \frac{dx_t}{\sqrt{x_t^2 + y_t^2}} \tag{2.21}$$

$$\phi_{m_{1,2}} = \mp \frac{1}{m}\left(\pi - \operatorname{acos}\left(\frac{me}{\rho}\right)\right) \tag{2.22}$$

$$r_{r,min} = \rho - \frac{\rho}{m} + e + d \tag{2.23}$$

$$e < \frac{\rho}{m} \tag{2.24}$$

The standard cycloidal gerotors used in this work are generated according to the tooth form shown in fig. 2.13. The equations for the outer gear tooth are given in eqs. (2.25) and (2.26), and the limit of contact is given in eq. (2.27). The outer gear roots are also taken to be arcs of a circle with tangent tooth extensions at the limit of contact just as for hypotrochoids, and the minimum allowable root radius to avoid interference is given in eq. (2.28). The limit on the center distance for standard cycloidal profiles is different that that for epitrochoidal and hypotrochoidal profiles, as the cycloidal curve uses the pitch circle as the base circle, so the normal to the curve is guaranteed to have a point that is tangent to the pitch circle. Instead, the pitch circle must be large enough for the rolling disk to trace a profile that does not cross over itself, and that relation is given in eq. (2.29).

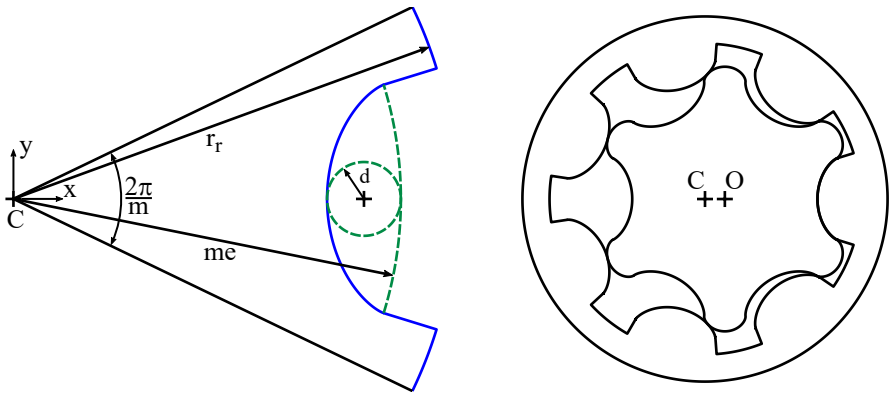

Figure 2.13. Standard cycloidal gerotor outer gear tooth form with $m = 7$, $e = 3$ mm, $d = 2$ mm, and $r_r = 23.5$ mm (left) with complete outer and matching inner gears (right) [27]

$$x = (me - d)\cos(\phi) - d\cos\left(\left(\frac{me}{d} - 1\right)\phi\right) \tag{2.25}$$

$$y = (me - d)\sin(\phi) + d\sin\left(\left(\frac{me}{d} - 1\right)\phi)\right) \tag{2.26}$$

$$\phi_{m_{1,2}} = \mp\frac{\pi d}{me} \tag{2.27}$$

$$r_{r,min} = \rho + 2e - 2d \tag{2.28}$$

$$e > d \tag{2.29}$$

Elliptical gerotors allow more design variation than a circular-toothed gearset and have the potential to have better wear characteristics than epitrochoidal gerotors [18], [24], [26]. For these reasons, they are included as a profile type for investigation. A diagram of the elliptical tooth form used in this work is shown in fig. 2.14, and the equations that define the tooth profile are given in eqs. (2.30) and (2.31). Just as for the epitrochoidal profile, horizontal tangent extensions are used if the root would intersect the tooth past its center ($r_r > \sqrt{\rho^2 + k^2}$). The minimum allowable root radius to avoid interference is the same as for circular profiles and is given in eq. (2.32). The limit of contact must be determined numerically, but the limit of the center distance is the same as that for epitrochoidal profiles given in eq. (2.33).

$$x = \rho - d\cos(\phi) \tag{2.30}$$

$$y = k\sin(\phi) \tag{2.31}$$

$$r_{r,min} = \rho - d + 2e \tag{2.32}$$

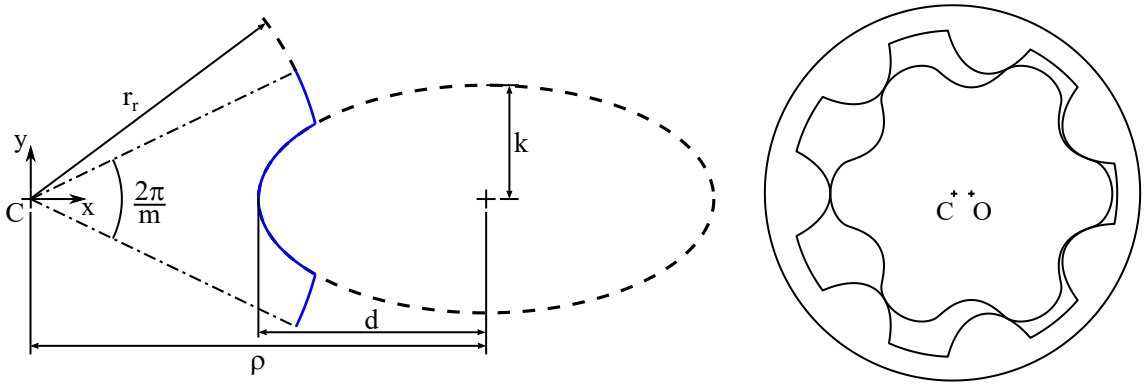

Figure 2.14. Elliptical gerotor outer gear tooth form with $m = 7$, $\rho = 25$ mm, $d = 12.5$ mm, $k = 6.25$ mm, and $r_r = 16.5$ mm (left) with complete outer and matching inner gears for $e = 1.75$ mm (right) [33]

$$e < \frac{\rho}{m} \tag{2.33}$$

The generalized cycloidal profile is new to this work and seeks to offer some improvement over the standard cycloidal profile. A diagram of its tooth form is shown in fig. 2.15. Two relations of the standard cycloidal profile are relaxed to give the generalized cycloidal profile. First, any circle can be used as the base circle to form the hypocycloidal outer gear tooth rather than just the pitch circle, which significantly increases the size of the design space. Second, the center distance can be reduced from its maximum value. In so doing, the portion of the hypocycloid that contacts the inner gear is reduced so that the regions with high curvature no longer contact the inner gear. This can significantly reduce the contact stress and results in only a small change in pump displacement while also further increasing the size of the design space. The equations that define the generalized cycloidal tooth are given in eq. (2.34). The minimum allowable root radius is given in eq. (2.36), and the limit on the center distance to give continuous secondary action is given in eqs. (2.35) and (2.37).

$$x = (r - d)\cos(\phi) - d\cos\left(\left(\frac{r}{d} - 1\right)\phi\right) - r + \rho \tag{2.34}$$

$$y = (r - d)\sin(\phi) + d\sin\left(\left(\frac{r}{d} - 1\right)\phi\right) \tag{2.35}$$

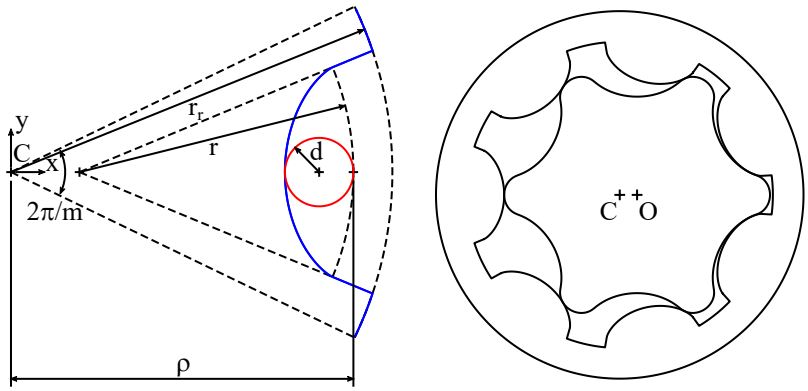

Figure 2.15. Generalized cycloidal gerotor outer gear tooth form with $m = 7$, $\rho = 25$ mm, $r = 20$ mm, $d = 2.5$ mm, and $r_r = 26.5$ mm (left) with complete outer and matching inner gears for $e = 3$ mm (right) [31]

$$r_{r,min} = \rho - 2d + 2e \tag{2.36}$$

$$e < \frac{\left|(r-\rho)\cos\left(\frac{\pi d}{r}\right) - r\right|}{m} \tag{2.37}$$

The cosine profile uses a portion of a cosine wave to define the outer gear tooth as shown in fig. 2.16. It is included in the analysis here as it has a possibility of offering improved performance over the conventional profiles due to an increased size of the design space. The cosine profile type was explored briefly in other previous work [13], [18], but in neither place was it considered extensively. It is included in this analysis to investigate if it can have improved performance over the other profile types. The parametric equations to describe the cosine tooth profile are given in eqs. (2.38) and (2.39). The minimum allowable root radius to prevent interference is given in eq. (2.40) and is the same as for the epitrochoidal and elliptical profiles, however the maximum value of the center distance to ensure continuous contact must be found numerically. The minimum distance between the normal line to the tooth profile and the origin of the outer gear is given by D in eq. (2.41). The upper limit of the center distance occurs when eq. (2.41) reaches a local maximum, and the pitch circle would be tangent to that normal line. Therefore the limit of the center distance to give continuous contact is given in eq. (2.42), which is found numerically.

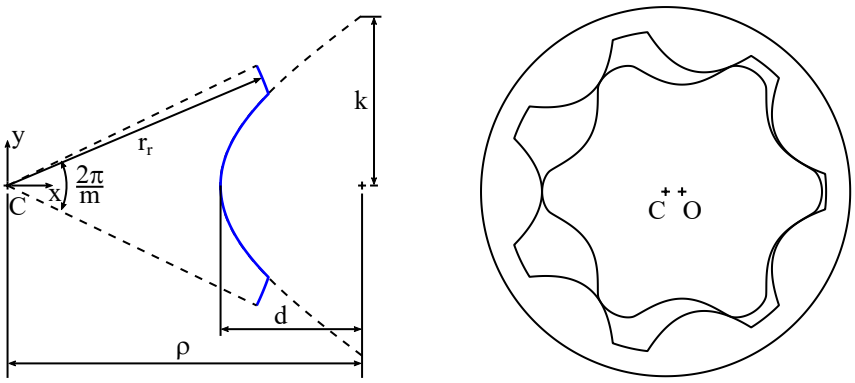

Figure 2.16. Cosine gerotor outer gear tooth form with $m = 7$, $\rho = 25$ mm, $d = 10$ mm, $k = 12$ mm, and $r_r = 19.5$ mm (left) with complete outer and matching inner gears for $e = 2$ mm (right)

$$x = \rho - d\cos\phi \tag{2.38}$$

$$y = \frac{2k\phi}{\pi} \tag{2.39}$$

$$r_{r,min} = \rho - d + 2e \tag{2.40}$$

$$D = \frac{\frac{2k\phi}{\pi} + \frac{\pi d\sin(\phi)(\rho - d\cos\phi)}{2k}}{\sqrt{\frac{d^2\pi^2\sin^2\phi}{4k^2} + 1}} \tag{2.41}$$

$$e < \frac{1}{m}\max\{D, 0 \leq \phi \leq \pi\} \tag{2.42}$$

The last profile for consideration is the asymmetric elliptical profile, which is formed by using an ellipse rotated about its center for the outer gear tooth and shown in fig. 2.17. The tooth shape was patented by M.F. Hill in 1945 [34]. The inventor claimed that the asymmetry could lead to an improved drive angle between the gear teeth, which could reduce both the wear and the contact stress in the profile. These claims however have not been evaluated in scientific literature, so the profile is considered in this work. The equations defining the tooth profile are given in eqs. (2.43) and (2.44), where α is the clockwise rotation angle

of the ellipse about its center. The minimum allowable outer gear root radius to prevent interference is found in eq. (2.45), where R is the polar radius of the outer gear tooth, and its maximum value is found numerically. The inner gear tooth height remains $2e$ for asymmetric profiles. The point of the outer gear tooth where the normal line is vertical determines the maximum allowable center distance and is given in eq. (2.46), where $\phi_{v_{1,2}}$ are the two points on the ellipse with a vertical normal line that are solutions to the arctangent function. The maximum allowable center distance for continuous contact is then given in eq. (2.47). Horizontal tangent tooth extensions are also used if the outer gear root would intersect the tooth past the point where it has a horizontal tangent line just as for epitrochoidal and elliptical profiles.

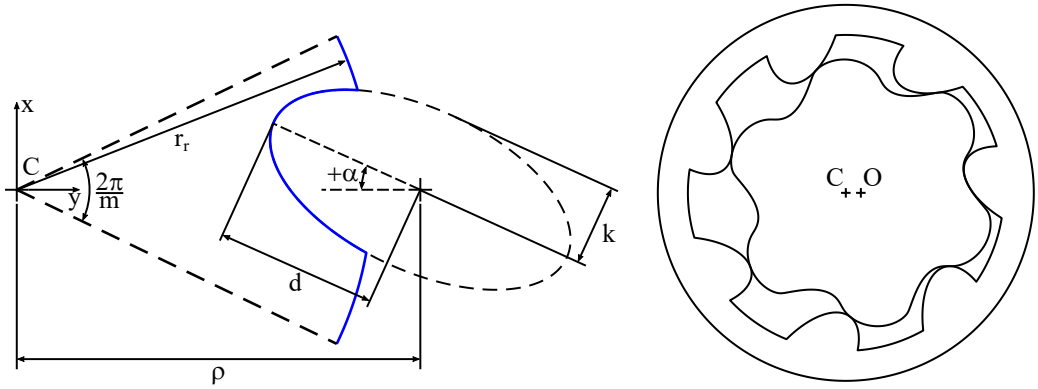

Figure 2.17. Asymmetric elliptical gerotor outer gear tooth form with $m = 7$, $\rho = 25$ mm, $d = 10$ mm, $k = 5$ mm, $\alpha = 25°$, $r_r = 21$ mm (left) with complete outer and matching inner gears for $e = 2$ mm (right) [32]

$$x = \rho - d\cos(\phi)\cos(\alpha) + k\sin(\phi)\sin(\alpha) \tag{2.43}$$

$$y = d\cos(\phi)\sin(\alpha) + k\sin(\phi)\cos(\alpha) \tag{2.44}$$

$$r_{r,min} = \min\{R, -\pi \leq \phi \leq \pi\} + 2e \tag{2.45}$$

$$\phi_{v_{1,2}} = \operatorname{atan}\left(\frac{-k}{d}\tan\alpha\right) \tag{2.46}$$

$$e < \frac{1}{m}\min\left\{x(\phi_{v_1}), x(\phi_{v_2})\right\} \tag{2.47}$$

Now that a description of how to generate gerotor gear profiles has been given, a method to optimize and compare the relative performance of the profile types is given in the following chapter.

3. MULTI-OBJECTIVE OPTIMIZATION FRAMEWORK

The preceding chapter showed how to generate several gerotor profile types, which leads to the questions of what defines a good gerotor profile, and which profile is the best for a given application? Multi-objective optimization is used in this work to determine the best gear designs given a set of performance goals, and it has found successful for many engineering applications including the design of positive displacement machines [35], [36]. In a multi-objective optimization, the performance goals are quantified as functions to be either minimized or maximized, and one or more constraints can be imposed to ensure a feasible design. The performance objectives in this work are called objective functions (OF), and the goal in defining them is to accurately quantify each performance goal of the gearset and to have a short computation time so that many designs can be evaluated. An algorithm is then used to find the best designs within the design space. Seven OF are to be minimized and include size for a given displacement, flow ripple, adhesive wear, contact stress, tooth tip leakage, lateral gap leakage, and mean fluid inlet velocity. These OF are more fully described in the next chapter. The designs are also subject to constraints to ensure a feasible profile geometry (i.e. without cusps or self-intersections in the gear profiles), that the gears possess a suitable driving relation, and that the values of each OF below an acceptable threshold value. The best possible designs of each profile type are to be identified, and then a comparison of the optimal designs can be made.

In a multi-objective optimization, rarely is a single design the best in every OF. When design goals are competing, the goal of an optimization is to identify the Pareto front, which is sometimes called the non-dominated front. The Pareto front is the set of designs where no known design can outperform it in every OF. An example of a set of Pareto designs for two OF is shown in fig. 3.1, where the goal is to minimize OF1 and OF2. In fig. 3.1, each design is represented as a point, and for every design on the Pareto front, improving in regard to one OF leads to worse performance in the other. Every one of these designs is said to be optimal, but which design should be chosen depends on the relative importance of each OF. The number of designs on the Pareto front increases as more OF are added, so in addition

to identifying the optimal designs, selecting a design from the many optimal solutions is also a challenge.

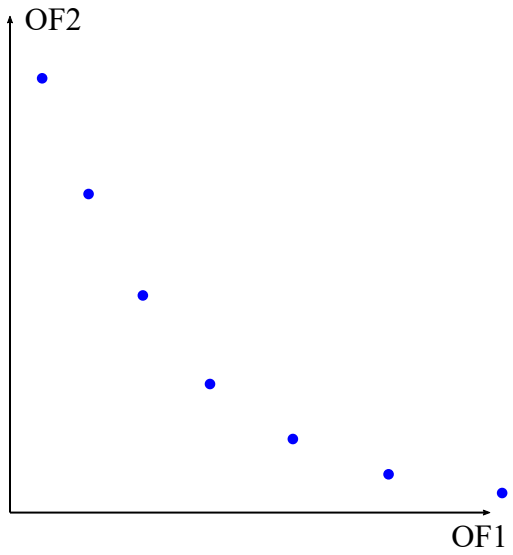

Figure 3.1. Illustration of example set of Pareto designs

The choice in algorithm to identify the Pareto front is very important for a multi-objective optimization to fully explore the design space without getting trapped in local minima and to find the optimal set of solutions with fewer function evaluations than a brute force method that samples every combination of input variables. Many approaches combine each of the OF into a single function by multiplying them by weights and summing the values. The minimum of the weighted function is then found, and the weights can be varied to find the Pareto front. The problem with this approach is that the weight values greatly influence the results, and many sets of weights must be tested to find the Pareto front. In this work the NSGA-II (Non-dominated Sorting Genetic Algorithm II) [37] is used because of the way it treats each OF independently and because it handles constraint functions without the need to impose a penalty function. The NSGA-II also handles discrete input variables (the number of gear teeth) and designs that cannot be evaluated due to a constraint violation. Genetic algorithms emulate natural selection to find the best designs. A population of designs is evaluated, and the traits of the best designs are passed to the next generation. The optimization will continue for a set number of generations. It also uses a crowding-

distance criterion to increase the diversity of the population as well as elitism, which allows the best designs in a generation to be cloned in the next generation. The downsides of using a genetic algorithm are that convergence is not guaranteed, as the gradient is not considered, and they tend to require more function evaluations than a gradient-based method to find the minimum of a function.

The optimization of each profile as shown in the flowchart in fig. 3.2 and proceeds as follows. Input variables for every design in the population are selected by the optimization algorithm. The speed of each optimization is improved by using non-dimensional input variables that describe the aspect ratios of the pump geometry and thereby reduce the number of input variables for each optimization. A summary of the non-dimensional input variables (excluding the number of outer gear teeth and tooth rotation angle for asymmetric elliptical profiles) for each profile type is shown in table 3.1. Additionally, the minimum allowable root radius is used for each profile to further reduce the number of input variables. As a design is evaluated, it is first checked if the geometry is geometrically feasible (without cusps or self-intersections). If the design is not geometrically feasible, the evaluation of that particular design is terminated to save computation time. However, if it is geometrically feasible, then the pump is scaled to have a facial displacement (displacement per unit face width) of 10 cm^2/rev. The pump displacement is scaled so that the values of the OF can be compared directly, and the exact displacement used is arbitrary, as the results of the optimization can be scaled to any desired pump displacement without changing which designs lie on the Pareto front. The pump scaling is quadratic such that doubling the dimension of each input variable except the number of teeth leads to a fourfold increase in displacement. An arbitrary value is selected for one of the input variables (e for standard cycloidal profiles and ρ for the others), and the pump dimensions are calculated from the nondimensional parameters. The pump displacement is then determined for the set of input variables, and the scaling factor for the pump is found in eq. (3.1), where λ_s is the scaling factor, $\tilde{v}_t$ is the target facial displacement, $\tilde{v}$ is the calculated facial displacement. Each of the input variables can be multiplied by the scaling factor to give the dimensional input parameters to give the desired 10 cm^2/rev displacement. As an example, this would be done for a circular profile as in eqs. (3.2)–(3.4), where the s subscript indicates a scaled input variable. Then the OF

are evaluated using the scaled input variables, and the OF were scaled to be on the order of one using the OF values from a good design in industry as normalization factors. This helps the algorithm weigh the relative performance between each OF and to find the feasible space more quickly. After all the designs in a generation have been evaluated, the algorithm selects the designs for the next generation. This continues until the number of generations has been completed. The Pareto front is then identified based on all of the designs that were evaluated in the entire optimization.

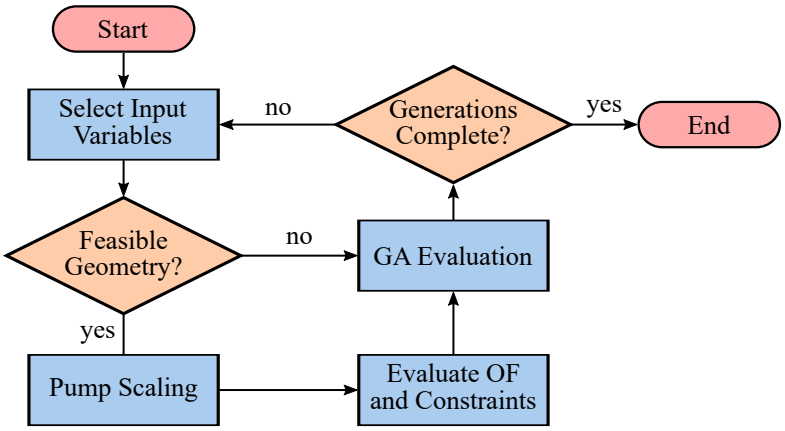

Figure 3.2. Flow chart of optimization with a genetic algorithm [27]

$$\lambda_s = \sqrt{\frac{\tilde{v}_t}{\tilde{v}}} \tag{3.1}$$

$$\rho_s = \lambda_s \rho \tag{3.2}$$

$$e_s = \lambda_s e \tag{3.3}$$

$$d_s = \lambda_s d \tag{3.4}$$

The optimization was implemented in the commercial software modeFRONTIER, and the gear generation and evaluation procedure was written in MATLAB. modeFrontier is an application that pairs multi-objective optimization and statistical techniques with engineer-

Table 3.1. Non-dimensional input variables for each profile type

Profile Type	$\boldsymbol{\lambda_p}$	$\boldsymbol{\lambda_d}$	$\boldsymbol{\lambda_t}$	$\boldsymbol{\lambda_e}$	$\boldsymbol{\lambda_r}$
Epitrochoidal	$\frac{me}{\rho}$	$\frac{d}{\rho}$			
Hypotrochoidal	$\frac{me}{\rho}$	$\frac{d}{\rho}$			
Std. Cycloidal		$\frac{d}{e}$			
Elliptical	$\frac{me}{\rho}$	$\frac{d}{\rho}$	$\frac{k}{d}$		
Gen. Cycloidal		$\frac{d}{\rho}$		$\frac{e}{\frac{1}{m}\left\|(r-\rho)\cos\left(\frac{\pi d}{r}\right)-r\right\|}$	$\frac{r}{\rho}$
Cosine	$\frac{me}{\rho}$	$\frac{d}{\rho}$	$\frac{k}{d}$		
Asym. Elliptical		$\frac{d}{\rho}$	$\frac{k}{d}$		

ing applications. All the profiles except the asymmetric elliptical and the standard cycloidal use a population size of 1000 and were run for 500 generations. Because the cycloidal profile only has two design variables and the number of teeth is discrete, fewer designs must be evaluated to fully explore the design space. For this reason, a reduced population size of 100 was run for 100 generations for the cycloidal profile. Conversely, because the asymmetric elliptical profile has the most input variables, it was run with a population size of 1000 for 750 generations. The population for each optimization was initially populated by a Sobol sequence that distributes the input variables pseudo-randomly while decreasing the likelihood of clustering the designs. The high number of evaluated designs gives a very clear Pareto front with no holes in the design space, and it is possible to evaluate that many designs because each OF has a very short computation time. The bounds of the input variables were selected based on experience with the problem to reduce the probability of selecting

designs with infeasible profile geometries while including the Pareto designs. The bounds on the input variables used for the optimization for each profile type are shown in table 3.2.

The chapters that follow give a description of the OF and constraints used in the optimizations. Then an analysis of the results of each optimization and a comparison of the best designs among each profile type is given.

Table 3.2. Input variable bounds

Profile Type	m		λ_p		λ_d		λ_t		λ_e		λ_r		α [deg]	
	min	**max**	**min**	**max**	**min**	**max**	**min**	**max**	**min**	**max**	**min**	**max**	**min**	**max**
Epitrochoidal	5	20	0.01	1.0	0.01	1.0								
Hypotrochoidal	5	20	0.01	1.0	0.01	1.0								
Std. Cycloidal	5	20			0.01	1.0								
Elliptical	5	20	0.01	1.0	0.01	1.0	0.01	5.0						
Gen. Cycloidal	5	20			0.001	0.5			0.01	1.0	0.01	100.0		
Cosine	5	20	0.01	1.3	0.01	1.0	0.01	5.0						
Asym. Elliptical	5	20	0.25	1.0	0.01	0.6	0.05	5.0					-45.0	45.0

4. OBJECTIVE FUNCTIONS

Objective functions (OF) are performance goals that are quantified into mathematical expressions that are to be minimized or maximized in an optimization. Gerotor gears have several performance goals such as minimizing the size to displacement ratio, outlet flow variability, adhesive wear, contact stress, internal leakage across the tooth tips, internal leakage across the lateral face of the teeth, and the tendency toward incomplete displacement chamber filling at high speeds. An optimization algorithm can then be used to find the best designs according to each of these functions. In this chapter, each of these seven OF are defined, and additional considerations on hydro-mechanical efficiency and how the OF scale with displacement are given as well.

Each of the OF have three requirements in addition to quantifying their respective performance objective. One is that each function should have fast computation times, since these functions are to be used in an extensive optimization with many function calls. Second, the functions should focus on the parts of the performance goals that are directly a function of the macro gear geometry, i.e. clearances and tolerances are to be considered at a later point. Third, the functions should be able to be scaled according to pump displacement so that an optimization only needs to be performed once. In this way, the Pareto front from the optimization can be used to identify the optimal designs for a pump of any displacement.

The performance of the pumps depends greatly on factors beyond the shape of the gears such as the operating conditions; port geometry; gap heights; fluid properties; and gear material properties such as hardness, surface roughness, etc. More sophisticated models will be able to better predict how the pump performs considering all of these very important factors, however their increased computation times make these types of models unsuitable for extensive optimization work. Instead, each of the OF should be normalized to these factors to arrive at the best gear geometry, and then these more sophisticated models can be used to fine-tune the design to arrive at the best pump design for a given application.

4.1 Objective Function 1: Minimize Pump Radius for a Given Displacement

The size per displacement of a pump should be as low as possible to improve power density, improve hydro-mechanical efficiency, reduce material costs, and allow for better assembly provided other considerations such as a large through-shaft do not require a large pump [5]. The kinematic or geometric displacement of a pump is given by eq. (4.1), where v is the displacement, m is the number of outer gear teeth, A_{max} is the maximum displacement chamber area, A_{min} is the minimum displacement chamber area, and h is the face width of the gears. The minimum and maximum displacement chamber areas are illustrated in fig. 4.1. The specific displacement $\bar{v}$ of a gerotor can be found by normalizing the pump displacement to its root radius r_r and face width in eq. (4.2), and it is a measure of the compactness of the pump. The reciprocal of the specific displacement is the size to displacement ratio, and minimizing this ratio is the goal of the OF1. In the optimization, each of the pumps are scaled so that the facial displacement (displacement per unit face width) of the gearset is held constant. Therefore, the size to displacement ratio can be minimized by minimizing the root radius. In this work, the minimum allowable root radius $r_{r,min}$ to avoid interference is used, and the first OF is defined in eq. (4.3), where the s subscript indicates the variable value after scaling. The minimum allowable root radii for each gear profile were given in section 2.2 but are also summarized in table 4.1 with the exception to the asymmetric profile which must be found numerically as stated in eq. (2.45).

$$v = (m-1)(A_{max} - A_{min})h \tag{4.1}$$

$$\bar{v} = \frac{v}{r_r h} \tag{4.2}$$

$$\text{OF1: minimize}\{r_{r,min,s}\} \tag{4.3}$$

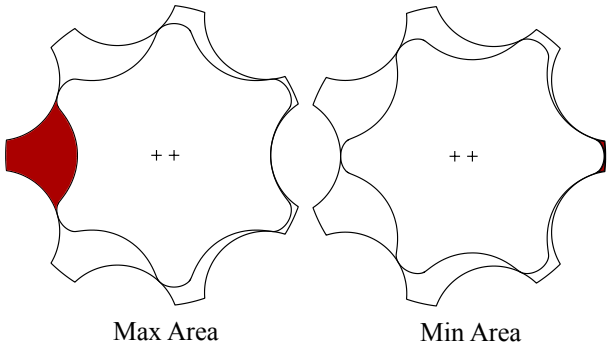

Figure 4.1. Minimum and maximum displacement chamber areas [33]

Table 4.1. Minimum allowable root radius for symmetric profile types

Profile Type	$r_{r,min}$
Epitrochoidal	$\rho - d + 2e$
Hypotrochoidal	$\rho - \frac{\rho}{m} + e + d$
Std. Cycloidal	$\rho - 2d + 2e$
Elliptical	$\rho - d + 2e$
Gen. Cycloidal	$\rho - 2d + 2e$
Cosine	$\rho - d + 2e$

The areas of the displacement chambers must be determined next to find the displacement of a pump so that the input variables can be scaled to the correct values to yield the desired displacement. A reference system for the displacement area as a function of rotation angle must first be established. In this work, the outer gear rotation angle θ_o is used as reference, as displacement chamber area is periodic with one outer gear rotation. A zero angle corresponds to when the outer gear tooth is centered on the x-axis on the minimum volume side, and a positive rotation angle corresponds to a counter-clockwise rotation. The displacement chamber corresponding to a given rotation angle is the one that immediately follows the

outer gear. In this way the rotation angle corresponding to the minimum and maximum displacement chamber areas are $\theta_o = \frac{\pi}{m}$ and $\theta_o = \pi + \frac{\pi}{m}$ respectively. For a given point on the outer gear, the two rotation angles at which it contacts the inner gear can be found explicitly in eqs. (2.8) and (2.9). However, an analytical solution to inverse of the function exists only for the conventional profile types. An interpolation table is made to approximate the solution to the function inverse (gear parameter and other quantities as a function of rotation), as it is much faster than solving eqs. (2.8) and (2.9) with a root finding method for each rotation angle.

At every point of rotation, three components to the displacement chamber area must be determined: the outer gear polar area A_o, the inner gear polar area A_i, and the area due to the difference in centers A_c. These three areas are illustrated in fig. 4.2. The displacement chamber area A can then be found by summing the components in eq. (4.4), where A_c can have a positive or negative sign depending on the sign of the y-value of the contact point.

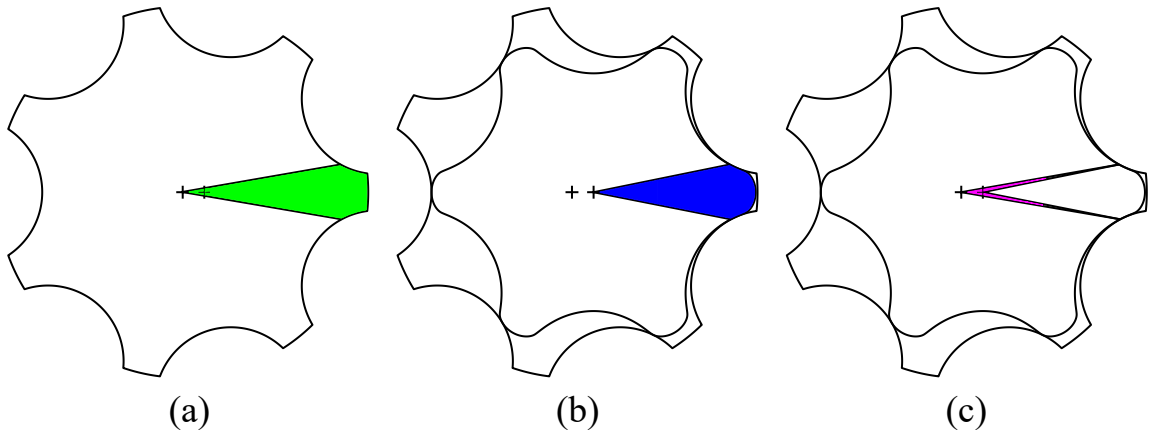

Figure 4.2. Illustration of components of the displacement chamber area: (a) outer gear area, (b) inner gear area, (c) area due to difference in centers

$$A = A_o - A_i - A_c \tag{4.4}$$

The outer gear polar area can be found in three components: the area between the contact point and the limit of contact on the reference tooth $A_{o,L}$, where the L subscript stands for leading, a constant area that includes the root area $A_{o,D}$, where the D subscript stands for

dead area, and the area between the limit of contact and the contact point on the following outer gear tooth $A_{o,F}$, where the F subscript stands for following. This is illustrated in fig. 4.3. The value of the constant area is does not affect the pump displacement, but it does influence the mean velocity of the fluid into the displacement chamber. The outer gear area can then be found in eq. (4.5), where ϕ_L and ϕ_F are the leading and following gear parameters of the contact points delineating the displacement chamber respectively. An analytical solution to eq. (4.5) was found for all the profile types with the exception of hypotrochoidal and asymmetric elliptical. The dead area is found changing the integration limits to account for the polar area accounting for the rest of the tooth curve, adding the area of the root sector, and adding or subtracting a triangular area term for the tooth profiles that use a tangent line to connect the tooth curve to the root arc. The details of these calculations are omitted for brevity.

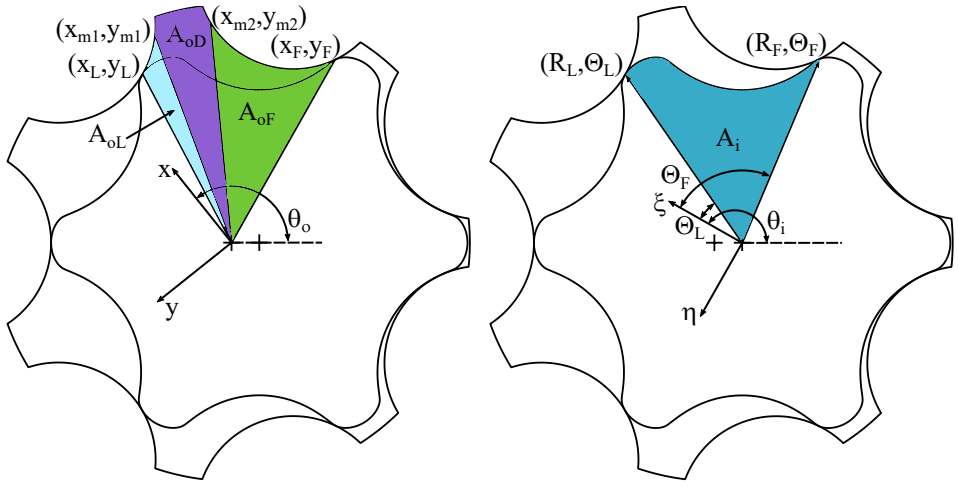

Figure 4.3. Illustration of outer (left) and inner gear (right) polar areas

$$A_o = A_{oL} + A_{oF} + A_{oD} = \frac{1}{2}\int_{\phi_{m,1}}^{\phi_L} xy' - yx' \, d\phi + \frac{1}{2}\int_{\phi_F}^{\phi_{m,2}} xy' - yx' \, d\phi + A_{o,D} \tag{4.5}$$

The polar area of the inner gear is calculated next. A challenge with determining this area is that the inner gear is generated in a piece-wise fashion as shown in fig. 2.9, so an alternative to the polar area integral in eq. (4.5) must be used to for numerical stability.

Instead, the radius and polar angle of the inner gear curve is tabulated in the interpolation table, and eq. (4.6) is used to determine the polar area, where R is the polar radius of the inner gear at the contact point, Θ is the polar angle of the inner gear, the L and F subscripts correspond to the leading and following contact points delineating the displacement chamber respectively. For each profile type eq. (4.6) must be solved numerically, which is done by trapezoidal integration of interpolated points. The limits of integration are found first by interpolation from the table that contains the gear parameter, outer gear coordinates, inner gear coordinates, and rotation angle. Then a second table is constructed that contains the inner gear polar radius as a function of the polar angle. The points to integrate for the inner gear polar area are then taken from this second table. In this way the integration points can be evenly spaced, which significantly reduces the time to compute the integral.

$$A_i = \frac{1}{2} \int_{\Theta_F}^{\Theta_L} R^2 \, d\Theta \tag{4.6}$$

The area that accounts for the difference in centers is given by eq. (4.7) where x and y are the coordinates of the contact point with respect to the outer gear center, and the L and F subscripts again refer to the leading and following contact points defining the displacement chamber. This is the same as the difference of the y-values of the contact points after rotation multiplied by half the center distance.

$$A_c = \frac{e}{2} \left[(x_L \sin\theta_{oL} + y_L \cos\theta_{oL}) - (x_F \sin\theta_{oF} + y_F \cos\theta_{oF}) \right] \tag{4.7}$$

The components of the displacement chamber area and the displacement chamber area as a function of rotation for a reference gerotor are shown in figs. 4.4 and 4.5 respectively. After each of the area components are determined at the minimum and maximum displacement chamber areas, the displacement of the pump can be determined by applying eqs. (4.1) and (4.4). The correct scaling factor by which each of the input variables with the exception of m and α should be multiplied to yield the desired pump displacement. Then the minimum allowable root radius for a pump with a given aspect ratio and displacement can be determined by inserting the scaled input variables into the expressions for the minimum allowable root radii in table 4.1 to give OF1.

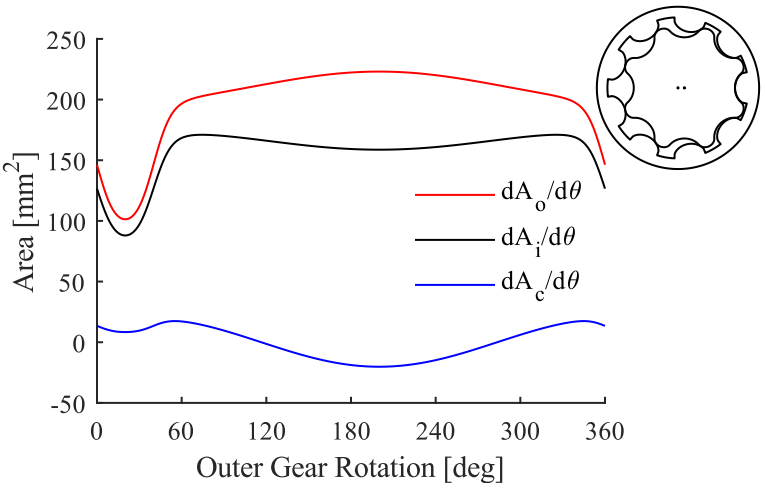

Figure 4.4. Displacement chamber area components for generalized cycloidal gerotor with $m = 9$, $e = 2.4$ mm, $\rho = 25$ mm, $d = 1.8$ mm, $r = 30$ mm, $r_r = 26.5$ mm (6.4 cm^2/rev)

4.2 Objective Function 2: Minimize Kinematic Flow Ripple

An ideal pump would have a constant outlet flow. However because most positive displacement pumps have discrete pumping chambers, a variable outlet flow, often called a flow ripple, is produced, and gerotors are not an exception. The flow ripple in a hydraulic system can lead to vibration, noise, and poor system dynamics, so it should be minimized as much as possible. The kinematic flow per unit face width of a gerotor is given by Q in eq. (4.8), where q_j is the outlet flow from the j^{th} displacement chamber. The flow from each displacement chamber is defined in eq. (4.9), where θ_i is the inner gear rotation angle. The kinematic flow assumes an incompressible fluid, no internal leakages within the pump, and ideal port timing so that when a displacement chamber is expanding it is connected to the suction port and to the delivery port when decreasing in volume.

$$Q = \sum_{j=1}^{m} q_j \tag{4.8}$$

$$q_j = \begin{cases} -\frac{dA_j}{d\theta_i} & \frac{dA_j}{d\theta_i} \leq 0 \\ 0 & \frac{dA_j}{d\theta_i} > 0 \end{cases} \tag{4.9}$$

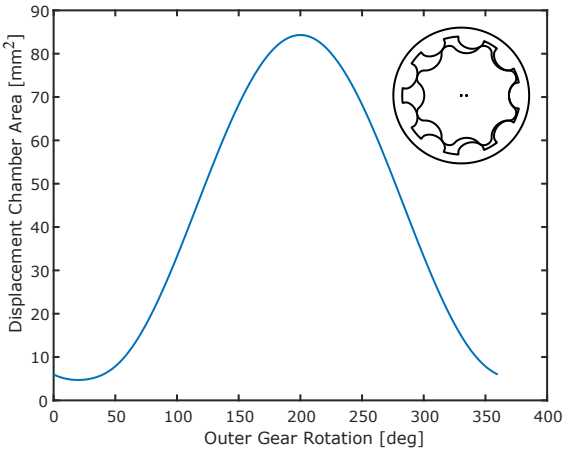

Figure 4.5. Displacement chamber area for generalized cycloidal gerotor with $m = 9$, $e = 2.4$ mm, $\rho = 25$ mm, $d = 1.8$ mm, $r = 30$ mm, $r_r = 26.5$ mm (6.4 cm^2/rev)

The area derivatives can be broken into the same components as in eq. (4.4) in eq. (4.10), and the second fundamental theorem of calculus can then be used so the integrals in eqs. (4.5) and (4.6) do not need to be evaluated as shown in eqs. (4.11)–(4.13). Almost all of the terms in eqs. (4.11)–(4.13) require a solving the inverse of an explicit function with no analytical solution, so an interpolation table is used again. For each outer gear parameter that contacts the inner gear, the rotation angle at which that point is in contact, the unrotated contact point coordinates on both gears, the inner gear polar radius and angle, the derivatives of the outer gear tooth with respect to the gear parameter, the derivative of the rotation angle with respect to the outer gear parameter, and the derivative of the inner gear polar angle with respect to the outer gear parameter are tabulated so that each of the quantities can be interpolated for a given rotation angle. The L and F subscripts again refer to leading and following contact points of the displacement chamber respectively. The leading contact point corresponds to the reference outer gear tooth rotated by the rotation angle θ_o, and the following contact point corresponds to the position of the reference outer gear tooth at phase shifted rotation angle $\theta_o - \frac{2\pi}{m}$.

$$\frac{\mathrm{d}A}{\mathrm{d}\theta_o} = \frac{\mathrm{d}A_o}{\mathrm{d}\theta_o} - \frac{\mathrm{d}A_i}{\mathrm{d}\theta_o} - \frac{\mathrm{d}A_c}{\mathrm{d}\theta_o} \tag{4.10}$$

$$\frac{\mathrm{d}A_o}{\mathrm{d}\theta_o} = \frac{1}{2}\left[\left(x_L \left.\frac{dy}{d\phi}\right|_{\phi=\phi_L} - y_L \left.\frac{dx}{d\phi}\right|_{\phi=\phi_L}\right)\left.\frac{\mathrm{d}\phi}{\mathrm{d}\theta_o}\right|_{\theta_o=\theta_{o,L}} - \left(x_F \left.\frac{dy}{d\phi}\right|_{\phi=\phi_F} - y_F \left.\frac{dx}{d\phi}\right|_{\phi=\phi_F}\right)\left.\frac{\mathrm{d}\phi}{\mathrm{d}\theta_o}\right|_{\theta_o=\theta_{o,F}}\right] \tag{4.11}$$

$$\frac{\mathrm{d}A_i}{\mathrm{d}\theta_o} = \frac{1}{2}\left[R^2\left.\frac{d\Theta}{d\phi}\right|_{\phi=\phi_L}\left.\frac{d\phi}{d\theta_o}\right|_{\theta_o=\theta_{o,L}} - R^2\left.\frac{d\Theta}{d\phi}\right|_{\phi=\phi_F}\left.\frac{d\phi}{d\theta_o}\right|_{\theta_o=\theta_{o,F}}\right] \tag{4.12}$$

$$\begin{aligned}\frac{\mathrm{d}A_c}{\mathrm{d}\theta_o} = \frac{e}{2}\Bigg[\Bigg(x_L\cos(\theta_{o,L}) + \left.\frac{dx}{d\phi}\right|_{\phi=\phi_L}\left.\frac{d\phi}{d\theta_o}\right|_{\theta_o=\theta_{o,L}}\sin(\theta_{o,L}) - y_L\sin(\theta_{o,L}) + \left.\frac{dy}{d\phi}\right|_{\phi=\phi_L}\left.\frac{d\phi}{d\theta_o}\right|_{\theta_o=\theta_{o,L}}\cos(\theta_{o,L})\Bigg) - \ldots \\ \ldots - \left(x_F\cos(\theta_{o,F}) + \left.\frac{dx}{d\phi}\right|_{\phi=\phi_F}\left.\frac{d\phi}{d\theta_o}\right|_{\theta_o=\theta_{o,F}}\sin(\theta_{o,F}) - y_F\sin(\theta_{o,F}) + \left.\frac{dy}{d\phi}\right|_{\phi=\phi_F}\left.\frac{d\phi}{d\theta_o}\right|_{\theta_o=\theta_{o,F}}\cos(\theta_{o,F})\right)\Bigg]\end{aligned} \tag{4.13}$$

The area derivative as a function of outer gear rotation angle for a reference pump are shown in fig. 4.6. The area derivative curve can then be phase shifted m times and summed in eq. (4.8) to give the kinematic flow as shown in fig. 4.7. Since the inner gear is typically used to drive the pump, the outlet flow should be given as a function of the inner gear rotation rather than the outer gear rotation. The outer gear rotation and flow can be divided and multiplied by the gear ratio to give the inner gear rotation and flow in eqs. (4.14) and (4.15) respectively.

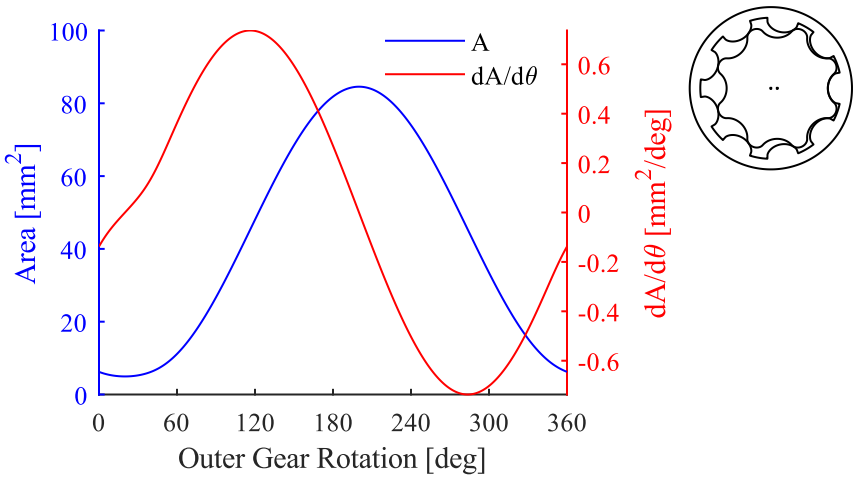

Figure 4.6. Displacement chamber area and its derivative for a generalized cycloidal gerotor with $m = 9$, $e = 2.4$ [mm], $\rho = 25$ [mm], $d = 1.8$ [mm], $r = 30$ [mm], $r_r = 26.5$ mm (6.4 cm^2/rev)

$$\theta_i = \theta_o \frac{m}{m-1} \tag{4.14}$$

$$Q_i = Q_o \frac{m-1}{m} \tag{4.15}$$

Many other researchers have evaluated the kinematic flow ripple on a peak-to-peak basis defined in eq. (4.16) [13], [17], [21], [25], [26], where ϵ is the percent variation in flow, and $\bar{Q}$ is the mean pump flow. However, this metric does not account for the shape of the flow ripple. The kinematic flow ripple can vary significantly between gear profiles as shown in fig. 4.8 for two circular gerotors with the same displacement and face width. A better metric would

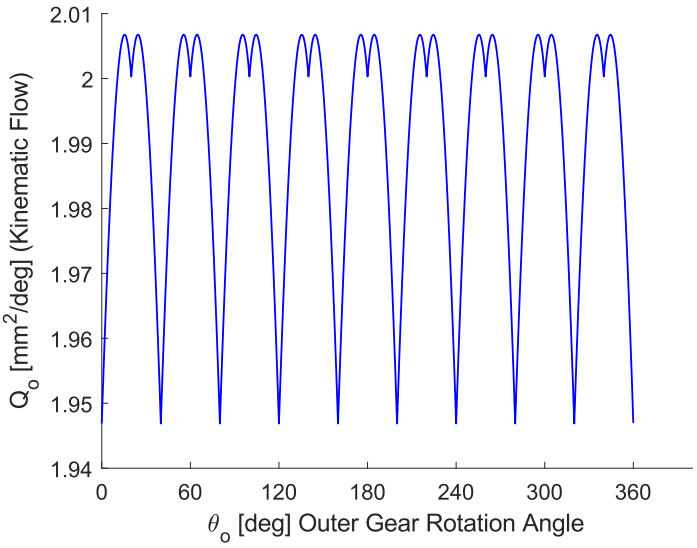

Figure 4.7. Kinematic flow for generalized cycloidal gerotor with $m = 9$, $e = 2.4$ [mm], $\rho = 25$ [mm], $d = 1.8$ [mm], $r = 30$ [mm] (6.4 cm^2/rev)

be to consider the signal power of the flow ripple, which considers the frequency content of the flow ripple. The signal power of the kinematic flow ripple $\bar{E}$ is given in eq. (4.17), where the bar over E indicates that the signal power is normalized to the operating conditions and face width. The second OF for the optimization is then defined in eq. (4.18), and using the signal power to quantify the kinematic flow ripple is new to this work.

$$\epsilon = \frac{Q_{max} - Q_{min}}{\bar{Q}} \tag{4.16}$$

$$\bar{E} = \frac{m-1}{2\pi} \int_0^{\frac{2\pi}{m-1}} \left[Q(\theta_i) - \bar{Q} \right]^2 \, d\theta_i \tag{4.17}$$

$$\text{OF2: minimize}\{\bar{E}\} \tag{4.18}$$

In pump operation usually a significant difference between the measured outlet flow and the kinematic flow is present because of fluid compressibility and internal leakages. This raises the question of whether the kinematic flow is a suitable metric for comparing gear geometries. To test this, a simulation study was performed with five elliptical gerotors with

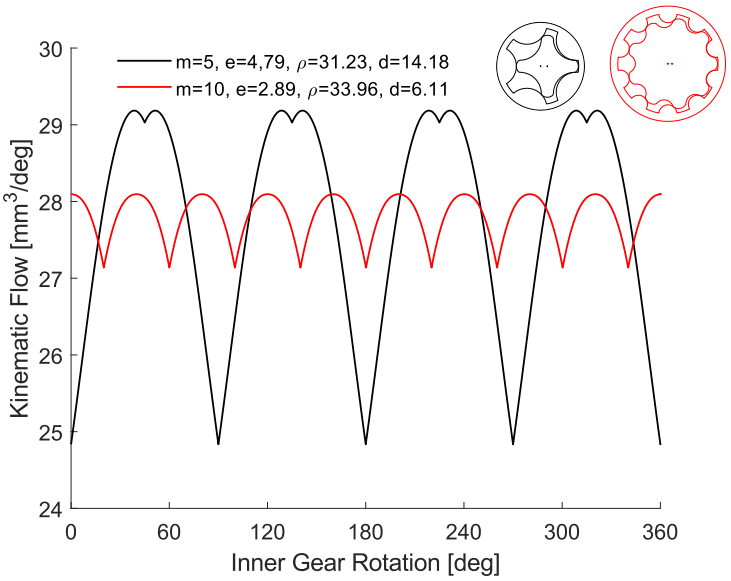

Figure 4.8. Comparison of kinematic flow ripple for two pumps with the same displacement

the same geometric displacement and face with but different values of kinematic flow signal power to test how well the kinematic flow predicted the simulated outlet flow. The design of the inlet and outlet ports has a significant effect on the pump performance, so each pump was tested with a good set of ports. The ports for the study were designed by multi-objective optimization to minimize the outlet flow ripple, displacement chamber pressure peak, and the displacement chamber pressure drop below the suction port pressure and to maximize the volumetric efficiency. The kinematic flow was then compared to the simulated outlet flow for each pump with optimized ports. The study found that while the kinematic flow ripple is a poor predictor of the simulated flow ripple, it does predict the correct ranking of the designs. The kinematic flow is therefore a suitable metric for designing gerotor gear geometry. A more thorough description of the validation procedure can be found in appendix A.

4.3 Objective Function 3: Minimize Adhesive Wear

Because gerotor are often used as lubrication pumps, their durability is very important to function of the entire system. The wear in a gerotor gearset is greatly affected by the working fluid, operating conditions, and material properties, but the shape of the gears is

also important. The volume of material worn in machine elements is generally thought to be proportional to the work done by friction as given in the popular Archard wear model in eq. (4.19), where W is the volume of worn material, K is a wear coefficient, F is the contact force, S is the sliding distance, and H is the hardness of the material. Determining the appropriate value of K is generally done empirically, but the value of K is assumed to remain constant among gerotors using the same materials and operating under the same conditions. The material hardness is also assumed to be constant across designs. The Archard model can then be modified to give a wear rate for use as an OF in gerotor gear design that is normalized to K, H, the face width h, operating pressure Δp, and inner gear rotation speed ω_i in eq. (4.20), where $\overline{F}$ is the normalized contact force and $\overline{S}$ is the normalized sliding speed. In this manner, the exact value of the wear coefficient does not matter as long as it remains constant across designs. Then OF3 is minimizing the peak value of the normalized wear rate over one full revolution of the inner gear in eq. (4.21).

$$W = \frac{KFS}{H} \tag{4.19}$$

$$\overline{W} = \frac{WH}{Kh\Delta p\omega_i} = \overline{FS} \tag{4.20}$$

$$\text{OF3: minimize} \left\{ \max \overline{W}, 0 \leq \theta_i < 2\pi + \frac{2\pi}{m-1} \right\} \tag{4.21}$$

The values of $\overline{F}$ and $\overline{S}$ must be determined next to give a value of OF3. In an ideal gerotor, every tooth on the outer gear contacts the inner gear for the whole rotation. This makes the system statically indeterminate. Several other researchers have used Hertzian contact equations to estimate the force at each contact point [14], [19], [38], however most gerotors in production usually have a constant radial clearance of 20-50 μm introduced to improve assembly, account for manufacturing tolerances, and to account for thermal expansion. If the bearings are assumed to be stiff, tooth deflections are assumed to be small since the pumps typically operate at pressures under 30 bar, and manufacturing errors in the profile are assumed to be small, then only one point of the inner gear will contact the outer

gear. If only one point actually comes into contact, then the system is no longer statically indeterminate, and the contact force can be found from the applied torque and position of the contact point. Assuming a single contact point also gives a sort of worst-case scenario, as if multiple points between the gears come into contact, the contact force will be reduced by load sharing. This single contact point assumption was also verified numerically [39], and a similar approach was used to determine the contact mechanics in a gerotor orbit motor [40].

The single contact point can be illustrated as follows. If the inner gear is driving, it will rotate a differential amount past its nominal position at each contact angle until one point comes into contact. This is shown in fig. 4.9 with a gearset that has a large clearance for illustration purposes. The exact point on the gears that comes into contact will shift slightly with the differential rotation, but since the clearance is assumed to be small, the shift in the contact point is also assumed to be small. The exact point that comes into contact will be a function of the gear geometry and the value of the clearance. However, the exact value of the clearance should not be considered in a gear geometry optimization, but it should be considered later when focusing on the fluid dynamic aspects of the pump. For these reasons, the position of the contact point in this work is assumed to be at its nominal position without clearance when determining the force and sliding speed.

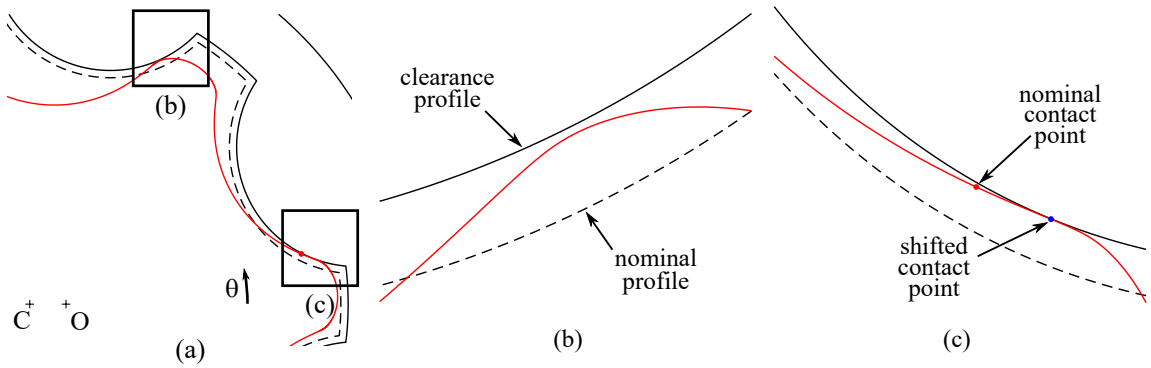

Figure 4.9. Illustration of single contact point in a gearset with clearance [41]

Exactly which contact point drives the gearset is predicted next. After the inner gear rotates by a differential angle $d\theta$, the vector of the contact point with respect to the inner

gear center $\mathbf{r_i}$ will move to $\mathbf{r_i'}$, and the change in position of the point will be **ds**. The displacement of the contact point can be broken into its tangential component **dt** and its normal component **dn**. The contact point with the greatest magnitude of **dn** is the point that is predicted to first make contact with the outer gear. The exact value of $d\theta$ required for the inner gear to contact the outer gear is again a function of the gear geometry and the clearance value, but since the clearance is to be neglected, the vector product $\left(\hat{k} \times \mathbf{r_i}\right) \cdot \hat{n}$ can be used to predict which point will contact first.

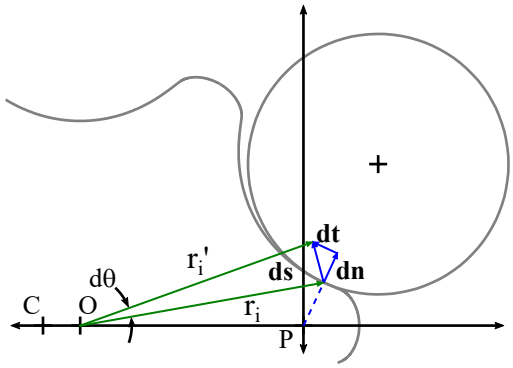

Figure 4.10. Illustration of differential rotation

The contact point for each outer gear tooth at each angle of rotation is found from an interpolation table as described section 4.1. The location of the contact point after rotation with respect to a fixed coordinate system located at center of the outer gear is (X, Y) and found by applying the rotation matrix in eq. (4.22). The position vector of the contact point with respect to the inner gear center can then be found in eq. (4.23). The angle that the normal to the profile makes with the x-axis of the coordinate system that rotates with the outer gear is Ψ and given in eq. (4.24), so the unit normal to the contact point in the fixed frame of reference is then given by eq. (4.25). At every instance in rotation, the contact point with the greatest value of $\left(\hat{k} \times \mathbf{r_i}\right) \cdot \hat{n}$ is taken to be the active contact point at which the entire load is transmitted. When this procedure is applied, the shortened path of contact that is the locus of active contact points is shown in fig. 4.11, where the nominal path of contact is shown in green, and the shortened path of contact is shown in blue and red. The

blue portion corresponds to primary contact with a positive pressure angle, and the red portion corresponds to secondary contact with a negative pressure angle.

$$\begin{bmatrix} X \\ Y \end{bmatrix} = \begin{bmatrix} \cos\theta_o & -\sin\theta_o \\ \sin\theta_o & \cos\theta_o \end{bmatrix} \begin{bmatrix} x \\ y \end{bmatrix} \tag{4.22}$$

$$\mathbf{r_i} = (X - e)\,\hat{i} + Y\hat{j} \tag{4.23}$$

$$\Psi = \arctan\left(\frac{-x'}{y'}\right) \tag{4.24}$$

$$\hat{n} = \cos(\Psi + \theta_0)\,\hat{i} + \sin(\Psi + \theta_0)\,\hat{j} \tag{4.25}$$

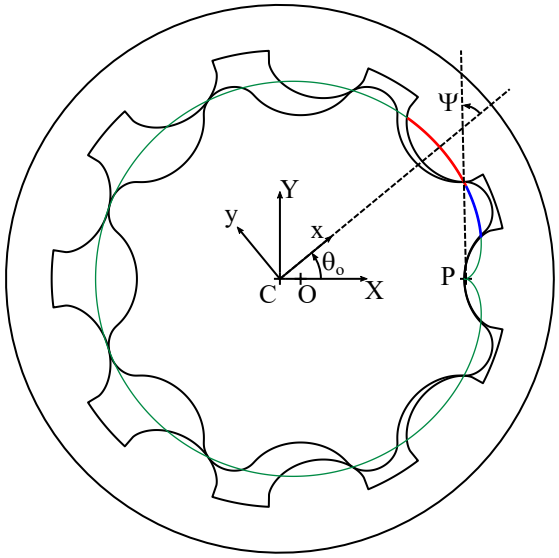

Figure 4.11. Active path of contact for a generalized cycloidal gerotor with $m = 9$, $e = 2.4$ mm, $\rho = 25$ mm, $d = 1.8$ mm, $r = 30$ mm (6.4 cm^2/rev)

After the contact point has been determined, the magnitude of the contact force can be calculated. The torque required to drive a pump is mainly a function of the operating pressure and displacement, but fluid shear in the lubricating interfaces can increase the

required torque. However, the torque can still be estimated by the kinematic torque to capture the correct geometric effects for gear design. The mean total torque to drive a hydraulic pump is given in eq. (4.26) as M_{avg}, and the instantaneous torque is given by M in eq. (4.27), where Q is the flow per face width in this case. This torque can then be normalized to the face width and operating pressure in eq. (4.28). However, eq. (4.28) considers the total torque required to drive the pump, but only the torque necessary to drive the outer gear (assuming the inner gear is driving) should be used to determine the contact force. The hydraulic pressure applied to each gear can be visualized in fig. 4.12, where the low pressure is shown in blue, and the high pressure is red. The moments on the outer and inner gear are then given in eqs. (4.29) and (4.30) respectively. The normalized contact force can then be found in eq. (4.31) after accounting for the gear ratio. A plot showing the percentage of the hydraulic torque required to drive the pump due to the inner and outer gears is shown in fig. 4.13 and reveals that most of the hydraulic moment is applied to the inner gear and that the moment on the outer gear can be assisting at some points of rotation. This could be an important consideration when choosing to drive the pump by the outer gear [4].

$$M_{avg} = v\Delta p \tag{4.26}$$

$$M = Qh\Delta p \tag{4.27}$$

$$\overline{M} = \frac{M}{h\Delta p} = Q \tag{4.28}$$

$$M_i = \frac{h\Delta p}{2}\left(\xi_1^2 - \xi_2^2 + \eta_1^2 - \eta_2^2\right) \tag{4.29}$$

$$M_o = \frac{h\Delta p}{2}\left(x_2^2 - x_1^2 + y_2^2 - y_1^2\right) \tag{4.30}$$

$$\overline{F} = \frac{F}{h\Delta p} = \frac{M_o{}^{\frac{m-1}{m}}}{h\Delta p\,|\mathbf{r_i} \times \hat{n}|} \tag{4.31}$$

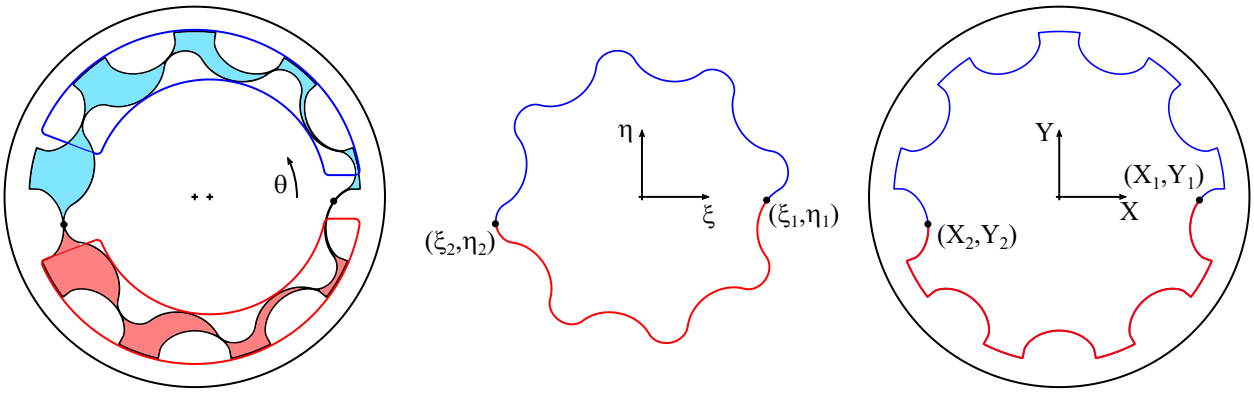

Figure 4.12. Pressure load on each gear

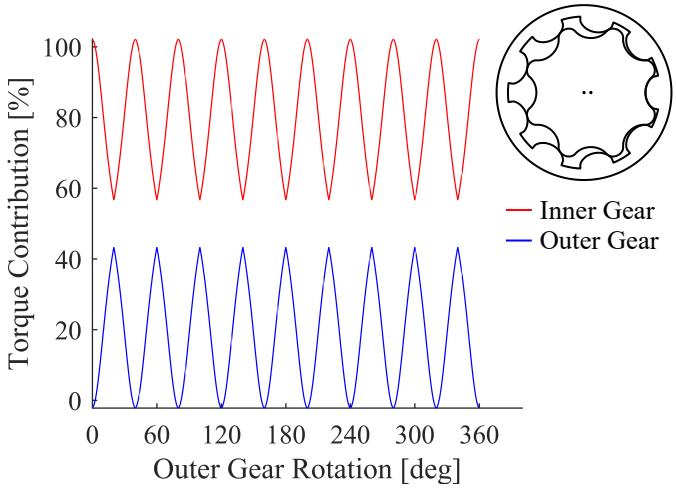

Figure 4.13. Contribution of each gear on total hydraulic moment for a generalized cycloidal gerotor with $m = 9$, $e = 2.4$ mm, $\rho = 25$ mm, $d = 1.8$ mm, $r = 30$ mm

Next, the relative sliding speed is determined. The instantaneous velocities of the contact point on the inner gear and on the outer gear are given by eqs. (4.32) and (4.33), where $\mathbf{v_i}$ and $\mathbf{v_o}$ are the respective velocities, and $\omega_\mathbf{o}$ is the outer gear rotation. The relative sliding speed is the difference in the velocity vectors in the tangential direction given in eq. (4.34),

where S is the relative sliding speed, and $\hat{t}$ is the unit tangent vector that is defined in eq. (4.35). The sliding speed can then be normalized to the inner gear speed in eq. (4.36).

$$\mathbf{v_i} = \omega_\mathbf{i} \times \mathbf{r_i} \tag{4.32}$$

$$\mathbf{v_o} = \omega_\mathbf{o} \times \mathbf{r_o} \tag{4.33}$$

$$S = \left| \mathbf{v_i} \cdot \hat{t} - \mathbf{v_o} \cdot \hat{t} \right| \tag{4.34}$$

$$\hat{t} = -\sin\left(\Psi + \theta_0\right)\hat{i} + \cos\left(\Psi + \theta_0\right)\hat{j} \tag{4.35}$$

$$\overline{S} = \frac{S}{\omega_i} \tag{4.36}$$

The normalized contact force and sliding speed are then multiplied to get the normalized wear function, which is shown is shown in fig. 4.14 for a reference gearset scaled to the same facial displacement of 10 cc/rev as the geometries in the optimization shown in the figure at the zero rotation angle.

4.4 Objective Function 4: Minimize Contact Stress

As two curved surfaces are pressed together, both will deform slightly to distribute the force over a small contact area. The stresses are usually called Hertizain stresses, and they can be very high. The peak shear stress experienced by the material occurs below the contact surface, and the sign of the stress will be opposite on either side of the contact point. When the surfaces move relative to one another, the material will experience an alternating shear stress below the surface of the material. This can lead to fatigue failure in the form of pitting, which can be observed in spur gears for power transmission applications.

However, the contact mechanics in gerotors are more complex than that predicted by Hertzian theory. Hertzian theory assumes dry contact, no friction, elastic deformation, and

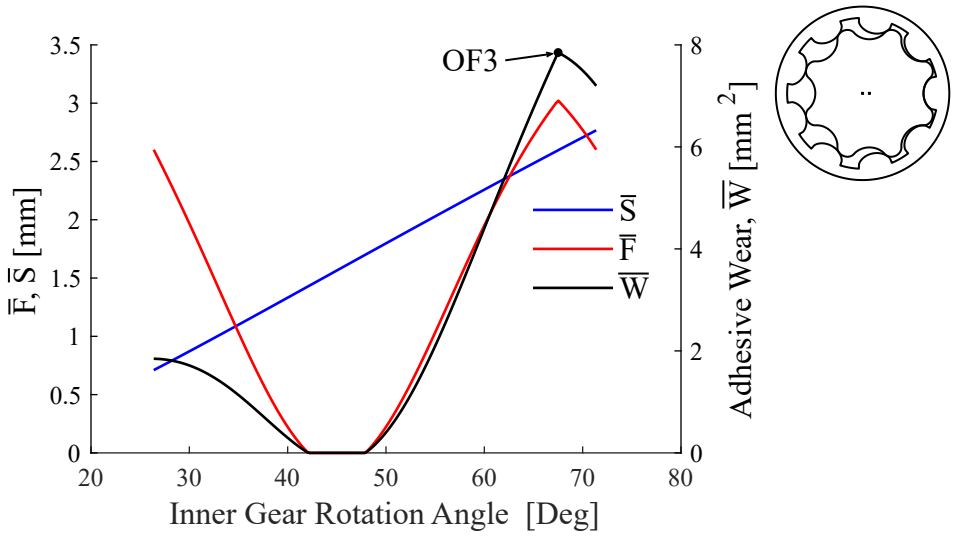

Figure 4.14. Illustration of normalized adhesive wear function for for a generalized cycloidal gerotor with $m = 9$, $e = 2.4$ mm, $\rho = 25$ mm, $d = 1.8$ mm, and $r = 30$ mm scaled to 10 cc/rev

that the curvature of the surfaces does not change appreciably near the contact patch. Gerotor gears at the driving contact point are likely operating in the elastohydrodynamic regime, where the load is partially supported by a thin film of oil, and only surface asperities make contact. A friction force is also generated because of the relative sliding of the profiles. Despite the limitations however of Hertzian contact assumptions, machine components including spur gears with higher Hertzian contact stresses have been shown empirically to have lower lifetimes [42, p. 376].

The Hertzian contact stress model is implemented by approximating the gears as two cylinders in contact with equivalent radii of curvature as the gear profiles at the contact point. This is illustrated in fig. 4.15. The radii of curvature of the inner and outer gear are given by R_i and R_o respectively. The contact is modeled as a cylinder with combined radius of curvature of the two contacting circles against a flat surface. The combined radius of curvature is given by R and defined in eq. (4.37). The combined modulus of elasticity is E^* and is defined in eq. (4.38), where ν_i and ν_o and E_i and E_o are the Poisson's ratio and modulus of elasticity for the inner and outer gears respectively. The radius of curvature of the outer gear at the contact point is found in eq. (4.39), where finding the gear parameter for

the specified rotation angle is found from an interpolation table as described previously. The radius of curvature of the inner gear could be found by the standard relation in eq. (4.40), but the second derivatives of the inner gear coordinates are quite cumbersome. Instead, the Euler-Savary equation for internal gears including secondary action can be used to find the inner gear radius of curvature with much less effort in eq. (4.41) [43, p. 234], where Φ is the pressure angle defined in eq. (4.42), $r_{p,i}$ is the inner gear pitch radius defined in eq. (4.43), $r_{p,o}$ is the outer gear pitch radius defined in eq. (4.44), and s is the distance from the contact point to the pitch point in the fixed frame of reference defined in eq. (4.45). Note that s has a negative value if the contact point is located inside the outer gear pitch circle. eq. (4.41) can be solved for R_i and simplified in eq. (4.46). The variable κ represents the curvature and is the reciprocal of the radius of curvature. A further simplification can also be made for epitrochoidal and hypotrochoidal profiles, as a portion of the curves are circular.

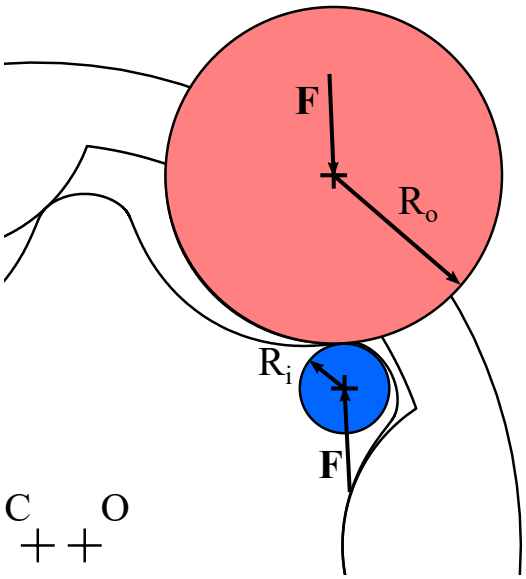

Figure 4.15. Illustration of cylinder contact model [41]

$$\frac{1}{R} = \frac{1}{R_i} + \frac{1}{R_o} \tag{4.37}$$

$$\frac{1}{E^*} = \frac{1-\nu_i^2}{E_i} + \frac{1-\nu_o^2}{E_o} \tag{4.38}$$

$$R_o = \frac{1}{\kappa_o} = \frac{(x'^2 + y'^2)^{\frac{3}{2}}}{x'y'' - y'x''} \tag{4.39}$$

$$R_i = \frac{1}{\kappa_i} = \frac{(\xi'^2 + \eta'^2)^{\frac{3}{2}}}{\xi'\eta'' - \eta'\xi''} \tag{4.40}$$

$$\frac{1}{R_i - s} + \frac{1}{R_o + s} = \frac{1}{\sin\Phi}\left(\frac{1}{r_{p,i}} - \frac{1}{r_{p,o}}\right) \tag{4.41}$$

$$\Phi = \frac{\pi}{2} + \theta_o - \Psi \tag{4.42}$$

$$r_{p,i} = (m-1)e \tag{4.43}$$

$$r_{p,o} = me \tag{4.44}$$

$$s = \begin{cases} -\sqrt{(X - me)^2 + Y^2}, & \sqrt{X^2 + Y^2} < me \\ \sqrt{(X - me)^2 + Y^2}, & \sqrt{X^2 + Y^2} \geq me \end{cases} \tag{4.45}$$

$$R_i = \frac{(R_o + s)\, m(m-1)e \sin\Phi}{(R_o + s) - m(m-1)e\sin\Phi} + s \tag{4.46}$$

After determining the contact force and the curvature of the gear profiles at the contact point, the standard Hertzian contact pressure is given in eq. (4.47), which can be normalized to the material properties and operating pressure in eq. (4.48) to give the normalized contact pressure $\overline{p_0}$. The peak value of $\overline{p_0}$ is the basis of OF4 in eq. (4.49). The components of OF4 are then illustrated in fig. 4.16 for a reference pump.

$$p_0 = \sqrt{\frac{FE^* \left|\kappa_i + \kappa_o\right|}{\pi h}} \tag{4.47}$$

$$\overline{p_0} = p_0\sqrt{\frac{\pi}{E^*\Delta p}} = \sqrt{\overline{F}\,|\kappa_i + \kappa_o|} \tag{4.48}$$

$$\text{OF4: minimize}\left\{\max \overline{p_0}, 0 \le \theta_i < 2\pi + \frac{2\pi}{m-1}\right\} \tag{4.49}$$

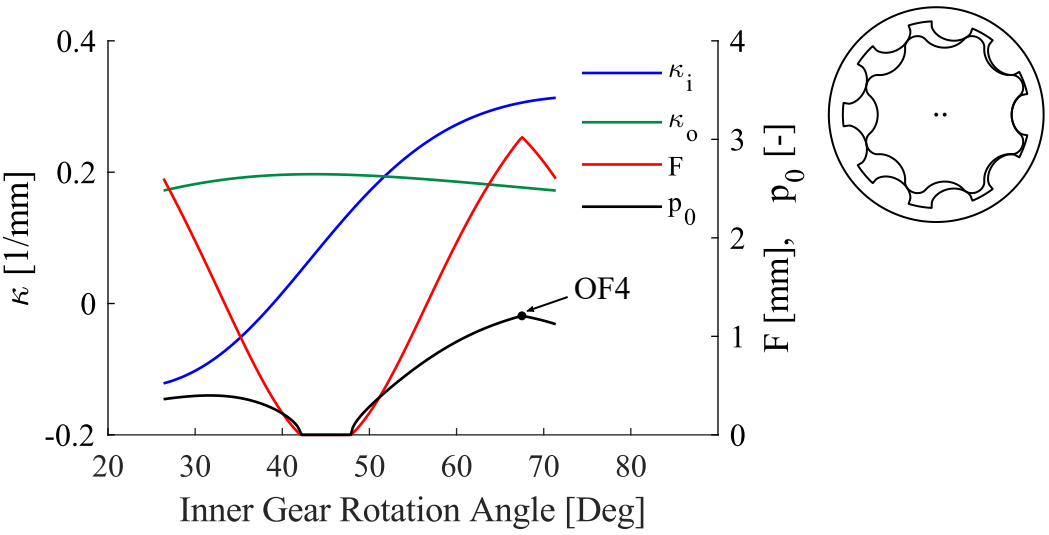

Figure 4.16. Components of OF4 for a generalized cycloidal gerotor with $m = 9$, $e = 2.4$ mm, $\rho = 25$ mm, $d = 1.8$ mm, and $r = 30$ mm scaled to 10 cc/rev

An additional consideration should be made for nonconformal contact. During part of the rotation of a gerotor, the outer gear convex tooth surface has nearly the same radius of curvature as the inner gear concave surface. This is illustrated in fig. 4.17. In this region of contact, the assumptions of Hertzian contact do not apply, however this is not a problem for the approach. As shown in fig. 4.16, the peak contact pressure occurs far from the region with possible conformal contact, so any small errors in determining the contact stress would not affect the value of OF4.

One of the downfalls of the standard cycloidal profile is that both profiles approach infinite curvature when the contact occurs at the pitch point. One question then is whether the point with an infinite combined curvature makes contact under the single contact point assumption. A plot of the shortened path of contact for a cycloidal gerotor is given in

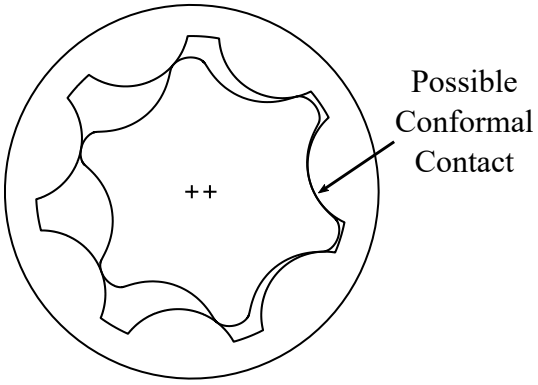

Figure 4.17. Possible conformal contact in a gerotor [41]

fig. 4.18 and illustrates that cycloidal gerotors are predicted to contact where their combined curvatures are infinite. Herzian equations don't apply in this region since the curvature changes very rapidly in comparison to the contact area after deformation. The curvatures of the surface also likely do not reach their theoretical values due to manufacturing tolerances, and the lubricant also would likely change the contact pressure distribution. However, after the gears rotate a few more degrees, Hertzian equations would likely begin to be applicable again. At this region though, the contact pressure woulds still be very high, as the curvatures are descending from an infinite value, which is also illustrated in fig. 4.18. For these reasons, the contact pressure for cycloidal profiles is taken to be greater than that for other profile types, but the exact determination of the contact pressure is beyond the scope of this work.

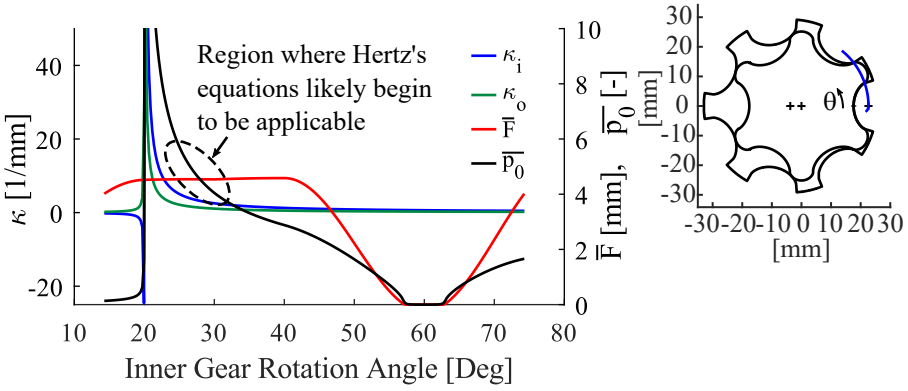

Figure 4.18. Components of OF4 for a cycloidal profile with $m = 7$ and $\lambda_d = 0.667$ scaled to 10 cm^2/rev [27]

4.5 Objective Function 5: Minimize Tooth Tip Leakage

The tooth tips of a gerotor must not only drive the gearset but also perform a sealing function as the displacement chamber transitions from the suction to the delivery port. In this region, high- and low- pressure fluid are separated by a small gap between the tooth tips through which fluid can leak from one displacement chamber to another. The amount of leakage is highly dependent on the operating pressure, the height of the gap, and viscosity of the working fluid, but the gear geometry also plays a role. Gears with higher curvature are expected to have higher leakage flow provided the other factors remain constant.

The most accurate way to predict the amount of leakage through the tooth tips would be to use a CFD model, but this method requires too much computation time to be used in an optimization. A faster approach could be to use the mean combined curvature in the sealing region $\overline{\kappa}$ of the pump as an OF, which is defined in eq. (4.50). This method would not be able to predict the amount of leakage flow, but it can rank the designs in the appropriate order. Then OF5 is to minimize $\overline{\kappa}$ in eq. (4.51).

$$\overline{\kappa} = \frac{m}{\pi} \int_{\theta_o=\pi-\frac{\pi}{m}}^{\theta_o=\pi} \kappa_i\left(\theta_o\right) + \kappa_o\left(\theta_o\right) \; d\theta_o \tag{4.50}$$

$$\text{OF5: minimize } \overline{\kappa} \tag{4.51}$$

To validate OF5 as a suitable OF for gear design, seven elliptical gerotors with different values of $\overline{\kappa}$ were selected, and the leakage across the tips of the teeth was simulated using a 2D CFD model in ANSYS Fluent. The pumps used in the study are shown in fig. 4.19. Each pump had a tooth tip clearance of 25μm, and the flow was simulated for each gearset at a position of $\theta_o = 180°$. The flow was assumed to be incompressible and laminar. The working fluid was ISO 46 oil with a constant viscosity. Two simulations were run for each pump at pressures of 5 bar and 60 bar. Typical solutions to the pressure and velocity streamlines are shown in figs. 4.20 and 4.21 respectively. The correlation between the simulated leakage and $\overline{\kappa}$ is shown in fig. 4.22. fig. 4.22 shows that $\overline{\kappa}$ correctly predicts the trend in leakage for all the pumps at both pressure cases, which indicates that it can be used as an OF for gear

design. The relationship between $\overline{\kappa}$ and the simulated leakage flows in fig. 4.22 is nonlinear, but it should be noted that the CFD simulations were performed only at $\theta_o = 180°$, while $\overline{\kappa}$ considers the combined curvature in the entire sealing region. If the simulation results were plotted as a function the combined curvature at $\theta_o = 180°$, the relationship would likely approximate $Q \propto \sqrt{\overline{\kappa}}$ [44].

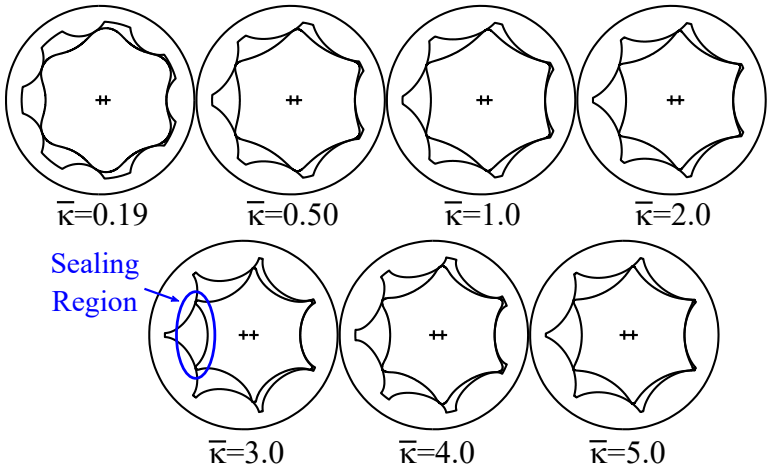

Figure 4.19. Pumps used in tooth tip gap leakage study [33]

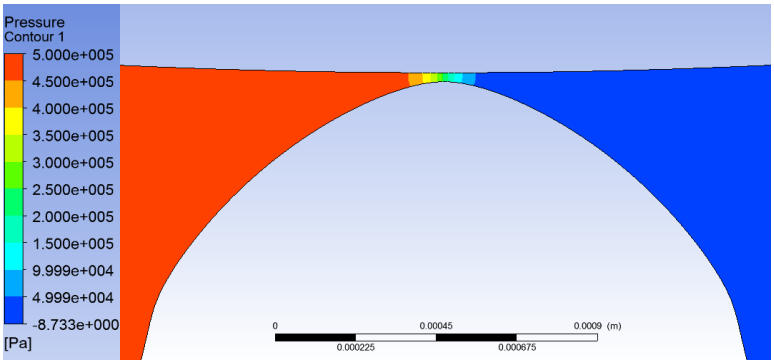

Figure 4.20. Simulated 2D pressure field [33]

4.6 Objective Function 6 Minimize Lateral Gap Leakage

The gear teeth must also perform a sealing function in the lateral face of the gears in addition to between the tooth tips. This is illustrated in fig. 4.23. Similar to the tooth tip

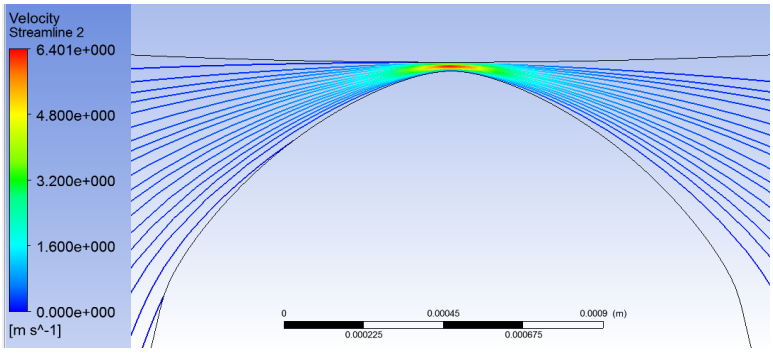

Figure 4.21. Simulated velocity streamlines [33]

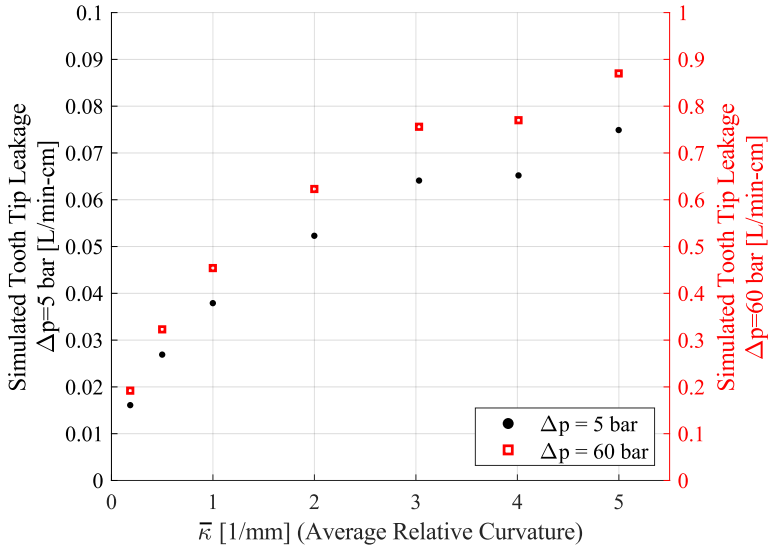

Figure 4.22. Correlation of OF5 with simulated leakage [33]

gap, the amount of flow in the tooth tip gap depends highly on the gap height, operating pressure, and viscosity, but the shape of the gear teeth is also a factor. Teeth with short lengths and tall heights would have more leakage in the lateral gap than teeth with long lengths and short heights provided other factors are the same. Again, the most accurate method to simulate the amount of leakage flow would be to perform a CFD simulation, but the computation time precludes it from use in an extensive optimization.

The correct geometric relationship to minimize can be determined my modeling each section of tooth as a differential section of flow through infinite parallel plates. Poiseuille flow per unit depth through infinite parallel plates is given in the standard equation in

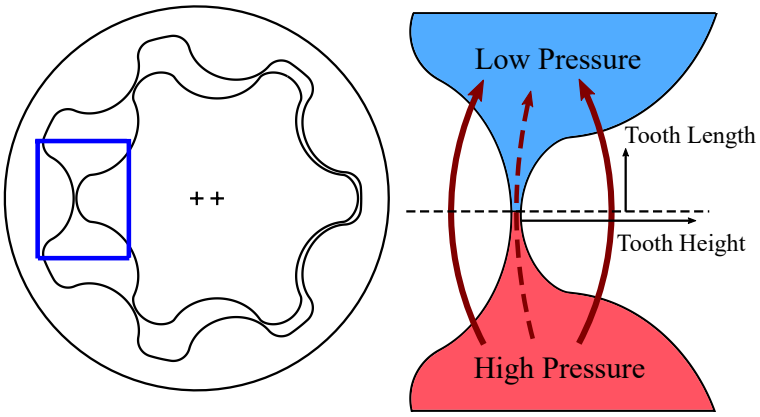

Figure 4.23. Illustration of tooth tip and lateral gap leakage paths [31]

eq. (4.52), where h_z is the gap height in the z-direction, μ is the dynamic viscosity, l is the length of the plate in the y-direction, and the infinite plate depth is in the x-direction. If each differential section of gear tooth can be treated as a differential section of parallel plates, the total leakage over the gear tooth could be found in eq. (4.53). This flow could then be normalized to the height of the gap, fluid properties, and operating conditions in eq. (4.54). Then OF6 is to minimize the normalized lateral gap flow $\overline{Q_L}$ over both gear teeth in eq. (4.55). In eq. (4.55), the inner gear tooth is integrated from its tip to the midpoint between the next tooth, and the outer gear tooth is integrated to the root.

$$\frac{dq}{dx} = \frac{2h_z^3 \Delta p}{3\mu l} \tag{4.52}$$

$$Q_L = \frac{2h_z^3 \Delta p}{3\mu} \int_{x_0}^{x_1} \frac{1}{l}\, dx \tag{4.53}$$

$$\overline{Q_L} = \frac{3Q_L \mu}{2h_z^3 \Delta p} \int_{x_0}^{x_1} \frac{1}{l}\, dx \tag{4.54}$$

$$\text{OF6: minimize} \left\{ \overline{Q_{L,i}} + \overline{Q_{L,o}} \right\} \tag{4.55}$$

This approach should not be used to quantify the total flow through the lateral gap, but it does capture the correct geometric relationship to minimize leakage through the gap. To test this assertion, six elliptical gerotors were selected that had different values of OF6 and are shown in fig. 4.24. The leakage through the gap of each tooth was then simulated in OpenFOAM. Reynolds equation was solved in the gap under steady state conditions with a height of 25 μm with ISO 46 oil at 50° for two pressure cases of 5 bar and 50 bar. The flow across the middle of the tooth was integrated, and the flow for each tooth of a gearset was added to give the total lateral gap leakage for each pump. The pressure field and boundary conditions for a typical simulation are shown in fig. 4.25. The correlation of OF6 with the simulated leakage flows is shown in fig. 4.26. For both pressure cases OF6 correctly predicts the trend in simulated leakage flow, which justifies it for use in a gear geometry optimization.

It should also be noted that OF6 does not account for flow from the displacement chamber

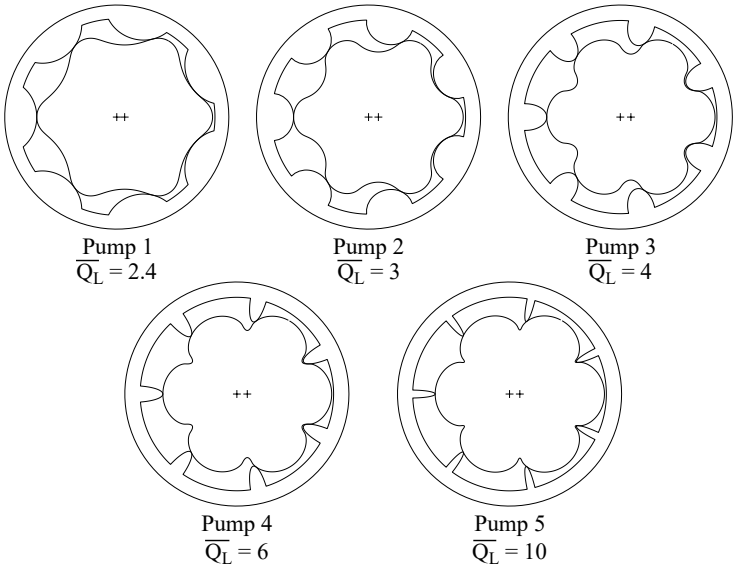

Figure 4.24. Pumps used in lateral gap leakage study [31]

to the bearing drain on the inner gear. This leakage path is not considered, as it is more a function of the shaft diameter than the gear geometry. A larger shaft will have its drain closer to the displacement chamber, so more leakage flow would be expected. This leakage path is important to consider in the pump design, but it should be considered in the design phase that considers fluid dynamic effects after the gearset has been determined.

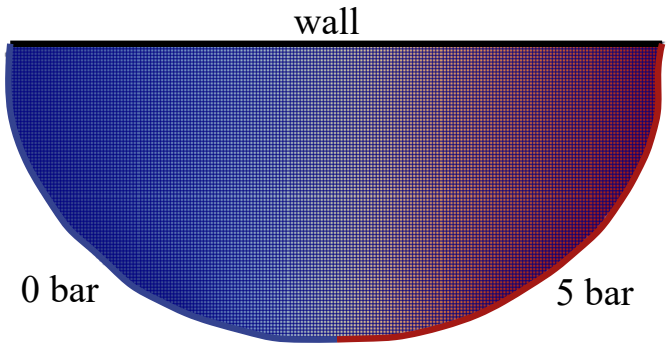

Figure 4.25. Pressure field of lateral gap flow simulation [31]

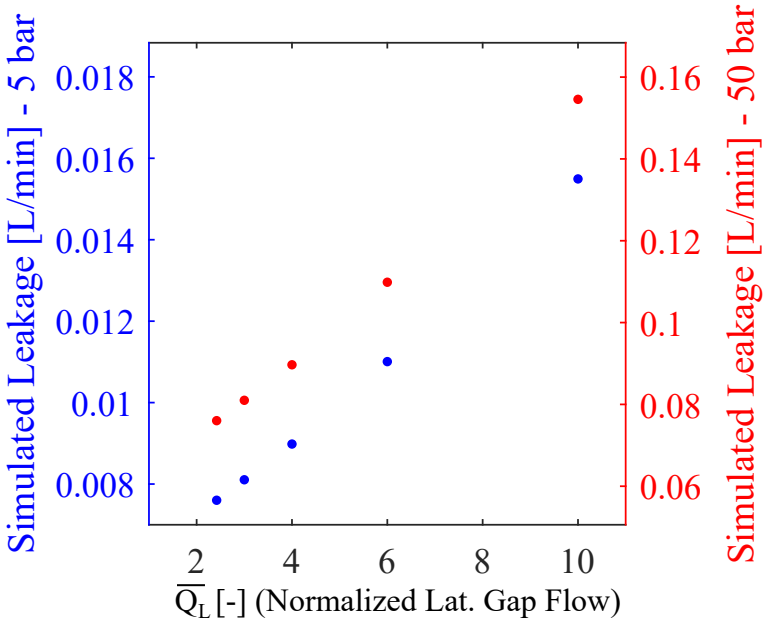

Figure 4.26. Correlation of OF6 with simulated leakage flow [31]

4.7 Objective Function 7: Minimize Inlet Throttling

Because gerotors usually operate in open circuit applications, one of the main factors that limits their maximum speed is incomplete filling. As the pump speed is increased, the pressure drop between the suction chamber and displacement chamber increases. This occurs because the flow into the displacement chamber increases, but the area through which the fluid must pass remains the same. Eventually the displacement chamber pressure will fall to the saturation pressure of the air dissolved in the fluid, and the air will begin to come

out of solution. When this happens, the displacement chamber will not fill completely, and the outlet flow will be less than expected. Exactly when a pump will begin to experience incomplete filling depends on several factors such as the amount of dissolved air, temperature, viscosity, port geometry, and also the gear geometry. The speed at which a pump begins to experience incomplete filling can be predicted by CFD [45], but these models are too slow for extensive optimization.

The gear shape determines both the flow into the displacement chamber and the flow area. When flow passes through an orifice, the pressure drop is a function of the mean flow velocity, so the mean velocity of flow into a displacement chamber can be used to predict a gearset's tendency to experience incomplete filling. The mean velocity of the flow into a displacement chamber is given in eq. (4.56), where V is the mean velocity. The mean velocity can then be normalized to the inner gear speed and face width as $\overline{V}$ in eq. (4.57). The mean inlet velocity is the basis of OF7 in eq. (4.58), which is to minimize the peak normalized mean inlet velocity.

$$V = \frac{\omega_i h}{A} \frac{dA}{d\theta_i} \tag{4.56}$$

$$\overline{V} = \frac{V}{\omega_i h} = \frac{1}{A} \frac{dA}{d\theta_i} \tag{4.57}$$

$$\text{OF7: minimize} \left\{ \max \overline{V}, \ \frac{\pi}{m-1} \leq \theta_i < \frac{\pi(m+1)}{m-1} \right\} \tag{4.58}$$

It is important to note that OF7 cannot predict the exact speed at which a pump will experience incomplete filling, but it can rank the designs in the correct order for an optimization. The normalized mean inlet velocity for a reference is shown in fig. 4.27 as an example, where the displacement chamber at with the maximum inlet velocity is highlighted. The shape of the ports affects the timing of when a displacement chamber connects to the ports, which can also affect leakage and cavitation (see appendix A, see also [45]). However fig. 4.27 shows that OF7 has a peak value after the displacement chamber is in full connection to the ports. This means that OF7 can be used to design gearsets apart from the shape of the ports.

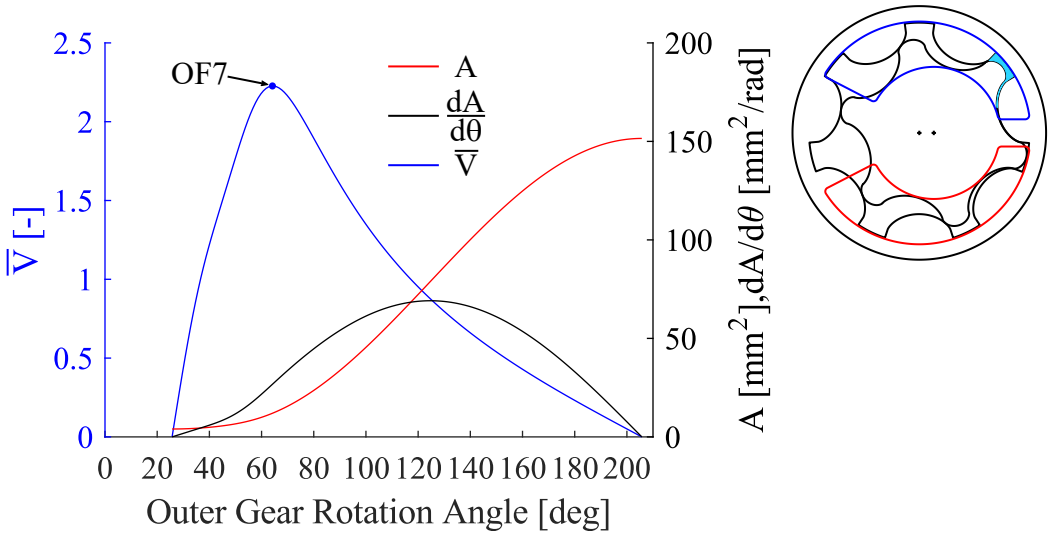

Figure 4.27. Mean inlet velocity for a cycloidal profile with $m = 7$, $\lambda_d = 0.7$ with open roots

As mentioned in section 4.1, the outer gear dead area does not affect the displacement and kinematic flow of the pump, however it does influence the mean inlet velocity. When gearsets have conjugate roots, the flow area can be very small while the area derivative is great. This can lead to larger values of OF7 and is illustrated in fig. 4.28. In fig. 4.28, the mean inlet velocity of the same cycloidal gearset as that in fig. 4.27 is plotted. The only difference is that the gearset in fig. 4.28 has conjugate roots, so the flow area can be very small. For the same gearset with conjugate roots, the peak mean inlet velocity was increased by a factor of 7.8. Based on this observation, adding some dead area to the root of the outer gear is suggested, and this can usually be accomplished without increasing the size of the pump.

4.8 Considerations on Hydro-mechanical Efficiency

A positive displacement pump's overall efficiency can be defined as the product of its volumetric and hydro-mechanical efficiencies. Two OF are designed to improve a gerotors volumetric efficiency by minimizing internal leakage between the tooth tips. However, the pump's hydro-mechanical efficiency should also be considered. The hydro-mechanical efficiency of a pump is the ratio of the ideal torque (eq. (4.26)) to the actual required input

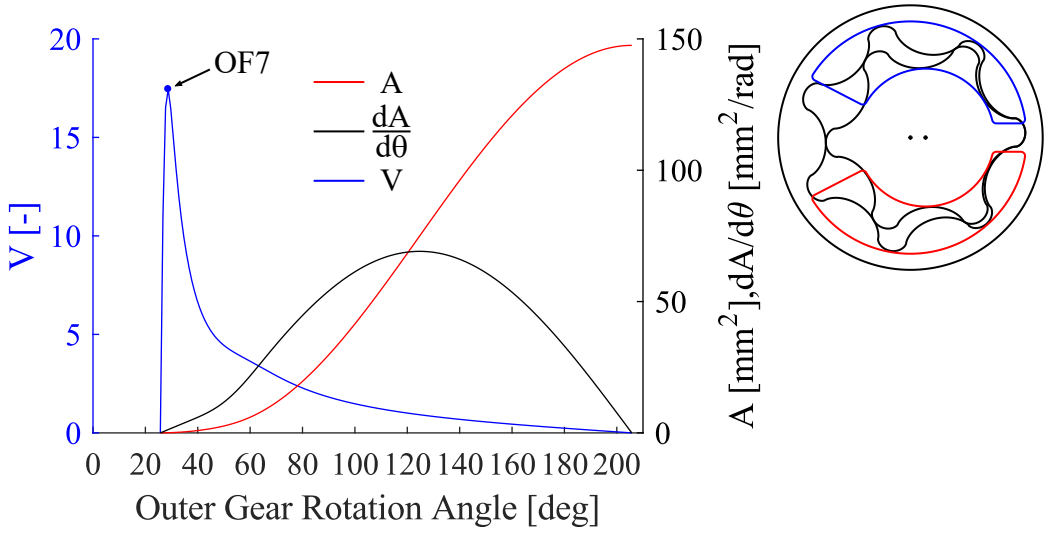

Figure 4.28. Mean inlet velocity for a cycloidal profile with $m = 7$, $\lambda_d = 0.7$ with conjugate roots

torque. The actual input torque to a gerotor must be increased relative to the ideal torque due to fluid shear in the lubricating interfaces and friction at the driving contact point(s). Accurately calculating the torque losses in a gerotor involves detailed CFD simulations of the journal bearing, lateral gap, tooth tip gap, and driving contact; all of which require significant computation time [46]. A faster method is necessary to capture the correct geometric relationships to minimize the torque losses in a pump. Simplified models of the torque losses in each of the interfaces are given here to determine the correct geometric factors to optimize to reduce torque loss. The analysis shows that no additional OF for hydro-mechanical efficiency must be considered in a gear optimization as the torque losses are strongly correlated with OF1 and OF3.

The first torque loss to consider is in the outer gear journal bearing. Petrov's equation for simplified journal bearings with no eccentricity can be solved to give the friction torque of a journal bearing in eq. (4.59) [47, p. 157], where $T_{f,j}$ is the torque loss in the journal bearing, μ is the dynamic viscosity, h is the bearing length (face width), R_b is the outer gear bearing radius, and c is the clearance between the outer gear and the housing. Although Petrov's equation does not consider bearing eccentricity, it is still accurate enough for a first order approximation for a geometric analysis. Then eq. (4.59) shows that the main geometric

effect to change in gerotor design to reduce the torque loss in the journal bearing is to reduce R_b. Although, the outer gear root radius is not the same as the outer gear bearing radius, they are closely correlated enough that minimizing OF1 will also minimize torque loss in the journal bearing.

$$T_{f,j} = \frac{2\pi\mu\omega_o h R_b^3}{c} \tag{4.59}$$

The next gap to consider for torque loss is the tooth tip gap. If the tooth tip gap can be approximated as two parallel plates moving relative to one another, the friction force in one gap would be given by F_f in eq. (4.60), where l is the gap length, c is the gap height, h is the face width, and $\frac{ds}{dt}$ is the relative sliding speed. Since the relative sliding speed is low on the minimum volume side of the pump (see fig. 4.14), the friction torque in the tooth tip gap is dominated by its behavior on the maximum volume side of the pump. If the contact can be modeled as two circles with radii r_o and r_i centered on the outer and inner gear centers respectively and having a point of tangency on the -x-axis that are moving relative to each other, the relative sliding speed would be $\frac{ds}{dt}$ given in eq. (4.61). Given that $r_i = r_o + e$ in that position and $\omega_o = \frac{m-1}{m}\omega_i$, eq. (4.61) can be substituted in eq. (4.60) and rearranged to give the friction torque due to the tooth tip gap $T_{f,t}$ in eq. (4.62). In eq. (4.62), the first term is the factors that are independent of geometry, and the second would be the geometric factors that contribute to the friction torque. In this second term, r_i is the dominant variable that would determine the friction torque. The relationship between the minimum allowable root radius r_r and r_i is given in eq. (4.63). Because $r_i > e$ usually by nearly an order of magnitude, r_i will correlate very strongly with r_r. Therefore, the torque loss due to friction in the tooth tip gaps will be also be minimized by minimizing OF1, so an additional OF is not warranted.

$$F_f = \frac{\mu h l \frac{ds}{dt}}{c} \tag{4.60}$$

$$\frac{ds}{dt} = r_i\omega_i - r_o\omega_o \tag{4.61}$$

$$T_{f,t} = \frac{\mu h l \omega_i}{c}\frac{1}{m}\left[r_i^2 + (m-1)e r_i\right] \tag{4.62}$$

$$r_r = r_i + e; \tag{4.63}$$

Next the torque loss in the lateral gap is considered. If the gearset can be modeled as a cylinder with outer gear bearing radius R_b and face width h rotating at a speed ω_o that is separated by a film height c on both sides, the torque loss due to fluid shear in both gaps would be given by $T_{f,l}$ in eq. (4.64). Here again, the torque loss would be strongly correlated with the size of the outer gear as far as the geometry is concerned. Therefore, the torque loss in the lateral gap can also be minimized by minimizing OF1.

$$T_{f,l} = \frac{\pi \mu \omega_o R_b^4}{c} \tag{4.64}$$

Lastly the torque loss due to friction at the driving contact is considered. The work done by friction while one contact point drives the gearset would be determined in eq. (4.65), where $W_{f,d}$ is the work done by friction due to driving. This can be equated to the integral in eq. (4.66) by conservation of work, where f is the coefficient of friction, F is the contact force, and s is the relative sliding distance at the contact point. The mean torque loss is then defined by eq. (4.67). If f can be considered to be constant or at least not to vary significantly with rotation, the term $F\frac{ds}{s\theta}$ would be the term to minimize. OF3 minimizes the peak value of $F\frac{ds}{s\theta}$ with F normalized to the operating pressure. Because OF3 is almost always monotonically increasing, as the relative sliding increases with rotation, and the contact force does not change as much, minimizing the peak value of $F\frac{ds}{s\theta}$ would also minimize the mean torque loss due to friction at the driving contact point. For this reason, the driving torque loss would be correlated strongly with OF3, so another OF is not necessary.

$$W_{f,d} = \int_{\theta_1}^{\theta_2} T_f \; d\theta \tag{4.65}$$

$$W_{f,d} = \int_{\theta_1}^{\theta_2} f F \frac{ds}{d\theta} \; d\theta \tag{4.66}$$

$$T_{f,d,avg} = \frac{f}{\theta_2 - \theta_1} \int_{\theta_1}^{\theta_2} F \frac{ds}{d\theta} \, d\theta \tag{4.67}$$

4.9 Objective Function Scaling

The gear design optimization would be most helpful if it must only be performed once in a way that the results can be scaled to give a pump of any displacement. If the facial displacement of a pump (displacement per unit face width) is given by $\dot{v}$, a pump can be scaled by a factor λ in eq. (4.68), where the subscript 1 indicates the value before scaling, and the subscript 2 indicates the value after scaling. The seven OFs can then be scaled according to eqs. (4.69)–(4.75), which are according to the dimensions of each OF.

$$\dot{v}_2 = \lambda \dot{v}_1 \tag{4.68}$$

$$\text{OF1: } r_{r,2} = \sqrt{\lambda} r_{r,1} \tag{4.69}$$

$$\text{OF2: } \overline{E}_2 = \lambda^2 \overline{E}_1 \tag{4.70}$$

$$\text{OF3: } \overline{W}_2 = \lambda \overline{W}_1 \tag{4.71}$$

$$\text{OF4: } \overline{p}_{0,2} = \overline{p}_{0,1} \tag{4.72}$$

$$\text{OF5: } \overline{\kappa}_2 = \frac{\overline{\kappa}_1}{\sqrt{\lambda}} \tag{4.73}$$

$$\text{OF6: } \overline{Q}_{L,2} = \overline{Q}_{L,1} \tag{4.74}$$

$$\text{OF6: } \overline{V}_2 = \overline{V}_1 \tag{4.75}$$

Note that for each OF, the OF values of the scaled pumps are that of the original multiplied by a constant factor. This means that the performance order of the designs of each OF will not change with scaling, so the Pareto front will remain the same regardless of the scaling applied. The scaled OFs are still helpful for comparing pumps of different facial displacements however.

5. CONSTRAINTS

Three types of constraints are used in the optimization. First is that the gear profiles would be machinable with no self-intersections in either the inner or outer gear curves. Second is that the profiles would have a self-driving relation. Third, the values of each of the objective functions for a design must be below a threshold value.

5.1 Geometric Constraints

Geometric constraints are imposed in the optimization to ensure the profile geometry is machinable (e.g. closed profile and free of self-intersections) and that continuous contact exists. For example, designs violating these constraints can have cusps (undercutting) in the inner gear profile, overlapping outer gear teeth, or a center distance too great for continuous contact. If one of these constraints are violated in an optimization, the design is discarded in an early exit, as the objective functions cannot be evaluated. This strategy reduces the number of function calls, so the speed of the optimization is increased.

A part of the definition of a gerotor is that continuous contact exists between the gear teeth throughout rotation. For this to occur, every point on the outer gear pitch circle must be intersected by a line normal to the outer gear tooth profile exactly once, including the points of tangency. As the radius of the size of the pitch circle increases due to an increasing center distance, eventually no line normal to the outer gear tooth curve will be tangent to the pitch circle. This effectively places an upper bound on the center distance for continuous contact to exist. The bounds of the input variables can be used to ensure the center distance is not too great for epitrochoidal, hypotrochoidal, standard cycloidal, and elliptical gerotors, but the maximum allowable center distance is imposed as a constraint for the generalized cycloidal, cosine, and asymmetric elliptical profiles in eqs. (2.37), (2.42) and (2.47) respectively.

In epitrochoidal and hypotrochoidal gerotor gear profiles, cusps can form in the inner or outer gear because parallel curves have cusps when the parallel offset distance is equivalent to the radius of curvature of the base curve. This is illustrated in fig. 5.1. The maximum outer gear tooth radius for epitrochoidal profiles to avoid cusps in the inner gear is given in eq. (5.1),

and it is the same relation given by Hall [12] and Colbourne [13]. For hypotrochoidal profiles, the gear parameter at which the base hypotrochoid of the outer gear has its minimum radius of curvature is given in eq. (5.2). This can be substituted into eq. (5.3) to give a maximum value of the inner gear tooth radius for hypotrochoidal profiles, which is a much simpler expression than the procedure recommended by Hwang and Hsieh [48]. The equations for the base hypotrochoid are given in eq. (2.18)

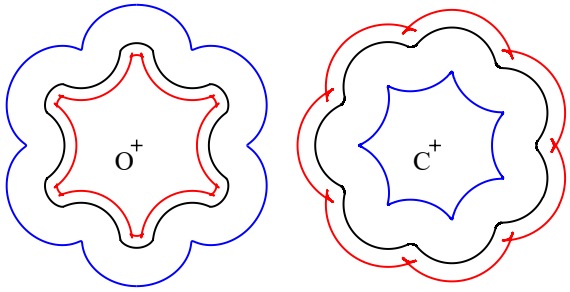

Figure 5.1. Epitrochoid (left) and hypotrochoid (right) with $m = 7$, $e = 3$ mm, $\rho = 25$ mm with maximum allowable offset distance (black) and an excessive offset distance leading to cusps (red) [27]

$$d_{epi} < \frac{3}{m+1}\sqrt{\frac{3(\rho^2 - m^2e^2)(m-1)}{m+1}} \tag{5.1}$$

$$\phi_c = \frac{1}{m}\text{acos}\left(\frac{\rho^2(m+1) - m^2e^2(2m-1)}{me\rho(m-2)}\right) \tag{5.2}$$

$$d_{hypo} < \left.\frac{(x_t'^{\,2} + y_t'^{\,2})^{\frac{3}{2}}}{|x_t'y_t'' - y_t'x_t''|}\right|_{\phi=\phi_c} \tag{5.3}$$

Cusps can appear in the other profile types as shown in fig. 5.2. However, for the other profile types a closed form expression to determine if a cusp is present was not found, so the cusps are detected numerically. When the inner gear profile has a cusp, the direction of the curve reverses at the cusp point. For this reason, the derivative of the polar angle with respect to the gear parameter of the secondary contact portion of inner gear (tooth tips) can be used to determine if a cusp is present in the inner gear. The polar angle of the inner gear is given by the standard equation in eq. (5.4), where Θ_2 is the polar angle

of the inner gear in secondary contact. The derivative of the polar angle is then given by eq. (5.5), where the derivatives of the inner gear profile are taken with respect to ϕ. The inner gear derivatives in eq. (5.5) are a little cumbersome due to several applications of the product rule, but they only need to be found once to be applied to any outer gear tooth curve described by $x(\phi)$ and $y(\phi)$. In the gear generation algorithm the minimum value of $|\ \frac{d\Theta_2}{d\phi}\ |$ is calculated numerically on the interval $0 \leq \phi \leq \phi_m$. If it is below an epsilon value, the algorithm checks for a sign change in the derivative at that point. If a sign change is present, the inner gear contains cusps, and the design is rejected. A multi-start method is suggested for finding the minimum of $|\ \frac{d\Theta_2}{d\phi}\ |$ with at least three intervals to avoid getting trapped in local minima.

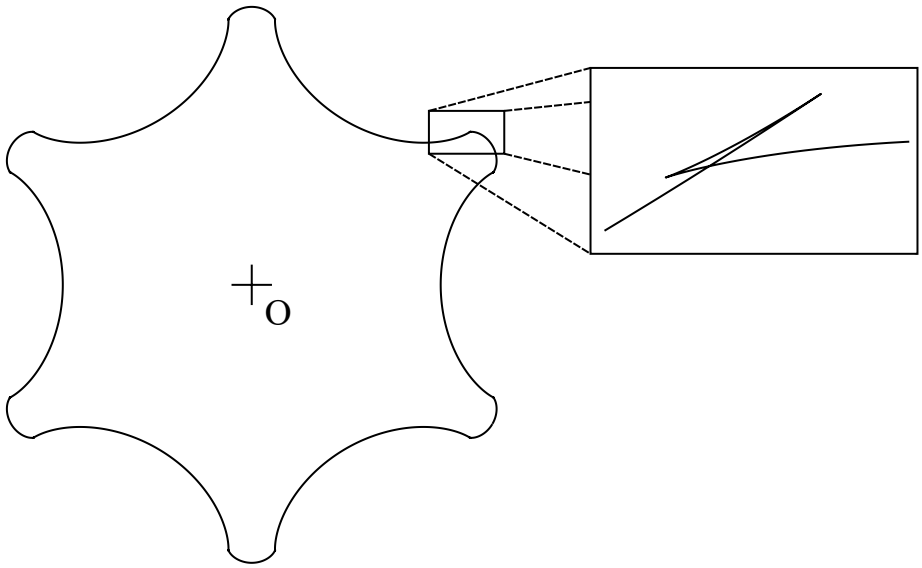

Figure 5.2. Inner gear with cusps

$$\Theta_2 = \arctan\left(\frac{\eta_2}{\xi_2}\right) \tag{5.4}$$

$$\frac{d\Theta_2}{d\phi} = \frac{\xi_2\eta_2' - \eta_2\xi'_2}{\xi_2^2 + \eta_2^2} \tag{5.5}$$

Geometric constraint violations in the outer gear occur when either outer gear teeth overlap either in the portion containing the tooth curve or the linear extensions as shown

in fig. 5.3. The mathematical relations for each profile type to determine when the teeth overlap are omitted here for brevity.

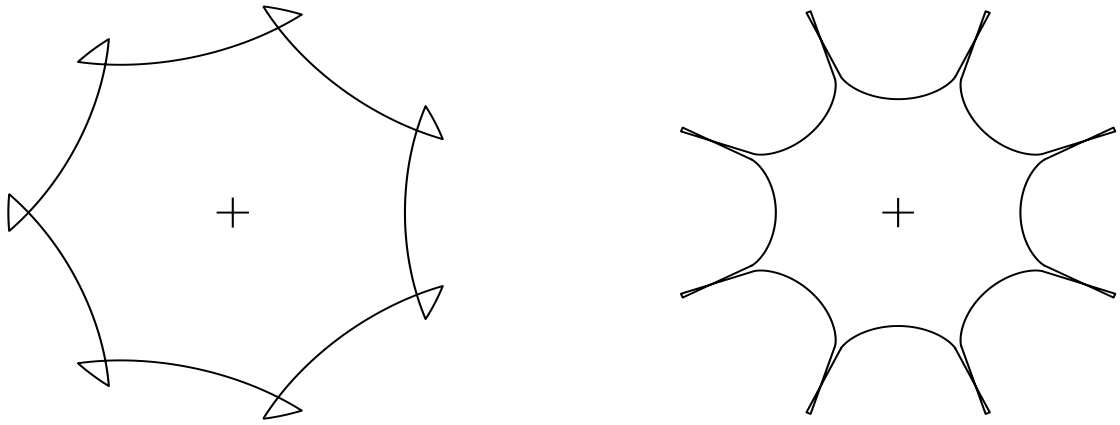

Figure 5.3. Outer gear tooth intersection in tooth form (left) and extension (right) for a generalized cycloidal outer gear [31]

Some additional geometric constraints are required that are unique to each profile type. For the generalized cycloidal profile, an additional constraint on the rolling disk radius in eq. (5.6) is required to ensure the hypocycloid is curved, as when $d = r/2$, a hypocycloid becomes a line as shown in fig. 5.4 (also known as a Tusi couple). For cosine profiles, an additional constraint is added in eq. (5.7) to ensure that the minimum allowable root radius intersects the cosine wave. An example of this type of constraint violation is shown in fig. 5.5. Lastly an additional constraint is required to ensure that the tip of the outer gear tooth of asymmetric elliptical profiles cannot extend past the center of the gear as shown in fig. 5.6. The gear parameters corresponding to the two points on the asymmetric ellipse with vertical tangent lines are given as $\phi_{v1,2}$ in eqs. (5.8) and (5.9), and the x coordinates of both points must be greater than zero as given in eqs. (5.10) and (5.11).

$$d_{gen\_cyc} < \frac{r}{2} \tag{5.6}$$

$$r_r < \sqrt{\rho^2 + 2d\rho + d^2 + 4k^2} \tag{5.7}$$

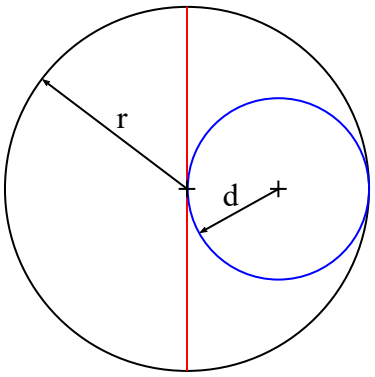

Figure 5.4. Hypocycloid (red) when d=r/2

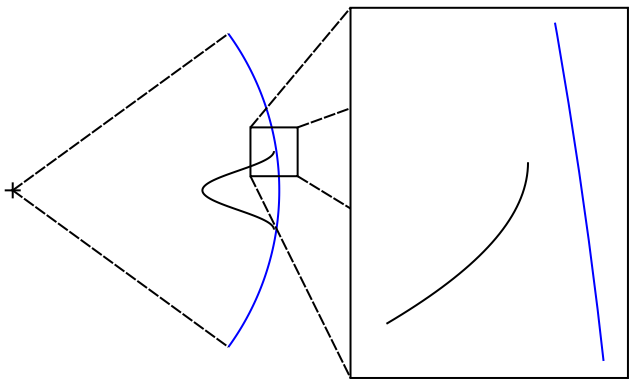

Figure 5.5. Cosine outer gear tooth with $m = 5$, $\lambda_p = 0.852$, $\lambda_d = 0.159$, and $\lambda_t = 0.548$ whose minimum allowable root radius does not intersect the cosine wave

$$\phi_{v1} = \arctan\left(-\frac{k}{d}\tan\alpha\right) \tag{5.8}$$

$$\phi_{v2} = \arctan\left(-\frac{k}{d}\tan\alpha\right) + \pi \tag{5.9}$$

$$x\left(\phi_{v,1}\right) > 0 \tag{5.10}$$

$$x\left(\phi_{v,2}\right) > 0 \tag{5.11}$$

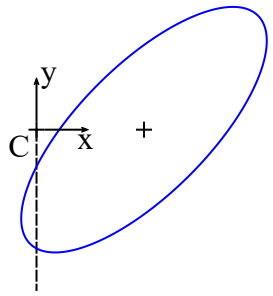

Figure 5.6. Asymmetric elliptical outer gear tooth that extends past the gear center

5.2 Drive Angle

In addition to performing a sealing function between variable volumes, a gerotor gearset must have a suitable driving relation so that one gear can drive the other without seizing. This would not be difficult for an ideal gerotor with no clearance between the gear teeth, as one of the tooth pairs would likely have an angle of the contact force that could drive the other gear. However, because of the clearance, only one or possibly two inner gear teeth will contact the outer gear. This can create a problem when the contact force at that point is at an angle that cannot rotate the opposite gear, and gearsets that are not self-driving should be considered infeasible in an optimization.

A good pump designer could likely determine if a gearset will have a suitable drive relation by inspection, but an optimization requires a more objective system of classification. The drive angle at the contact point can be used as a constraint, and it is shown in fig. 5.7. The drive angle is represented by Θ and is defined as the angle between the contact force and the velocity vector of the contact point with respect to the outer gear center. A drive angle of zero therefore means that all of the contact force contributes to rotating the outer gear, while a drive angle of 90° means the contact force does not rotate the outer gear directly (the friction force could still contribute to rotation). The pressure angle in fig. 5.7 is given by Φ and is defined as the angle between the common normal line at the contact point and the line tangent to the pitch circles. Using the drive angle was introduced in other work [17], [21], but it was called the "pressure angle". The more classical definition of the term "pressure angle" is used in this work to avoid confusion in nomenclature, since the term can

have varied meanings depending on the context [43, p. 3]. The angle of the force vector is known at each point in rotation, as it must extend to the pitch point to satisfy the Law of Gearing (the pitch circles are plotted in dashed blue in fig. 5.7 for reference).

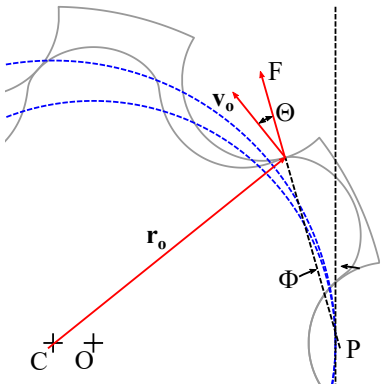

Figure 5.7. Illustration of the drive angle at a given contact point [27]

Pumps used in industry typically have maximum drive angles less than 45°, although the maximum drive angle that would still allow the gears to be self-driving would likely be higher. Determining the maximum allowable drive angle is not simple, and it depends greatly on the clearance between the gears, the type of bearings (journal vs rolling element), operating pressure, lubricity, manufacturing tolerances, surface finish, etc. Since the purpose of this work is to be a geometric optimization, the maximum drive angle of a gearset is constrained to be less than 60°. The goal is to pick a value large enough so good designs are not eliminated, but small enough that feasible gearsets could be expected to have a self-driving relation. Since pumps used in industry can have maximum drive angles of 45°, 60° is a logical choice. Designs can also be further filtered in post-processing to select a final design with a lower drive angle.

5.3 Objective Function Limit Constraints

The optimization algorithm will seek to find designs on the Pareto front regardless of their location on the front. Some designs can have a very good value in one OF, but very poor values in one or more other OF so that the design would not be selected in practice. This effect can be mitigated by imposing seven constraints to limit the maximum allowable

value on each OF. These values were selected to be significantly greater than pumps used in industry but also low enough to give a useful Pareto front. The maximum allowable values of each OF are shown in table 5.1.

Table 5.1. Maximum allowable values of each objective function

Objective Function	Maximum Allowable Value
OF1: Radius, r_r [mm]	45
OF2: Flow Ripple, $\bar{E}$ [mm^4]	20
OF3: Adhesive Wear, $\bar{W}$ [mm^2]	20
OF4: Contact Stress, $\overline{p_0}$ [-]	3
OF5: Tooth Tip Leakage, $\bar{\kappa}$ [1/mm]	2
OF6: Lateral Gap Leakage, $\overline{Q_L}$ [-]	7
OF7: Mean Inlet Velocity, $\bar{V}$ [-]	6

Now that the objective functions and constraints for the multi-objective optimization process have been defined, the results of the optimizations are given in the following chapter.

6. OPTIMIZATION RESULTS

In this chapter the results of the optimizations are presented. First the results for each individual profile type are shown. This is followed by a comparison of the conventional gerotor profile types (epitrochoidal, hypotrochoidal, and cycloidal), and then a comparison between all the profile types are made. Lastly two methods to select an optimal design are presented and a few example optimized gearsets are presented.

6.1 Epitrochoidal Gerotors

A total of 485,314 designs were evaluated in 55 hours on a desktop PC (Intel i7-7700, 16 GB RAM) in the optimization of epitrochoidal gerotor profile. Of the evaluated designs, 35% were feasible. Then of the feasible designs 78% were on the Pareto front. Because of the relatively high number of objective functions, the high proportion of designs on the Pareto front is expected. With an increasing number of OF, the likelihood of a design performing better than another in every OF decreases. The effect of varying each of the input variables on the appearance of epitrochoidal gerotor is shown in figs. 6.1–6.3 to better understand the relationships between the input variables and the results. Each of the gearsets plotted in figs. 6.1–6.3 are scaled to have the same displacement per unit face width of 10 cm^2/rev.

A plot of the design space is shown in fig. 6.4, where each evaluated design is shown as a point. The subplots are split by the number of outer gear teeth m, λ_p (pitch radius to tooth position ratio) is plotted on the x-axis, and λ_d (tooth size ratio) is plotted on the y-axis. The type of each design is represented by the color. Designs with cusps are plotted in red as impossible designs, as their OF cannot be evaluated. Designs that are infeasible due to high values of one or more OF or have a high drive angle are plotted in gold. Feasible designs are plotted in green, and Pareto designs are plotted in blue. The range of λ_p and λ_d for feasible designs decreases with the number of outer gear teeth, and designs with an odd value of m are preferred (although plenty of Pareto designs have an even value of m). Because such a large portion of the design space makes up the Pareto front especially for the most common number of outer gear teeth used in industry (7-13), it is quite likely that many pumps used in industry are on the Pareto front, so no absolute improvement for a given design is likely.

The value of the optimization in this case then is to answer which part of the design space contains the Pareto front and also to help a designer navigate the performance trade-offs among the optimal designs.

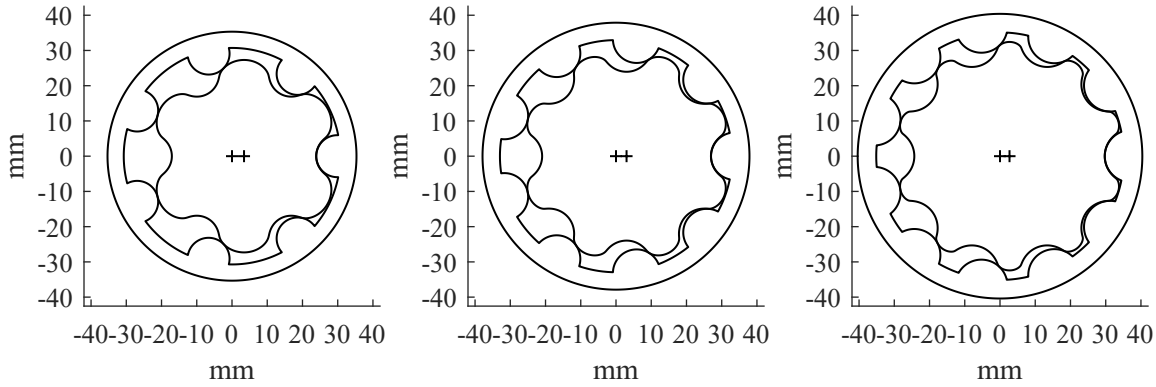

Figure 6.1. Epitrochoidal gerotors with $\lambda_p = 0.8$ and $\lambda_d = 0.2$. Left: $m = 7$ Center: $m = 9$ Right: $m = 11$

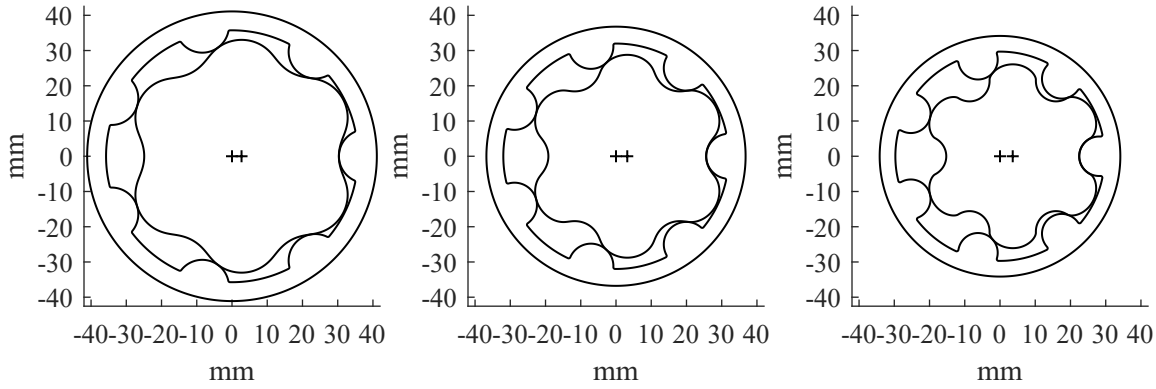

Figure 6.2. Epitrochoidal gerotors with $m = 7$ and $\lambda_d = 0.2$. Left: $\lambda_p = 0.5$ Center: $\lambda_p = 0.7$ Right: $\lambda_p = 0.9$

Showing the effect of varying each of the input variables on each OF would be prohibitively long, however some of the most important correlations can still be shown. The first is the effect of the input variables on size of the pumps displayed in fig. 6.5. In fig. 6.5 the value of λ_p for each design is plotted on the x-axis, the value of λ_d on the y-axis, and the value of the minimum allowable root radius to give a displacement of 10 cc/rev assuming a 1 cm face width is plotted on the color axis. Designs with $m = 7$ are plotted on the left and designs with $m = 17$ are plotted on the right. As the center distance is increased for a given

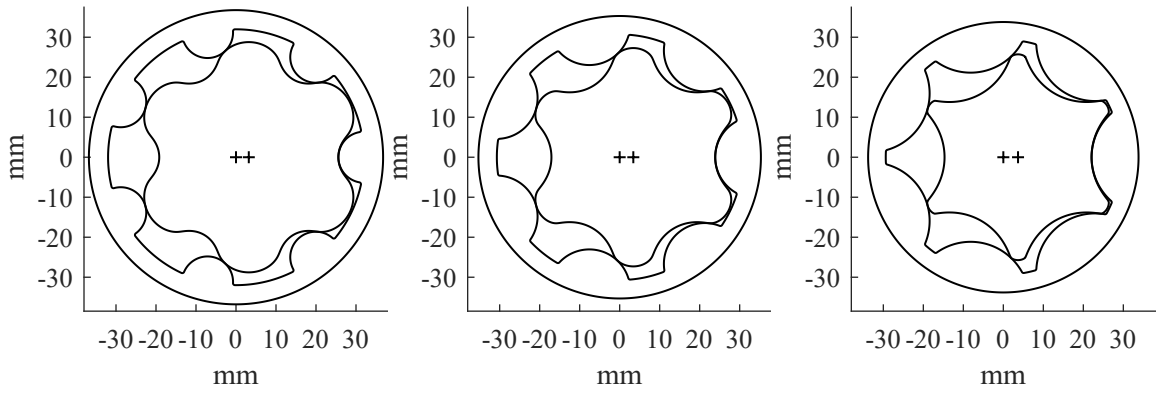

Figure 6.3. Epitrochoidal gerotors with $m = 7$ and $\lambda_p = 0.8$. Left: $\lambda_d = 0.2$ Center: $\lambda_d = 0.3$ Right: $\lambda_d = 0.4$

outer gear tooth position and size, the pump radius is reduced. Additionally, increasing the number of teeth also increases the pump size.

The flow ripple generally decreases with an increasing number of teeth, but the flow ripple also depends on whether m is even or odd as shown in fig. 6.6. Pumps with an odd value of m tend to have a lower flow ripple than their $m + 1$ even counterparts. Further, for pumps with an odd value of m, the flow ripple tends do decrease as λ_p and λ_d are increased together, but the opposite is true for pumps with even values of m.

Many of the pumps have a region with the highest adhesive wear as shown in fig. 6.7 for pumps with $m = 7$. The contact stress tends to increase with an increased value of λ_p and λ_d and is the constraint boundary that is reached immediately before cusps form in the profiles.

The tooth tip leakage tends to increase sharply with either low or high values of λ_d as shown in fig. 6.8, as pumps with low values of λ_d have sharp outer gear teeth, and pumps with high values of λ_d tend to have sharp outer gear teeth. A similar trend is observed for the lateral gap leakage as shown in fig. 6.8 for pumps with $m = 7$. For small values of λ_d, the outer gear teeth have a small width and usually require extensions to meet the root. Pumps with higher values of λ_d tend to have inner gear teeth with low widths that have higher lateral gap leakage as well.

The mean inlet velocity tends to have low values except where both λ_p and λ_d are large as shown in fig. 6.9. In that region the displacement chamber area at the minimum volume

is quite small, which leads to the increased maximum mean inlet velocity. The maximum drive angle of a pump is very strongly correlated to λ_p as also shown in fig. 6.9. The drive angle constraint effectively sets a lower bound on acceptable values of λ_p.

Some of the interesting trade-offs between the OF are shown in figs. 6.10 and 6.11. In each of the plots each design on the Pareto front is represented as a point. In fig. 6.10 (left) a clear relationship between boundary for what is possible between size and flow ripple is evident. Additionally, some of the best designs in terms of size and flow ripple have high lateral gap leakage. These designs tend to have very narrow gear teeth that lead to the compactness and low flow ripple but also explain the higher lateral gap leakage. The same is true for contact stress as shown in fig. 6.10 (right). As the center distance increases for a given outer gear geometry, the pump tends to become more compact, but the profile develops points of high curvature that lead to contact stress in the process.

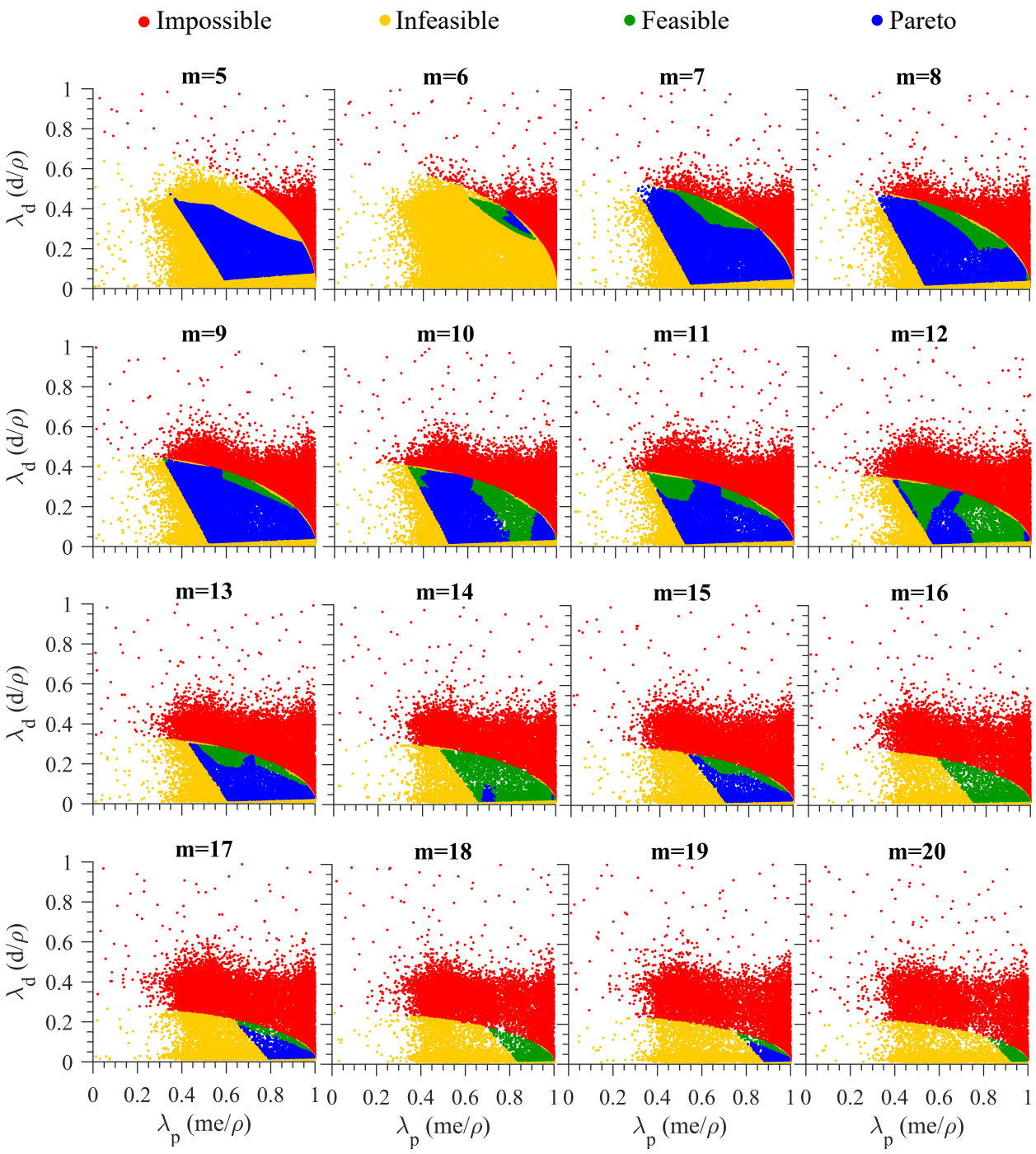

Figure 6.4. Design space of epitrochoidal gerotors

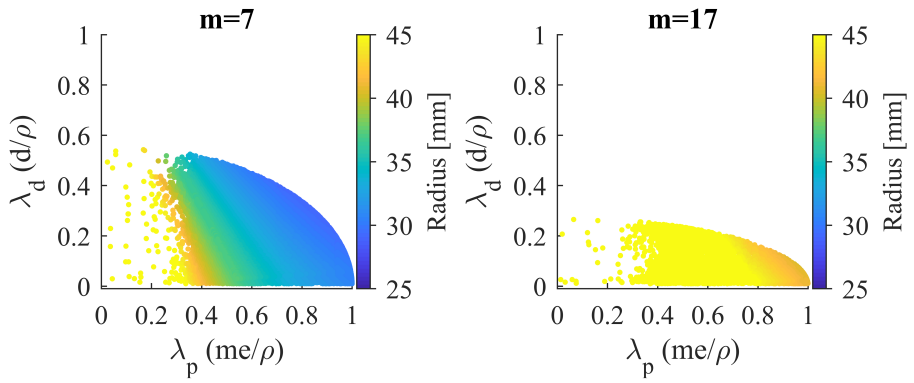

Figure 6.5. Plots of the minimum root radius for epitrochoidal pumps with $m = 7$ (left) and $m = 17$ (right).

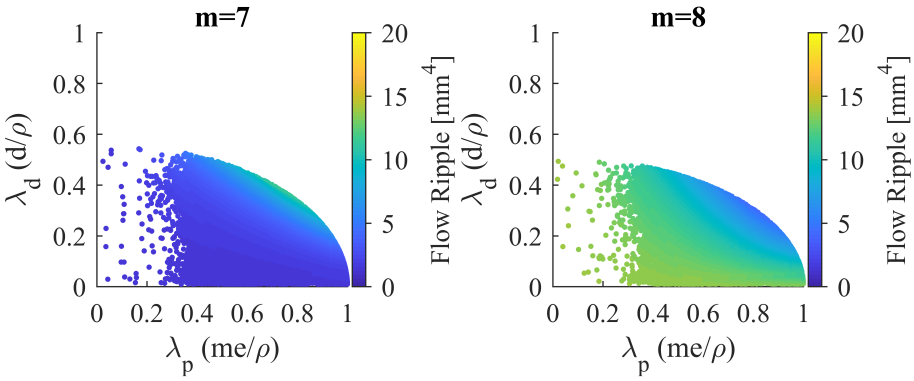

Figure 6.6. Plots of the flow ripple for epitrochoidal pumps with $m = 7$ (left) and $m = 8$ (right).

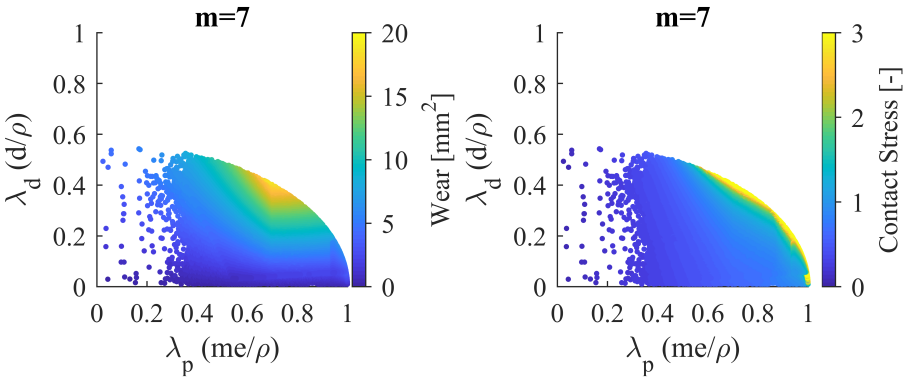

Figure 6.7. Plots of the adhesive wear (left) and contact stress (right) for epitrochoidal pumps with $m = 7$.

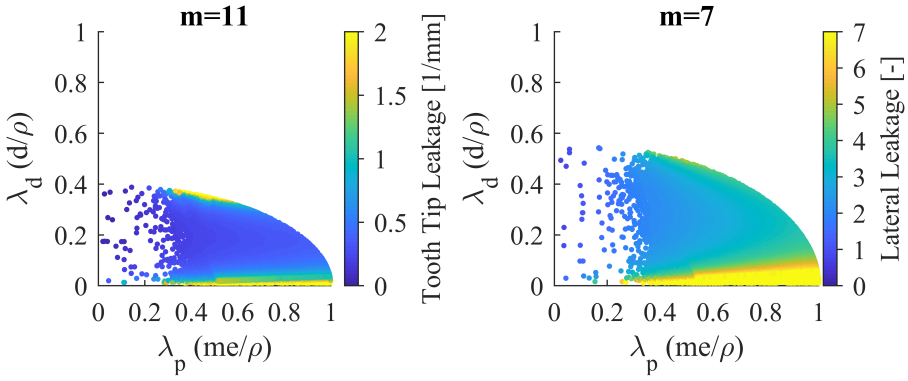

Figure 6.8. Plots of the tooth tip leakage for epitrochoidal pumps with $m = 11$ (left) and lateral gap leakage for epitrochoidal pumps with $m = 7$ (right).

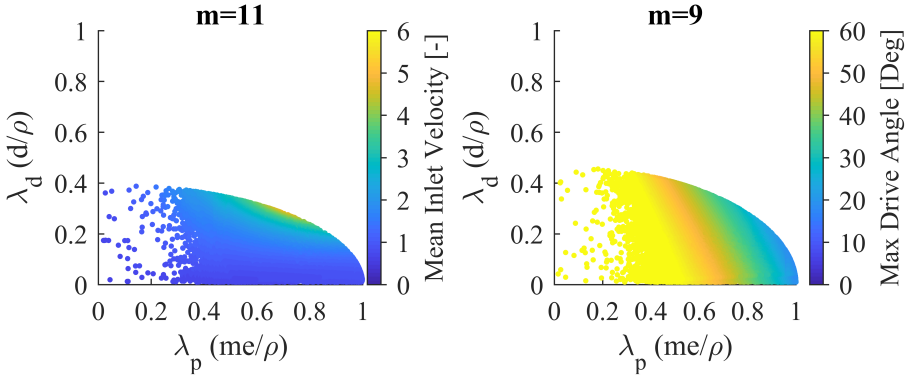

Figure 6.9. Plots of the maximum mean inlet velocity for epitrochoidal pumps with $m = 11$ (left) and maximum drive angle for epitrochoidal pumps with $m = 9$ (right).

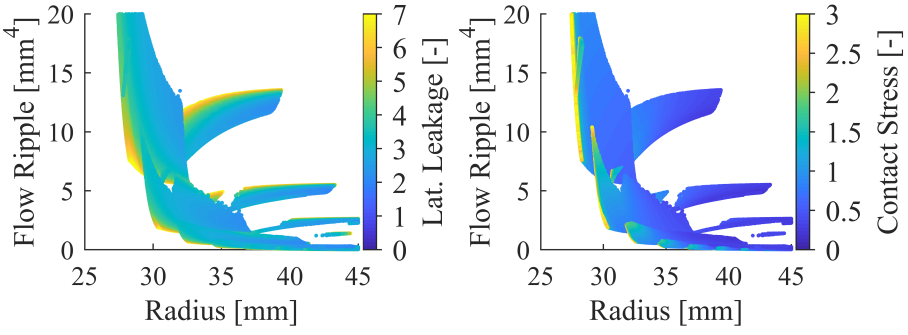

Figure 6.10. Left: Plot of size, flow ripple, and lateral leakage for epitrochoidal designs on the Pareto front. Right: Plot of size, flow ripple, and contact stress for epitrochoidal designs on the Pareto front [27]

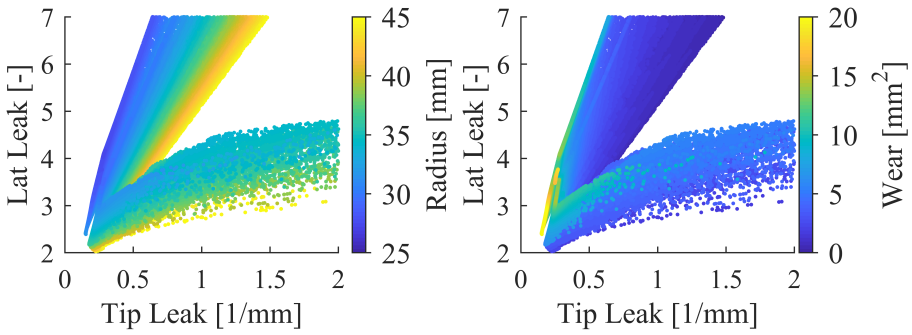

Figure 6.11. Left: Plot of tip leakage, lateral leakage, and radius for epitrochoidal designs on the Pareto front. Right: Plot of tip leakage, lateral leakage, and wear for epitrochoidal designs on the Pareto front. [27]

6.2 Hypotrochoidal Gerotors

In the optimization of hypotrochoidal gerotors a total of 486,474 designs were evaluated in 46 hours. Of the evaluated designs 44% were feasible, but only 30% of the feasible designs were on the Pareto front. The smaller percentage of designs on the Pareto front for the hypotrochoidal profile type show that the optimization procedure is especially useful. Plots showing the effect of each input variable on the geometry of a gearset scaled to a displacement per unit face width of 10 cm^2/rev are shown in figs. 6.12–6.14. Then plots showing the feasibility of the design space are shown in fig. 6.15 just as for the epitrochoidal profile. One of the main reasons for the difference between fig. 6.15 and fig. 6.4 is that λ_d describes the size of the outer gear tooth for epitrochoidal profiles, while it describes the size of the inner gear tooth for hypotrochoidal profiles.

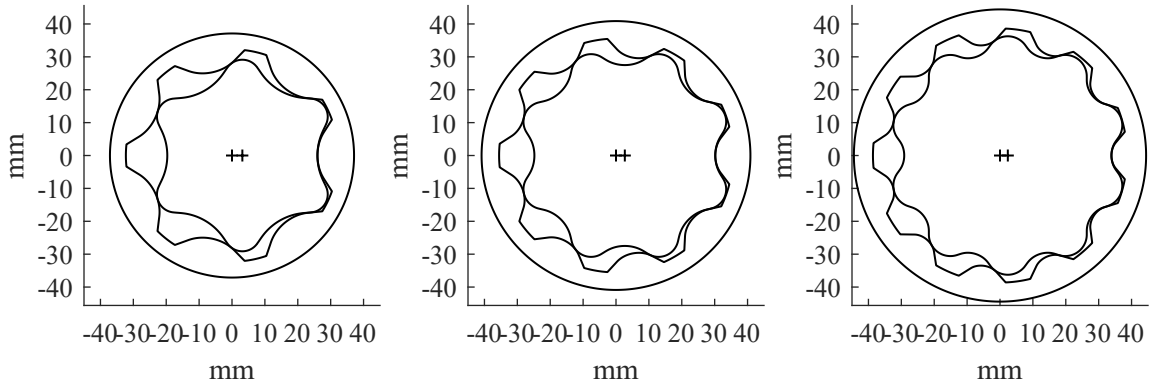

Figure 6.12. Hypotrochoidal gerotors with $\lambda_p = 0.8$ and $\lambda_d = 0.2$. Left: $m = 7$ Center: $m = 9$ Right: $m = 11$

As expected, a greater number of teeth leads to a lower flow ripple, and an increased value of λ_p leads to more compact pumps as shown in fig. 6.16. Pumps with high values of λ_p and low values of λ_d tend to have higher flow ripples for pumps with an odd value of m but lower flow ripples for pumps with an even value of m as shown in fig. 6.17. Because of this effect pumps with an even value of m may be preferred if only considering size and flow for hypotrochoidal profiles. However, designs with low values of λ_d have higher values of each of the remaining OF as shown in figs. 6.18–6.20. Just as for the epitrochoidal profile,

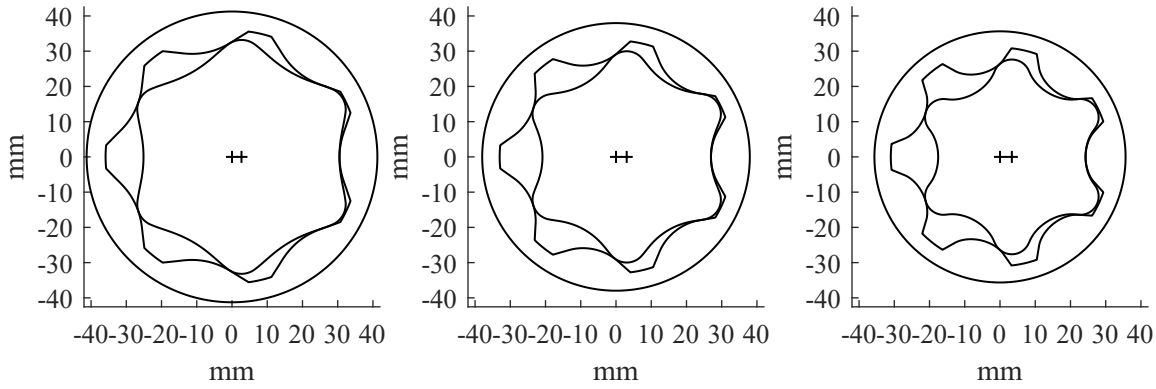

Figure 6.13. Hypotrochoidal gerotors with $m = 7$ and $\lambda_d = 0.2$. Left: $\lambda_p = 0.6$ Center: $\lambda_p = 0.75$ Right: $\lambda_p = 0.9$

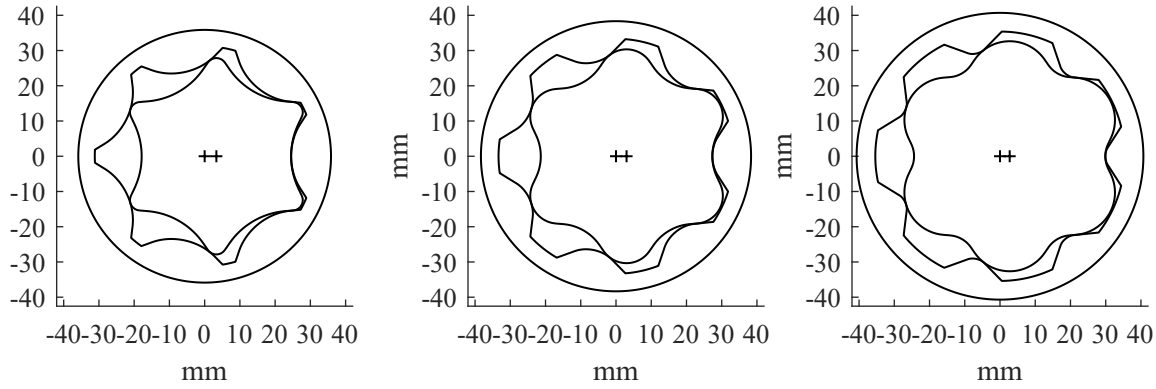

Figure 6.14. Hypotrochoidal gerotors with $m = 7$ and $\lambda_p = 0.8$. Left: $\lambda_d = 0.1$ Center: $\lambda_d = 0.3$ Right: $\lambda_d = 0.5$

the maximum drive angle for the pump is strongly correlated with the value of λ_p, which effectively creates a minimum allowable center distance as shown in fig. 6.20

Some of the most interesting relationships between OF of the Pareto designs are shown in figs. 6.21 and 6.22. In fig. 6.21, for designs on the Pareto front with an even value of m, a single design exists with the best relationship between size and flow ripple. This occurs because the maximum and minimum volumes occur at the same point in rotation rather than out of phase for pumps with an odd value of m. These designs can out-perform odd m designs when only considering size and flow ripple entirely, but it comes at a cost of an increased value of every other OF. The effect of this is shown in fig. 6.22 for lateral gap leakage and contact stress, but it is present for the other OF as well. Epitrochoidal designs

are the same in that designs with an even value of m have a single design with the best combination of size and flow ripple, however they do not have the same improvement in performance when compared to the designs with an odd value of m. The hypotrochoidal profile also has a region of its design space with very low wear and contact stress as shown in fig. 6.22, however this comes at the cost generally of an increased size. Other designs also have very low values of the leakage functions as shown in, but this also generally also comes at the cost of an increased size as shown in fig. 6.22.

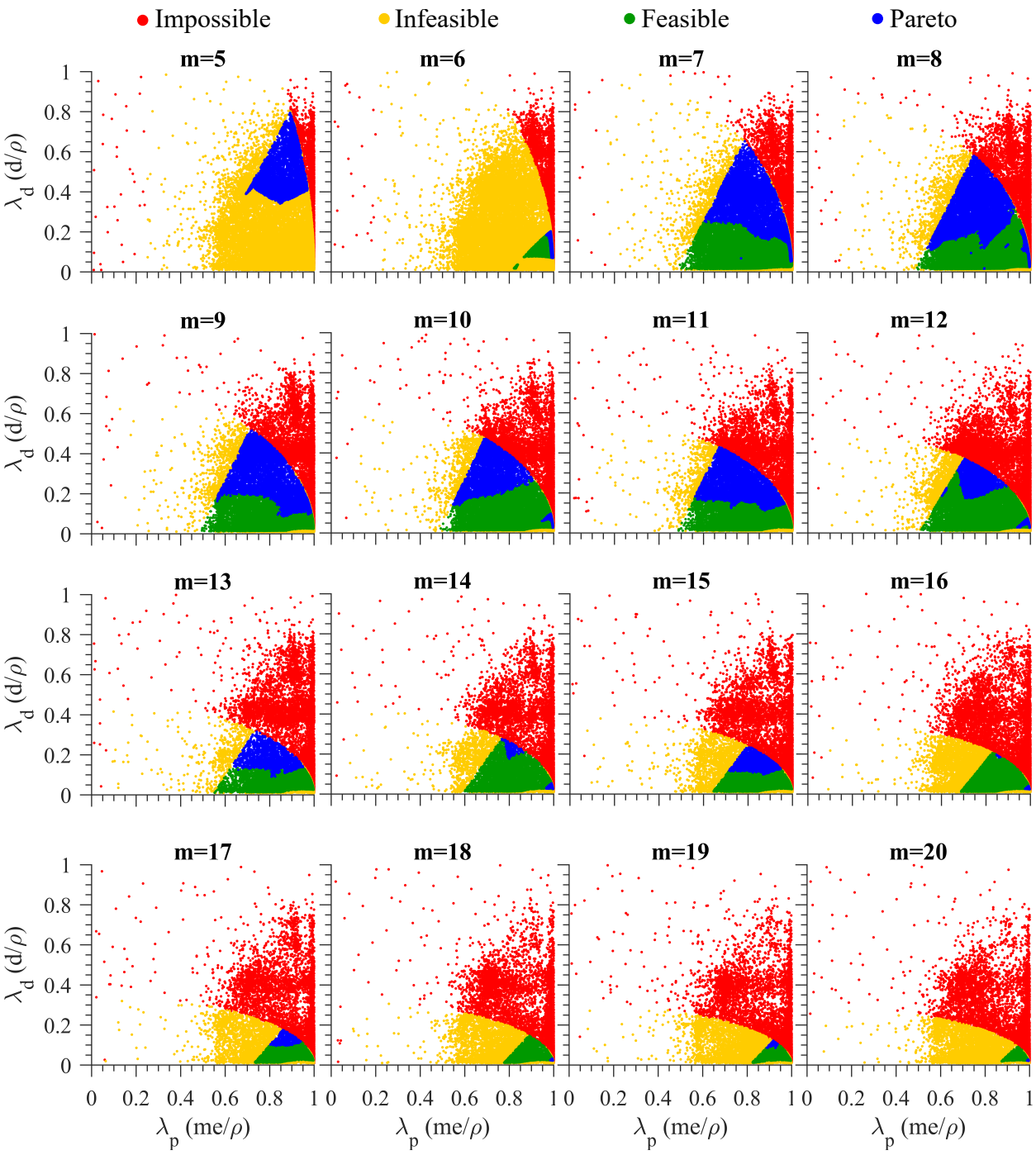

Figure 6.15. Design space of hypotrochoidal gerotors

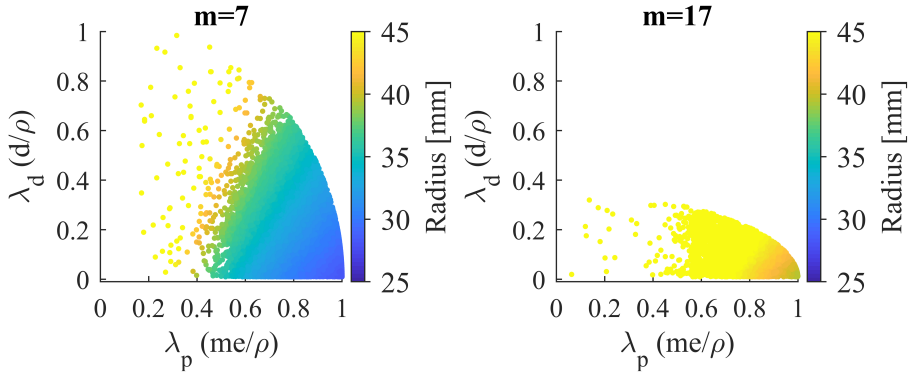

Figure 6.16. Plots of the minimum root radius for hypotrochoidal pumps with $m = 7$ (left) and for pumps with $m = 17$ (right).

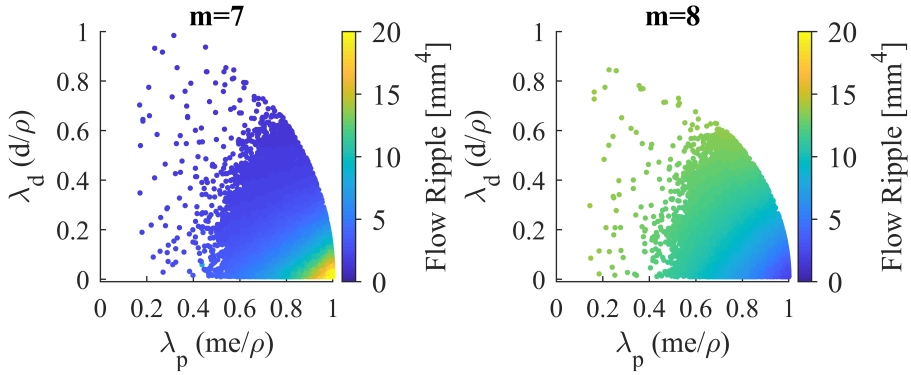

Figure 6.17. Plots of the flow ripple signal power for hypotrochoidal pumps with $m = 7$ (left) and for pumps with $m = 8$ (right).

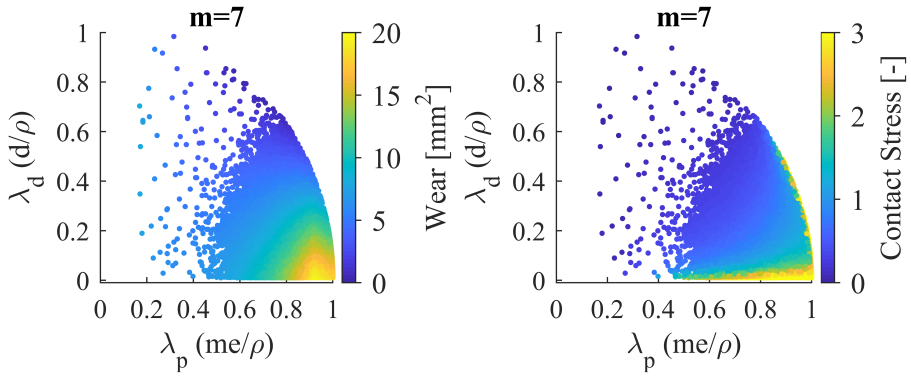

Figure 6.18. Plots of the adhesive wear (left) and contact stress (right) for hypotrochoidal pumps with $m = 7$.

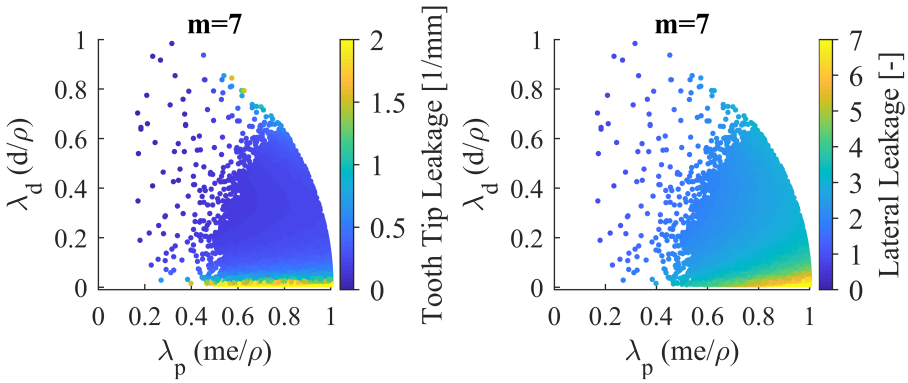

Figure 6.19. Plots of the tooth tip leakage (left) and lateral gap leakage (right) for hypotrochoidal pumps with $m = 7$.

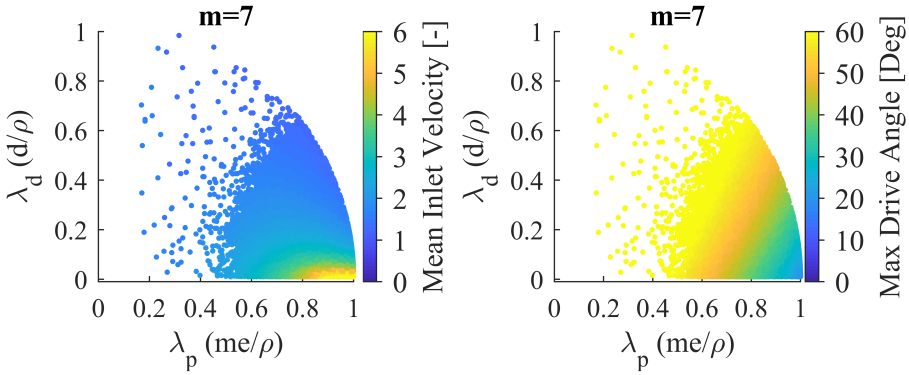

Figure 6.20. Plots of the maximum mean inlet velocity (left) and maximum drive angle (right) for hypotrochoidal pumps with $m = 7$.

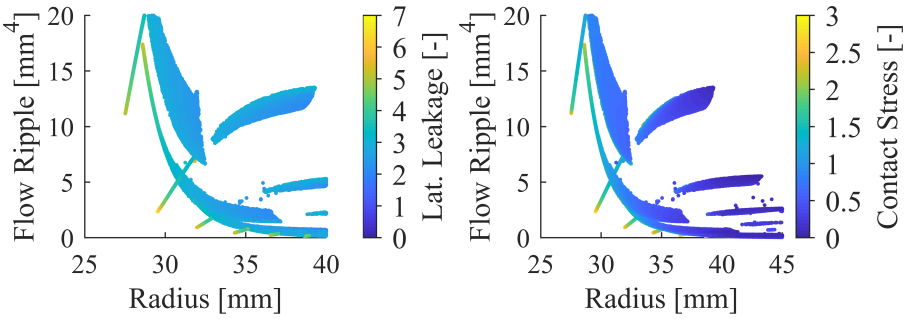

Figure 6.21. Left: Plot of size, flow ripple, and lateral leakage for hypotrochoidal designs on the Pareto front. Right: Plot of size, flow ripple, and contact stress for hypotrochoidal designs on the Pareto front [27]

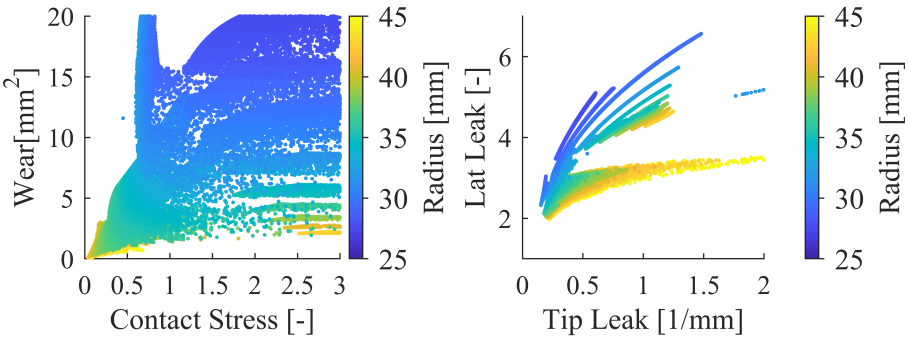

Figure 6.22. Left: Plot of contact stress, wear, and radius for hypotrochoidal designs on the Pareto front. Right: Plot of tip leakage, lateral leakage, and radius for hypotrochoidal designs on the Pareto front [27]

6.3 Cycloidal Gerotors

The cycloidal optimization was completed much faster than the others since it only has two input variables. A total of 20,000 designs were completed in 1.5 hours, and 73% of the designs were feasible. Of the feasible designs, 89% were on the Pareto front. The effect of varying the tooth size parameter λ_d on the gear geometry is shown in fig. 6.14, and the design space of the cycloidal profile is shown in fig. 6.24. Because the design space is composed of only two input variables, the value of each OF as a function of the input variables is displayed in fig. 6.24. Additionally no drive angle constrain violations were present for the standard cycloidal profile. As the value of λ_d approaches zero, the two gears become epicycloids, and the outer gear teeth become points. However, when the value of λ_d approaches one, the two gears become hypocycloids, and the inner gear tooth tips become points. Gears with the highest value of λ_d are the most compact. When m is odd, the most compact designs also have the highest flow ripples, while designs with an even value of m have a single point with the best combination of size and flow ripple. However, as the value of λ_d approaches its bounds, both the leakage functions increase significantly as shown in fig. 6.25.

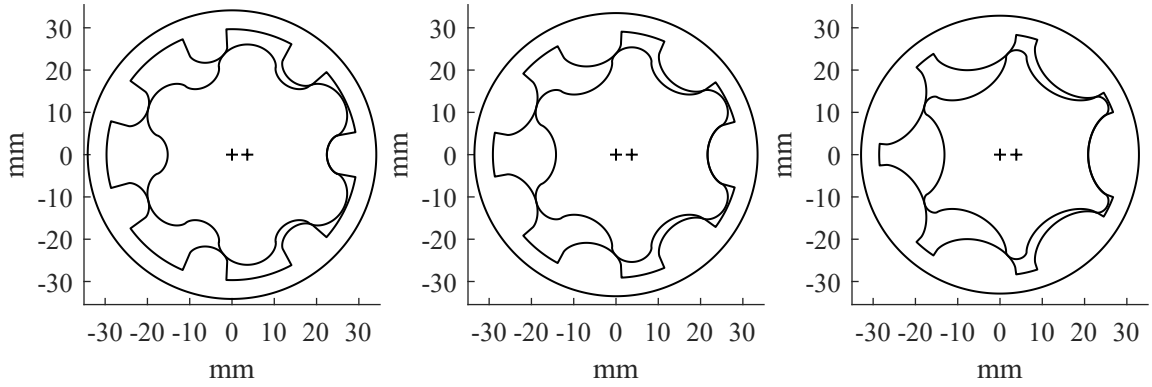

Figure 6.23. Standard cycloidal gerotors with $m = 7$. Left: $\lambda_d = 0.4$ Center: $\lambda_d = 0.6$ Right: $\lambda_d = 0.8$

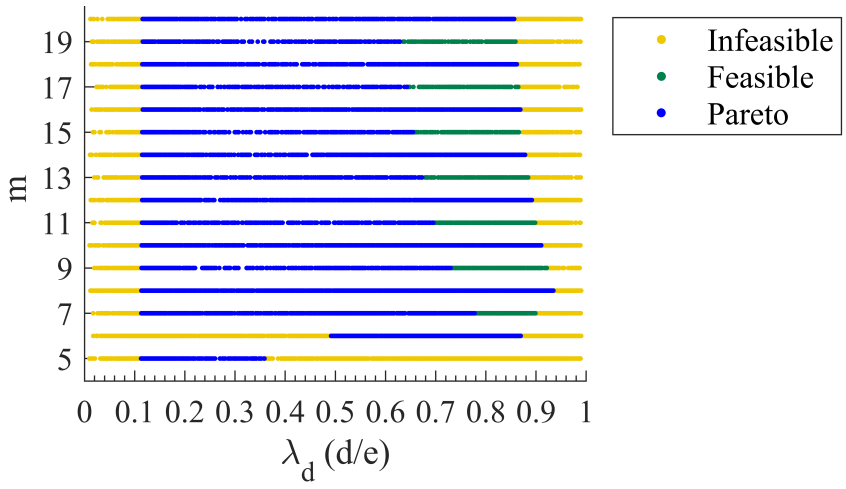

Figure 6.24. Design space of standard cycloidal gerotors

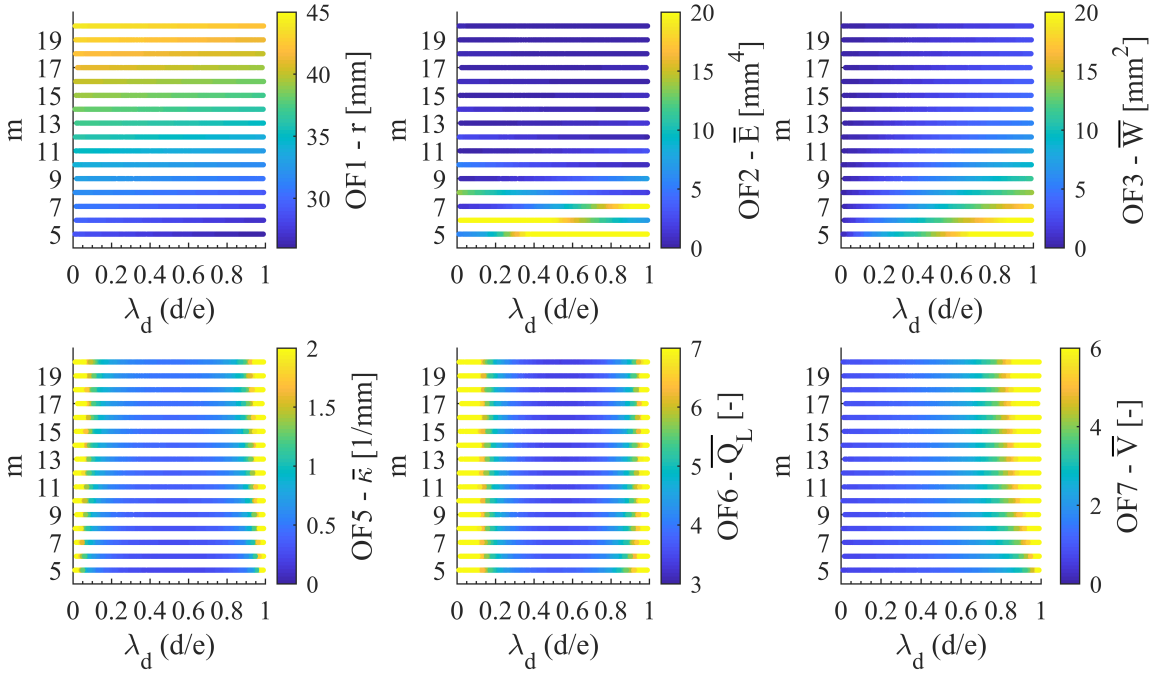

Figure 6.25. Plots showing the objective function values of standard cycloidal gerotors over their entire design space.

6.4 Elliptical Gerotors

A total of 489,254 designs were evaluated in 43 hours in the elliptical optimization. Of the evaluated designs 35% were feasible, and 67% of the feasible designs were on the Pareto front. The effect of the input variables on the shape of the geometry is very similar to that of epitrochoidal gerotors with the exception of the tooth aspect ratio $\lambda_t(k/d)$. Its effect is shown in fig. 6.26. Adding the fourth input variable makes showing the design space graphically more difficult, but a scatter matrix can be used to show the correlation between each input variable and the value of each OF to give some level of visualization. A scatter matrix for the feasible designs is shown in fig. 6.27. The non-dimensional center distance e/ρ added for comparison, and red lines indicate where $\lambda_t = 1$. In the upper triangular section, each design is represented by a point, so the the relationship between each pair of inputs and outputs can be visualized. The diagonal entries in the scatter matrix show the histograms of each quantity among the Pareto designs. Lastly, the lower triangular portion shows the Pearson correlation coefficient for each pair. A correlation of one corresponds to a strong positive correlation, zero indicates no correlation, and negative one indicates a strong negative correlation. The equation for the Pearson correlation coefficient is given in eq. (6.1), where $\rho_{A,B}$ in this instance is the correlation coefficient of two variables, cov is the covariance function, A and B are the variables, and σ is the standard deviation.

A few general trends can be observed in the scatter matrix. As the number of teeth increases, the maximum allowable center distance decreases while the size of the pump increases. Size and flow ripple are generally opposing goals as well as the size and the adhesive wear. Flow ripple and adhesive wear are also loosely correlated. Beyond these general observations that mostly hold true for the other profile types, the scatter matrix shows that the design space is quite complex and simple rules for picking geometric parameters leading to a good pump cannot be defined. This highlights the need for an optimization process to fully navigate the trade-offs in performance between different designs.

$$\rho_{A,B} = \frac{\operatorname{cov}(A, B)}{\sigma_A \sigma_B} \tag{6.1}$$

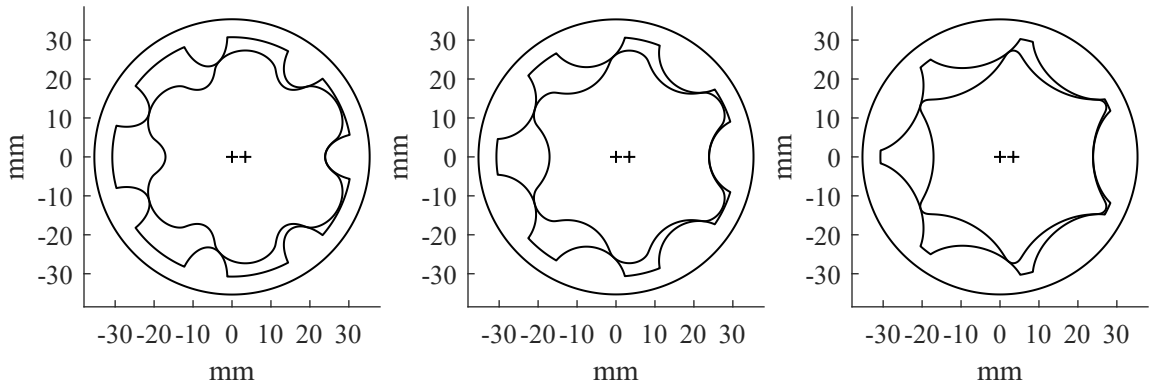

Figure 6.26. Elliptical gerotors with $m = 7$, $\lambda_p = 0.7$, and $\lambda_d = 0.3$. Left: $\lambda_t = 0.6$ Center: $\lambda_d = 1.0$ Right: $\lambda_d = 1.4$

A few of the relationships between the OF values of designs on the Pareto front are shown in figs. 6.28 and 6.29. As with the other designs, the pump size and radius tend to be a compromise as shown in fig. 6.28. Further as a pump gets smaller, the contact stress tends to increase sharply as it approaches the size limit for a given number of teeth. Additionally, the designs with the best combination of size and flow ripple also tend to have high lateral gap leakage. Designs with low adhesive wear tend to be large as shown in fig. 6.29. Also designs with the best combination of tooth tip and lateral gap leakage tend to have a large radius.

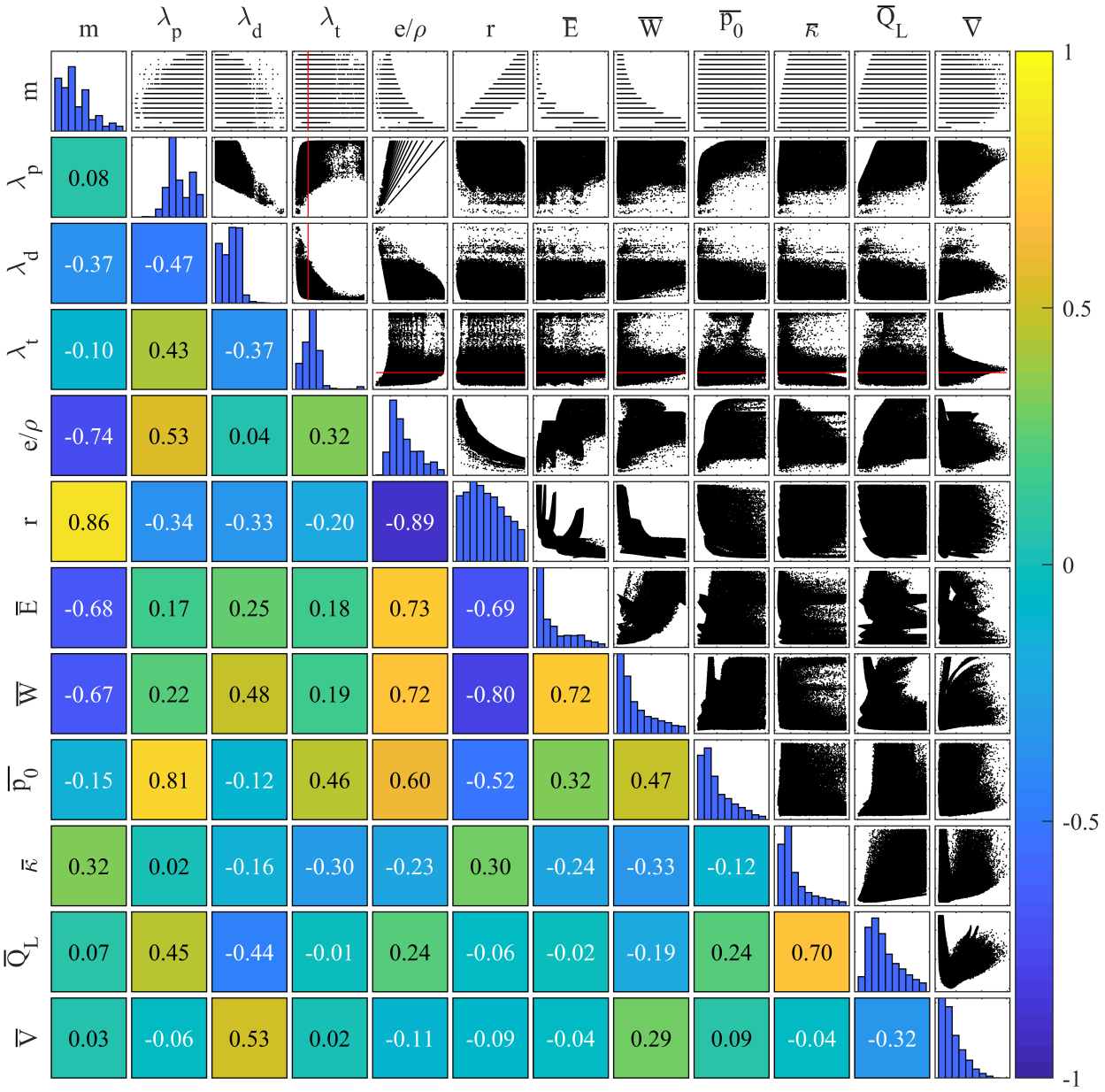

Figure 6.27. Scatter matrix of feasible elliptical gerotors

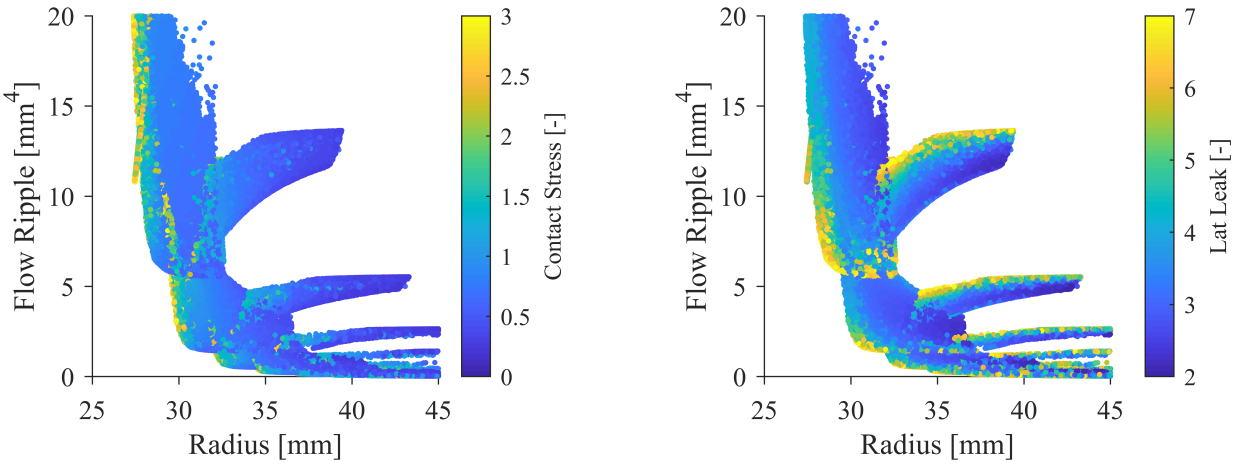

Figure 6.28. Left: Plot of radius, flow ripple, and contact stress for elliptical designs on the Pareto front. Right: Plot of radius, flow ripple, and lateral gap leakage for elliptical designs on the Pareto front

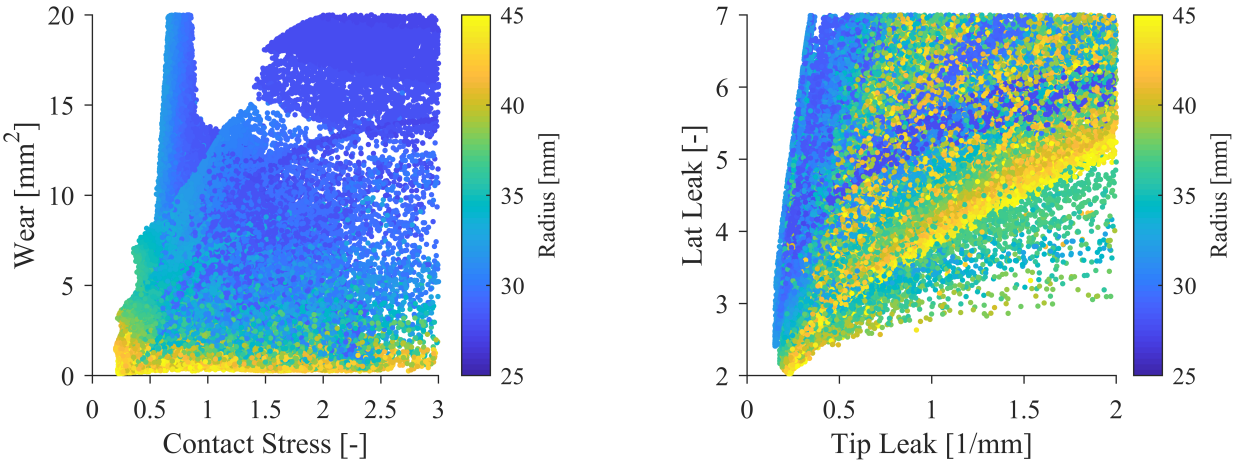

Figure 6.29. Left: Plot of contact stress, wear, and radius for elliptical designs on the Pareto front. Right: Plot of tooth tip leakage, lateral gap leakage, and radius for elliptical designs on the Pareto front

6.5 Generalized Cycloidal Gerotors

A total of 489,494 designs were evaluated in 53 hours in the generalized cycloidal gerotor optimization. Of the evaluated designs 39% were feasible, and 65% of the feasible designs were on the Pareto front. Just as for the other profiles, the effect of varying each of the input parameters on the appearance of the gearsets is shown in figs. 6.30–6.33. A scatter matrix of the input variables and objective functions is then given in fig. 6.34. The scatter matrix shows the similar general trends to the other profiles. A greater center distance tends to result in a smaller pump, size and flow ripple are a trade-off, a greater flow ripple generally leads to increased wear, and the design space is complex making it difficult to make simple generalizations on the influence of each input variable. Similar patterns to those for the elliptical profile emerged among the relationships between the OF values of designs on Pareto front as shown in figs. 6.35 and 6.36. Minimizing size and flow ripple are generally opposing goals, and designs with the best combination of size and flow ripple also tend to have either high contact stress or high lateral gap leakage. Designs with low wear also tend to be larger pumps as well as designs that have both low tooth tip and lateral gap leakage.

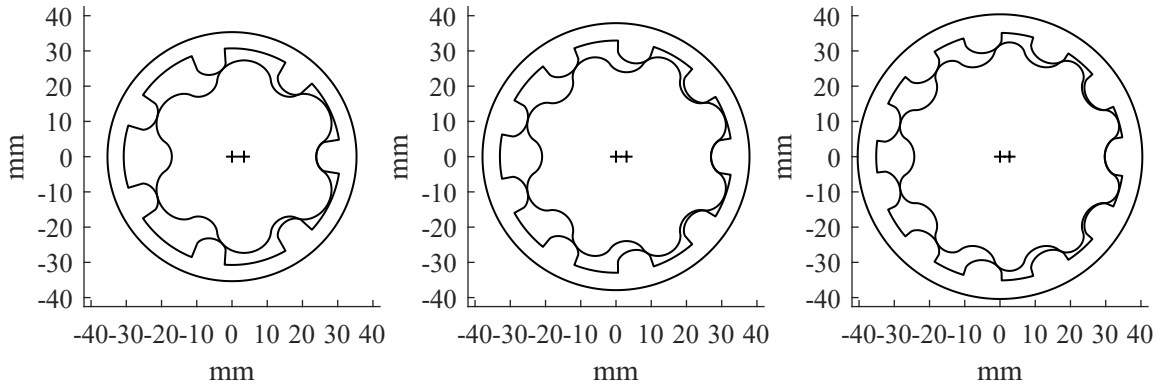

Figure 6.30. Generalized cycloidal gerotors with $\lambda_e = 0.9$, $\lambda_d = 0.05$, and $\lambda_r = 1.0$. Left: $m = 7$ Center: $m = 9$ Right: $m = 11$

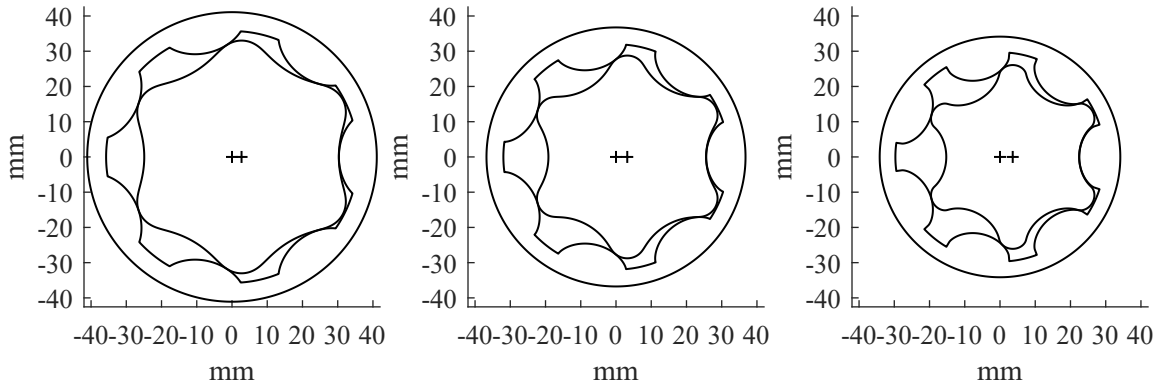

Figure 6.31. Generalized cycloidal gerotors with $m = 7$, $\lambda_d = 0.1$, and $\lambda_r = 1.0$. Left: $\lambda_e = 0.5$ Center: $\lambda_e = 0.7$ Right: $\lambda_e = 0.9$

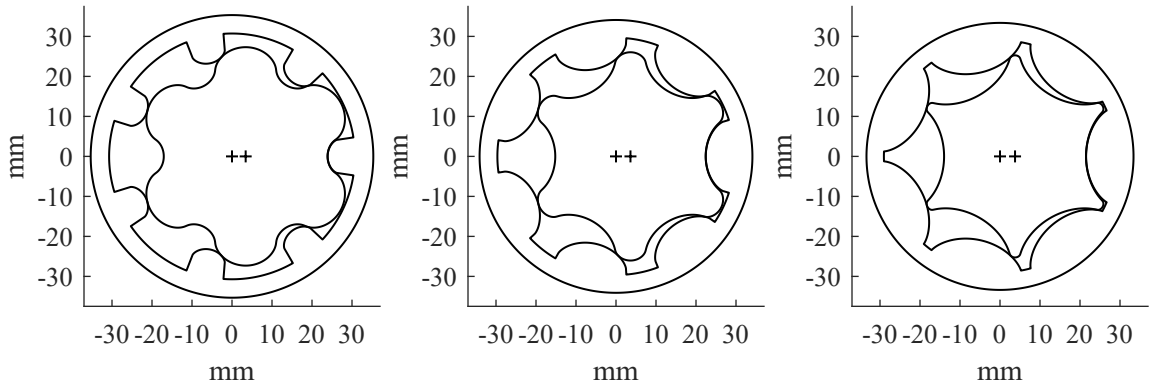

Figure 6.32. Generalized gerotors with $m = 7$, $\lambda_e = 0.9$, and $\lambda_r = 1.1$. Left: $\lambda_d = 0.05$ Center: $\lambda_d = 0.1$ Right: $\lambda_d = 0.13$

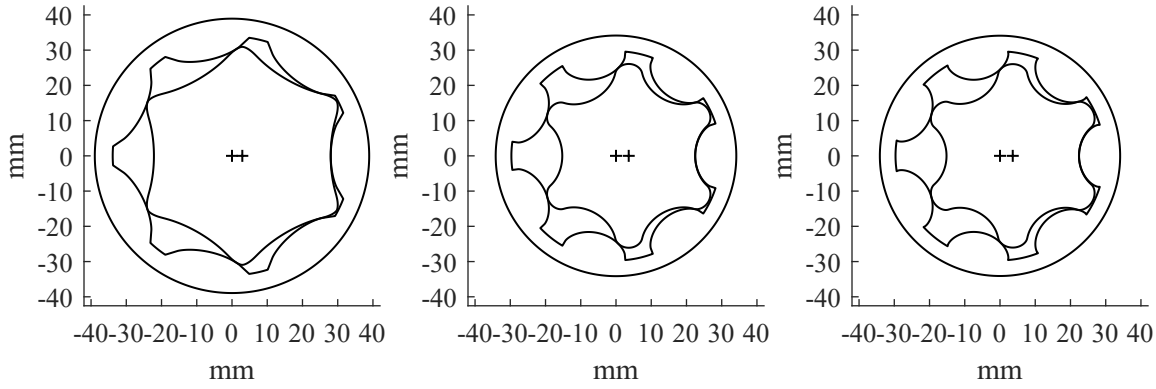

Figure 6.33. Generalized cycloidal gerotors with $m = 7$, $\lambda_e = 0.9$, and $\lambda_d = 0.1$. Left: $\lambda_r = 0.3$ Center: $\lambda_r = 1.0$ Right: $\lambda_r = 1.0$

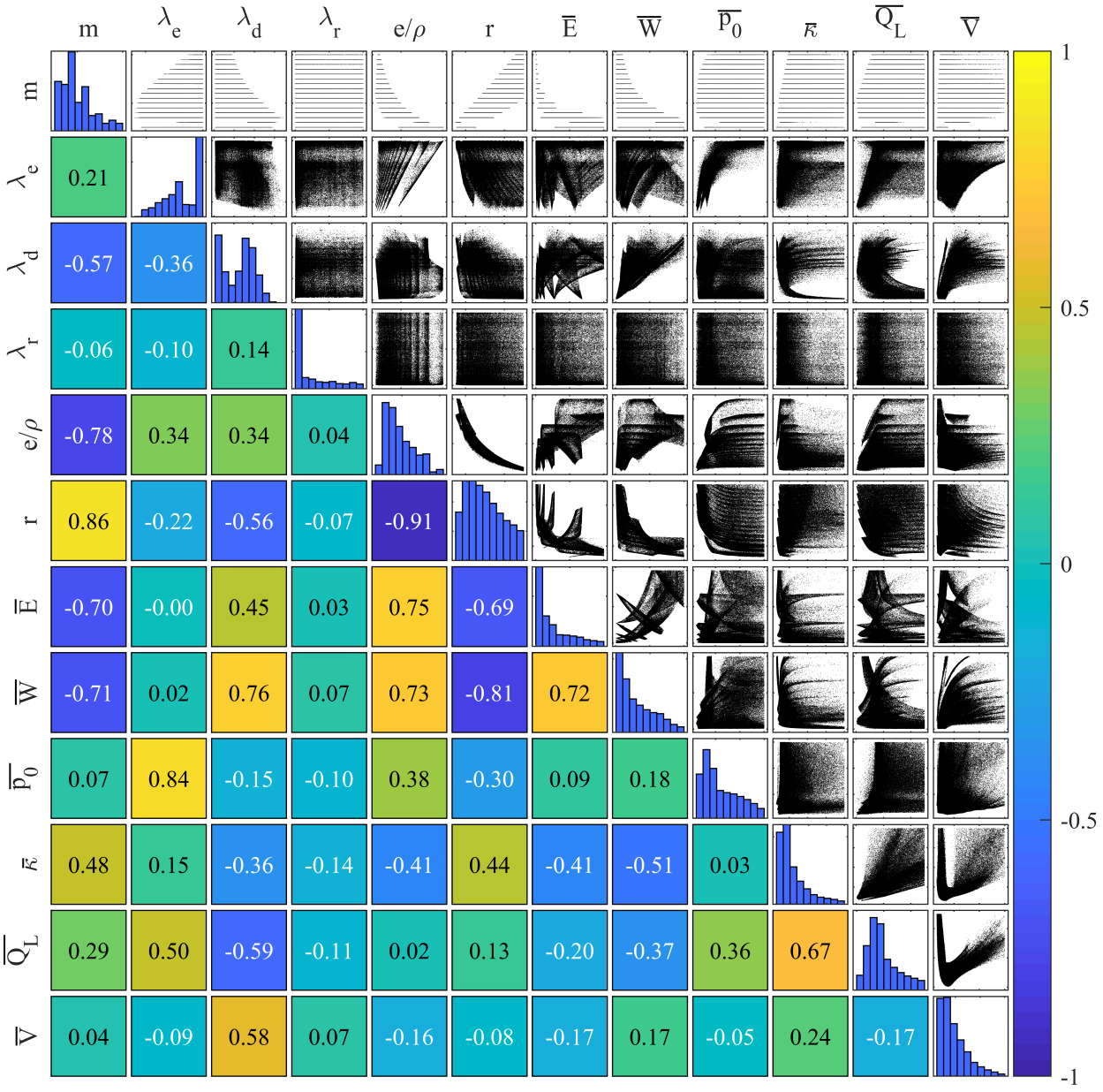

Figure 6.34. Scatter matrix of feasible generalized cycloidal gerotors

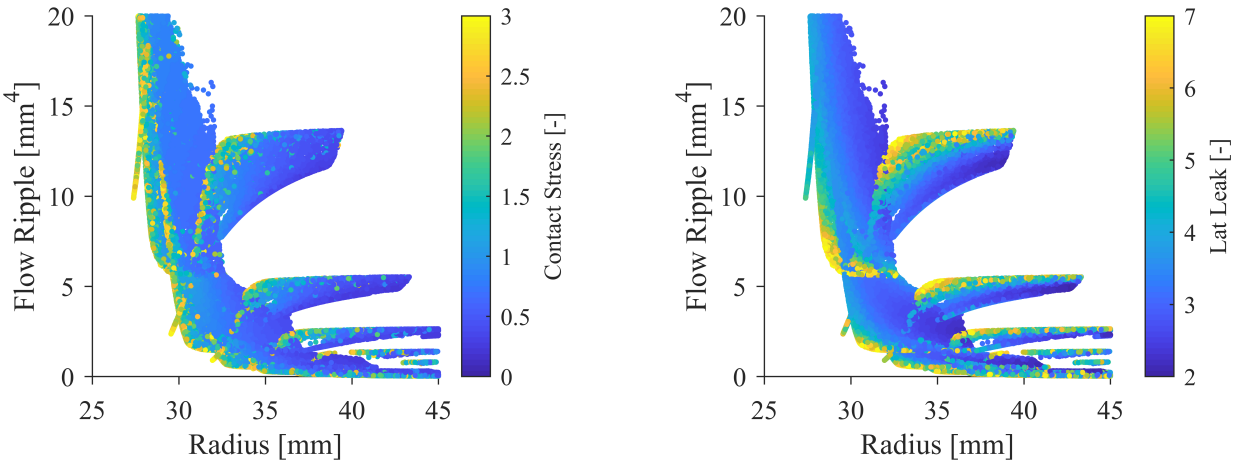

Figure 6.35. Left: Plot of radius, flow ripple, and contact stress for generalized cycloidal designs on the Pareto front. Right: Plot of radius, flow ripple, and lateral gap leakage for generalized cycloidal designs on the Pareto front

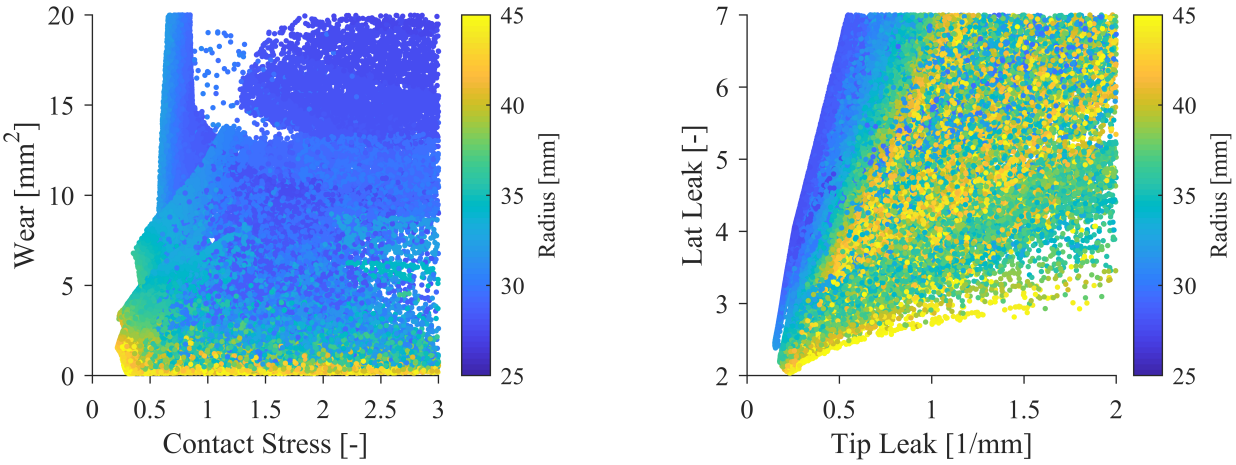

Figure 6.36. Left: Plot of contact stress, wear, and radius for generalized cycloidal designs on the Pareto front. Right: Plot of tooth tip leakage, lateral gap leakage, and radius for generalized cycloidal designs on the Pareto front

6.6 Cosine Gerotors

A total of 488,719 designs were evaluated in 44 hours in the optimization of the cosine profile. Of the evaluated designs 33% were feasible, and 65% of the feasible designs were on the Pareto front. As was shown for the other profiles, the effect of varying the input variables on the gear geometry are shown in figs. 6.37–6.40, and a scatter matrix of the feasible designs is given in fig. 6.41. The scatter matrix shows some interesting trends for the cosine profile. The number of teeth and the size of the pump and flow ripple are strongly correlated as for the profile types. Additionally pumps with fewer teeth tend to have more wear. The maximum allowable value of λ_p cannot be known a priori as for the epitrochoidal, hypotrochoidal, and elliptical profiles, but the scatter matrix shows that the upper bound was sufficiently high to capture the feasible design space. The same is true for λ_t. The same general compromise between size and flow ripple is true for cosine profiles as for the others. The tooth tip and lateral gap leakage for cosine profiles are correlated that they generally increase together. Additionally, a compromise relationship is present for the leakage and the mean inlet velocity. Plots showing the relationship between some OF values for designs on the Pareto front are shown in figs. 6.42 and 6.43 that largely confirm the same general trends as observed for the other profile types. Size and flow ripple tend to be opposing goals, and designs with the best combination of size and flow ripple typically have either high contact stress or high lateral gap leakage. Designs with low wear tend to also be larger pumps, and the same is true for designs with low leakage.

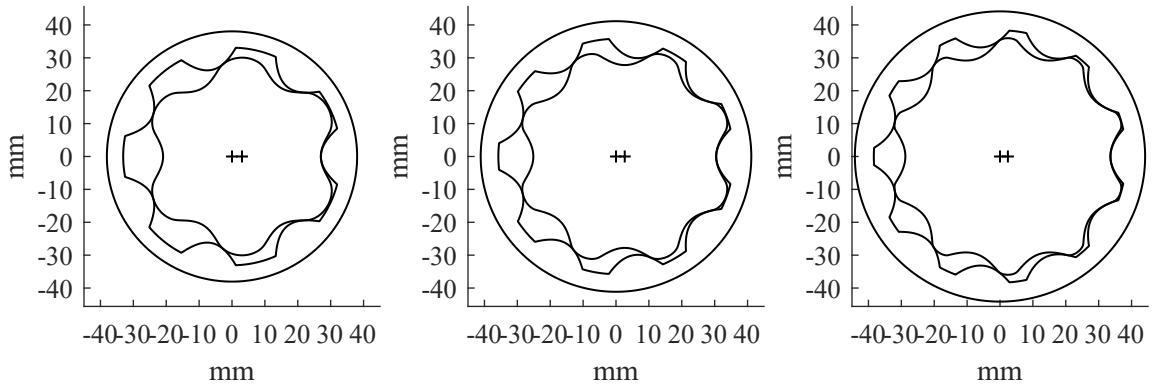

Figure 6.37. Cosine gerotors with $\lambda_p = 0.55$, $\lambda_d = 0.3$, and $\lambda_t = 1.2$. Left: $m = 7$ Center: $m = 9$ Right: $m = 11$

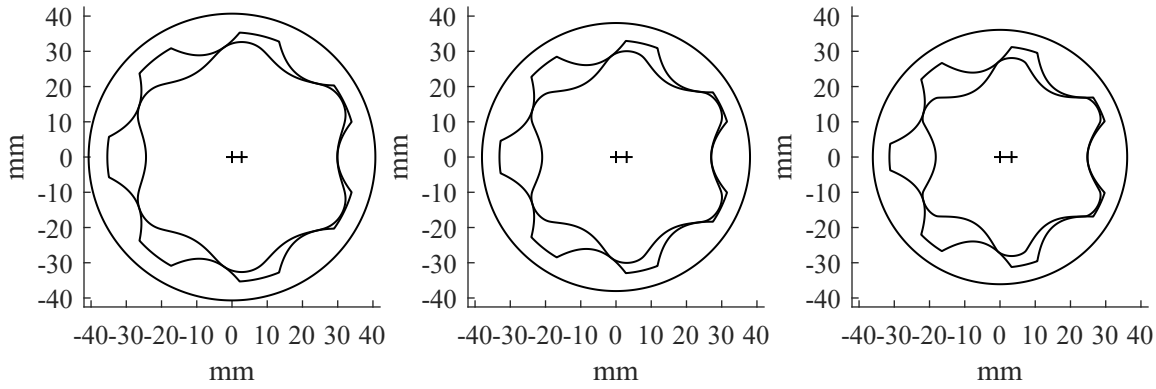

Figure 6.38. Cosine gerotors with $m = 7$, $\lambda_d = 0.3$, and $\lambda_t = 1.5$. Left: $\lambda_p = 0.45$ Center: $\lambda_p = 0.55$ Right: $\lambda_p = 0.65$

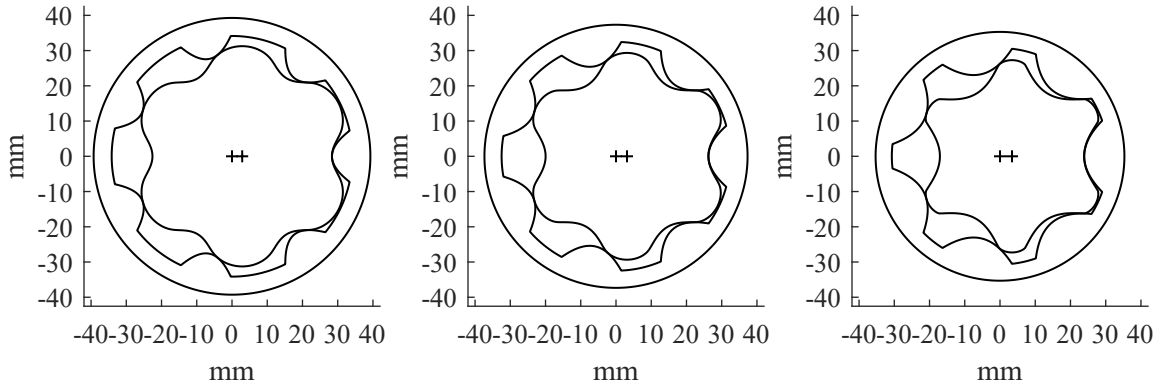

Figure 6.39. Cosine gerotors with $m = 7$, $\lambda_p = 0.5$, and $\lambda_t = 1.0$. Left: $\lambda_d = 0.3$ Center: $\lambda_d = 0.4$ Right: $\lambda_d = 0.5$

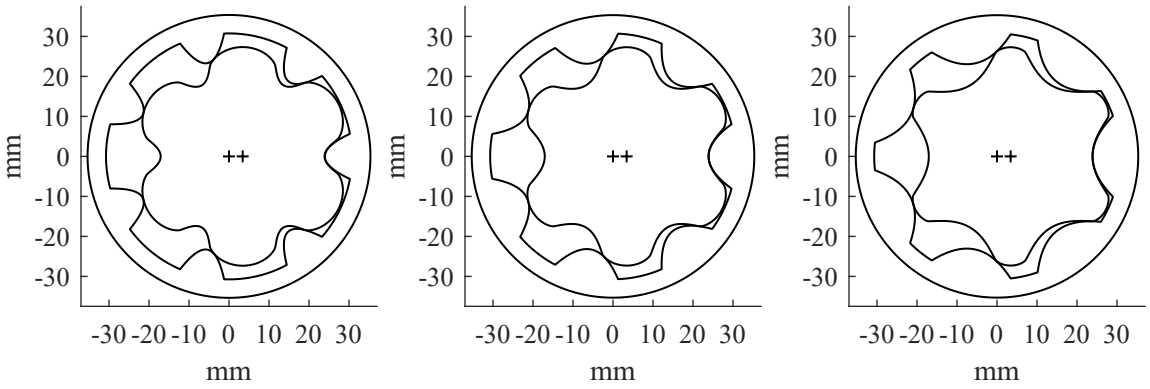

Figure 6.40. Cosine gerotors with $m = 7$, $\lambda_p = 0.5$, and $\lambda_d = 0.5$. Left: $\lambda_t = 0.5$ Center: $\lambda_t = 0.75$ Right: $\lambda_t = 1.0$

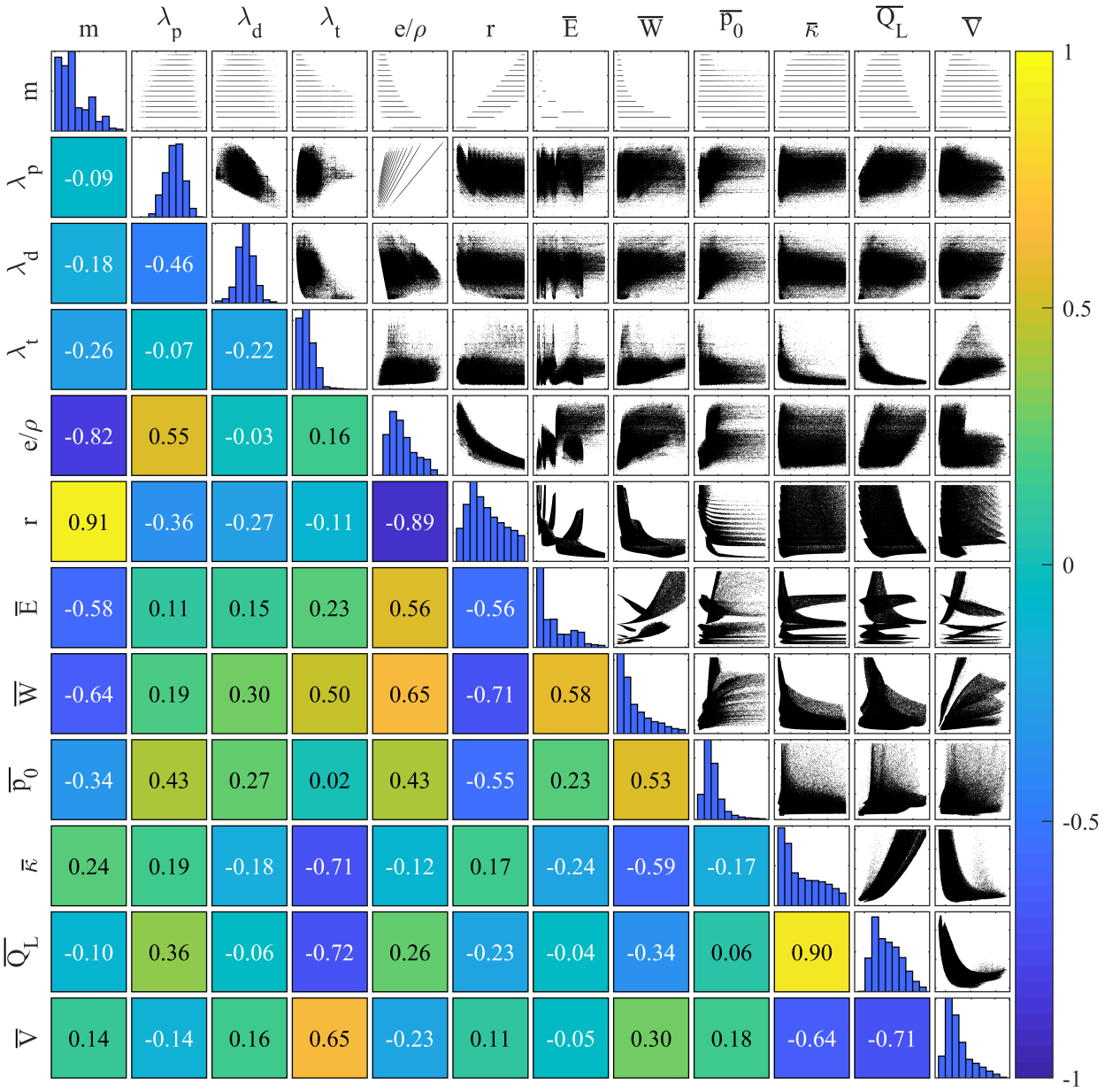

Figure 6.41. Scatter matrix of feasible cosine gerotors

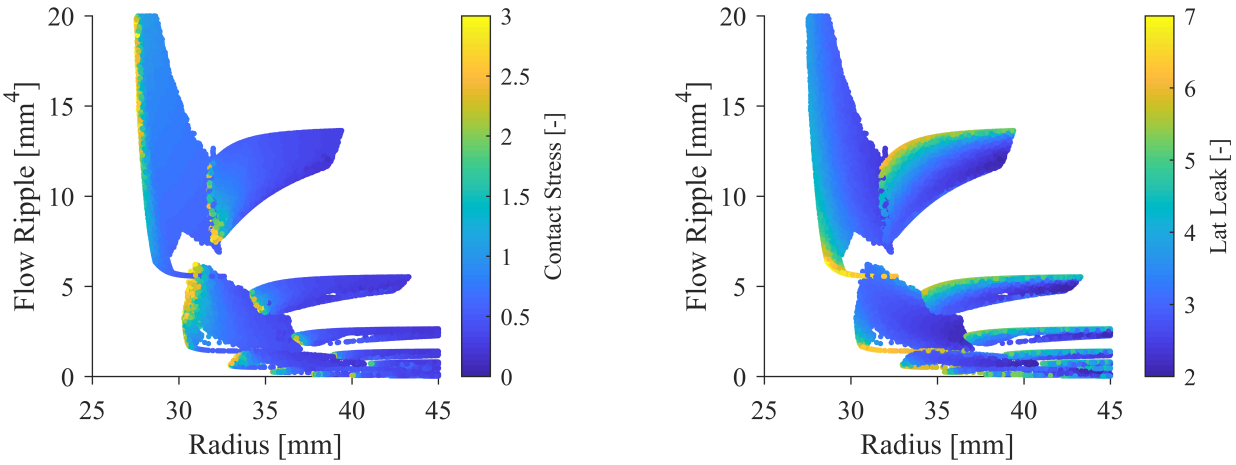

Figure 6.42. Left: Plot of radius, flow ripple, and contact stress for cosine designs on the Pareto front. Right: Plot of radius, flow ripple, and lateral gap leakage for cosine designs on the Pareto front

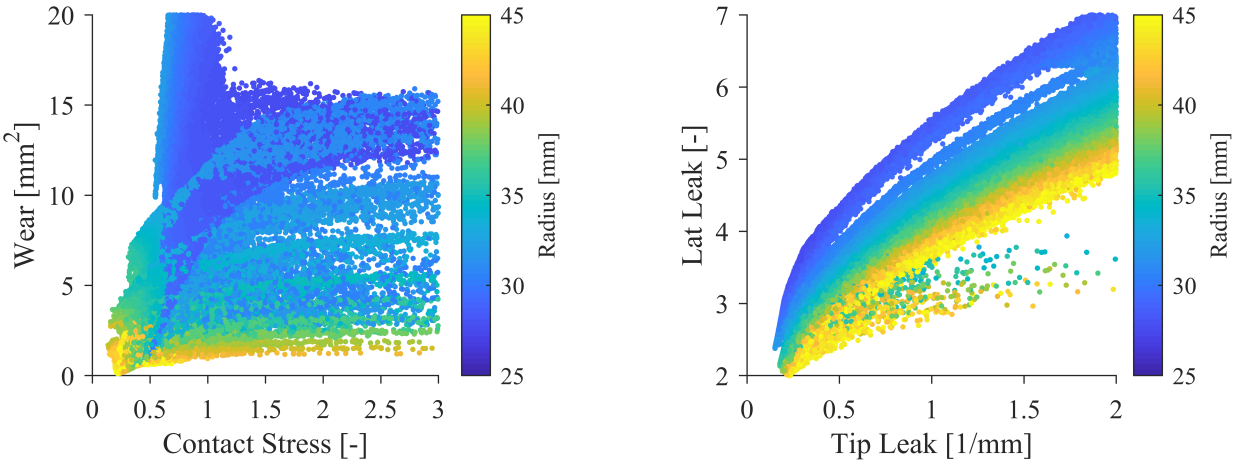

Figure 6.43. Left: Plot of contact stress, wear, and radius for cosine designs on the Pareto front. Right: Plot of tooth tip leakage, lateral gap leakage, and radius for cosine designs on the Pareto front

6.7 Asymmetric Elliptical Gerotors

A total of 693,517 designs were evaluated in 78 hours in the optimization of the asymmetric elliptical profile. Of the evaluated designs 32% were feasible, and 62% of the feasible designs were on the Pareto front. The optimization was run for more generations to allow a greater exploration of the design space since the asymmetric elliptical profile has an additional input variable over the other profile types. The effect of varying the tooth rotation angle on the gear geometry is shown in fig. 6.44 for designs with $\lambda_t < 1$ and $\lambda_t > 1$, and a scatter matrix of the feasible designs is given in fig. 6.45. In the scatter matrix, red lines are used to highlight where $\lambda_t = 1$ corresponding to a circular profile and $\alpha = 0$ corresponding to a symmetric profile. The scatter matrix shows the same general trends as the other profile types regarding number of teeth, size, flow ripple, and wear. Additionally, the effect of varying the tooth rotation angle does not appear to have an effect on the OF that is simple to identify. Designs with a greater value of α do tend to have lower inlet velocities. This could be because designs with high rotation angles can have a larger dead volume than their symmetric counterparts as can be seen in the second row of designs in fig. 6.44.

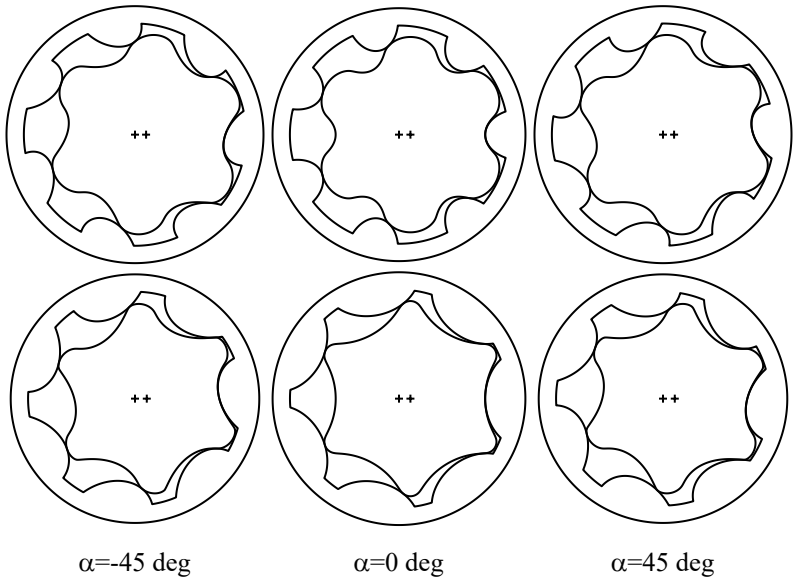

Figure 6.44. Illustration of the effect of changing α in asymmetric elliptical profiles. Top: $m = 7$, $\lambda_p = 0.65$, $\lambda_d = 0.3$, $\lambda_t = 0.7$. Bottom: $m = 7$, $\lambda_p = 0.65$, $\lambda_d = 0.3$, $\lambda_t = 1.3$ [32]

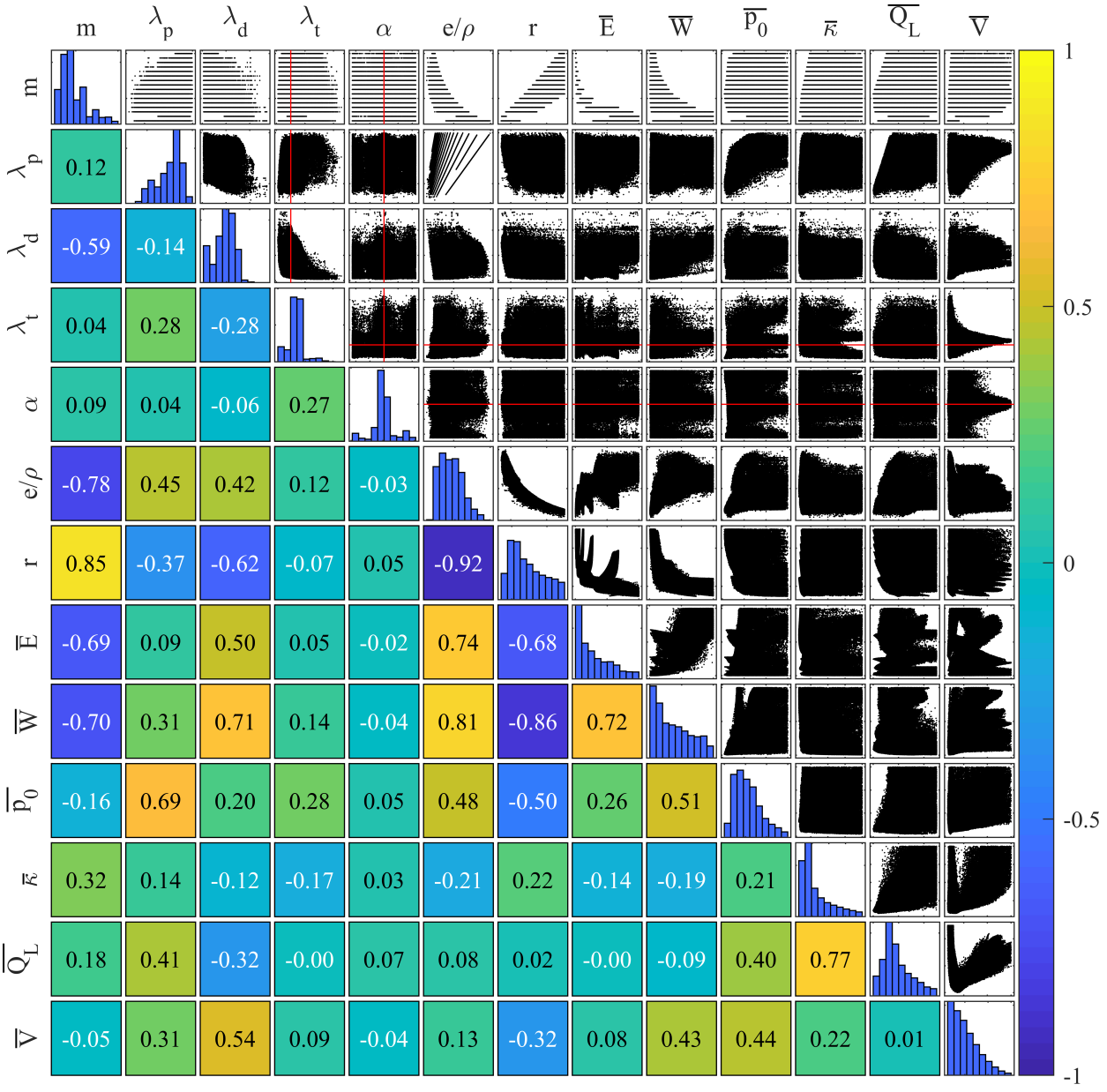

Figure 6.45. Scatter matrix of feasible asymmetric elliptical gerotors

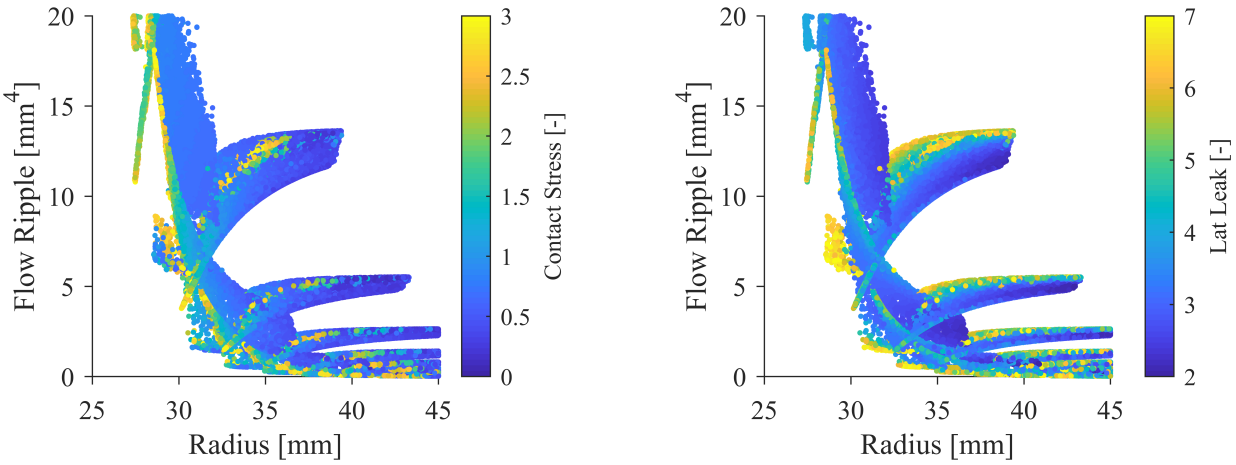

Figure 6.46. Left: Plot of radius, flow ripple, and contact stress for asymmetric elliptical designs on the Pareto front. Right: Plot of radius, flow ripple, and lateral gap leakage for asymmetric elliptical designs on the Pareto front

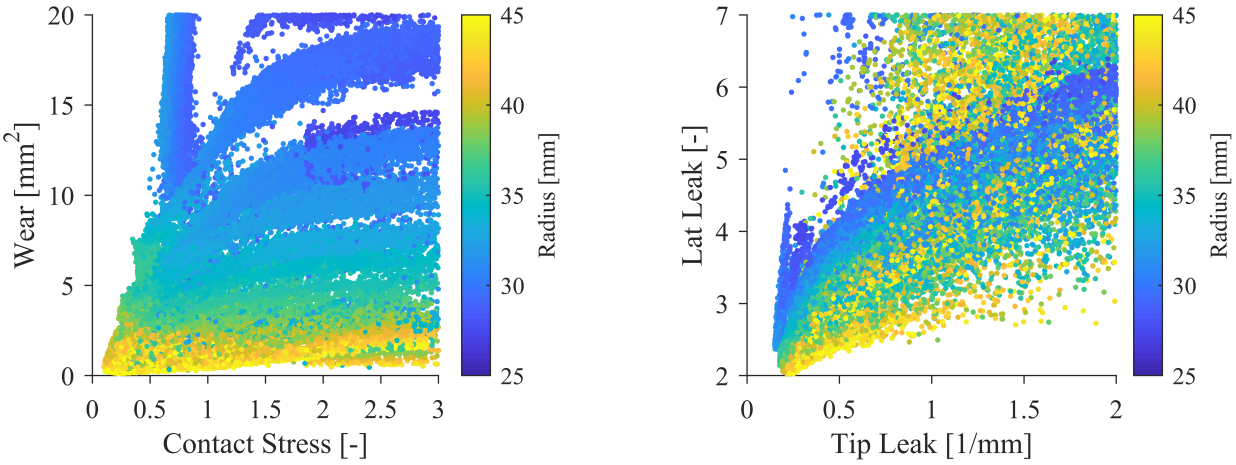

Figure 6.47. Left: Plot of contact stress, wear, and radius for asymmetric elliptical designs on the Pareto front. Right: Plot of tooth tip leakage, lateral gap leakage, and radius for asymmetric elliptical designs on the Pareto front

6.8 Discussion

The results presented in this chapter warrant a brief discussion. First, the optimization process was successful for each profile type to identify both the feasible and Pareto designs for each profile type. In each case, the design space was fully explored and the upper bounds on the input variables without an obvious limit were high enough to capture the best designs of each profile type. Second, major trends in the compromise of performance regarding various OF are similar between the profile types. The main benefit in using a different profile type then is to open up new regions of the design space to give a different combination of OF values that would not be possible with a single profile type, but the exact benefit cannot be known before the optimization is performed. The interior regions of the Pareto front with good performance regarding each OF are not as easy to visualize as the edges where designs tend to perform poorly regarding one or more OF despite very good performance regarding other OF. Because upon first glance no single profile type appears to be the front runner, a more detailed comparison is necessary and is presented in the next chapter.

7. PROFILE COMPARISON

In this chapter a comparison between the performance of the gerotor profile types is made. First the conventional profile types (epitrochoidal, hypotrochoidal, and standard cycloidal) are compared, and two methods to select optimal designs are presented. This is followed by adding the less conventional profile types to the comparison to find any relative advantage.

7.1 Conventional Profile Types

The Pareto fronts from the epitrochoidal, hypotrochoidal, and standard cycloidal optimizations were combined, and then a new combined Pareto front was identified to give a new set of optimal designs. When this was done, 87% of the epitrochoidal designs, 69% of the hypotrochoidal designs, and 70% of the cycloidal designs remained on the new combined Pareto front. This means that no single profile type can be thought of as objectively better as the others, but rather the different profile types offer different performance trade-offs. In this process though, many designs were still eliminated, so the overall design of the pump geometry is improved. The challenge for the pump designer then becomes applying a multi-criteria decision making strategy to identify the most suitable design from the combined Pareto front for a given application. Additionally, some interesting observations can still be made from the combined Pareto front that generally what other researchers have found [15], [21] while giving a much more extensive comparison.

The standard cycloidal gerotor has been claimed anecdotally by engineers in industry to be more compact than the epitrochoidal gerotor, but this claim has not been validated in scientific literature. The results of the present work show this statement to be only partially true. In fig. 7.1, each design from the combined Pareto front are plotted as a point. The pump radius is plotted on the x-axis, the flow ripple on the y-axis, and the profile type is represented by the color. The epitrochoidal designs were plotted first, followed by the hypotrochoidal, and the standard cycloidal designs were plotted on top. This reveals that the epitrochoidal profile with an odd number of outer gear teeth can be more compact for a given flow ripple than the standard cycloidal profile type if the designer is willing to give up some performance in another area. However, the standard cycloidal profiles can indeed be

more compact than the epitrochoidal profile when they have an even number of outer gear teeth. The hypotrochoidal profile can match the size and flow performance of the standard cycloidal profile in this region with significantly reduced contact stress. To illustrate this, two designs were taken from the combined Pareto front in fig. 7.1 that are shown in fig. 7.2. Their size and flow performance are the same, but the hypotrochoidal profile is able to have much less contact stress in the process. However, this comes at the cost of increased tooth tip and lateral gap leakage that can be seen in fig. 7.2 by inspection. Outside of those regions, the epitrochoidal generally outperforms the hypotrochoidal profile in terms of size and flow ripple.

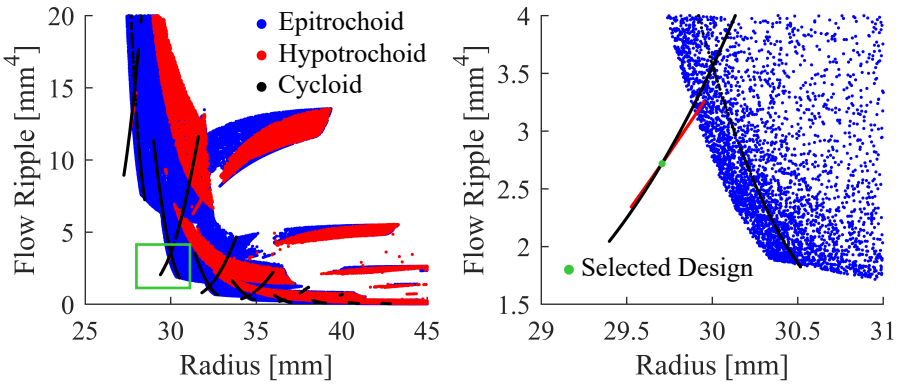

Figure 7.1. Plot of size vs flow ripple for designs on the combined Pareto front (left) and magnified plot (right) [27]

A couple other differences between the profiles should be noted as well. A region of the hypotrochoidal design space exists that has less wear and contact stress than the best epitrochoidal designs. This region is illustrated in fig. 7.3 where the hypotrochoidal designs are plotted first followed by the epitrochoidal designs over the top. In fig. 7.3 a design is selected from this region with very good wear performance. Regarding leakage, both the epitrochoidal and hypotrochoidal profiles have regions of their design space that can significantly out-perform the standard cycloidal profile type, and this is illustrated in fig. 7.4. An epitrochoidal design is selected from this region also in fig. 7.4. As the value of λ_d increases for the standard cycloidal profile with a given number of teeth, the size of the outer gear tooth increases while the size of the inner gear tooth decreases. This leads to both reduced tooth tip and lateral gap leakage for the pump until a minimum is reached. At that point

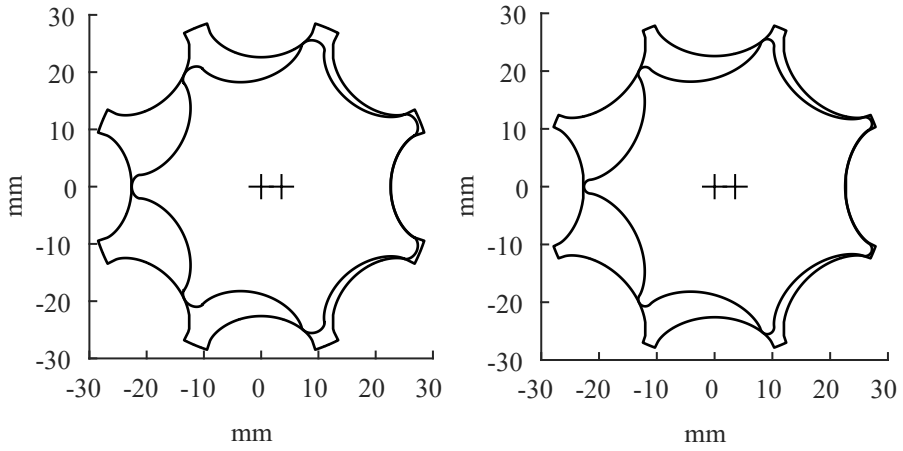

Figure 7.2. Cycloidal ($m = 8$, $\lambda_d = 0.816$) and hypotrochoidal ($m = 8$, $\lambda_p = 0.997$, $\lambda_d = 0.042$) gearsets with the same size and flow characteristics [27]

the inner gear tooth becomes prohibitively small and both leakage metrics begin to increase again with λ_d. These curves are visible in fig. 7.4.

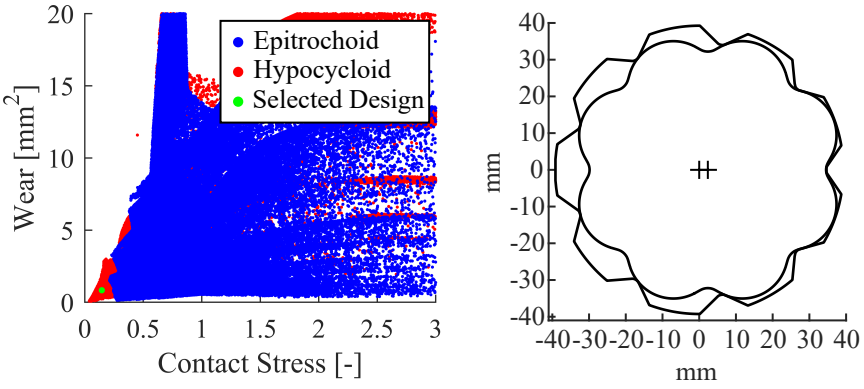

Figure 7.3. Left: Plot of contact stress vs wear for epitrochoidal and hypotrochoidal designs on global Pareto front (Epitrochoidal designs plotted on top of hypotrochoidal). Right: Selected hypotrochoidal design ($m = 9$, $\lambda_p = 0.766$, $\lambda_d = 0.449$) with low wear and contact stress [27]

Selecting a design from a Pareto front with seven OF is its own challenge. The selected designs shown in figs. 7.2–7.4 are examples of choosing designs for maximum performance in one area at the cost of making significant compromise in other areas. However, a gearset used in production would likely require good performance in all the OF. A simplified method

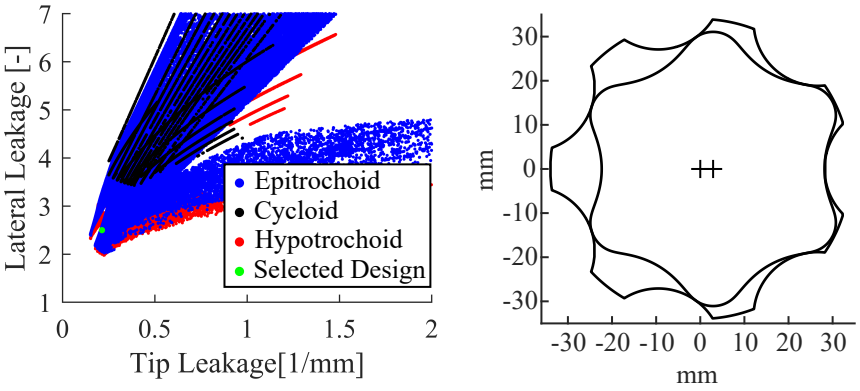

Figure 7.4. Left: Plot of tooth tip gap leakage vs lateral gap leakage for designs on global Pareto front (Epitrochoidal designs plotted on top of hypotrochoidal). Right: Selected epitrochoidal design with low leakage for $m = 7$, $\lambda_p = 0.477$, $\lambda_d = 0.341$ [27]

of selecting a design would be to use a weighting strategy shown in eq. (7.1). In eq. (7.1) a weight is assigned to each OF by the pump designer in a heuristic manner, and the hat indicates a normalized value. The OFs are normalized such that a value of zero corresponds to the lowest value of that function among the designs in the Pareto front, and a value of one corresponds to the maximum allowable value for the optimization given in table 5.1. When using this strategy, the weight function is calculated for each design, and the designs are then ranked accordingly. A possible set of weights to give good energy efficiency is given in table 7.1, and when this weighting was applied the best design for each profile type is shown in fig. 7.5. For this particular weighting scheme, the hypotrochoidal profile performed 2.5% better than the epitrochoidal and 12% better than the standard cycloidal. The relative performance of each design is shown in fig. 7.6. Many designs used in industry are larger and have more teeth than the designs shown in fig. 7.5. This is likely because they either must have a very low flow ripple or use a through-shaft that requires a larger pump size. However the designs selected using the weighting strategy do resemble a pump used in a fuel injection application shown in fig. 7.7. If the drive angle is further constrained to 45°, the

winning epitrochoidal design would resemble the pump used in industry even more closely as shown in fig. 7.7.

$$F_W = w_1\hat{r_r} + w_2\hat{\overline{E}} + w_3\hat{\overline{W}} + w_4\hat{\overline{p_0}} + w_5\hat{\overline{\kappa}} + w_6\hat{\overline{Q_L}} + w_7\hat{\overline{V}} \tag{7.1}$$

Table 7.1. Example OF weights to give a pump with good energy efficiency

w_1	w_2	w_3	w_4	w_5	w_6	w_7
1	0.25	0.5	0.1	1	0.75	0.1

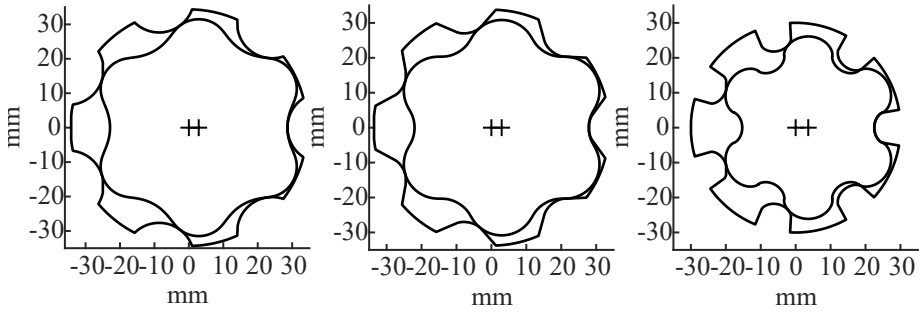

Figure 7.5. Best designs of each profile type according to weighting strategy. Left: Epitrochoid ($m = 7$, $\lambda_d = 0.262$, $\lambda_p = 0.517$). Center: Hypotrochoid ($m = 7$, $\lambda_d = 0.399$, $\lambda_p = 0.838$). Right: Cycloid ($m = 7$, $\lambda_d = 0.382$) [27]

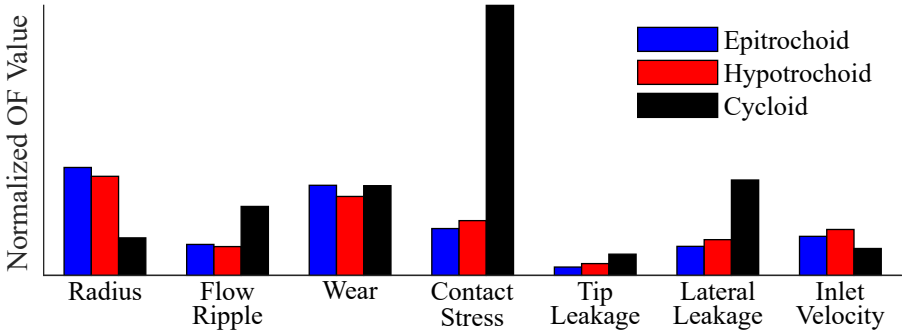

Figure 7.6. Bar chart showing best designs of each profile type according to a suggested weighting function [27]

A design can also be selected from the combined Pareto front by eliminating designs systematically by applying stricter constraints successively until just one design remains.

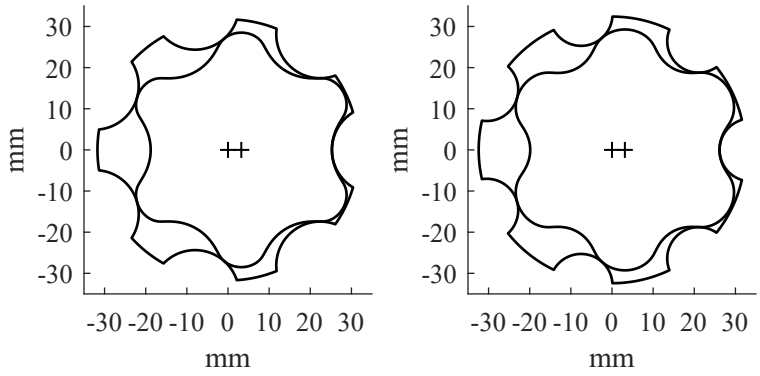

Figure 7.7. Left: Industry gerotor resembling designs selected from weighting strategy. Right: Epitrochoidal design selected using weighting strategy when the drive angle is constrained to 45°. [32]

A parallel coordinates chart can be used to visualize this process. In this type of chart, each design is represented by a series of line segments that connect the OF on the x-axis to its normalized value on the y-axis. The new constraint value can be plotted as a slider and can be adjusted heuristically. When a design has an OF value greater than any of the new constraint values the design is removed from the chart. Note that when many designs are plotted, the chart appears to look more like regions of color rather than distinct line segments. This method was applied to select three designs from the combined Pareto front with different design goals. The first design was selected to be ultra-compact, the second allows a moderate increase in size to give improved performance in other areas, and the third seeks for very good fluid dynamic and wear performance and allows a large size to accomplish this. The results of this process are shown in fig. 7.8.

In fig. 7.8 (top), an ultra-compact design was selected by eliminating all designs with a minimum allowable root radius greater than 28 mm for a 10 cc/rev pump with a 1 cm face width. Stricter constraints were then applied to the flow ripple, adhesive wear, and lateral gap leakage. After this was done, no hypotrochoidal designs remained. Of the remaining designs, the epitrochoidal profiles showed a significant performance advantage regarding wear and contact stress that comes at a cost of a small increase in flow ripple and lateral gap leakage. An epitrochoidal and a standard cycloidal design that were selected from this parallel coordinates chart are shown in fig. 7.9. The design selection process for a moderately

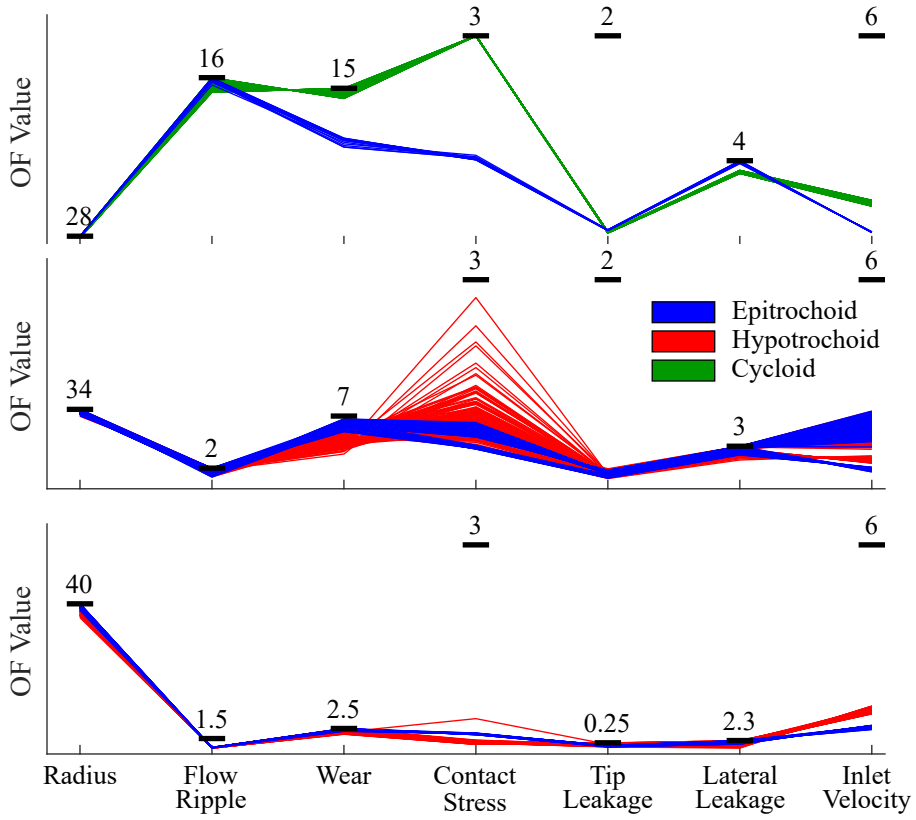

Figure 7.8. Top: Parallel coordinates chart selecting ultra compact designs. Middle: Parallel coordinates chart selecting moderately compact designs. Bottom: Parallel coordinates chart selecting designs primarily for fluid dynamic and wear performance

compact pump is shown in fig. 7.8 (middle) by first eliminated all the designs with a minimum allowable root radius greater than 34 mm. After stricter constraints were applied to the flow ripple, wear, and lateral gap leakage, all the standard cycloidal designs were eliminated without being penalized for their high contact stress. The epitrochoidal and hypotrochoidal designs that remained had similar performance with the epitrochoidal designs having a small advantage in contact stress and the hypotrochoidal designs having a slight advantage in wear. Two designs selected from this parallel coordinates chart are shown in fig. 7.10. Lastly, a design was selected that allowed a large size of a minimum allowable root radius of 40 mm to give improved performance in the other OF that is shown in fig. 7.8 (bottom). Once again, the standard cycloidal designs were eliminated without needing to penalized them for their contact stress. From the remaining designs, the epitrochoidal profiles have a small advantage

in inlet velocity, while the hypotrochoidal profiles have advantages in size and contact stress. Two designs selected from this parallel coordinates chart are shown in fig. 7.11. A summary of the performance of these designs is shown in fig. 7.12.

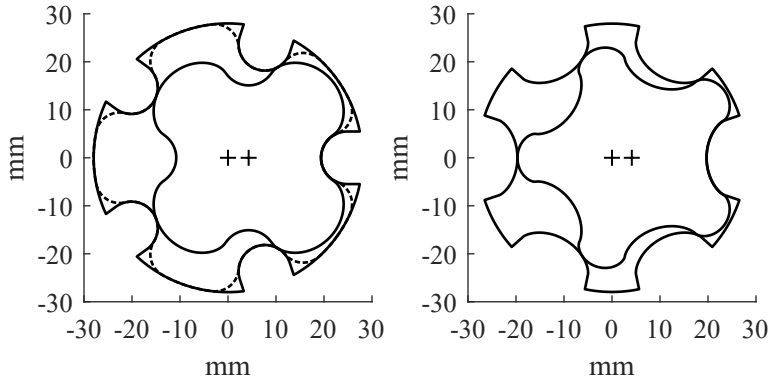

Figure 7.9. Designs selected using a parallel coordinates chart to be ultra compact. Left: Epitrochoidal design with $m = 5$, $\lambda_p = 0.865$, and $\lambda_d = 0.220$ (Possible fillets shown as dashed lines). Right: Cycloidal design with $m = 6$ and $\lambda_d = 0.612$ [27]

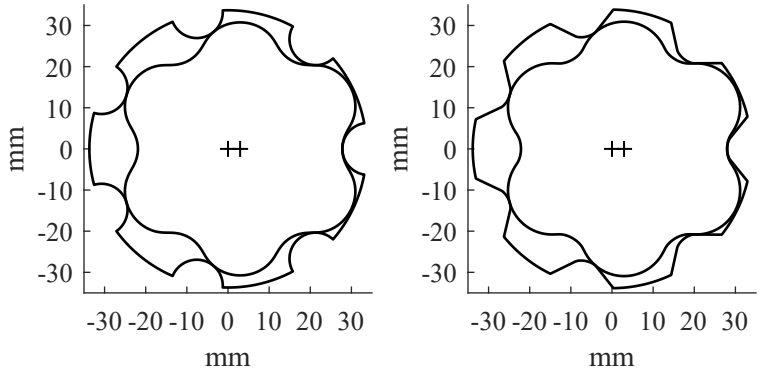

Figure 7.10. Designs selected using a parallel coordinates chart to be moderately compact. Left: Epitrochoidal design with $m = 7$, $\lambda_p = 0.605$, and $\lambda_d = 0.185$. Right: Hypotrochoidal design with $m = 7$, $\lambda_p = 0.865$, and $\lambda_d = 0.453$ [27]

Although none of the conventional profiles are objectively the best since they all have designs on the combined Pareto front, some more considerations can be made. First, the standard cycloidal designs can be eliminated for other performance criteria other than their contact stress, and when an ultra compact design was selected, the an epitrochoidal design

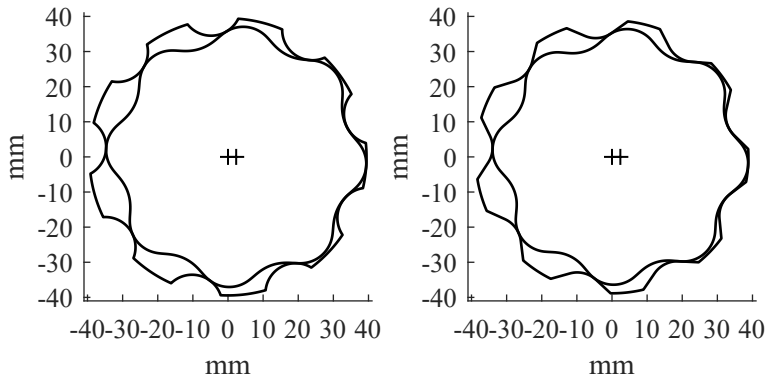

Figure 7.11. Designs selected using a parallel coordinates chart for improved fluid dynamic and wear performance. Left: Epitrochoidal design with $m = 9$, $\lambda_p = 0.484$, and $\lambda_d = 0.198$. Right: Hypotrochoidal design with $m = 9$, $\lambda_p = 0.696$, and $\lambda_d = 0.296$ [27]

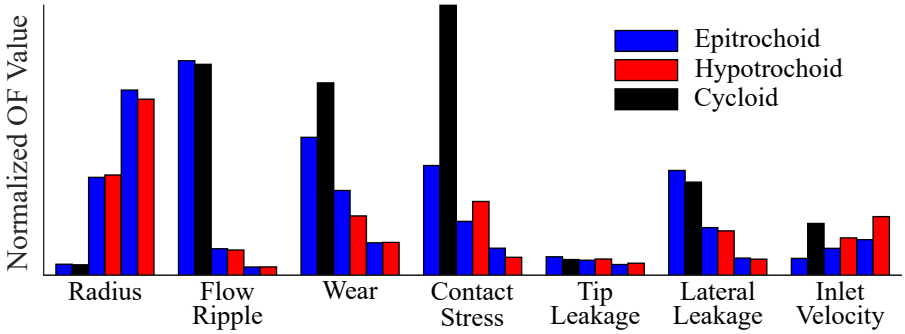

Figure 7.12. Bar chart showing selected designs from the parallel coordinates charts [27]

was identified that could match the size and flow ripple performance of the standard cycloidal profile and could do so with improved wear and contact stress performance. From this analysis, the epitrochoidal profile is quite versatile in finding optimal designs with differing performance goals. If a larger pump size is possible, the hypotrochoidal profile can give good fluid dynamic and wear performance in a slightly more compact package than the epitrochoidal profile.

7.2 Epitrochoidal, Elliptical, and Asymmetric Elliptical Profile Comparison

The epitrochoidal, elliptical, and asymmetric elliptical profile types are interesting in that each profile type progressively adds one input variable. Comparing these profiles can give

insight in how the tooth shape and rotation angle affect the the performance of gerotors. Because the entire design space of the elliptical profile is within the design space of the asymmetric profile, and the epitrochoidal is within both other profiles a brief note is required on how the preference is given in sorting the combined Pareto front. Preference is given to the simpler profile type such that if an epitrochoidal design is included more than once, it will only be counted among the epitrochoidal designs. The same is true for a symmetric elliptical design in the asymmetric Pareto front. When the three profile types were combined and a new Pareto front was found, 93% of the epitrochoidal, 98% of the elliptical, and only 27% of the asymmetric Pareto designs remained on the combined Pareto front. These results show that in general allowing for a modification to the tooth shape is helpful, but the asymmetry is not overwhelmingly beneficial.

A comparison between the profile types to give the best performance in a single area is made next. The Pareto designs are plotted in fig. 7.13 (left) to show the best designs between size and flow ripple. The elliptical designs are plotted in red first, followed by the epitrochoidal designs in blue, and lastly the asymmetric designs in black. This plot shows that two small regions exist where the elliptical and asymmetric profile can have improved performance in terms of size and flow ripple over the epitrochoidal profile. In fig. 7.16 (right) the elliptical designs are again plotted first, followed by the elliptical, and lastly the asymmetric. This plot shows that a region exists where the elliptical and asymmetric profiles can have reduced tooth tip leakage as compared to the epitrochoidal profile. Both plots show little advantage of the asymmetric over the elliptical profile in terms of finding pumps with the best performance regarding size and flow ripple and with leakage. The contact stress and wear values for designs on the combined Pareto front are shown in fig. 7.14 (left). This plot shows that the asymmetric profile can have improved performance in contact stress and wear over the two other profile types, and a pump selected from this region of the design space is shown in fig. 7.14 (right).

The asymmetric profile also still has some merit when selecting a design with a weighting strategy with the weights in table 7.1. When this is done, the asymmetric profile out-performs the epitrochoidal and elliptical profiles by 5%, and the performance of the epitrochoidal and

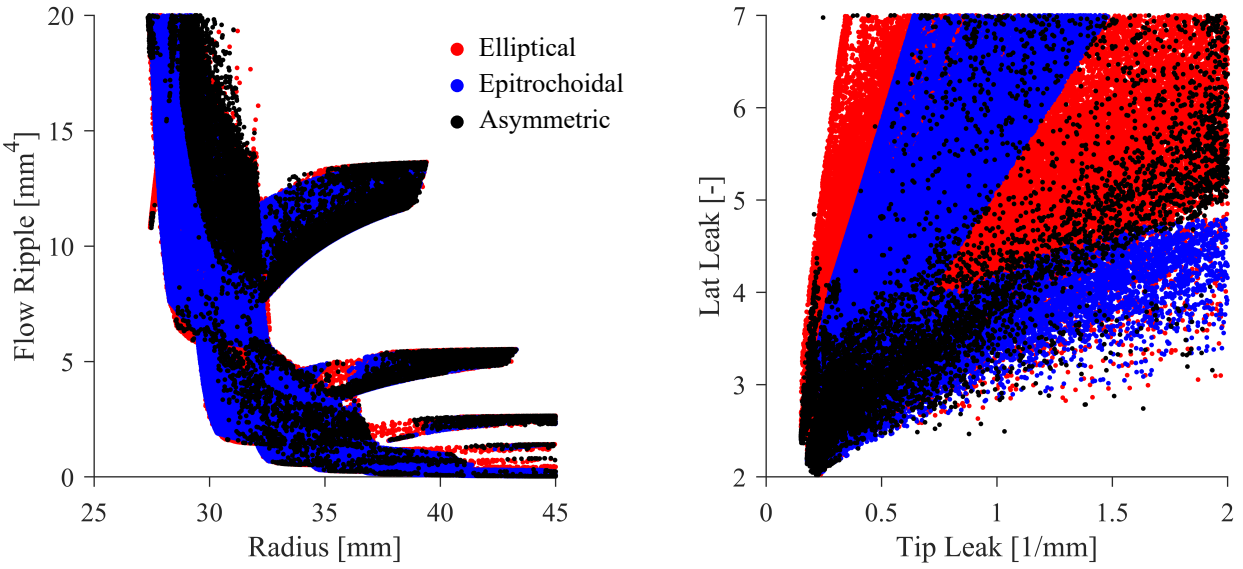

Figure 7.13. Plot of the OF values of designs on the combined Pareto front separated by profile type.

elliptical profiles are quite similar. The best designs according to this weighting strategy are shown in fig. 7.15, and a bar chart showing their relative performance is shown in fig. 7.16.

A few designs are then selected from the combined Pareto front using a parallel coordinates chart slider values as in the previous section. The parallel coordinates charts are plotted in fig. 7.17. For this particular set of maximum allowable OF values, the asymmetric elliptical profile was eliminated, and the epitrochoidal and elliptical profiles give similar performance in middle and bottom plots. However, in the top plot the elliptical profile can offer improved flow ripple and lateral gap leakage at a cost of increased wear, tooth tip leakage, and inlet throttling. Many of the elliptical designs have values of λ_t close to one, which would correspond to an epitrochoidal profile. Three elliptical designs were then selected from the designs in fig. 7.17 that are shown in fig. 7.18.

7.3 Comparison of All Profile Types

When the Pareto designs from all the profile types were combined and a new Pareto front was identified, 80% of the epitrochoidal, 61% of the hypotrochoidal, 48% of the standard cycloidal, 88% of the elliptical, 74% of the generalized cycloidal, 66% of the cosine, and

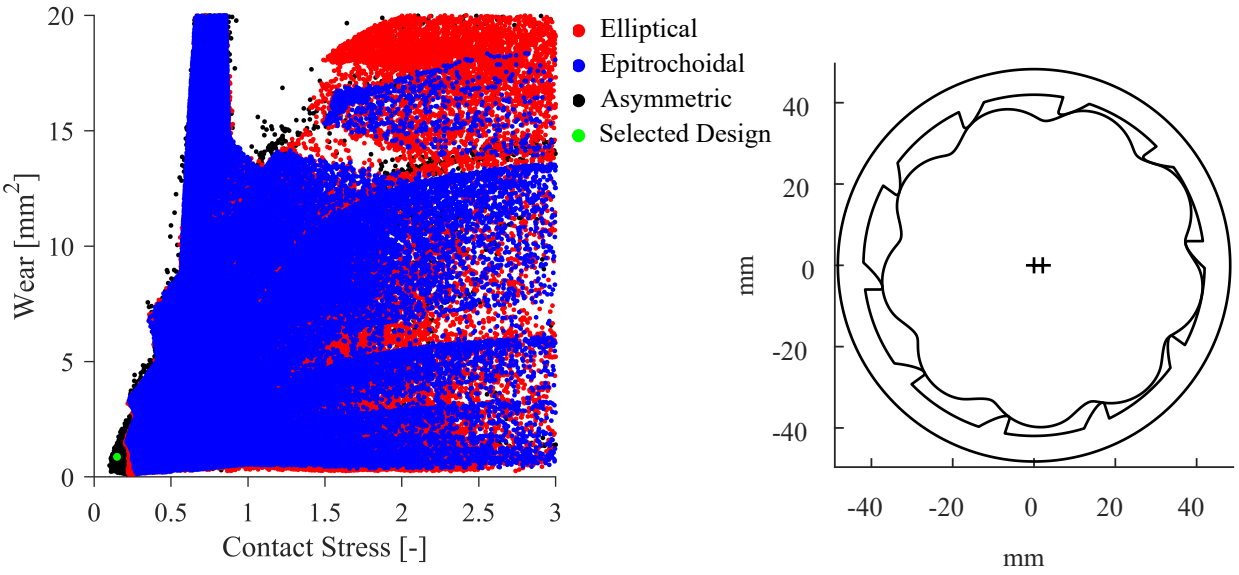

Figure 7.14. Left: Plot of the contact stress and wear values of designs on the combined Pareto front separated by profile type. Right: Selected asymmetric profile ($m = 10$, $\lambda_p = 0.486$, $\lambda_d = 0.201$, $\lambda_t = 0.222$, $\alpha = 40.256°$) with improved wear and contact stress than what is possible for the epitrochoidal and elliptical profiles

23% of the asymmetric designs remained on the combined Pareto front. Once again none of the profile types can be said to be universally better than the others, but since many designs are still eliminated in the process, the optimization process still proves to be quite useful. A plot of the size and flow ripple of all the designs on the combined Pareto front separated by profile type is shown in fig. 7.19. When looking at the designs with the best combinations of size and flow ripple, none of the profile types are a clear winner, although some small regions exist where one profile type can be slightly more compact than the others. In the places where the standard cycloidal profile has an even value of outer gear teeth, the generalized cycloidal profile can match its performance until it hits the contact stress constraint boundary. Hypotrochoidal profiles can also offer similar performance in that region. The contact stress and wear values of the combined Pareto front are plotted in fig. 7.20 with the profile types separated by color. For designs seeking the best combination of contact stress and wear within the constraint boundaries, the hypotrochoidal profile has a region with the best performance followed by the asymmetric profile. However, as shown

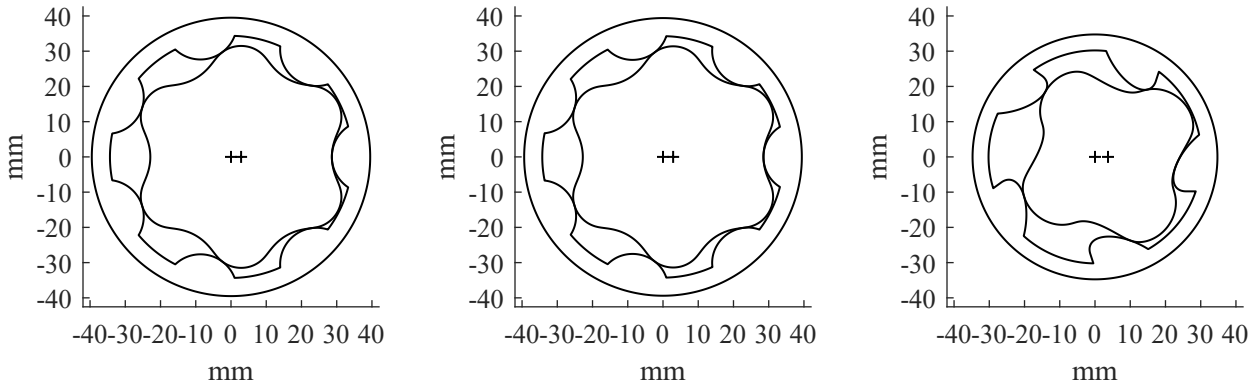

Figure 7.15. Best designs of epitrochoidal, elliptical, and asymmetric profiles according to weighting strategy. Left: Epitrochoid ($m = 7$, $\lambda_p = 0.514$, $\lambda_d = 0.266$). Center: Ellipse ($m = 7$, $\lambda_p = 0.534$, $\lambda_d = 0.245$, $\lambda_t = 1.061$). Right: Asymmetric ($m = 5$, $\lambda_p = 0.585$, $\lambda_d = 0.187$, $\lambda_t = 2.051$, $\alpha = 42.616°$)

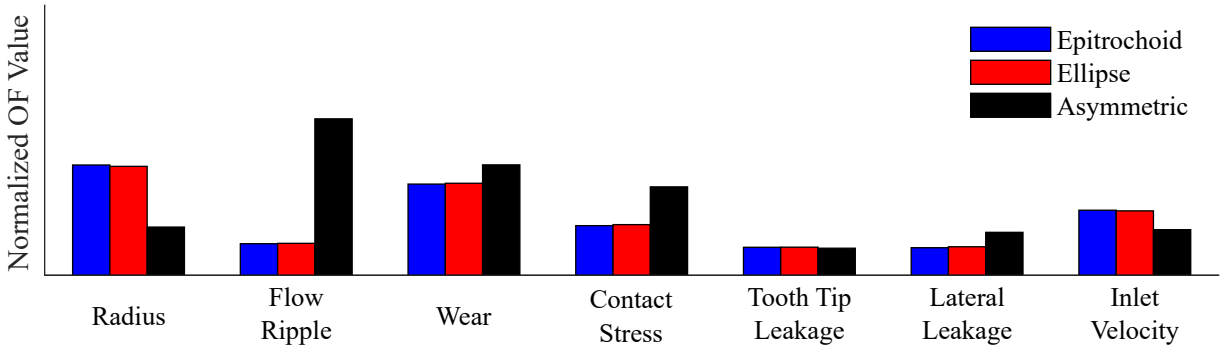

Figure 7.16. Bar chart showing selected designs selected using the weighting strategy

in figs. 6.22 and 6.36, the cost of selected designs from that region is an increased size. A plot of the tooth tip leakage and lateral gap leakage of the designs on the combined Pareto front is shown in fig. 7.21. The plot shows that none of the profiles have a clear advantage in producing designs with very low tooth tip and lateral gap leakage.

The weights given in table 7.1 were used to rank the designs on the combined Pareto front. When this was done, an asymmetric design was the winner that performed 2.5% better than the best hypotrochoidal design; 4.9% better than the best elliptical, epitrochoidal, and generalized cycloidal; 5.3% better than the best cosine, and 14.6% better than the standard cycloidal profile. The pumps selected with the weighting process are shown in fig. 7.22, and

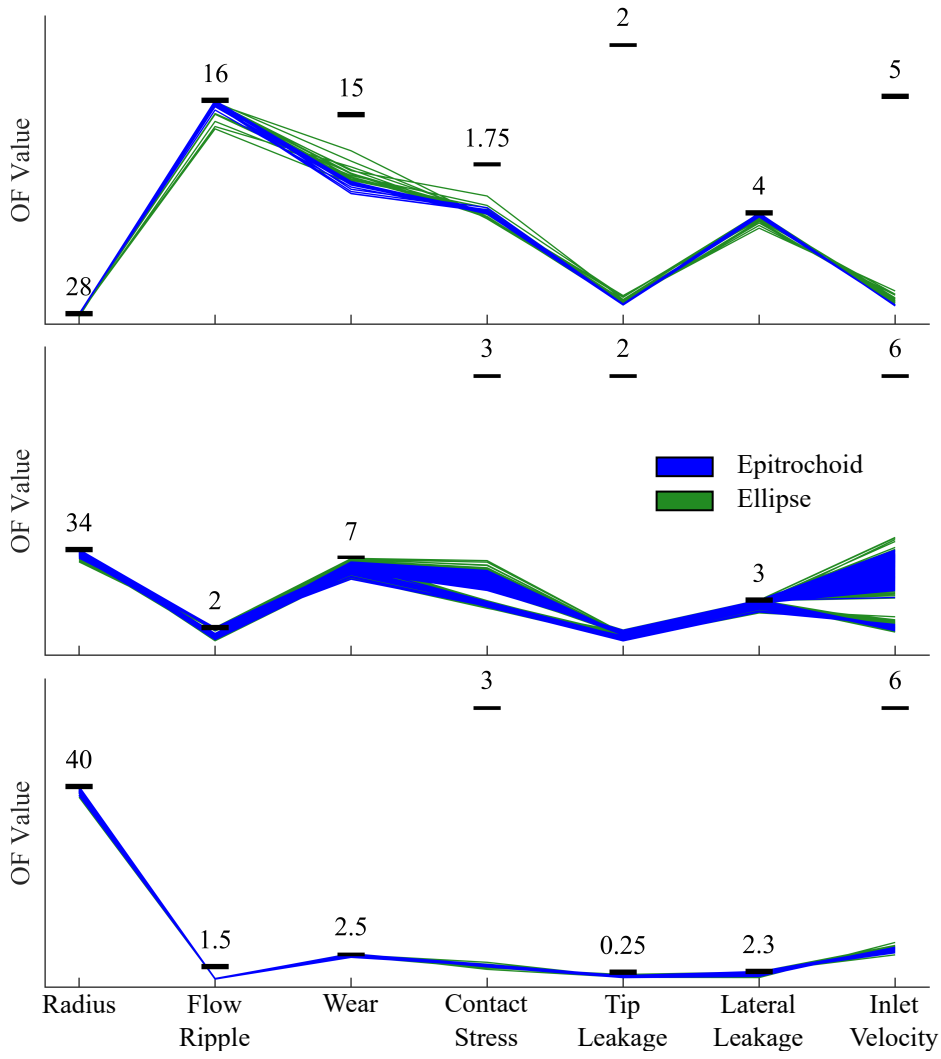

Figure 7.17. Top: Parallel coordinates chart selecting ultra compact designs. Middle: Parallel coordinates chart selecting moderately compact designs. Bottom: Parallel coordinates chart selecting designs primarily for fluid dynamic and wear performance

their design variables are given in table 7.2. Their relative performance is shown in the bar chart in fig. 7.23.

Designs with three different performance goals were then selected using a parallel coordinates chart. The goals were the same as for the other profile types: one to be very compact, one to be a moderately sized design with better fluid dynamic performance, and one to give very good fluid dynamic and wear performance at the cost of a larger size. These parallel coordinates charts are shown in fig. 7.24, the selected designs are shown in figs. 7.25–7.27,

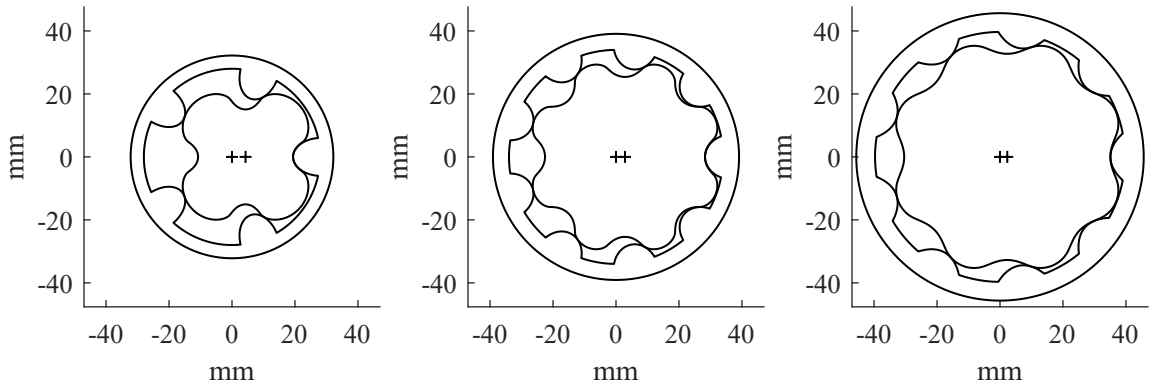

Figure 7.18. Selected elliptical designs using parallel coordinates chart. Left: $m = 5$, $\lambda_p = 0.759$, $\lambda_d = 0.316$, $\lambda_t = 0.676$ Center: $m = 9$, $\lambda_p = 0.700$, $\lambda_d = 0.231$, $\lambda_t = 0.838$. Right: $m = 9$, $\lambda_p = 0.241$, $\lambda_d = 0.594$, $\lambda_t = 0.379$

Table 7.2. Input variables defining the selected design of each profile type using a weighting strategy

Profile	m	λ_p	λ_e	λ_d	λ_t	λ_r	α [deg]
Asymmetric	5	0.5852		0.1875	2.0511		42.616
Hypotrochoid	7	0.8383		0.3986			
Ellipse	7	0.5487		0.2242	1.1149		
Epitrochoid	7	0.5169		0.2623			
Gen. Cycloid	7		0.7718	0.0583		0.2793	
Cosine	7	0.3413		0.5021	0.9176		
Std. Cycloid	7			0.3815			

and the relative performance of the designs is shown in the bar charts in figs. 7.28–7.30. In selecting designs from each performance area, both the standard cycloidal and asymmetric profile were eliminated entirely.

7.4 Discussion

When the combined Pareto fronts are plotted on top of each other, the patterns of the relationships between the objective function values are also quite similar. Additionally, when selecting a design from the combined Pareto front using either the weighting strategy or a

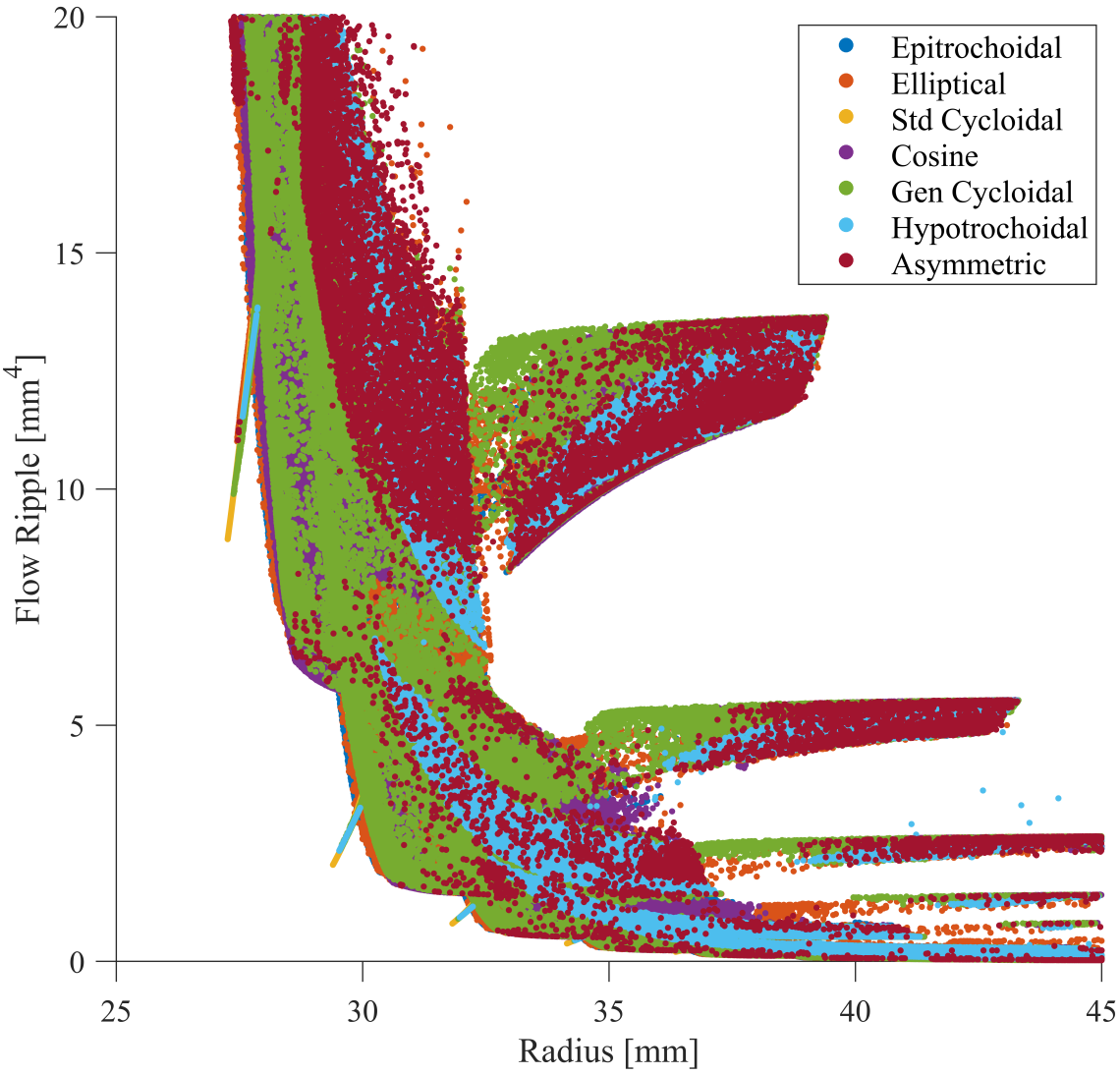

Figure 7.19. Plot of the Size and flow ripple values of designs on the combined Pareto front separated by profile type.

parallel coordinates chart, in many cases the selected designs look quite similar independent of the profile type. One way to explain this behavior is that the optimization algorithm finds designs with an outer gear tooth curve of a specific shape for a certain region of the Pareto front, and the parameters of different parent curves can be adjusted to yield approximately the same shape. Some differences in performance between the designs of differing profile types still exist, and epitrochoidal, hypotrochoidal, elliptical, and generalized cycloidal gerotors are preferred over the standard cycloidal, cosine, and asymmetric gerotors. Using several curve

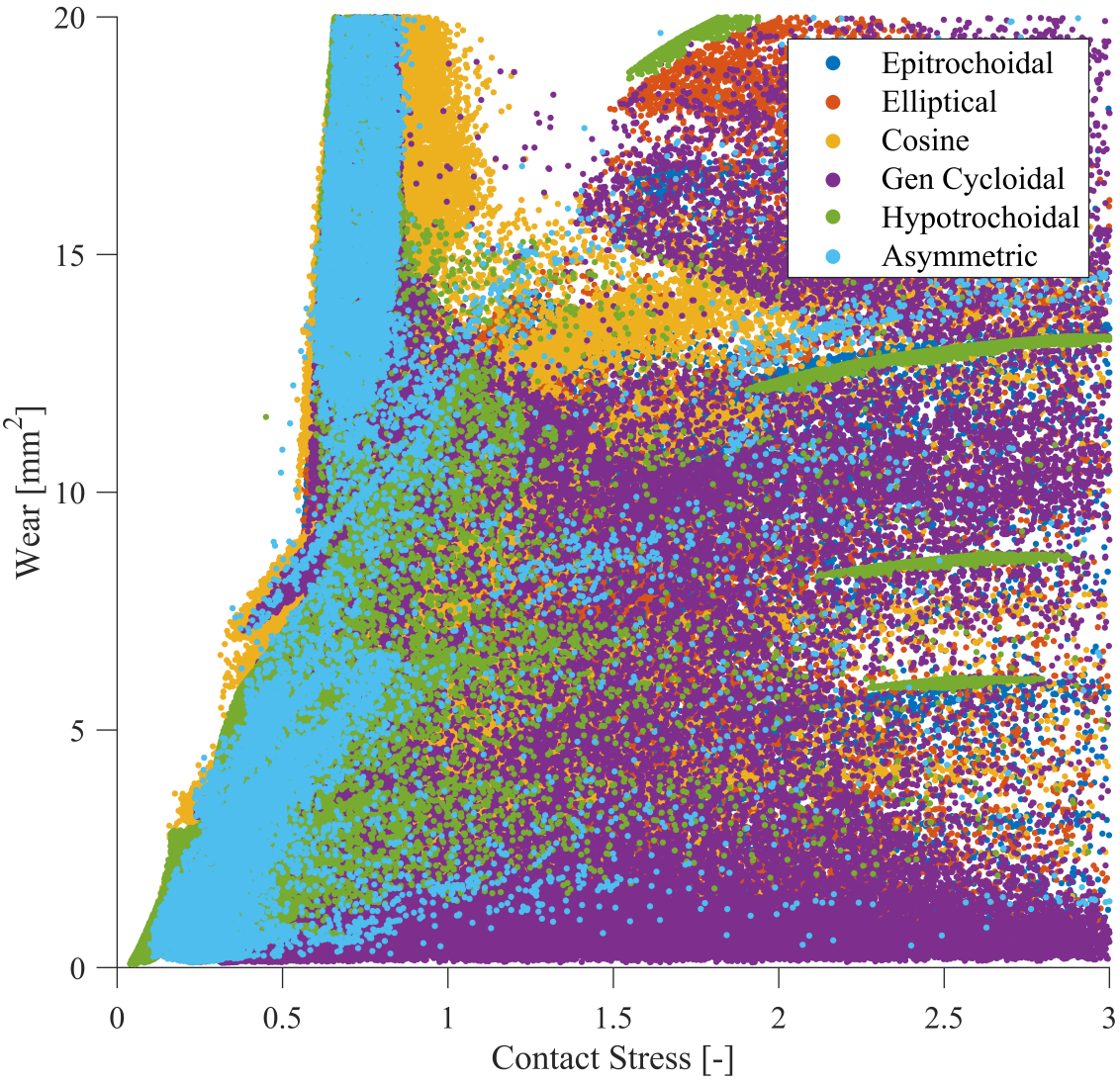

Figure 7.20. Plot of the contact stress and wear values of designs on the combined Pareto front separated by profile type.

types is still helpful though, as many designs are eliminated when combining the Pareto fronts. Using an optimization strategy to identify the optimal design space and a decision making strategy to select design from the desired position on the Pareto front seems to be generally more important than starting with the best type of curve to define the gearset.

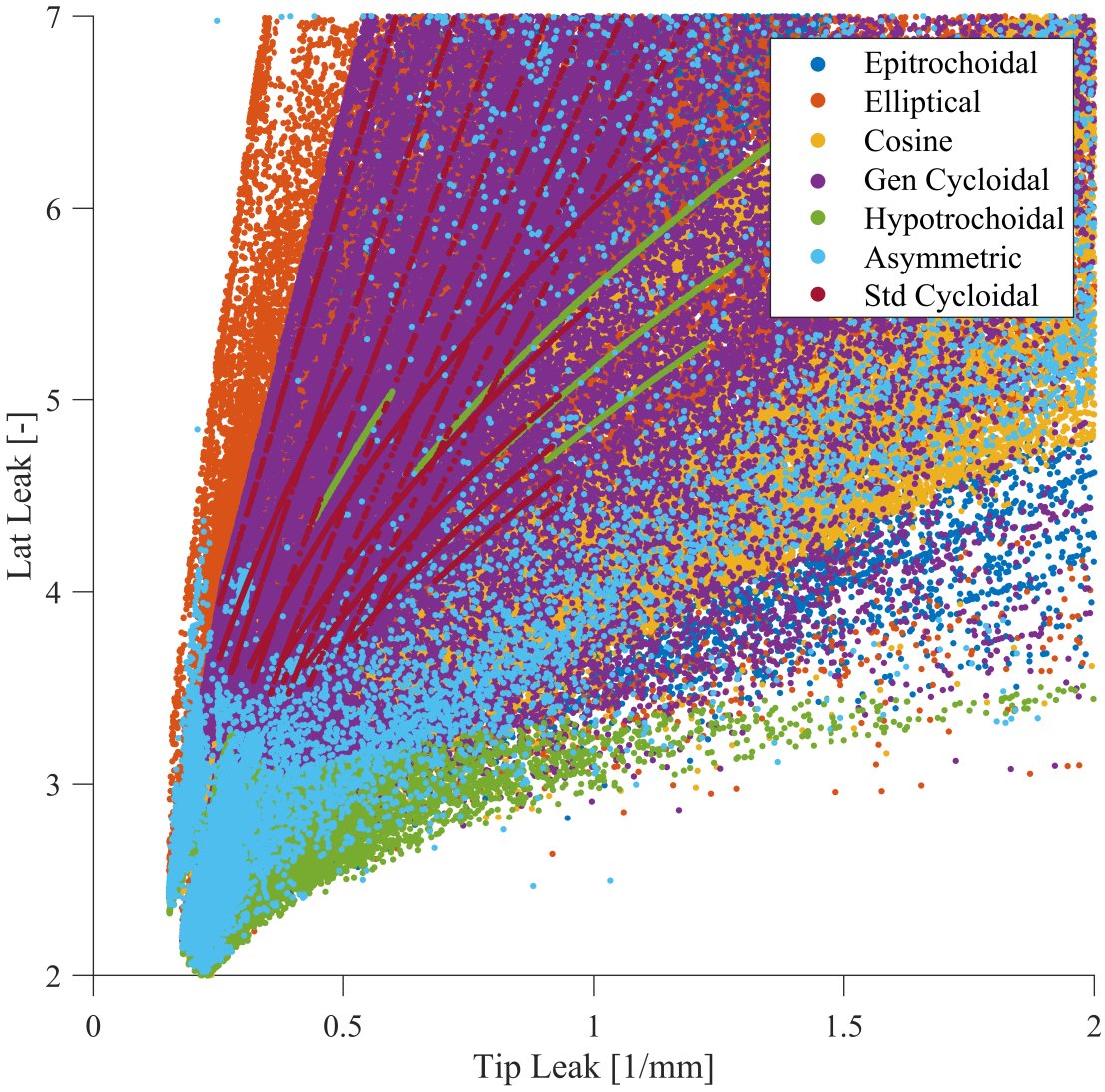

Figure 7.21. Plot of the tooth tip and lateral gap leakage values of designs on the combined Pareto front separated by profile type.

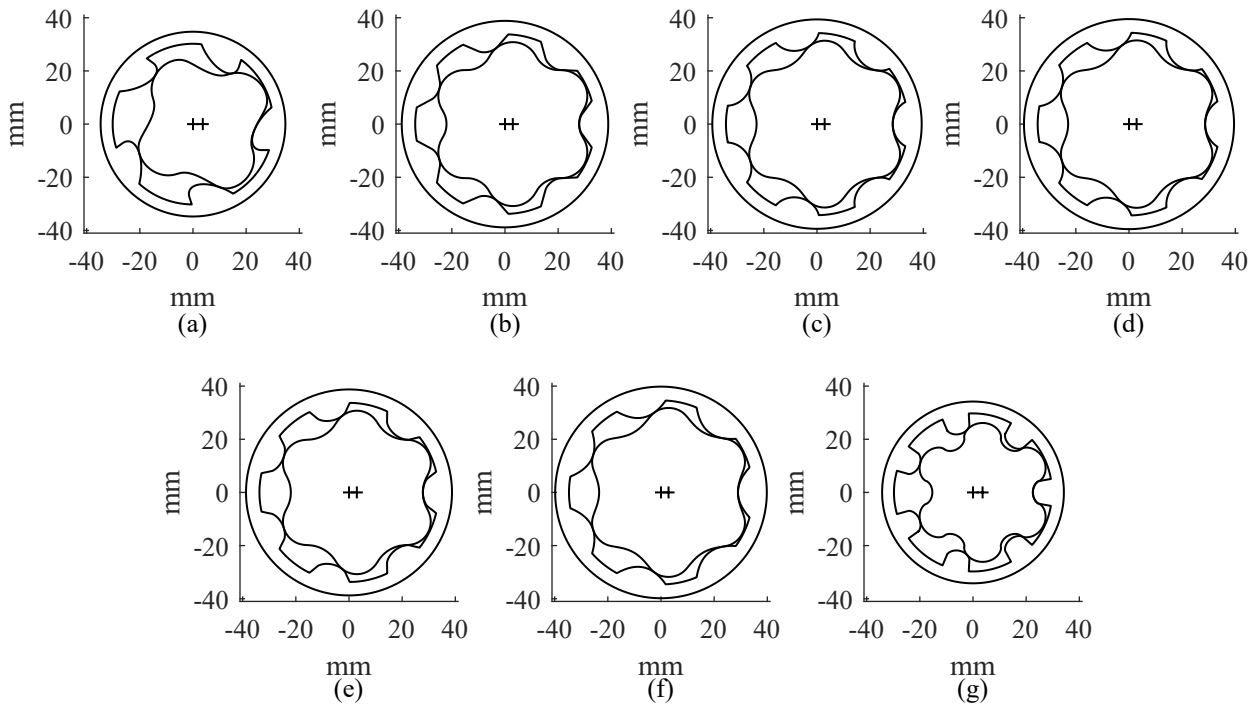

Figure 7.22. Designs selected using weighting strategy. a) asymmetric b) hypotrochoidal c) elliptical d) epitrochoidal e) generalized cycloidal f) cosine g) standard cycloidal

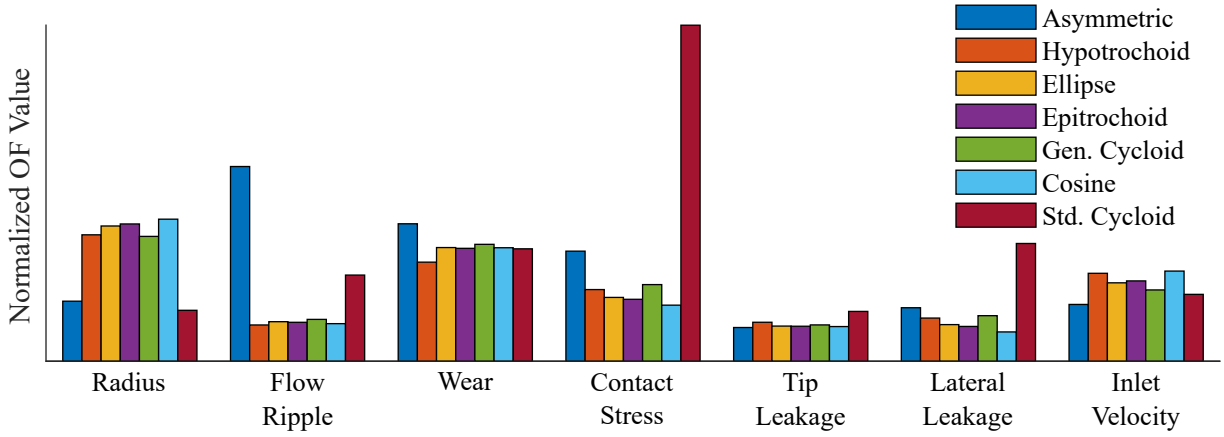

Figure 7.23. Relative performance of optimal designs selected using a weighted strategy

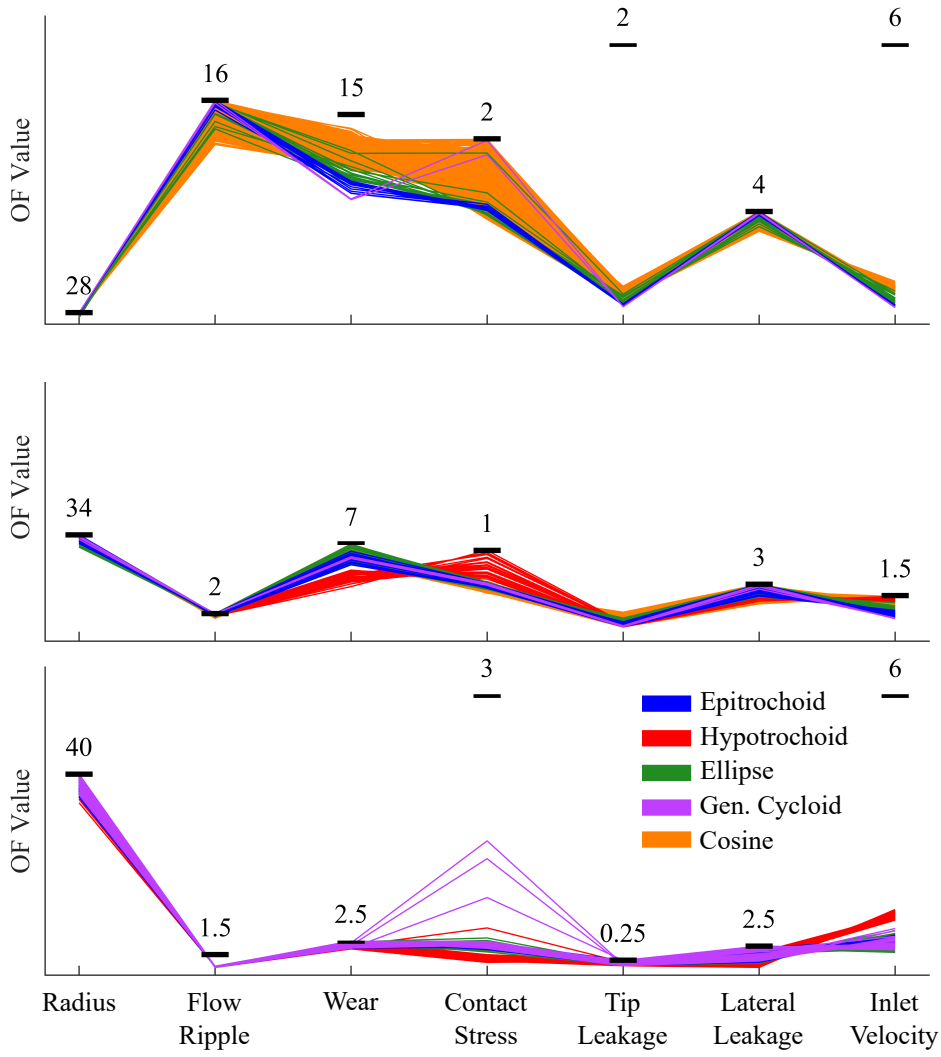

Figure 7.24. Parallel coordinates chart used to select designs from the combined Pareto front of all the profile types. Top: Parallel coordinates chart selecting ultra compact designs. Middle: Parallel coordinates chart selecting moderately compact designs. Bottom: Parallel coordinates chart selecting designs primarily for fluid dynamic and wear performance

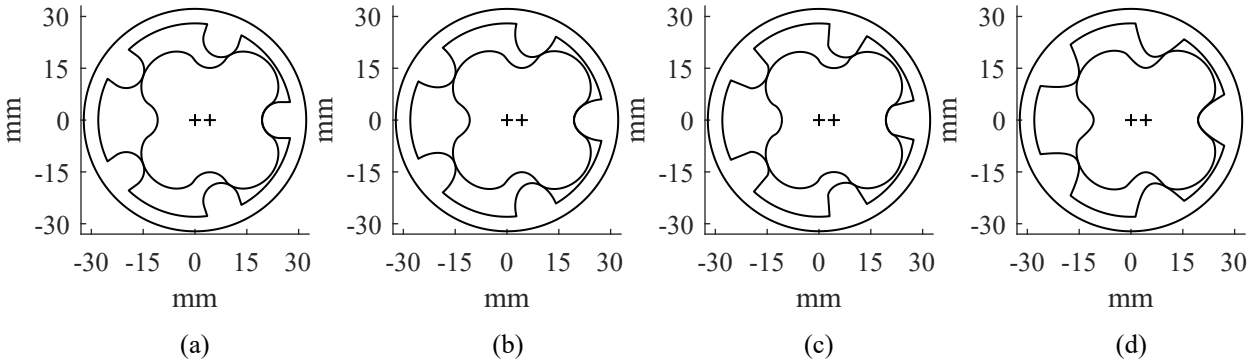

Figure 7.25. Gearsets selected from the top parallel coordinates chart in fig. 7.24. a) epitrochoidal with $m = 5$, $\lambda_p = 0.8735$, $\lambda_d = 0.2122$. b) elliptical with $m = 5$, $\lambda_p = 0.7592$, $\lambda_d = 0.3162$, $\lambda_t = 0.6762$. c) generalized cycloidal with $m = 5$, $\lambda_e = 0.9813$, $\lambda_d = 0.0618$, $\lambda_r = 0.8043$. d) cosine with $m = 5$, $\lambda_p = 0.7463$, $\lambda_d = 0.3264$, $\lambda_t = 0.9001$

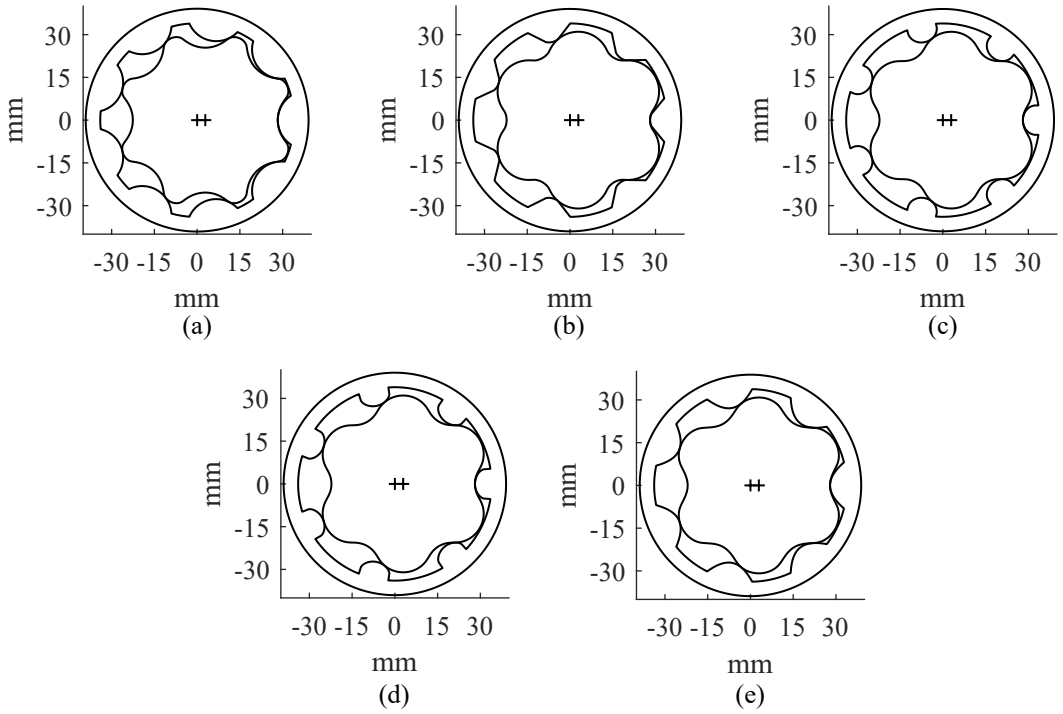

Figure 7.26. Gearsets selected from the middle parallel coordinates chart in fig. 7.24. a) epitrochoidal with $m = 9$, $\lambda_p = 0.6666$, $\lambda_d = 0.2670$. b) hypotrochoidal with $m = 7$, $\lambda_p = 0.8747$, $\lambda_d = 0.4689$ c) elliptical with $m = 7$, $\lambda_p = 0.6273$, $\lambda_d = 0.1394$, $\lambda_t = 1.1379$. d) generalized cycloidal with $m = 7$, $\lambda_e = 0.6492$, $\lambda_d = 0.0523$, $\lambda_r = 2.296$.

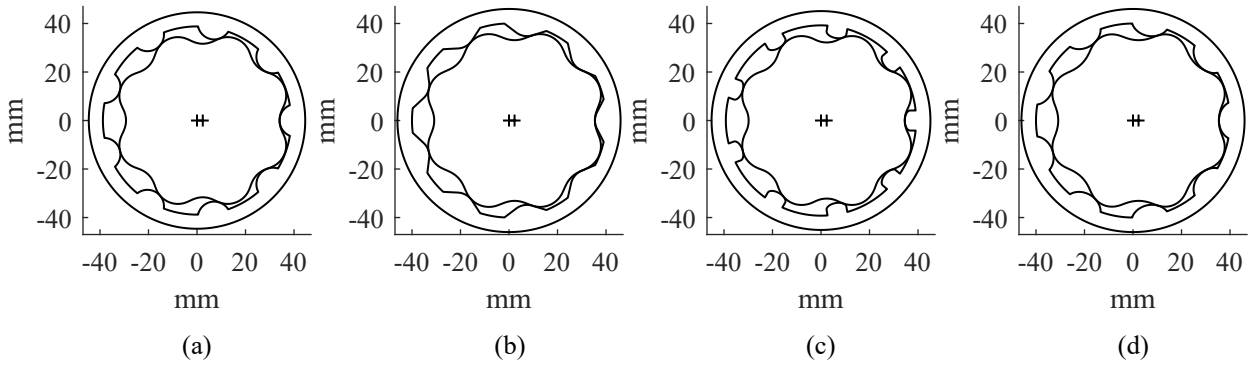

Figure 7.27. Gearsets selected from the bottom parallel coordinates chart in fig. 7.24. a) epitrochoidal with $m = 9$, $\lambda_p = 0.5249$, $\lambda_d = 0.1671$. b) hypotrochoidal with $m = 9$, $\lambda_p = 0.6655$, $\lambda_d = 0.3284$ c) elliptical with $m = 9$, $\lambda_p = 0.5751$, $\lambda_d = 0.0605$, $\lambda_t = 1.8680$. d) generalized cycloidal with $m = 9$, $\lambda_e = 0.5114$, $\lambda_d = 0.05948$, $\lambda_r = 4.9750$.

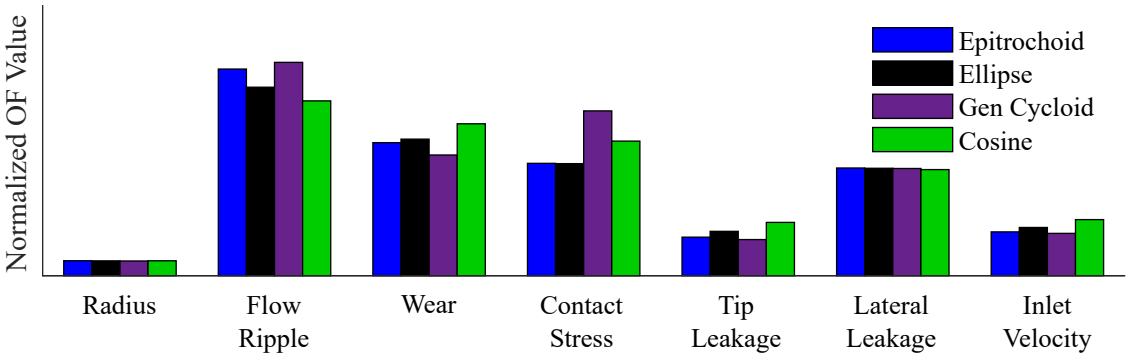

Figure 7.28. Bar chart showing relative performance of designs shown in fig. 7.25

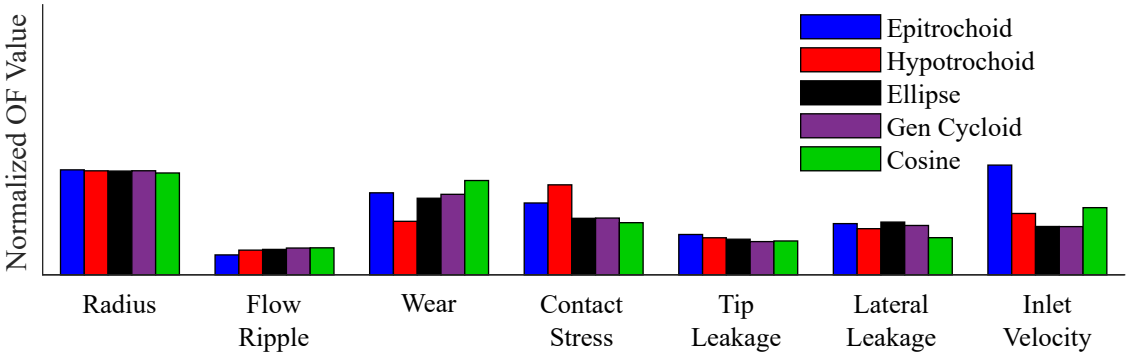

Figure 7.29. Bar chart showing relative performance of designs shown in fig. 7.26

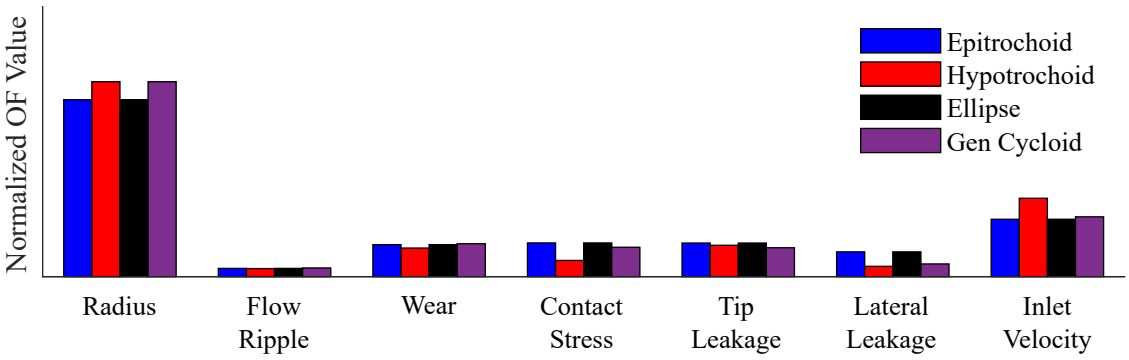

Figure 7.30. Bar chart showing relative performance of designs shown in fig. 7.25

8. VALIDATION

Validation of using the proposed optimization strategy to design gerotor gear geometry relies primarily on validating that the objective functions are the correct functions to minimize to improve the pump performance in a specific area. To that end, using the kinematic flow ripple is validated in simulation in appendix A, the tooth tip leakage by simulation in section 4.5, and the lateral gap leakage by simulation in section 4.6. The design approach is further validated in this chapter by showing the performance of gearsets used in industry and possible performance improvements that can be made from the optimization data. Next an industry research sponsor sought improvement in the gearset of an existing standard cycloidal gerotor pump. As a means to validate the design procedure outlined in this work experimentally, a generalized cycloidal gerotor design was selected to match the fluid dynamic performance of the reference design with significantly reduced contact stress. A second design was also selected to reduce the kinematic flow ripple of the reference design while still fitting within the existing journal bearing housing. Both the alternative gearsets were manufactured and tested. The contact stress between the reference and optimized designs is compared using finite element analysis, and the experimental pressure ripples of the optimized designs are compared. This further analysis will validate the contact stress objective function, using the generalized cycloidal profile, and the process of selecting a design from the Pareto front found in the optimization.

8.1 Comparison with Industry Designs

Several gerotor gear profiles used in industry are used as a baseline for validating the optimization approach. The dimensions of the gears were either supplied by the manufacturer or reverse engineered from commercial units. The exact dimensions are not given for confidentiality, but each of the profiles are shown in fig. 8.1 after scaling them to the same 10 cc/rev with a 1 cm face width as the optimized designs. Each of the designs are epitrochoidal except for design H which is a standard cycloidal. The relative performance of each design is shown in the bar chart in fig. 8.2 where the OF are normalized so the best encountered value in the optimization has a value of zero and a value of one corresponds to the constraint

boundary in table 5.1. Industry designs B and F were on the combined Pareto front, so no objective improvement could be made, but each of the other designs can be improved upon significantly by the results of this work. For each design a parallel coordinates chart is made with the limits set to the performance of the industry design in fig. 8.3. A design was selected to give the most improvement in a single OF for each industry design, and possible performance benefit is shown in fig. 8.4. Although the alternative designs were selected for the maximum improvement in a single OF, the performance in other areas is also improved. Seeking maximum improvement in two or more OF would reduce the possible benefit for any single OF, but fig. 8.4 gives a way to quantify performance benefit. The alternative designs are shown in fig. 8.5. The gerotor design methodology presented in this work has clear practical benefit for improving the performance of state-of-the-art units.

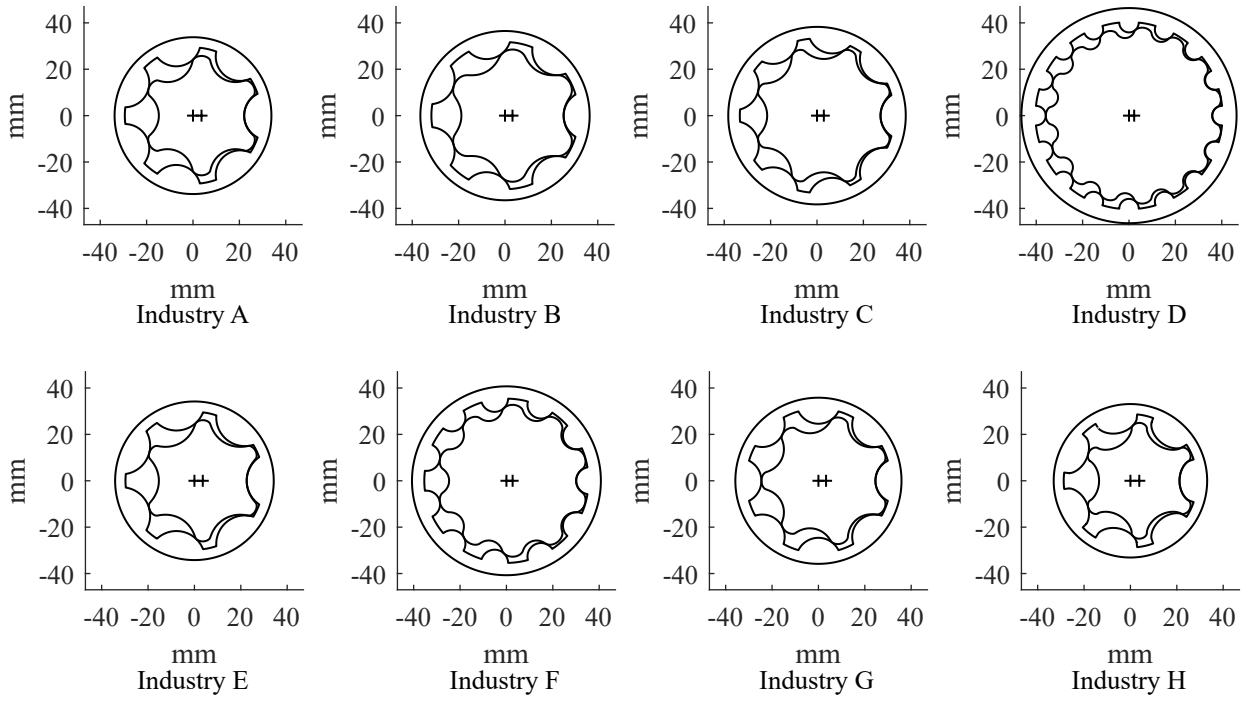

Figure 8.1. Gerotor profiles used in industry

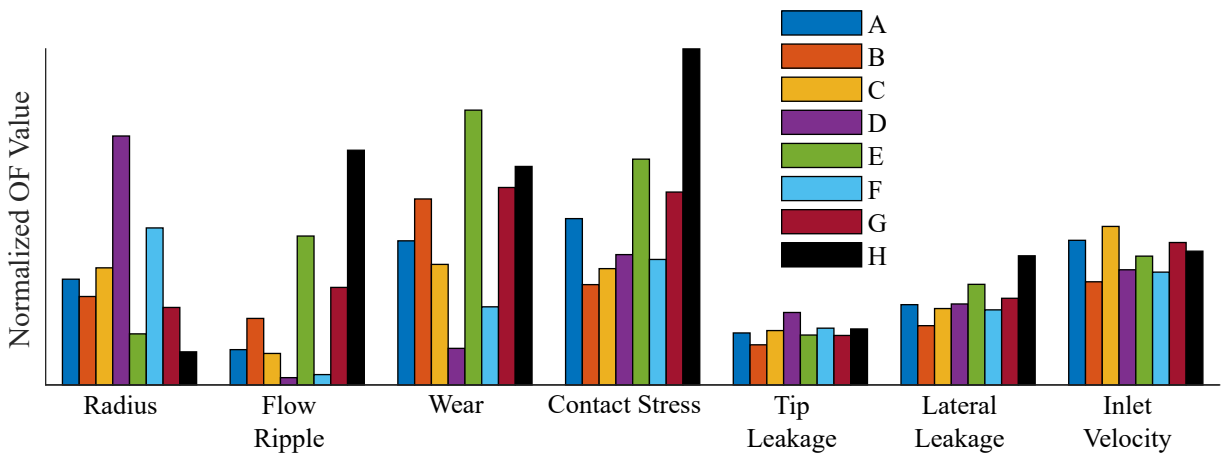

Figure 8.2. Relative performance of gerotor profiles used in industry

8.2 Case Study

A case study is presented next to demonstrate the use of multi-objective optimization to improve gerotor gear design in simulation and experiment. An industry research sponsor had a cycloidal gear profile with $m = 9$ that was experiencing both pitting and scoring, and they requested to see if an optimized profile could improve the performance of the gearset. Two designs were selected from the generalized cycloidal Pareto front as alternative designs. The generalized cycloidal profile was used instead of another profile type to validate that it can be manufactured and that it functions in operation, as the profile type is new to this work.

The first design was selected to match the performance of the reference design while significantly improving OF4 (contact stress). The second design allowed an increase in size as long as the gearset could still fit within the existing pump housing with the goal of primarily reducing the flow ripple. The industry reference pump and the two selected designs are shown in fig. 8.6. Note that the pumps are scaled from the displacement of reference pump to the 10 cm^3/rev displacement with a 1 cm face width as all the other pumps in this work to compare the results with the other designs in this work and for confidentiality. The nondimensional parameters of the pumps are also not published for confidentiality. A conjugate root profile was selected for the first alternative design so the pumps would have

the same constraints for micro-motions in operation and so that the ports could be the same. In this sense the first alternative gearset can be a direct replacement for the reference case that significantly reduces the contact stress. A comparison of the relative performance of the reference design and the prototype designs on the basis of their OF is shown in fig. 8.7. Photos of the reference and optimized gearsets are shown in figs. 8.8–8.10.

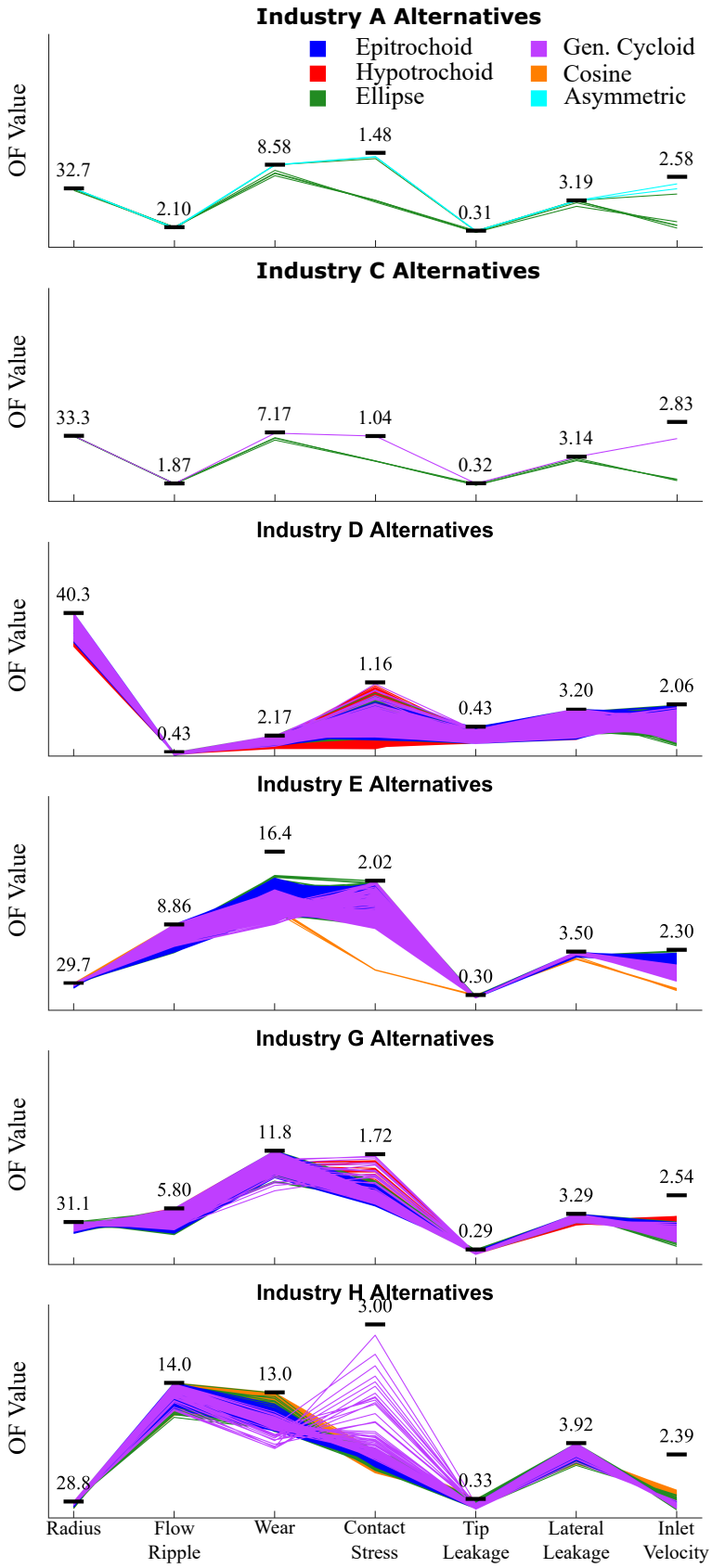

Figure 8.3. Parallel coordinates charts with limits set to industry pump performance

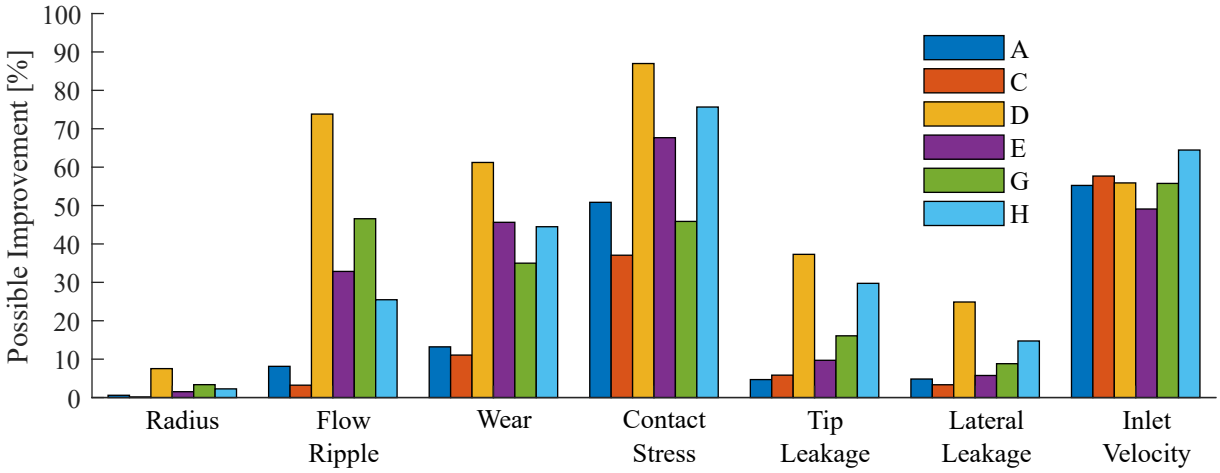

Figure 8.4. Performance improvement of designs selected to give the maximum possible improvement in a single OF

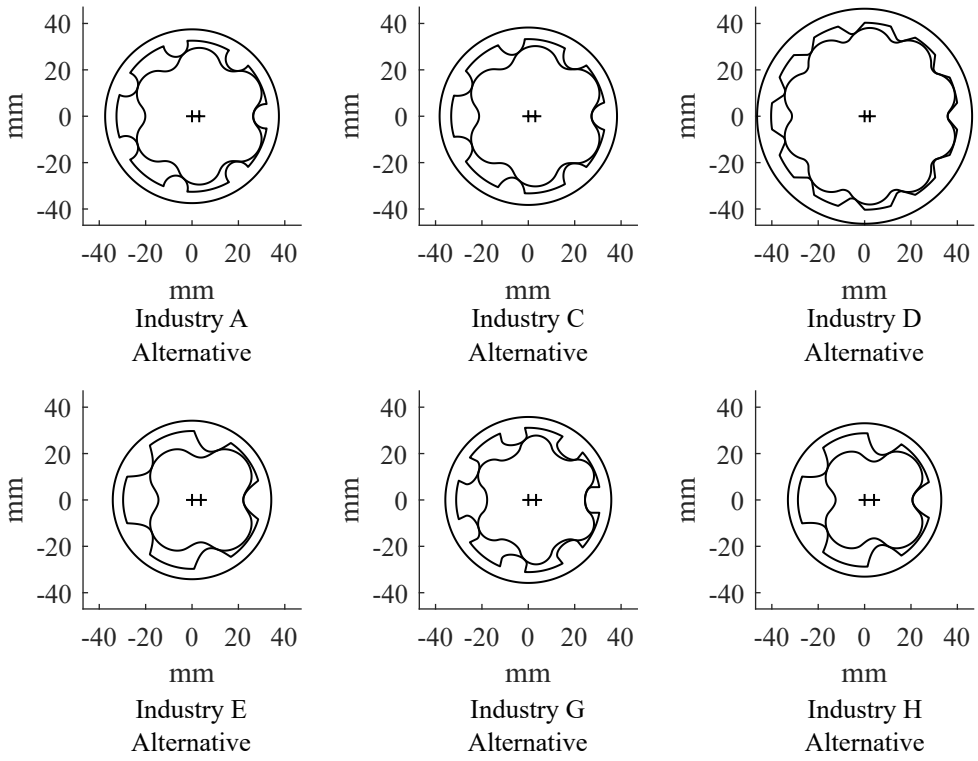

Figure 8.5. Alternative industry designs selected for maximum improvement in a single OF

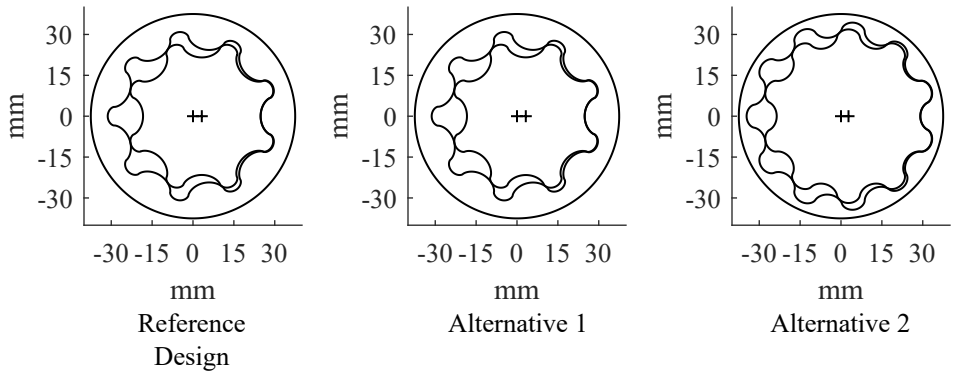

Figure 8.6. Industry reference pump and alternative designs

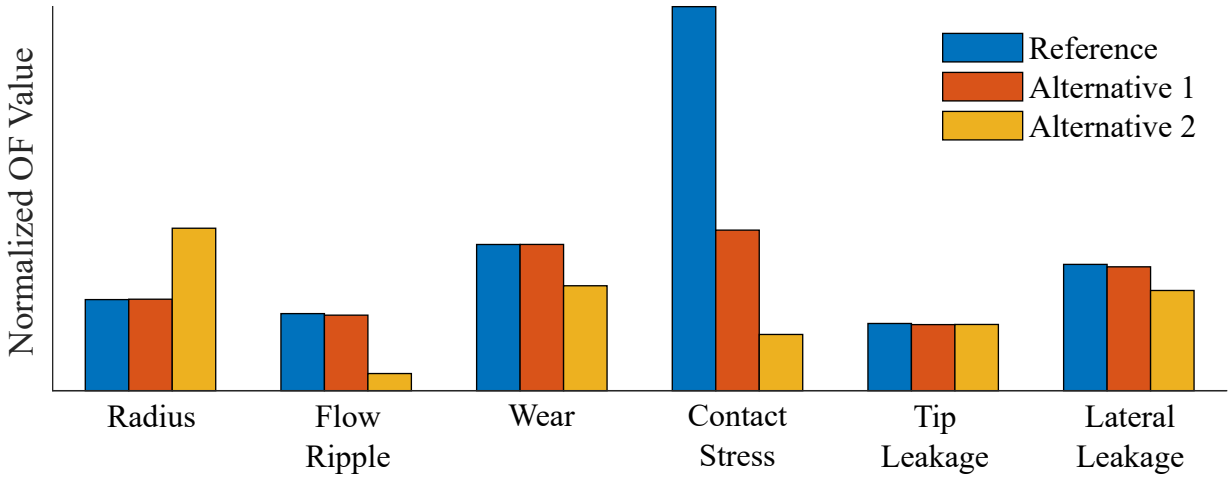

Figure 8.7. Performance comparison of industry reference pump and alternative designs

Figure 8.8. Photos of the reference gears in assembled and disassembled positions

Figure 8.9. Photos of the first set of optimized gears in assembled and disassembled positions

Figure 8.10. Photos of the second set of optimized gears in assembled and disassembled positions

The main advantage of alternative design 1 over the reference profile is that it has significantly reduced contact stress. Plots of the components of OF4 for both designs are shown in fig. 8.11, and the equation for OF4 is given in eq. (8.7) for reference. However, as was discussed in section 4.4, Hertzian contact might not be applicable to the standard cycloidal profile where the cycloids meet, as the curvature approaches positive infinity from one direction and negative infinity at the other where the cycloids meet. When contact occurs at the points where the cycloids meet, the value of OF4 approaches infinity as well. For this reason, a more detailed analysis is required to determine the applicability of using Hertzian contact theory to evaluate the contact stress of the standard cycloidal profile in comparison to the alternative design. To do this, finite element simulations were performed to compare the simulated contact stress with Hertzian theory for both gear profiles that include clearances. Both gearsets were scaled to the reference design displacement of 3.3 cm^3/rev and were rotated to the position with the peak value of OF4. The outer gear including the clearance was then rotated clockwise until it made contact with the inner gear. This is illustrated in figs. 8.12 and 8.13. Note that for the reference design the gearset was rotated by approximately one degree past the point of peak contact stress predicted by OF4 to ensure contact occurred where both gears have a convex shape. The gear profiles and their curvatures at the contact point were then extracted and rotated so that the normal to the profiles at the contact point was vertical. They were then imported into ANSYS to simulate the contact stress for the frictionless elastic plane strain case with a modulus of elasticity of 200 GPa and Poisson's ratio of 0.3. A pressure was applied to the top surface to correspond to the contact force corresponding to an outlet pressure of 50 bar.

The mesh of the contact region for the profiles is shown in figs. 8.14 and 8.15, and contours of the normal and shear stresses for both cases are shown in figs. 8.16–8.19. Typically more elements are required for good results, but the relatively low contact pressures in comparison to other machine elements likely gave improved stability with fewer elements. The alternative design showed significant improvement over the reference design, which further validates the contact stress objective function in this work. Additionally, a comparison between the simulated and Hertzian contact stresses along the line x=0 for both cases are shown in figs. 8.20 and 8.21. The Hertzian equations equations given as follows from a textbook

[49]. The contact half width is given by a in eq. (8.1), where R is the combined radius of curvature, ν is Poisson's ratio, E is the modulus of elasticity, and the subscripts refer to the two contacting surfaces. The peak contact pressure is then given as p_0 in eq. (8.2), where F is the contact force per unit length. The normal stresses are then given as a function of distance from the contact point in eqs. (8.3)–(8.5). The maximum in plane shear stress is then $\tau_{xy,\max}$ given in eq. (8.6) from Mohr's circle. The simulation and Hertzian stresses agree well, which serves as a further validation for OF4 as a design metric.

$$a = \sqrt{\frac{4RF}{\pi}\left(\frac{1-\nu_1^2}{E_1} + \frac{1-\nu_2^2}{E_2}\right)} \tag{8.1}$$

$$p_0 = \frac{2F}{\pi a} \tag{8.2}$$

$$\sigma_x = -p_0\left[\left(2 - \frac{1}{1+\left(\frac{y}{a}\right)^2}\right)\sqrt{1+\left(\frac{y}{a}\right)^2} - \frac{2y}{a}\right] \tag{8.3}$$

$$\sigma_y = \frac{-p_0}{\sqrt{1+\left(\frac{y}{a}\right)^2}} \tag{8.4}$$

$$\sigma_z = -2\nu p_0\left(\sqrt{1+\left(\frac{y}{a}\right)^2} - \frac{y}{a}\right) \tag{8.5}$$

$$\tau_{xy,\max} = \frac{\sigma_x - \sigma_y}{2} \tag{8.6}$$

$$\overline{p_0} = p_0\sqrt{\frac{\pi}{E^*\Delta p}} = \sqrt{\overline{F}\,|\kappa_i + \kappa_o|} \tag{8.7}$$

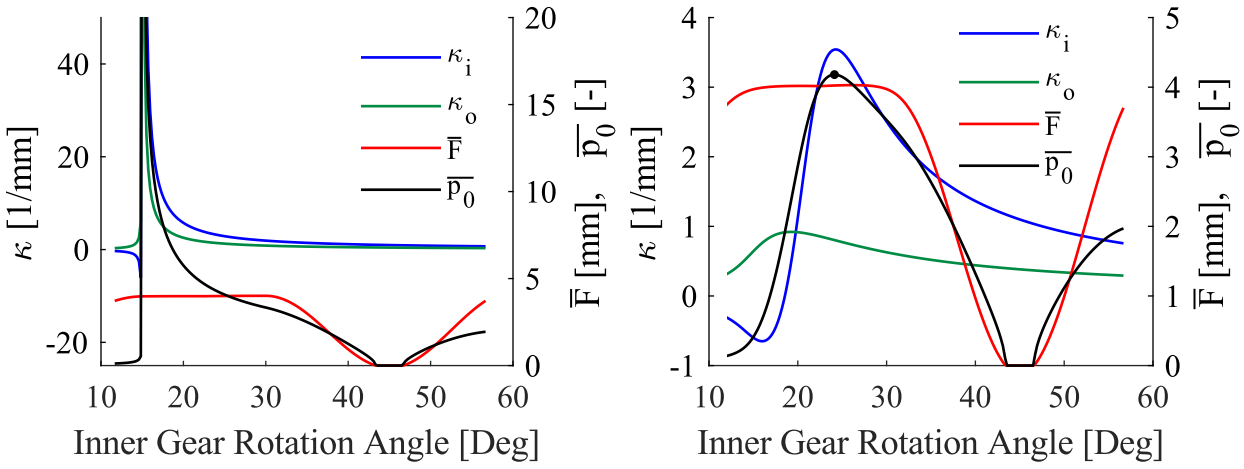

Figure 8.11. Comparison of components of OF4 for the reference design (left) and first alternative design (right).

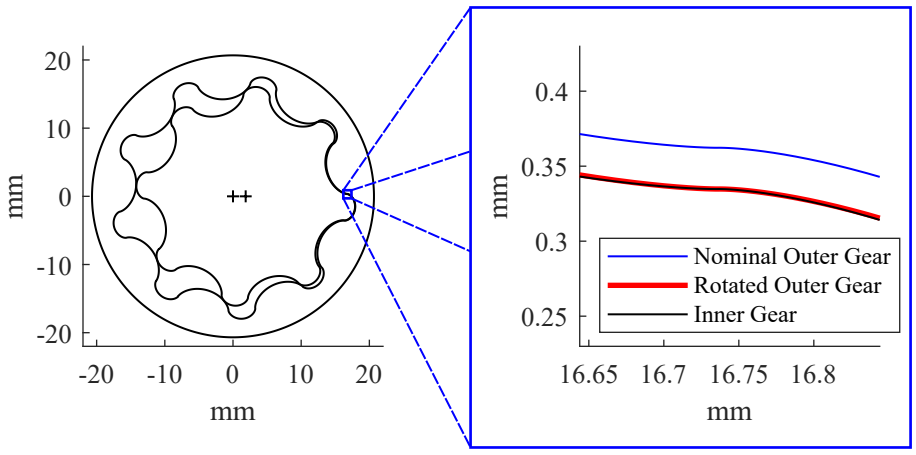

Figure 8.12. Reference design shown at the rotation angle with the maximum value of OF4

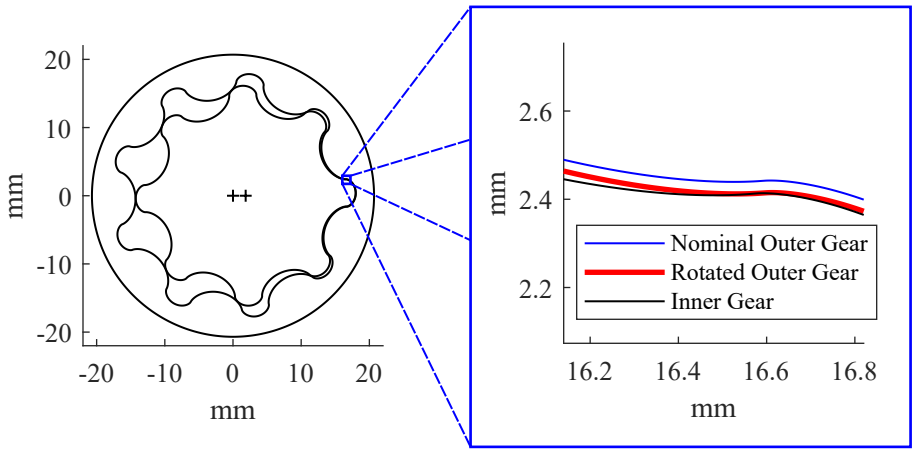

Figure 8.13. Alternate design shown at the rotation angle with the maximum value of OF4

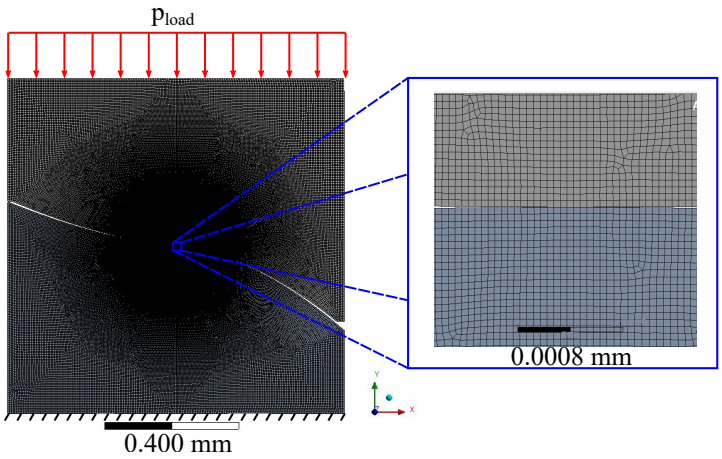

Figure 8.14. Loading and mesh for reference profile

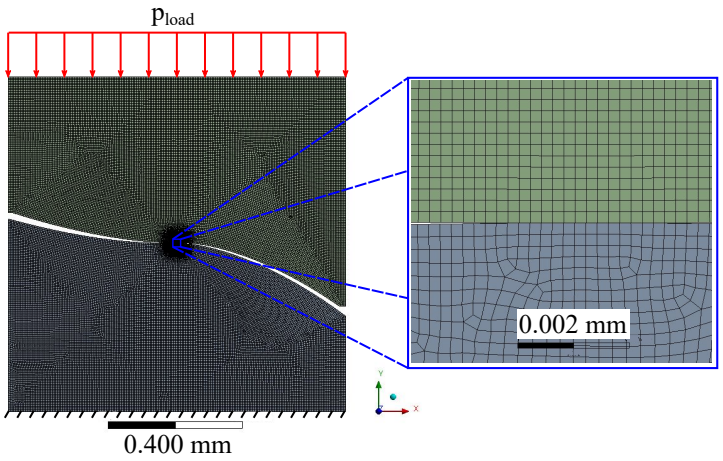

Figure 8.15. Loading and mesh for alternate profile

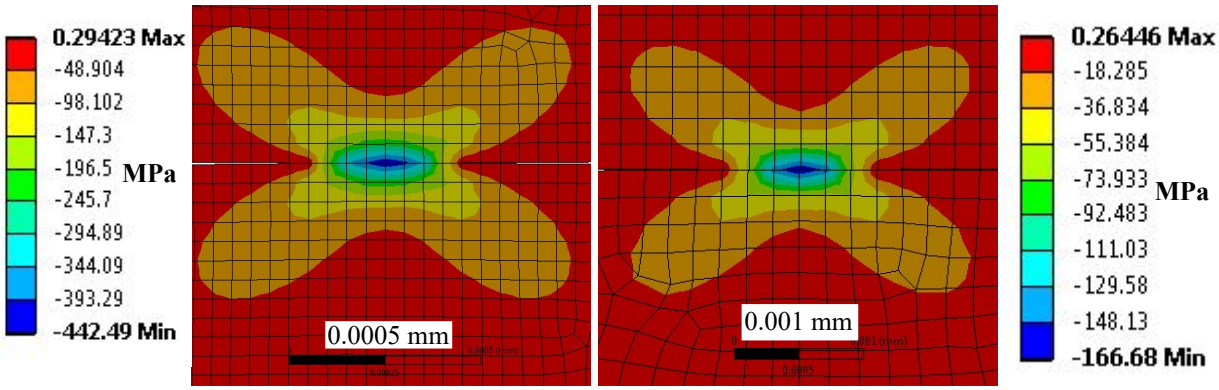

Figure 8.16. Contour plot of σ_x for reference design (left) and alternate design (right)

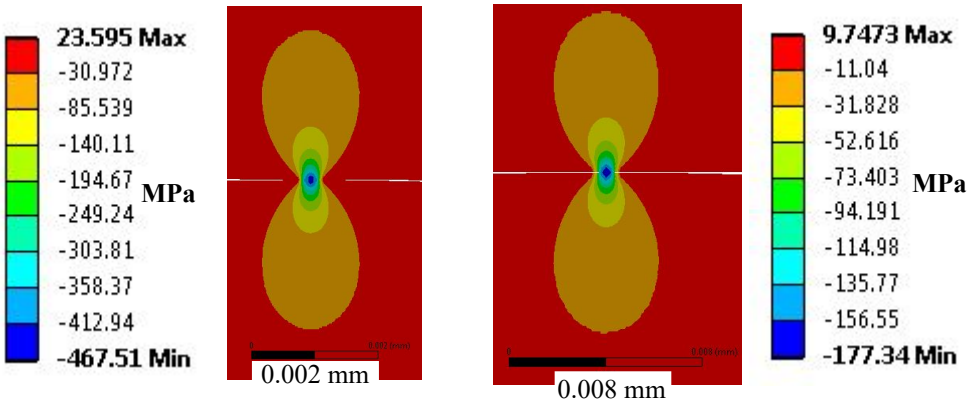

Figure 8.17. Contour plot of σ_y for reference design (left) and alternate design (right)

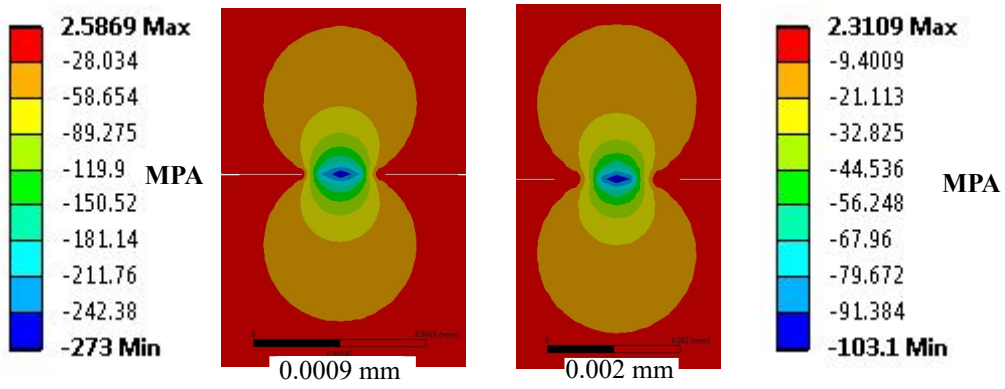

Figure 8.18. Contour plot of σ_z for reference design (left) and alternate design (right)

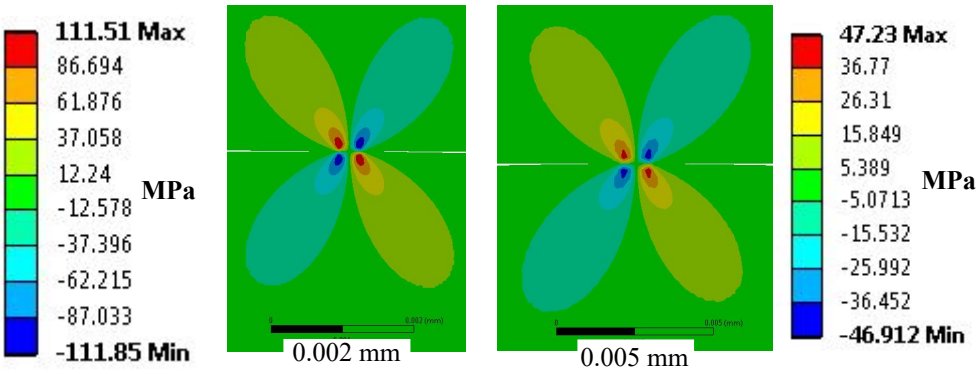

Figure 8.19. Contour plot of τ_{xy} for reference design (left) and alternate design (right)

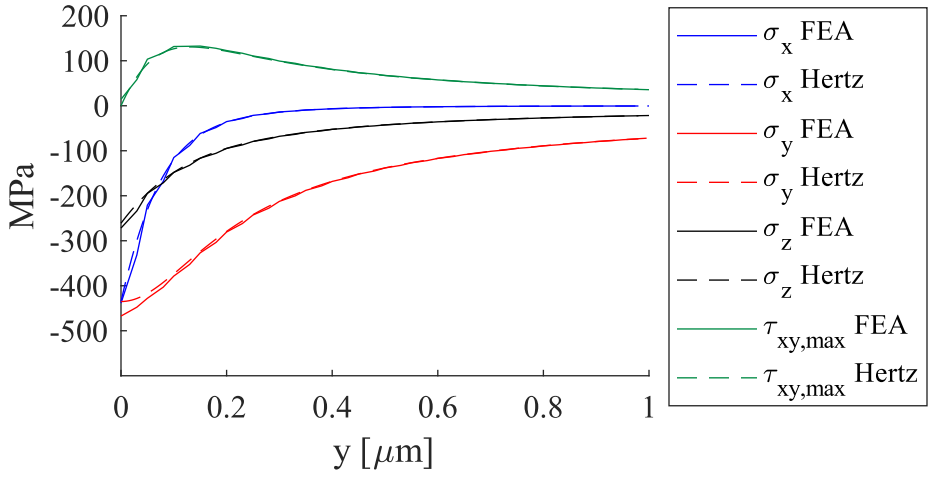

Figure 8.20. Comparison of Hertzian and FEA normal stress and maximum in plane shear stress of reference design at x=0

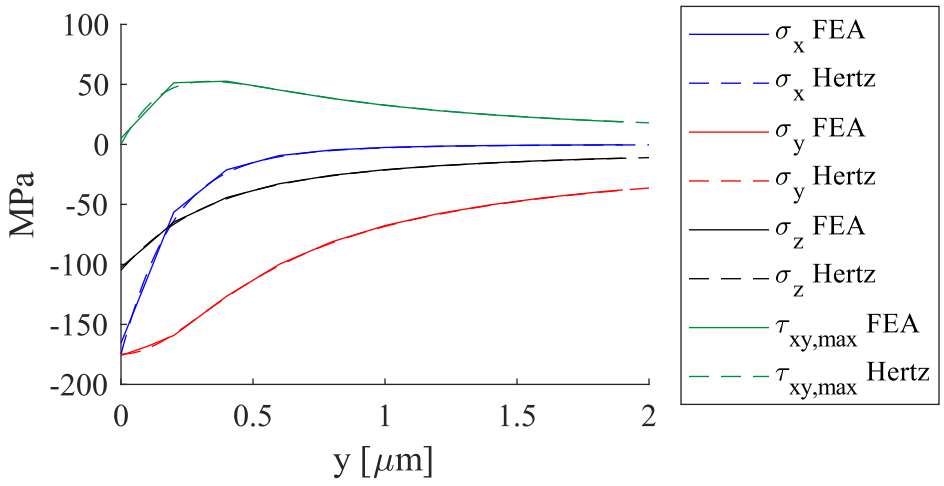

Figure 8.21. Comparison of Hertzian and FEA normal stress and maximum in plane shear stress of alternate design at x=0

The pressure ripples of the two optimized profiles were then compared in experiment to demonstrate that an alternative design to the reference profile can be selected to give a reduced pressure ripple while fitting in the same housing by using the optimization strategy presented in this work. The ports for the second alternative design were designed according to the procedure given in appendix A to give good performance in terms of volumetric efficiency and pressure ripple. The simplified hydraulic schematic is shown in fig. 8.22, and a photo of the prototype pump mounted in the test stand is shown in fig. 8.23. The pumps were loaded with a fixed orifice with a diameter of 1 mm, and the speed of the pump was adjusted to give pressure drop across the orifice of 2, 5, 15, and 30 bar with a temperature of 30C. Comparisons of the pressure ripple over two revolutions for both gear profiles at the different loading conditions are shown in fig. 8.24. In each case the pressure ripple for the second alternative design at the displacement chamber frequency was lower. However, a significant variation in pressure was observed at twice the shaft frequency for both pumps, which is indicative of manufacturing errors or shaft misalignment. This demonstrates how the gear geometry for a gerotor pump can be selected with the procedure presented in this work, but significant additional work in designing the ports and journal bearings as well as precise manufacturing are required to make a high-performance pump.

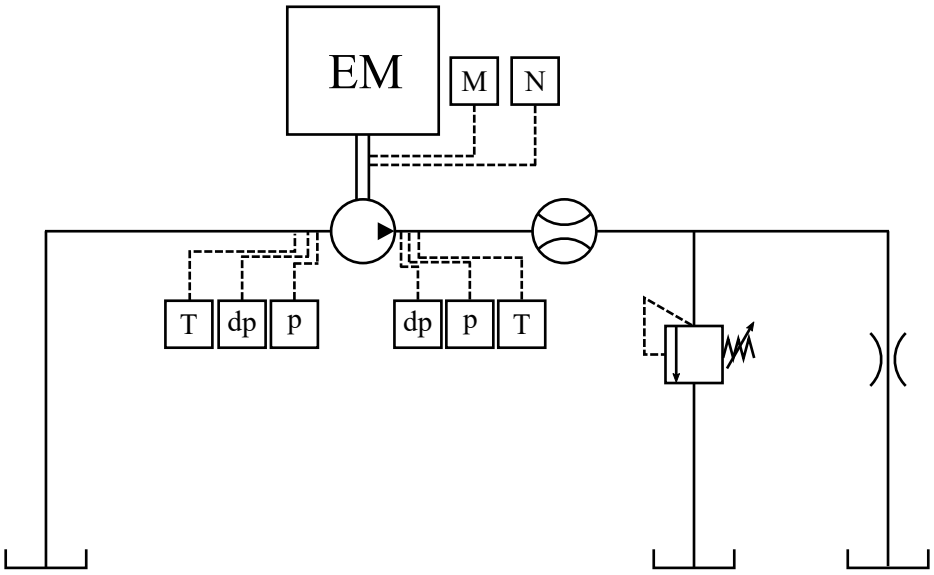

Figure 8.22. Hydraulic circuit for comparing the pressure ripple of the optimized gearsets

Figure 8.23. Photo of prototype pump mounted in the test stand

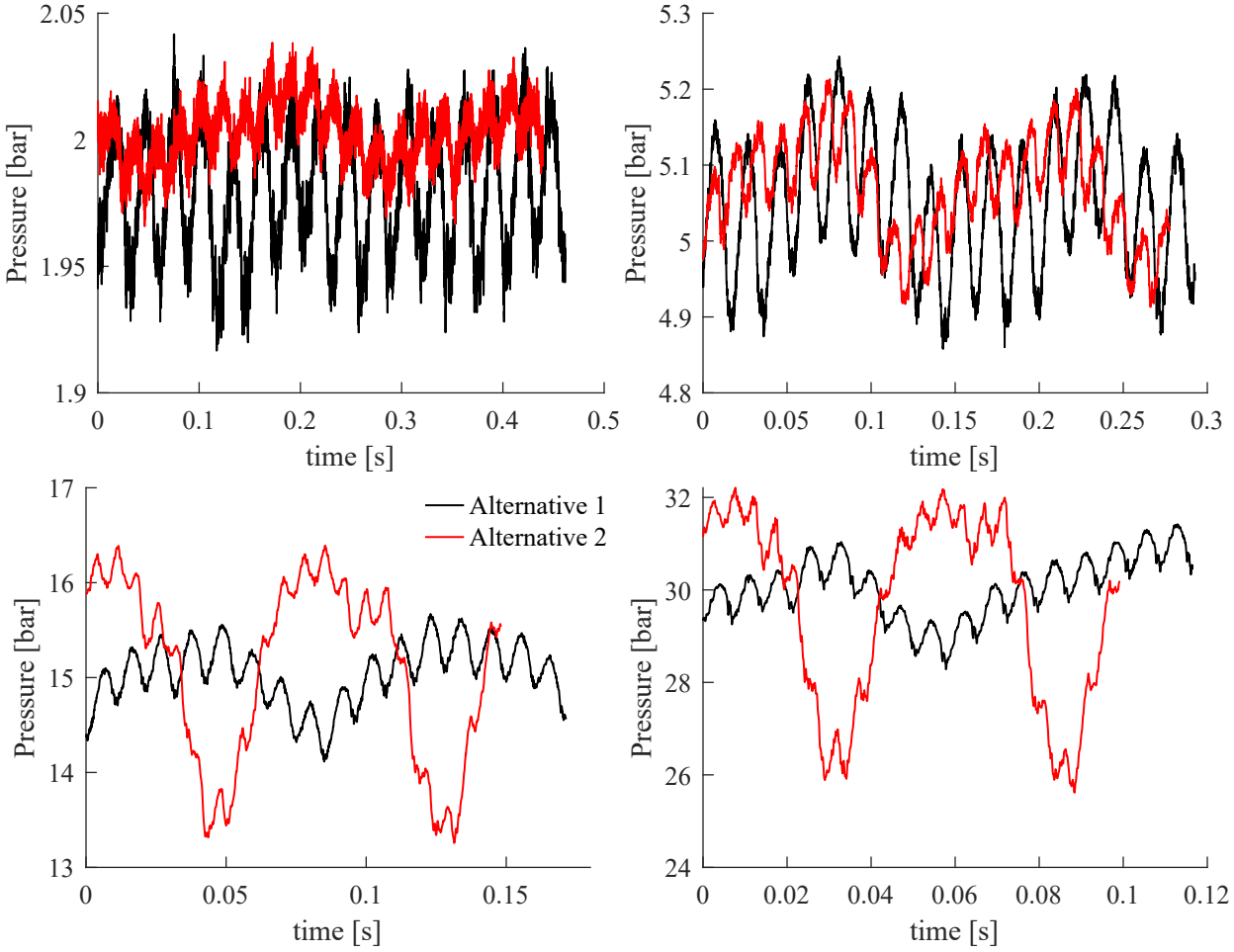

Figure 8.24. Comparison of measured outlet pressure ripple for the two optimized pumps at four pressure conditions

9. CONCLUSION

Despite the widespread application of gerotors, no design method before this work had been presented that considers all of the main performance goals of the gears nor to compare the performance between the infinite number of possible gerotor profiles. The main contribution of this work was to define a method to determine the best gear geometries for a given profile type, compare the best designs among each profile, and give designers a way to select an optimal pump geometry for their application.

A description of generating conventional gerotor profiles was given and serves as a compilation of gerotor gear geometry in a single source and offers a conceptional description different than what is available in literature. The epitrochoidal (circular) gerotor profile is the most common profile type in industry, and a clear conceptual explanation of how the profile can be generated is given as well as simple parametric equations that define both the inner and outer gear profiles. The cycloidal gerotor profile is also common in industry, but its prevalence is not well reflected by its presence in scientific literature. An explanation of the cycloidal profile is given as well as the parametric equations that define the profile. The main limitation of the cycloidal profile was shown that the radius of curvature approaches zero when the gear teeth contact at the pitch point, which can lead to high contact stress. Another method of gerotor gear generation that can use any smooth curve as the outer gear tooth was implemented, and the method was applied to elliptical, generalized cycloidal, cosine, and asymmetric elliptical gerotors. The generalized cycloidal profile is new to this work and allows a reduced center distance to decrease the curvature of the profiles and also increases the design freedom in comparison to the cycloidal profile.

Multi-objective optimization was then presented as a good design strategy to find the best designs of each gerotor profile and to compare the profile types. In an optimization, each performance goal is quantified by a function to be minimized or maximized, and one or more constraints can also be applied to ensure a feasible profile. One of the challenges of a multi-objective optimization is that many function evaluations are necessary to find the Pareto front. Existing models to predict the performance of gerotor pumps are not suitable for optimization, because they require too much computation time. New objective functions

were therefore defined that have a very short evaluation time but still capture the correct geometric effects to rank the relative performance of the different pumps.

Seven performance metrics to minimize were quantified as objective functions: radius for a given geometric displacement and face width, outlet flow variability, adhesive wear, contact stress, tooth tip leakage, lateral gap leakage, and mean inlet velocity into a displacement chamber. The geometric displacement and radius of a gerotor pump were then defined, and a method to compute the maximum and minimum displacement chamber areas for any pump geometry was given. A method to calculate the kinematic flow was then presented, and the signal power of the kinematic flow was suggested as a good metric to compare flow ripples with different shapes and magnitudes. Many factors contribute to the wear in a gerotor pump including the shape of the gears. The Archard wear model and Hertzian contact pressures were selected as two objective functions to reduce adhesive wear and pitting in a gerotor pump. The contact force is calculated by assuming a single contact point, and a procedure was given to predict the location of the contact point after introducing small clearances in the gearset. Both the adhesive wear and contact stress objective functions were normalized to the operating pressure, inner gear rotation speed, face width, and material properties to define fast objective functions that focus on the correct geometric relations. Two objective functions were defined to minimize both tooth tip leakage and lateral gap leakage that considered only the gear geometry. Both objective functions were validated by a CFD study. The seventh objective function then was defined to minimize a pump's tendency to experience incomplete filling at high rotation speeds by minimizing the mean inlet velocity into the displacement chamber.

The three types of constraints imposed in the optimization were described next. The first type ensures that a gear profile is geometrically feasible (e.g. without cusps or self-intersection). The second type of constraint gives a more usable Pareto front by placing a maximum allowable value for each objective function. Lastly the drive angle was defined as a means to ensure the inner gear can drive the outer gear without seizing.

The seven profile types were then optimized and then compared to one another. The input variables that lead to Pareto designs for the conventional profile types were given, which could help a designer select input variables that lead to the optimal profiles without

performing the optimizations. The results of each optimization can also be scaled to give any pump displacement, so the optimizations each must only be performed once. For all the profile types the size and flow ripple of the pumps tend to have a trade-off relationship such that reducing the size of the pump tends to lead to an increase in the flow ripple. The best designs from each profile type were then combined, and a new Pareto front from the combined designs was marked. Designs from each profile type were on the combined Pareto front, so no profile type is objectively better than the others. Designs from different profile types with similar performance often had similar appearance. This indicates that the optimization algorithm that designs with similar performance have the same tooth shape, and the parameters of the tooth curve can be adjusted to give the similar shape. Two methods were then proposed to select a design for a specific application based on the relative importance of each objective function: a weighting function and a parallel coordinates chart. When using the weighting function with weights selected for improving energy efficiency, an asymmetric design was selected that performed 2.5% to 14.6% better than the other profile types due to its compact design, but other designs could be selected with different weighting criteria. Designs were also selected using a parallel coordinates charts to give pumps with different levels of size vs. fluid dynamic performance, and a preference for epitrochoidal, hypotrochoidal, elliptical, and generalized cycloidal profiles was identified.

The optimization and design selection methods presented in this work were validated by comparison with state-of-the-art designs and by a case study. A significant possible improvement for six of the eight reference designs was identified. In the case study, a standard cycloidal design used in industry by a research sponsor seeking design improvement was taken as reference. A generalized cycloidal design was identified that matched the fluid dynamic and size performance while significantly reducing the contact stress objective function. The contact stress for the two designs was then simulated in ANSYS for the designs including clearances. The alternative design showed a significant reduction in contact stress in simulation, and the simulated stresses closely matched those predicted by Hertzian theory. Another alternative design was selected that could fit within the existing pump housing and reduce the kinematic flow ripple. Both prototype designs were manufactured and tested. A comparison of the performance of the reference designs in experiment showed a measurable

reduction in the pressure ripple when the two pumps were loaded with a fixed orifice, which validates the design procedure suggested in this work.

The methodology to design a gerotor gearset considering all of the main performance goals has been developed and has successfully identified the best designs among the most common gerotor profile types in industry as well as four less conventional and one novel profile type. The objective functions have been validated in simulation, and the design selection process has been evaluated in both simulation and experiment. The gear design procedure presented in this work will allow designers to push the limits of gerotor performance by starting with an optimal gear geometry and can also significantly reduce development time for designing gerotor gears for a new application.

9.1 Original Contributions

- Invented the generalized cycloidal gerotor profile type
- Identified geometric relations necessary to define feasible gerotor geometries for seven different profile types that were validated by an extensive number of function calls in optimization
- Developed seven objective functions to rank gerotor gear performance. All of the functions were new to this work with exception of minimizing the radius for a given geometric displacement and face width
- Fully explored the design space of conventional gerotor profiles and identified the optimal designs.
- Defined a methodology to compare the best designs among conventional profile types with the less conventional and novel profile types
- Determined a method to select the best gear design for a specific application
- Validated the proposed proposed design procedure and optimization approach by simulation and experiment

- Implemented the gear generation and optimal design selection procedure outlined in this work into a software package that is currently being used in industry.

9.2 Future Work

This work has largely found the performance limits of what is possible for the gerotor pump mechanism. However similar alternative mechanisms exist that can be compared to the performance of a gerotor. One of these mechanisms is a crescent internal gear pump that is illustrated in fig. 9.1. In this type of mechanism, a crescent separates the high and low-pressure regions that allows for improved sealing compared to a gerotor. This type of mechanism is generally preferred over a gerotor for medium pressure applications (75-300 bar) due to the enhanced sealing. At lower pressures though, gerotors are generally preferred for their lower manufacturing costs due to fewer parts. One characteristic of the gerotor mechanism is that the gear teeth remain in contact throughout their rotation. Removing this requirement results in a different type of mechanism that could possibly lead to more compact pumps due to an increased possible center distance. This type of mechanism can be thought of as an internal gear pump with secondary action that creates a seal between the low and high pressure regions of the pump. A "crescentless internal gear pump" would be a the proposed nomenclature. One example of this type of mechanism is shown in fig. 9.2 produced by Eckerle Hydraulic Division [50]. Several other examples of this alternative mechanism exist in literature, but none of them give a rigorous mathematical description of the profile. Examples include removing the undercutting regions of circular-toothed gerotors to allow for a greater center distance [51], connecting cycloids and circular arcs to form the outer gear tooth [30], combining involutes and cycloidal arcs (Megafloid) [52], combining line segments and cycloidal arcs (Geocloid or k-floid) [52], [53], using a variable offset distance from an epitrochoid (Parachoid EX) [52], and another proprietary profile that resembles an involute internal gearset with tooth tips that touch on the maximum volume side of the pump to provide sealing [54].

A crescentless internal gear pump is more comparable to a gerotor than a crescent internal gear pump, as the number of parts and sealing mechanism are the same. Several of these

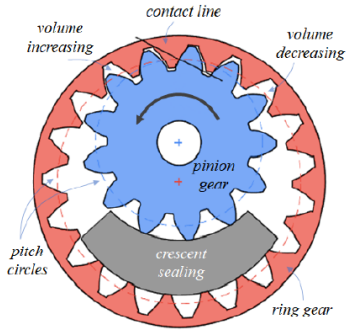

Figure 9.1. Example internal gear pump mechanism [55]

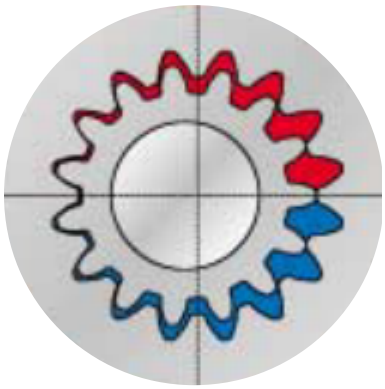

Figure 9.2. Example crescentless internal gear pump produced by Eckerle [50]

profiles are proprietary and claim advantages over the standard gerotor mechanism, but a proof of this has not been given in scientific literature. A natural extension of this work would be to develop a gear generation algorithm for a pump of this type and identify the feasible design space, apply the same optimization strategy presented in this work, and evaluate the performance improvement (if any) that is possible with this mechanism over a gerotor. This comparison was deemed to be outside of the scope of the present work, as these types of pumps are not gerotors but rather an entirely different mechanism that would require an entirely different gear generation algorithm and a significant amount of development time.

REFERENCES

[1] M. F. Hill, *Kinematics of Gerotors*, 2nd ed. Philadelphia: The Peter Reilly Company, 1927.

[2] Parker Hannifin Corporation, *Gerotor Pump and Motor Aluminum High Speed, Low Torque Series*. Catalog HY09-PGG/MGG/US, 2003.

[3] S. Mancò, N. Nervegna, M. Rundo, and M. Margaria, "Miniature Gerotor Pump Prototype for Automotive Applications," in *3rd International Fluid Power Conference (3rd IFK)*, 2002, pp. 153–167.

[4] P. J. Gamez-Montero, R. Castilla, E. Codina, J. Freire, J. Morató, E. Sanchez-Casas, and I. Flotats, "GeroMAG: In-house Prototype of an Innovative Sealed, Compact and Non-Shaft-Driven Gerotor Pump with Magnetically-Driving Outer Rotor," *Energies*, vol. 10, no. 4, pp. 1–14, 2017. DOI: 10.3390/en10040435.

[5] Y. Michikoshi, D. Kusamoto, H. Ota, M. Ikemura, N. Takebayashi, I. Nobukazu, Y. Takashi, and I. Ryohei, "Toyota New TNGA High-Efficiency Eight-Speed Automatic Transmission Direct Shift-8AT for FWD Vehicles," *SAE Technical Paper Series*, vol. 1, 2017. DOI: 10.4271/2017-01-1093.

[6] C. Dörr, M. Homm, and G. Indlekofer, "The New Automatic Transmission 9G-TRONIC from Mercedes-Benz," in *12th International CTI Symposium*, Berlin, 2013.

[7] I. Baus, A. Schumacher, R. Rahmfeld, and H. C. Pedersen, "Systematic Methodology for Reliability Analysis of Components in Axial Piston Units," in *ASME/BATH 2019 Symposium on Fluid Power and Motion Control (FPMC)*, Sarasota, FL, 2019, pp. 1–11.

[8] R. Castilla, P. J. Gamez-Montero, G. Raush, and E. Codina, "Method for Fluid Flow Simulation of a Gerotor Pump Using OpenFOAM," *Journal of Fluids Engineering*, vol. 139, no. 11, p. 111 101, 2017, ISSN: 0098-2202. DOI: 10.1115/1.4037060.

[9] G. Altare and M. Rundo, "Advances in Simulation of Gerotor Pumps: An Integrated Approach," *Proceedings of the Institution of Mechanical Engineers, Part C: Journal of Mechanical Engineering Science*, vol. 231, no. 7, pp. 1221–1236, 2017. DOI: 10.1177/0954406217694663.

[10] M. Pellegri, V. H. B. Manne, and A. Vacca, "A simulation model of Gerotor pumps considering fluid–structure interaction effects: Formulation and validation," *Mechanical Systems and Signal Processing*, vol. 140, p. 106 720, 2020. DOI: 10.1016/j.ymssp.2020.106720.

[11] E. Buckingham, *Analytical Mechanics of Gears*. New York: Dover Publications, Inc., 1949, pp. 42–43.

[12] J. A. S. Hall, "Pin Gearing," *ASME*, no. 68-MECH-58, pp. 1–5, 1968.

[13] J. R. Colbourne, "Gear Shape and Theoretical Flow Rate in Internal Gear Pumps.," *Transactions of the Canadian Society for Mechanical Engineering*, vol. 3, no. 4, pp. 215–223, 1975, ISSN: 03158977.

[14] J. R. Colbourne, "Reduction of the Contact Stress in Internal Gear Pumps," *Journal Of Engineering For Industry*, vol. 98, no. 4, pp. 1296–1300, 1976. DOI: 10.1115/1.3439103.

[15] J. E. Beard, A. S. Hall, and W. Soedel, "Comparison of Hypotrochoidal and Epitrochoidal Gerotors," *Journal of Mechanical Design*, vol. 113, no. June 1990, pp. 133–141, 1991.

[16] J. E. Beard, D. W. Yannitell, and G. R. Pennock, "The effects of the generating pin size and placement on the curvature and displacement of epitrochoidal gerotors," *Mechanism and Machine Theory*, vol. 27, no. 4, pp. 373–389, 1992. DOI: 10.1016/0094-114X(92)90030-L.

[17] G. Mimmi, P. Pennacchi, and C. Savi, "Internal Lobe Pump Design," *Transactions of the Canadian Society for Mechanical Engineering*, vol. 21, no. 2, pp. 109–121, 1997.

[18] G. Mimmi and P. Pennacchi, "Rotor Design and Optimization in Internal Lobe Pumps," *Applied Mechanics Reviews*, vol. 50, no. 11, S133–S141, 1997.

[19] S.-M. Kwon, M. S. Kim, and J.-H. Shin, "Analytical Wear Model of a Gerotor Pump without Hydrodynamic Effect," *Journal of Advanced Mechanical Design, Systems, and Manufacturing*, vol. 2, no. 2, pp. 230–237, 2008. DOI: 10.1299/jamdsm.2.230.

[20] C.-F. Hsieh and H.-S. Yan, "Feasible design region and sealing property of hypotrochoidal gerotor geometry," *Proc. IMechE Part C: J. Mechanical Engineering Science*, vol. 222, pp. 1847–1854, 2008, ISSN: 0954-4062. DOI: 10.1243/09544062JMES774.

[21] G. Bonandrini, G. Mimmi, and C. Rottenbacher, "Theoretical Analysis of Internal Epitrochoidal and Hypotrochoidal Machines," *Proc. IMechE Part C: J. Mechanical Engineering Science*, vol. 223, no. 6, pp. 1469–1480, 2009.

[22] S.-M. Kwon, C.-H. Kim, and J.-h. Shin, "Optimal rotor wear design in hypotrochoidal gear pump using genetic algorithm," *Journal of Central South University of Technology*, vol. 18, no. 3, pp. 718–725, 2011.

[23] P. Yun, H. Nam, C. Kim, J.-H. Shin, and S.-M. Kwon, "Optimal Wear Design for a Gerotor Pump using Genetic Algorithm," in *Proceedings of the 2010 IEEE International Conference on Mechatronics and Automation*, 2010, pp. 207–212, ISBN: 9781424451418.

[24] M. R. Karamooz Ravari, "Elliptical lobe shape gerotor pump design to minimize wear," *Frontiers of Mechanical Engineering*, vol. 6, no. 4, pp. 429–434, 2011, ISSN: 20950233. DOI: 10.1007/s11465-011-0247-6.

[25] M. R. Karamooz Ravari, M. R. Forouzan, and H. Moosavi, "Flow Irregularity and Wear Optimization in Epitrochoidal Gerotor Pumps," *Meccanica*, vol. 47, no. 4, pp. 917–928, 2012. DOI: 10.1007/s11012-011-9473-6.

[26] G. Jacazio and A. De Martin, "Influence of Rotor Profile Geometry on the Performance of an Original Low-Pressure Gerotor Pump," *Mechanism and Machine Theory*, vol. 100, pp. 296–312, 2016. DOI: 10.1016/j.mechmachtheory.2016.02.012.

[27] A. J. Robison and A. Vacca, "Performance comparison of epitrochoidal, hypotrochoidal, and cycloidal gerotor gear profiles," *Mechanism and Machine Theory*, vol. 158, p. 104 228, 2021. DOI: 10.1016/j.mechmachtheory.2020.104228.

[28] G. Figliolini, H. Stachel, and J. Angeles, "On Martin Disteli's Spatial Cycloidal Gearing," *Mechanism and Machine Theory*, vol. 60, pp. 73–89, 2013. DOI: 10.1016/j.mechmachtheory.2012.09.005.

[29] L. Litvin Faydor and A. Fuentes, *Gear Geometry and Applied Theory*, 2nd ed. Cambridge: Cambridge University Press, 2004.

[30] T. H. Choi, M. S. Kim, G. S. Lee, S. Y. Jung, J. H. Bae, and C. Kim, "Design of Rotor for Internal Gear Pump Using Cycloid and Circular-arc Curves," *Journal of Mechanical Design*, vol. 134, no. 1, p. 011 005, 2012.

[31] A. J. Robison and A. Vacca, "Multi-Objective Optimization of Modified Cycloidal-Toothed Gerotor Pumps by Genetic Algorithm," in *Proceedings of the ASME/BATH 2019 Symposium on Fluid Power and Motion Control*, Sarasota, FL, 2019, pp. 1–14. DOI: 10.1115/FPMC2019-1696.

[32] A. J. Robison and A. Vacca, "Design of Asymmetric Gerotor Pumps," in *Advances in Hydraulic and Pneumatic Drives and Control 2020*, J. Stryczek and U. Warzynska, Eds., Wroclaw, Poland: Springer International Publishing, 2021, pp. 90–101, ISBN: 978-3-030-59509-8.

[33] A. J. Robison and A. Vacca, "Multi-Objective Geometric Optimization of Elliptical-Toothed Gerotor Pumps for Kinematics and Wear by Genetic Algorithm," in *Proceedings of the 2018 Bath/ASME Symposium on Fluid Power and Motion Control*, Bath, United Kingdom, 2018, pp. 1–12. DOI: 10.1115/FPMC2018-8876.

[34] M. F. Hill, *Elliptical Contours for Rotor Teeth*. United States Patent 2,389,728, 1945.

[35] R. S. Devendran and A. Vacca, "Optimal Design of Gear Pumps for Exhaust Gas Aftertreatment Applications," *Simulation Modelling Practice and Theory*, vol. 38, pp. 1–19, 2013. DOI: 10.1016/j.simpat.2013.06.006.

[36] P. K. Kalbfleisch and M. Ivantysynova, "Computational Valve Plate Design in Axial Piston Pumps/Motors," *International Journal of Fluid Power*, vol. 20, no. 2, pp. 177–208, 2019. DOI: 10.13052/ijfp1439-9776.2022.

[37] K. Deb, A. Pratap, S. Agarwal, and T. Meyarivan, "A Fast and Elitist Multiobjective Genetic Algorithm: NSGA-II," *IEEE Transactions on Evolutionary Computation*, vol. 6, no. 2, pp. 182–197, 2002. DOI: 10.1109/4235.996017.

[38] R. Maiti, "Active Contact Stresses at Epitrochoid Generated Rotor-Stator Set of Fixed Axis or Equivalent system 'ROPIMA' Type Hydrostatic Units," *Journal of Manufacturing Science and Engineering, Transactions of the ASME*, vol. 113, no. 4, pp. 465–473, 1991. DOI: 10.1115/1.2899723.

[39] M. Pellegri, A. Vacca, R. S. Devendran, E. Dautry, and B. Ginsberg, "A Lumped Parameter Approach for GEROTOR Pumps : Model Formulation and Experimental Validation," *10th IFK International Fluid Power Conference*, pp. 465–476, 2016.

[40] L. Ivanović, G. Devedžić, S. Ćuković, and N. Mirić, "Modeling of the Meshing of Trochoidal Profiles With Clearances," *ASME Journal of Mechanical Design*, vol. 134, no. 4, p. 041 003, 2012. DOI: 10.1115/1.4005621.

[41] A. Robison and A. Vacca, "Multi-Objective Optimization of Circular-Toothed Gerotors for Kinematics and Wear by Genetic Algorithm," *Mechanism and Machine Theory*, vol. 128, pp. 150–168, 2018. DOI: 10.1016/j.mechmachtheory.2018.05.011.

[42] R. Juvinall and K. M. Marshek, *Fundamentals of Machine Component Design*, 4th ed. Hoboken, NJ: John Wiley & Sons, Inc., 2006, pp. 368–372.

[43] J. R. Colbourne, *The Geometry of Involute Gears*. New York: Springer-Verlag, 1987, p. 286.

[44] F. Rituraj and A. Vacca, "An Investigation of Tooth Tip Leakages in Gerotor Pumps: Modelling and Experimental Validation," *Journal of Verification, Validation and Uncertainty Quantification*, vol. 5, no. March, pp. 1–13, Feb. 2020. DOI: 10.1115/1.4046295.

[45] G. Altare and M. Rundo, "CFD Analysis of Gerotor Lubricating Pumps at High Speed : Geometric Features Influencing the Filling Capability," *ASME/BATH Conference 2015*, pp. 1–10, 2015, ISSN: 1528901X. DOI: 10.1115/1.4033675.

[46] Z. Mistry, M. H. Babu, A. Vacca, E. Dautry, and M. Petzold, "A Numerical Model for the Evaluation of Gertotor Torque Considering Multiple Contact Points and Fluid-Structure Interactions," in *12th International Fluid Power Conference*, Dresden, 2020.

[47] B. J. Hamrock, S. R. Schmid, and B. O. Jacobson, *Fundamentals of Fluid Film Lubriction*, 2nd ed. New York: Marcel Dekker, 2004.

[48] Y.-W. Hwang and C.-F. Hsieh, "Geometric Design Using Hypotrochoid and Nonundercutting Conditions for an Internal Cycloidal Gear," *Journal of Mechanical Design*, vol. 129, no. 4, p. 413, 2007. DOI: 10.1115/1.2437806.

[49] A. C. Ugural and S. K. Fenster, *Advanced Mechanics of Materials and Applied Elasticity*, 5th ed. Upper Saddle River, NJ: Prentice Hall, 2012.

[50] Eckerle Hydraulic Division, *EIPR1 Innenzahnradpumpen*. Findynamica Drive and Control Products, pp. 1–4. [Online]. Available: https://findynamica.nl/en/content/eckerle-internal-gear-pumps.

[51] G. Bonandrini, M. Strutturale, V. Ferrata, and I. Pavia, "Theoretical Analysis of an Original Rotary Machine," *ASME Journal of Mechanical Design*, vol. 132, pp. 1–8, 2010. DOI: 10.1115/1.4000698.

[52] S. Arinaga, K. Yoshida, S. Takada, M. Noda, and K. Inoue, "The Latest Trends in oil pump rotors for automobiles," *SEI Technical Review*, vol. 82, no. April, pp. 59–65, 2016.

[53] H. Liu and J.-c. Lee, "Profile Design and Volumetric Efficiency Analysis of Gerotor Pumps for Gerotor Pumps for AWD Vehicles," *International Journal of Mechanical And Production Engineering*, vol. 5, no. 4, pp. 20–23, 2017.

[54] Y. Nishida, F. Toyoda, H. Terashima, H. Ono, and K. Nunami, "Development of Continuously Variable Discharge Oil Pump," *SAE Technical Paper 2018-01-0932*, vol. 1, pp. 1–7, 2018. DOI: 10.4271/2018-01-0932.

[55] D. Pan and A. Vacca, "A numerical method for the analysis of the theoretical flow in crescent-type internal gear machines with involute tooth profile," in *ASME/BATH 2019 Symposium on Fluid Power and Motion Control, FPMC 2019*, Sarasota, FL, 2020, pp. 1–11. DOI: 10.1115/FPMC2019-1605.

[56] M. Pellegri and A. Vacca, "Numerical Simulation of Gerotor Pumps Considering Rotor Micro-Motions," *Meccanica*, vol. 52, pp. 1851–1870, 2017. DOI: 10.1007/s11012-016-0536-6.

[57] A. Robison and A. Vacca, "Multi-Objective Optimization of Gerotor Port Design by Genetic Algorithm with Considerations on Kinematic vs. Actual Flow Ripple," in *SAE WCX 2019*, Detroit, MI US: SAE Technical Paper 2019-01-0827, 2019, pp. 1–12. DOI: 10.4271/2019-01-0827.

[58] P. J. Gamez-Montero, R. Castilla, and E. Codina-Macia, "Methodology Based on Best Practice Rules to Design a New-Born Trochoidal Gear Pump," *Proceedings of the Institution of Mechanical Engineers. Part C, journal of mechanical engineering science*, vol. 0, no. 0, pp. 1–12, 2017. DOI: 10.1177/0954406217697355.

[59] H.-J. Sung, H.-K. Min, Y.-J. Nam, and M.-K. Park, "Design and Experimental Verification of a Port Plate in a Gerotor Pump to Reduce Pressure Pulsation," *Journal of Mechanical Science and Technology*, vol. 32, no. 2, pp. 671–678, 2018. DOI: 10.1007/s12206-018-0114-4.

[60] H. S. Kwak, S. H. Li, and C. Kim, "Performance Improvement of an Oil Pump: Design of Port Assembled with Gerotor (2-Ellipses-Combined Lobe)," *International Journal of Precision Engineering and Manufacturing*, vol. 17, no. 8, pp. 1017–1024, 2016. DOI: 10.1007/s12541-016-0124-7.

[61] J. H. Kim, C. Kim, and Y. J. Chang, "Optimum design on lobe shapes of gerotor oil pump," *Journal of Mechanical Science and Technology*, vol. 20, no. 9, pp. 1390–1398, 2006. DOI: 10.1007/BF02915962.

[62] International Organization for Standardization, *Hydraulic Fluid Power - Pumps and Motors - Geometric Displacents (ISO 3662:1976)*, 1976.

[63] Y. G. Shah, A. Vacca, S. Dabiri, and E. Frosina, "A Fast Lumped Parameter Approach for the Prediction of both Aeration and Cavitation in Gerotor Pumps," *Meccanica*, vol. 53, pp. 175–191, 2018. DOI: 10.1007/s11012-017-0725-y.

APPENDIX: COMPARISON OF KINEMATIC AND SIMULATED PUMP FLOW AND DESIGN OF PORTS BY MULTI-OBJECTIVE OPTIMIZATION

The kinematic flow ripple does not consider the important effects of compressibility, internal leakages, and port timing, so a significant difference is usually present between the kinematic and measured flow. This raises the question: Is the kinematic flow ripple still a good metric for comparing gerotor gearsets? Perhaps a more sophisticated tool is required to evaluate the flow ripple for gerotors beyond the kinematic flow ripple. The hypothesis of this work is that the kinematic flow ripple can correctly predict the trend of the flow ripples of real pumps, provided they have well-designed ports, so it can be used as an effective objective function in gerotor gear optimization. To test this hypothesis, the flow ripples of pumps with different kinematic flow ripples will be simulated, and the correlation between the kinematic simulated flow ripples will be evaluated.

One of the challenges in testing this hypothesis is that gerotors with kinematic port timings often have poor performance, so the pumps should not be tested simply with kinematic port timings. This is illustrated in fig. A.1, which shows the simulated displacement chamber pressure of a pump with kinematic port timings operating at 2000 RPM at 5 bar with ISO 46 oil at 50°. The simulation for this pump was performed with an experimentally-validated, multi-domain, lumped parameter gerotor simulation tool [56]. The simulation model does not include a proper cavitation model, so the tank pressure was increased to 5 bar-A to better highlight the inlet throttling. With kinematic ports, the area of the displacement chamber that overlaps the ports becomes very small when the chamber is transitioning between the low- and high- pressure environments. This leads to significant pressure dips and peaks as shown in fig. A.1.

Both the timing of when the displacement chamber is connected to the ports and the overlap area of the displacement chamber with the ports can be modified to improve pressure pulsation, internal leakages, and localized cavitation by careful design of the ports [45], [58]–[61]. These studies showed that changing the port geometry can lead to improved

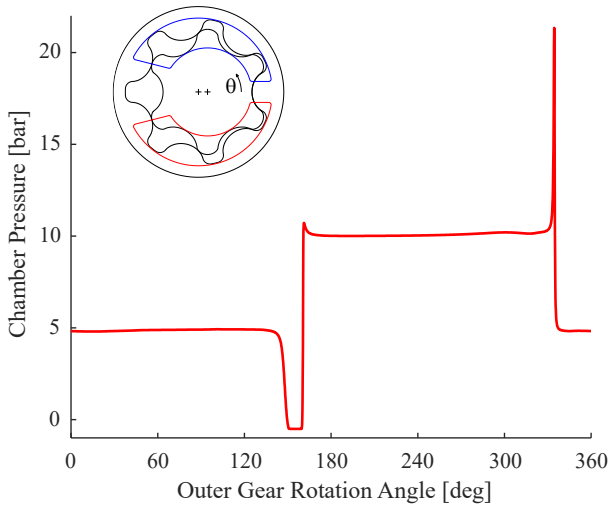

Figure A.1. Simulated displacement chamber pressure for a pump with kinematic port timings [57]

performance, but each one only considered a few port designs. A better design for the port geometry almost certainly exists than that which can be found by simplified approaches.

A.1 Optimization

The effect of the port geometry on the performance of the pumps is pronounced enough that a pump with a good gearset with poorly designed ports can very easily have worse performance than a pump with a worse gearset and well-designed ports. To make a fair comparison of the gearsets then, a design methodology is required to determine a good port design for each pump. Multi-objective optimization is one approach that can be used to arrive at a good design of the ports, and while it has not been used in literature to design gerotor ports, it has been used successfully to design the valve plate for axial piston machines [36] and for the bearing blocks of external gear machines [35].

The design of gerotor ports my multi-objective optimization proceeds as follows. A gearset is selected, and the port geometry is parameterized. An optimization algorithm is selected to vary the port geometry parameters to determine the optimal designs. For each port design the pump is simulated using a pump simulation tool that had been developed previously [56]. After the pump performance has been simulated, five OFs are calculated:

minimize outlet flow ripple, minimize displacement chamber pressure peaks, minimize displacement chamber pressure dips, minimize inlet throttling, and maximize volumetric efficiency. The algorithm then selects new design variables for the next generation of designs and continues for a set number of generations. After all the designs have been evaluated, the Pareto designs are determined, and a final design is selected from the Pareto front.

This optimization was performed for five pumps with elliptical gerotor profiles with the same 10 cm^3/rev volumetric displacement but different values of their kinematic flow ripple signal power. The pumps used for the study are shown in fig. A.2. Elliptical gerotors were chosen over circular gerotors, as they have more design variability. This tests both the usefulness of the port optimization as well as the effect of tooth shape on the produced flow ripple. After a good port design for each pump was determined, the kinematic and simulated flow ripples are compared to evaluate whether the kinematic flow ripple is a good predictor of the real flow ripple for pumps with well-designed ports.

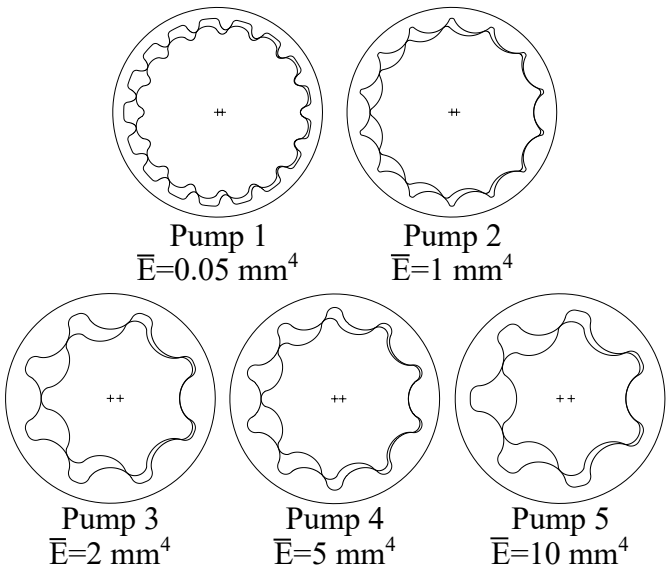

Figure A.2. Pumps with different kinematic flow ripples used in validation study [57]

Gerotor ports can take many shapes, but a standard port shape was used in this work. The ports typically consist of two circular arcs that are concentric with the inner and the outer gear centers respectively, and either line segments or circular arcs connect the concentric circles. Typically, small fillets are also used to connect all of the arcs to improve

manufacturability and to eliminate any possible stress concentrations. A diagram of the port parameterization used in each optimization is shown in fig. A.3. In this work, the ends of the ports on the minimum volume side of the pump are defined by horizontal line segments, and the ends of the ports on the maximum volume side of the pump are connected by line segments that extend through the pitch point P. The timing of when the displacement chamber connects to the low pressure and high pressure environments is determined by the angles $\theta_1 - \theta_4$ in fig. A.3. The input variables for the optimization were the deviation angles $d\theta$ from the kinematic port timings with a positive counterclockwise direction rather than the absolute angles. This helps to normalize the input variable values in the optimization. Novel port types could certainly improve the performance of a gerotor [45], [58]–[61], but the goal of this research is to define a method to design standard port types that can offer good performance overall. Additional port profiles could be tested by this methodology, but that is a subject of future work.

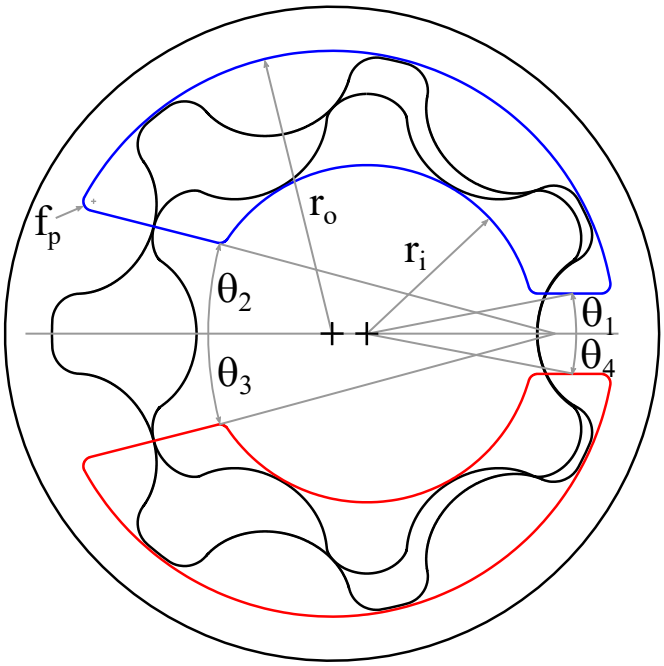

Figure A.3. Diagram of port parameterization used in validation study [57]

The port optimization for each test pump in the study was implemented in the commercial software modeFRONTIER that combines engineering software with optimization and

statistical tools. For this work the NSGA-II algorithm was selected because of its ability to handle each OF separately in determining a Pareto front for a multi-objective optimization, which is difficult to achieve with a gradient-based method [37]. Each port optimization was run for for 30 generations with a population size of 50. These values were selected to allow for sufficient exploration of the design space while limiting the total optimization time. The operating conditions for every simulation were 2000 RPM at 5 bar with ISO 46 oil at 50° C. The OF values were also scaled to be on the order of one to help the algorithm better find the Pareto front.

Each gearset had a face width of 1 cm and a kinematic displacement of 10 $\frac{\text{cm}^3}{\text{rev}}$ according to ISO 3662 [62]. Each gearset had a constant radial clearance of 25 μm. The input variable bounds and parameter values are displayed in tables A.1 and A.2 respectively. The input variable bounds were selected heuristically to avoid overlap of the suction and delivery ports and to give a suitable maximum distance between the end of one port and the beginning of the other. The inner circular arc defining the ports was 1% smaller than the inner dedendum circle, and the outer circular arc was 1% larger than the outer gear root.

Table A.1. Port input variable bounds

	$d\theta_1$ [deg]		$d\theta_2$ [deg]		$d\theta_3$ [deg]		$d\theta_4$ [deg]	
	min	max	min	max	min	max	min	max
Pump 1	-7.5	7.5	0	6	-2	10	0	7.5
Pump 2	-7.4	7	0	8	-2	8	0	7.4
Pump 3	-5.5	8	0	10	-2	10	0	5.5
Pump 4	-7.5	7.5	0	13	-2	10	0	7.5
Pump 5	-9	9	0	9	-2	9	0	9

Table A.2. Port parameters of pumps used in the study

	r_i [mm]	r_o [mm]	f_p [mm]
Pump 1	43.27	35.29	1.00
Pump 2	43.39	34.93	1.00
Pump 3	34.15	24.07	1.00
Pump 4	31.62	20.39	1.00
Pump 5	30.13	17.96	1.00

The computation time required for each port optimization ranged from 22 to 72 hours on a desktop PC (Intel i7 7^{th} generation, 16 GB RAM) depending on the number of gear teeth (more displacement chambers requires more simulation time for the fluid model). Running the optimization for longer could find still better designs, but evaluating a total of 1500 designs gives a sufficiently good designs to compare flow ripples between the pumps base on the performance improvement in comparison to the kinematic port timings.

A.2 Simulation Model

The simulation model used was a lumped parameter model that has been validated experimentally that predicts the pressures in each displacement chamber, the internal leakages between the chambers, and the outlet flow ripple. The commercial software Simcenter Amesim was used to implement and solve the coupled ODEs to determine the pump performance. A more complete description of the model is given in [56]. In the lumped parameter assumption, each displacement chamber is assumed to have a uniform pressure throughout the chamber. The pressure in the j^{th} displacement chamber can then be found in eq. (A.1), where ρ in this case is the density of the fluid that is a function of both pressure and temperature, $\dot{m}$ is the mass flow rate, V is is the displacement chamber volume, and t is time.

$$\frac{dp_j}{dt} = \frac{1}{V_j}\left.\frac{dp}{d\rho}\right|_{p=p_j}\left[\sum \dot{m_{in}} - \sum \dot{m_{out}} - \rho|_{p=p_j}\frac{dV_j}{dt}\right] \tag{A.1}$$

The flows from the ports into the displacement chambers was modeled using the orifice equation in eqs. (A.2)–(A.4), where p_j is the pressure inside the j^{th} displacement chamber, p_p is the pressure in the port, $\overline{p_{j,p}}$ is the mean pressure between the port and the j^{th} displacement chamber, α is the discharge coefficient in the orifice equation, α_{max} is the maximum discharge coefficient that was taken to be 0.7, A_j is the area of the j^{th} displacement chamber that overlaps the port, Re is the Reynolds number, Re_{crit} is the critical Reynolds number taken to be 1000, D_h is the hydraulic diameter of the displacement chamber area overlapping

the port, and ν is the kinematic viscosity of the fluid. An illustration of the area of the displacement chamber overlapping the suction port is shown in green in fig. A.4.

$$\dot{m} = \frac{p_j - p_p}{|p_j - p_p|} \left.\rho\right|_{p=\overline{p_{j,p}}} \alpha A_j \sqrt{\frac{2\left(p_j - p_p\right)}{\left.\rho\right|_{p=\overline{p_{j,p}}}}} \tag{A.2}$$

$$\alpha = \alpha_{max} \tanh\left(\frac{2\mathrm{Re}}{\mathrm{Re}_{\mathrm{crit}}}\right) \tag{A.3}$$

$$\mathrm{Re} = \frac{D_h}{\nu} \sqrt{\frac{2\left|p_j - p_p\right|}{\left.\rho\right|_{p=\overline{p_{j,p}}}}} \tag{A.4}$$

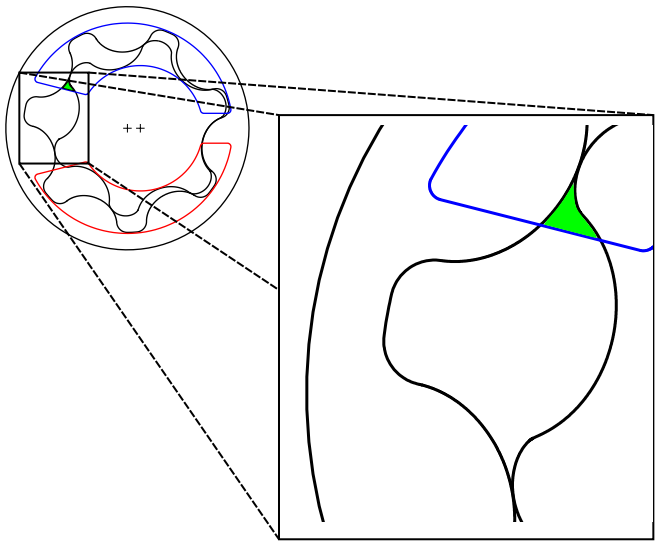

Figure A.4. Illustration of displacement chamber area overlap with suction port

The flow between the tooth tips was modeled as flow between two moving parallel plates in eq. (A.5), where h is this case is the height of the gap, μ is the dynamic viscosity, ω_i and ω_o are the inner and outer gear rotation speeds respectively, r_{in} and r_{out} are the magnitude of the position vector of the contact point with respect to the inner and outer gear centers respectively, l is the equivalent gap length, and b is the face width of the gears in this case.

The tooth tip gap is illustrated in eq. (A.5), where the height of the gap is exaggerated for illustration.

$$\dot{m} = \rho b \left[-\frac{h^3}{12\mu} \frac{p_j - p_{j-1}}{l} + \pi h \left(\omega_{out} r_{out} - \omega_{in} r_{in} \right) \right] \tag{A.5}$$

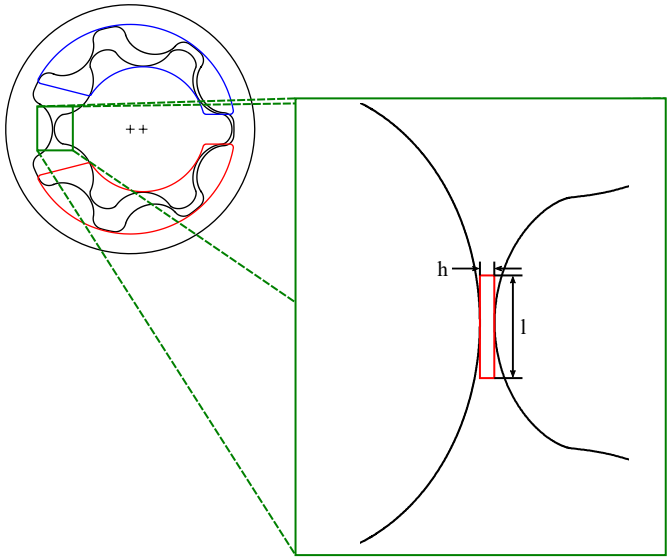

Figure A.5. Illustration of model of gap between tooth tips

The leakage in the lateral gap of the gears was neglected for the port optimizations, as it is typically much less than the leakage across the tooth-tip gap, is mainly affected by the height of the gap independent of the gears, and requires a full CFD model to simulate properly, which would make each optimization take an excessive amount of time. The main goal of the simulations, however, is to predict the performance of the port geometer, and this lumped parameter model can do that very well.

A.3 Objective Functions and Constraints

A total of five objective functions were used to optimize the performance of gerotor ports. The OF for the port optimization are referred to as OF1b, OF2b, etc to avoid confusion with the OF for the gear design optimization. The first OF for the port optimization is to minimize the signal power of the simulated flow ripple. It is defined in eq. (A.6) and is

the same as eq. (4.18), except it uses the simulated flow instead of the kinematic flow. The second OF is to minimize the pressure peaks in the displacement chamber which can lead to noise, vibration, and damage to the pump and other hydraulic components, and is defined in eq. (A.7), where $p_{\max}$ is the maximum displacement chamber pressure, p_{high} is the value of the delivery pressure, and Δp is the difference in pressure between the suction and delivery ports. The components of eq. (A.7) are illustrated in fig. A.6.

$$\text{OF1b: minimize}\{\bar{E}\} \tag{A.6}$$

$$\text{OF2b: minimize}\{\frac{p_{max} - p_{high}}{\Delta p}\} \tag{A.7}$$

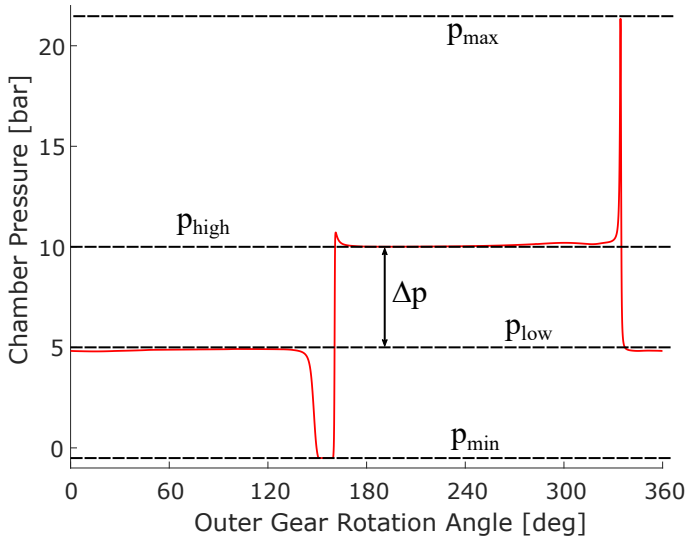

Figure A.6. Illustration of displacement chamber pressure values [57]

Two different OF were used to minimize the localized cavitation in a pump. Localized cavitation occurs when the pressure in the displacement chamber drops below the saturation pressure of the gasses dissolved in the fluid. Some of the gasses come out of the fluid, and the bubbles will implode when repressurized. This leads to noise generation and destruction of the pump surfaces in the form of pitting. A cavitation model is required to accurately

simulate the pump under these conditions, as the lumped parameter model used in this study simply saturates the pressure. A cavitation model that works with the lumped parameter approach has been developed [63], but its increased computation time makes it unsuitable for optimization. While the lumped parameter model used in this study does not predict pump operation under cavitating conditions with great accuracy, it can predict which designs should avoid operation in that regime, as pumps that avoid reaching saturation pressure are not expected to experience localized cavitation. The third OF for the study is defined in eq. (A.8), where p_{low} is the suction port pressure, and p_{min} is the minimum displacement chamber pressure. The suction port pressure was increased to 5 bar in the simulations so that a greater pressure dip could occur before reaching the saturation pressure for poor designs. A good port design will have a small pressure dip from the suction pressure.

$$\text{OF3b: minimize}\{p_{low} - p_{min}\} \tag{A.8}$$

Localized cavitation in a positive displacement pump is a function of both time and pressure. To account for the time aspect, eq. (A.9) defines a throttled pressure p_t, which is the magnitude of the pressure drop from the suction port. This function can be integrated to account for both the magnitude and duration of the pressure dip in a displacement chamber, which is the basis for OF4b defined in eq. (A.10). In general, OF3b and OF4b will be correlated strongly, but both are necessary to account for the exceptions. One exception would be a sharp pressure dip over a short period of time. This design would be penalized by OF3b but ignored by OF4b. In a similar fashion, designs with a displacement chamber pressure near the saturation pressure for a long time would be penalized by OF4b, but a design that only briefly nears saturation pressure would have the same value of OF3b as the one that is near the saturation pressure longer. Implementing these two simplified cavitation functions as OF instead of constraints helps the optimized pumps to be less sensitive to changes in operating conditions. A pump with a good value of OF3 and OF4 would be expected to perform well for many operating conditions, but a pump that would only meet

constraints for the two functions would perhaps only perform well at the operating conditions of the optimization.

$$p_t = \begin{cases} p_{low} - p & p \leq p_{low} \\ 0 & p > p_{low} \end{cases} \tag{A.9}$$

$$\text{OF4b: minimize} \left\{ \int_{\theta_o=0}^{\theta_0=2\pi} p_t \; dt \right\} \tag{A.10}$$

Another OF is required to improve pump performance. A pump with a very low volumetric efficiency can have very good values of OF1b-OF4b, e.g. a pump with significant cross porting won't have very large pressure peaks or dips. However, these pumps would not be very useful. Therefore OF5b is defined in eq. (A.11), where N is the inner gear rotation speed, and v is the kinematic displacement of the pump.

$$\text{OF5b: maximize} \left\{ \frac{\overline{Q}}{Nv} \right\} \tag{A.11}$$

In a multi-objective optimization, the algorithm will search for Pareto designs in every region of the design space. This can result in finding designs that have a good value of some OF but a very poor value in one or more OF such that the design would not be selected in a real application. For this reason, three constraints were imposed to give a maximum allowable value of OF2b and OF3b and a minimum allowable value of OF5b. This ensures that the algorithm searches for usable Pareto designs. The values of these constraints are shown in table A.3.

Table A.3. Constraints on OF values in port optimization

Constraint 1	OF2b $<$ 0.25 (pressure peak)
Constraint 2	OF3b $<$ 0.5bar (pressure dip)
Constraint 3	OF5b $>$ 0.95 (volumetric efficiency)

A.4 Results

After the optimization for each pump was completed, the Pareto designs were identified. As an example, the Pareto front for Pump 5 is shown in fig. A.7. The value of OF1b (flow

ripple) for each design is plotted on the x-axis, the value the OF2b (pressure peak) for each design is plotted on the x-axis the y-axis axis, the value the OF3b (pressure dip) for each design is plotted as the marker size, and the value the OF4b (inlet throttle) for each design is plotted as the marker color. Although only 1500 port designs were evaluated for each gearset, fig. A.7 shows that the Pareto front was still clearly identified. fig. A.7 also shows that the designs with the lowest values of OF1b (flow ripple) had higher values of the other OF.

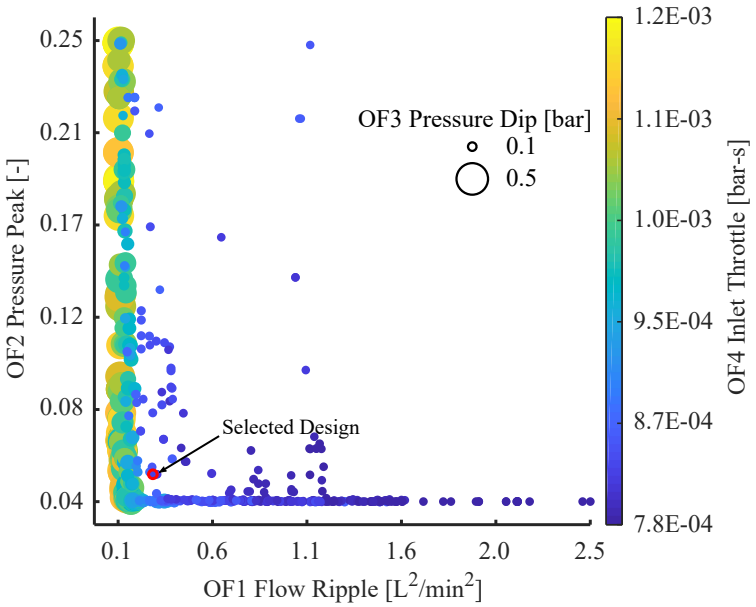

Figure A.7. Plot of Pareto front for port designs for Pump 5 [57]

After the Pareto front is marked, the designer must select a single design based on the perceived relative importance of each OF. One way to select a design is to use a parallel coordinates chart in fig. A.8. A parallel coordinates chart represents each design as a line that connects the value of each of the designs OFs plotted on the y-axis. The advantage of a parallel coordinates chart is that it can display all of the designs and their values on the same plot, but it can become crowded as the number of designs plotted increases. A design can be selected by eliminating designs with any of their OF values worse than threshold values represented as black bars in fig. A.8. If any of a design's OF values are worse than their threshold value, the design is plotted as a grey line, but if all of a design's OF values are

better than their threshold values, the design is plotted as a blue line. The threshold values can be adjusted heuristically until only a single design remains. In this case, the design was selected that gave good performance regarding every OF, but it was not the best for any single OF. The selected design from the parallel coordinates chart in fig. A.8 is plotted in fig. A.7 with a red outline.

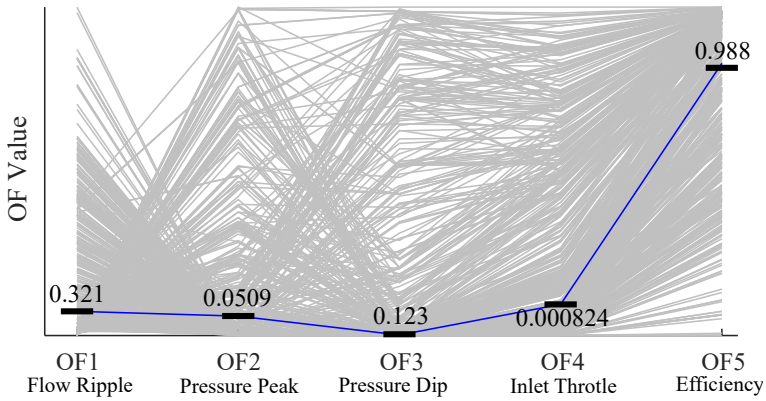

Figure A.8. Parallel coordinates chart of port designs for Pump 5 [57]

An optimal port design for Pumps 1-4 was selected in the same manner as for Pump 5, and the selected ports for each pump is shown in fig. A.9, and the input variables for the selected designs are shown in table A.4. In fig. A.9, each gearset is plotted in two positions so that both the minimum and maximum displacement chamber area positions are visible. Each of the selected designs share some common design features. The timing of θ_2 is advanced so that sufficient flow area is present for fluid to enter the displacement chamber. Then θ_2 is adjusted so that the displacement chamber pressurizes without cross porting or pressure peaks as it connects to the delivery port. Similarly, the timing of θ_3 is advanced to prevent pressure peaks as the fluid exits the displacement chamber through a restricted volume. Then θ_1 is adjusted to achieve the correct pressurization as the displacement chamber overlaps the suction chamber again.

The performance of the optimized ports is compared to that of the kinematic ports and the ideal kinematic flow ripple as well in fig. A.10. In fig. A.10, the OF values were normalized to the worst values found in the study overall to give a better relative comparison

Table A.4. Input variables of selected port designs

	$d\theta_1$ [deg]	$d\theta_2$ [deg]	$d\theta_3$ [deg]	$d\theta_4$ [deg]
Pump 1	-1.62	3.89	1.76	0.75
Pump 2	-5.97	4.15	1.54	3.12
Pump 3	-3.82	3.61	0.12	0.55
Pump 4	-2.56	4.67	-0.38	1.18
Pump 5	-6.82	6.25	-0.15	0.76

between the pumps. Note that for Pump 1, the signal power of the kinematic flow ripple is so small that it is hardly visible on the plot. For each pump, a design was found that could significantly improve the performance of OF1b-OF4b without impacting the performance of OF5b, which indicates that the optimization procedure was successful. However, even the optimized designs had a significantly greater flow ripple than the idealized kinematic flow ripple, which shows the importance of accounting for fluid dynamic effects in pump design.

Another way to view the improvement in the pump performance with the optimized ports is shown in fig. A.11 for Pump 5. In fig. A.11, the simulated displacement chamber pressures with the kinematic and optimized ports is displayed, and the reduction in pressure dips and peaks is very evident. A comparison between the ideal kinematic, simulated kinematic, and simulated optimal flow ripples is shown in fig. A.12. By inspection, the optimized port performance improves the outlet flow ripple over the simulated kinematic flow ripple, but the ideal kinematic flow ripple is better than both. Similar observations were made for Pumps 1-4 as well.

This study shows that the kinematic flow ripple is not a good predictor of the actual flow ripple when considering fluid dynamic effects, but it does predict the trend correctly. The signal power of the kinematic flow ripple and the simulated flow ripple with optimized ports for each pump is plotted in fig. A.13. It shows that the signal power of the kinematic flow ripple predicts the trend of the signal power of the simulated flow ripples with optimized ports almost linearly.

The correlation of the kinematic flow ripple with the simulated flow ripples at higher pressure was also tested by simulating the pumps again at 2000 rpm and 50 bar. This tests the correlation not only at higher pressures, but also at operating conditions that deviate

from the operating conditions of the optimization to test the correlation with well-designed but not optimized ports. The selected port designs are expected to perform well at a different operating condition, but the change in pressure means that the selected designs are likely no longer optimal for that operating condition. The results of this comparison are shown in fig. A.14. Again, the kinematic flow ripple predicts the correct trend of the simulated flow ripples even though the signal power of the simulated flow ripples was greater. This further validates the use of the kinematic flow ripple as an OF for gear optimization

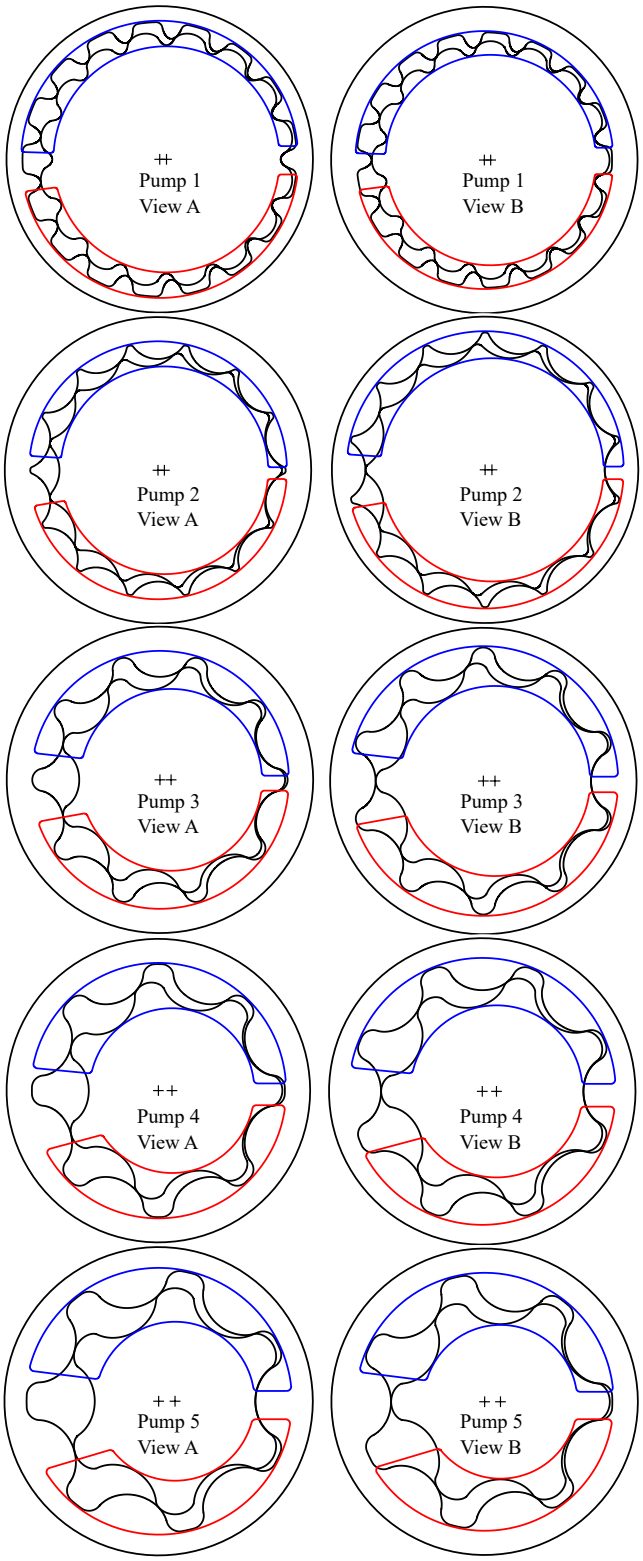

Figure A.9. Test pumps with optimized port designs [57]

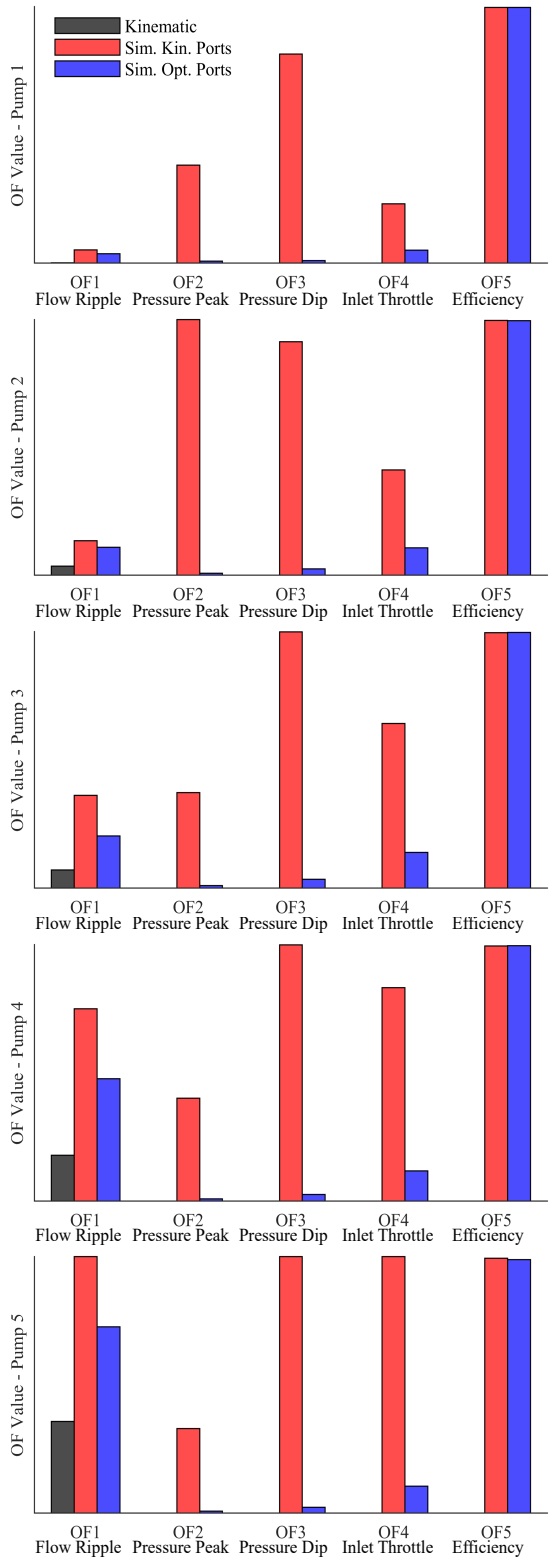

Figure A.10. Comparison of port performance [57]

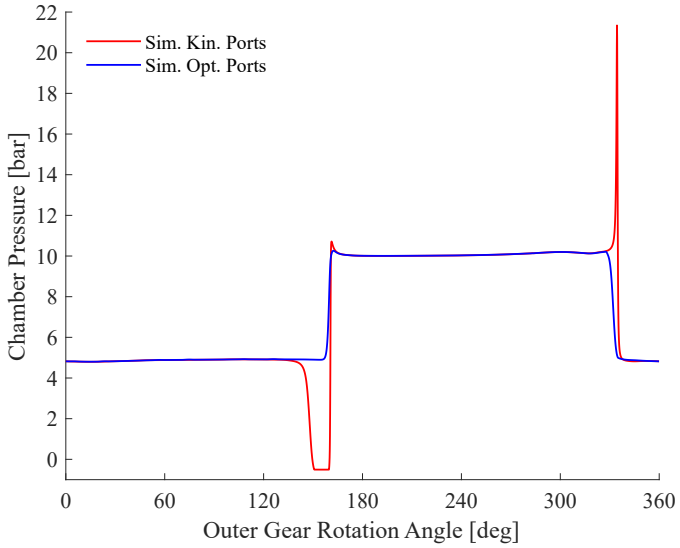

Figure A.11. Simulated displacement chamber pressure with optimized ports [57]

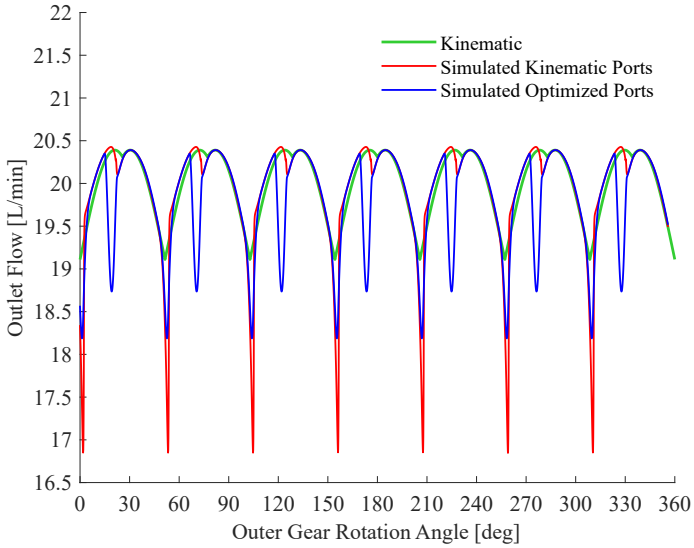

Figure A.12. Simulated flow with optimized ports [57]

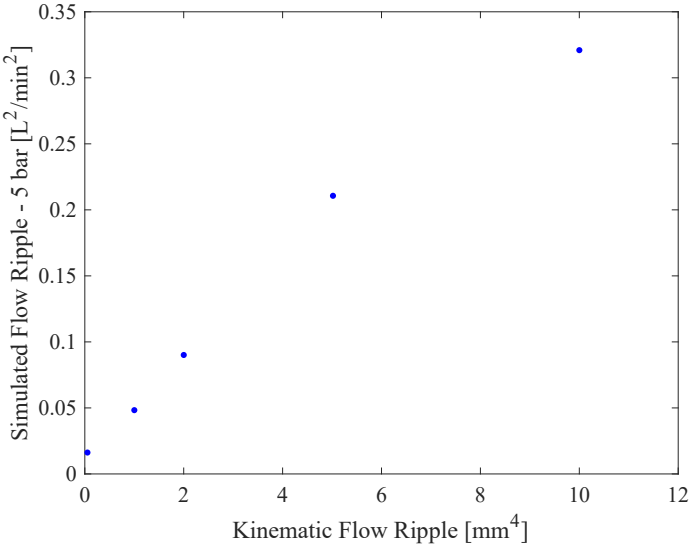

Figure A.13. Correlation of kinematic flow ripple and simulated flow ripple with optimized ports at 5 bar [57]

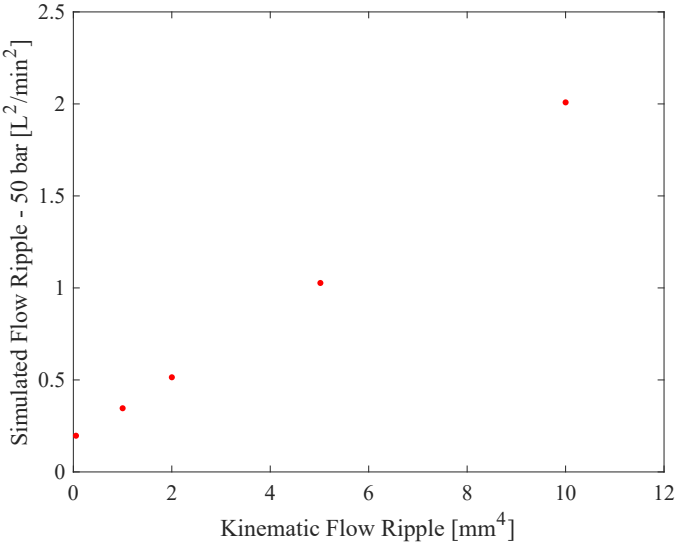

Figure A.14. Correlation of kinematic flow ripple and simulated flow ripple with optimized ports at 50 bar [57]

A.5 Conclusions of Study

Because the kinematic flow ripple neglects important fluid dynamic effects such as compressibility and internal leakages, its value as an OF for gear design needed to be tested. To test this, five pumps with different kinematic flow ripples were selected to test in simulation to compare the kinematic flow ripple with the simulated flow ripple. Because ports with ideal timing perform poorly due to the presence of pressure peaks and dips when considering compressibility, a design procedure is necessary to match each test gearset with a good port design. Ports for each test gearset were designed by multi-objective optimization for five OF: minimize outlet flow ripple, minimize pressure peaks, minimize pressure dips, minimize inlet throttling, and maximize volumetric efficiency. A port design for each gearset was selected from the results of each optimization that offered good performance regarding all five OF. The kinematic flow ripples were compared to the simulated flow ripples for pumps with the optimized ports. This showed that the kinematic flow ripple is a poor predictor of the simulated flow ripple, but that it predicts the trend of the simulated flow ripples at both low and medium pressures. This indicates that the signal power of kinematic flow ripple is a suitable OF for gerotor gear design.

VITA

Andrew Robison was born in 1991 in Brookings, South Dakota. After finishing high school in Minnesota, he attended South Dakota State University and received a BS in Mechanical Engineering, a BS in Chemistry, and a BA in German in 2014. After working for a non-profit organization in Berlin, Germany for a year, Andrew began his PhD studies at Purdue University under the supervision of Prof. Andrea Vacca in 2015. During his first year of studies, Andrew received a National Science Foundation Graduate Research Fellowship. Then in 2020 in the midst of a global pandemic, he married the love of his life Emily. He has recently began work as a Research Engineer for Med Institute in West Lafayette, Indiana where he will focus on the development and testing of medical devices.

PUBLICATIONS

Journal Articles

Robison, A., Vacca, A., 2021, "Performance comparison of epitrochoidal, hypotrochoidal, and cycloidal gerotor gear profiles," Mechanism and Machine Theory, 158, DOI: 10.1016/j.mechmachtheory.2020.104228.

Robison, A., Vacca, A., 2018, "Multi-objective optimization of circular-toothed gerotors for kinematics and wear by genetic algorithm," Mechanism and Machine Theory, 128, pp 150-168, DOI:10.1007/s11012-018-0852-0.

Conference Papers

Robison, A., Vacca, A., 2020, "Design of Asymmetric Gerotor Pumps.," NSHP 2020: Advances in Hydraulic and Pneumatic Drives and Control 2020, pp 90-101, DOI: 10.1007/978-3-030-59509-8_8.

Robison, A., Vacca, A., 2019, "Multi-Objective Optimization of Modified Cycloidal-Toothed Gerotor Pumps by Genetic Algorithm," ASME/Bath Symposium on Fluid Power and Motion Control, Oct. 7-9, 2019, Sarasota, FL, USA.

Robison, A., Vacca, A., 2019, "Multi-Objective Optimization of Gerotor Port Design by Genetic Algorithm with Considerations on Kinematic vs. Actual Flow Ripple," SAE WCX 2019, April 9-11, 2019, Detroit, MI, USA.

Robison, A., Vacca, A., 2018, "Multi-Objective Geometric Optimization of Elliptical-toothed Gerotor Pumps for Kinematics and Wear by Genetic Algorithm," ASME/Bath Symposium on Fluid Power and Motion Control, Sep 12-14, 2018, University of Bath, United Kingdom. **Best Paper Award**

Robison, A., Vacca, A., 2017, "Kinematic Multi-Objective Optimization of Circular-Toothed Gerotor Pumps by Genetic Algorithm," ASME/Bath Symposium on Fluid Power and Motion Control, Oct. 16-19, 2017, Sarasota, FL, USA.